New Regularization Method for EXAFS Analysis

Application to Uranium and Plutonium Sorption onto Kaolinite

Dissertation
zur Erlangung des Grades

"Doktor der Naturwissenschaften"

im Promotionsfach Kernchemie

am Fachbereich Chemie, Pharmazie
und Geowissenschaften
der Johannes Gutenberg-Universität Mainz

Tatiana Reich
geb. in Tscheljabinsk/Russland

Mainz, 2008

Dekan:

1. Berichterstatter:
2. Berichterstatter:

Tag der mündlichen Prüfung: 11.11.2008

To my husband
and all who enjoy EXAFS

INDEX

ACRONYMS, ABBREVIATIONS, and SYMBOLS

α	Regularization parameter
Å	Ångstrom (10^{-10} m)
$A(k,r)$	Kernel of EXAFS equation
ANKA	Angströmquelle Karlsruhe (Germany)
$\chi(E)$	Normalized oscillating part of the X-ray absorption in energy space
$\chi(k)$	Normalized oscillating part of the X-ray absorption in *k* space
$\chi(r)$	Fourier transformed pseudo radial distribution function
c	Speed of light, $2.998\times10^{8}\, m\cdot s^{-1}$
C	Concentration of an element in a material
$\delta_c(k)$	Phase shift on atomic potential of absorbing atom
DCM	Double-crystal monochromator
$\hat{\epsilon}\cdot r$	Dipole operator
E	X-ray photon energy, eV
E_0	Absorption threshold energy, eV
ESRF	European Synchrotron Radiation Facility (France)
eV	Electron volt, $1eV = 1.602\times10^{-19}\, J$
EXAFS	Extended X-ray absorption fine structure
$\left\|f_{eff}(k)\right\|$	Effective backscattering amplitude
F	Goodness of fit in least-square fitting method
$\Phi(k)$	Phase shift on atomic potential of neighboring atom
FT	Fourier transformation
FWHM	Full width at half-maximum, Å
$g(r)$	Partial radial atomic distribution function
$\hbar$	Planck's constant, $\hbar = h/2\pi = 6.582\times10^{-16}\, eV\cdot s$
I	Transmitted X-ray photon intensity
I_0	Incident X-ray photon intensity
I_f	Intensity of fluorescence radiation
I_{pp}	Identity matrix of size *p*
INE	Institut für Nukleare Entsorgung (Germany)
k	Photoelectron wave number, $Å^{-1}$
λ	De Broglie wavelength
$\lambda(k)$	Photoelectron mean-free path

Λ	Value of separating functional
$\mu(E)$	Experimental X-ray absorption coefficient, cm^2/g
$\mu_0(E)$	Atomic background absorption, cm^2/g
$\Delta\mu_0(E_0)$	Jump in the atomic background absorption, cm^2/g
μM	Micromol (10^{-6} mol L^{-1})
m	Electron rest mass, $9.1094\times10^{-31}\ kg$
M	Tikhonov functional
MS	Multiple scattering
ν	X-ray photon frequency, s^{-1}
N	Coordination number or number of equivalent scatterers
N_P	Number of independent parameters in least-square fitting method
ψ_i	Initial state wave function
ψ_f	Final state wave function
$\psi(k)$	Total phase shift, $\psi(k)=2\delta_c(k)+\Phi(k)$
$\langle\psi_f\|\psi_i\rangle$	Transition matrix element
pH	Negative logarithm (base 10) of hydrogen ion concentration
ppm	parts per million
PRDF	Pseudo radial distribution function
ρ_0	Density of a material
$\rho(T)$	Density of available final states
r	Interatomic distance, Å
ΔR	Expected resolution in distance in PRDF, Å
RDF	Partial radial distribution function
ROBL	Rossendorf Beamline
RSMS	Real space multiple scattering theory
σ^2	Debye-Waller factor, $Å^2$
S_0^2	Overall amplitude factor
SS	Single scattering
τ	Peak width in RDF
T	Kinetic energy of photoelectron, eV
$\hat{U}$	Separating functional
$W(k)$	Window function
x	Surface density of absorbing material, g/cm^2
XAFS	X-ray absorption fine structure

XANES	X-ray absorption near-edge structure
XRD	Single-crystal X-ray diffraction

SUMMARY

Extended X-ray absorption fine structure (EXAFS) spectroscopy is a powerful tool for direct speciation of heavy metals in a wide range of environmentally relevant systems. To determine structural parameters, i.e., coordination numbers (*N*), interatomic distances (*r*), and Debye-Waller factors (σ^2) for the near-neighbor surrounding of an absorbing atom, it is common to perform least-squares fits to experimental EXAFS spectra using structural models. However, often several structural models with completely different chemical implications can describe the experimental EXAFS data equally well.

As an attractive alternative to conventional curve fitting, the modified Tikhonov regularization method has been proposed. In addition to the standard variation Tikhonov method, the algorithm proposed in this work contains two more steps, i.e., the application of the method of separating functionals [1] and an iteration procedure with filtration in real space [2].

To test and validate the modified Tikhonov regularization method, both theoretically simulated and experimentally measured EXAFS spectra of a crystalline U(VI) compound of known structure, i.e., soddyite $(UO_2)_2SiO_4$ x $2H_2O$ were analyzed [3]. The potential of this new approach is illustrated by applying it to the EXAFS analysis of samples with unknown structures, i.e., surface complexes of U(VI) and Pu(III)/Pu(IV) sorbed onto kaolinite [4].

Generally, the dissertation has been devoted to demonstrate the still not fully exploited potential of the modified regularization method for the evaluation of EXAFS data. The results can be divided into two categories. The first contains the development of the Tikhonov regularization method for the analysis of EXAFS spectra of multi-component systems, including some important recommendations such as the choice of regularization parameters or the influence of multi-scattering contributions, experimental data noise, etc. on the derived structural parameters (i.e., *r, N,* σ^2). The second category includes the speciation of U(VI) and Pu(III)/Pu(IV) sorbed onto kaolinite, based on experimental EXAFS spectra, which were analyzed by the modified regularization method, and confirmed by the results of the conventional EXAFS analysis by means of least-squares fitting.

[1] A.L. Ageev, T.V. Antonova, T.Ye. Reich, T. Reich, C. Hennig: Method of separating functionals for extracting local atomic structure. *Math. Modelling* **16**, 81 - 92 (2004) (in Russian).

[2] A.L. Ageev, M.E. Korshunov, T.Ye. Reich, T. Reich, H. Moll: Application of regularization methods to analysis of EXAFS spectra in chemical complexes. *J. Inverse Ill-Posed Problems* **15**, 767 - 784 (2007).

[3] T.Ye. Reich, M.E. Korshunov, T.V. Antonova, A.L. Ageev, H. Moll, T. Reich: New regularization method for EXAFS analysis. (Conference Proceedings of 13th International Conference (XAFS13), 2006) *Am. Inst. Phys.* **882**, 153 – 155 (2007).

[4] T.Ye. Reich, N.L. Banik, R.A. Buda, S. Amayri, J. Drebert, J.V. Kratz, N. Trautmann, A.L. Ageev, M.E. Korshunov, T. Reich: EXAFS study of plutonium sorption onto kaolinite. (Workshop Proceedings „Speciation, Techniques and Facilities for Radioactive Materials at Synchrotron Light Sources", 2006) *OECD* **6288**, 273 – 279 (2007).

ZUSAMMENFASSUNG

Die Röntgenabsorptionsspektroskopie (Extended X-ray absorption fine structure (EXAFS) spectroscopy) ist eine wichtige Methode zur Speziation von Schwermetallen in einem weiten Bereich von umweltrelevanten Systemen. Um Strukturparameter wie Koordinationszahl (*N*), Atomabstand (*r*) und Debye-Waller Faktoren (σ^2) für die nächsten Nachbarn eines absorbierenden Atoms zu bestimmen, ist es für experimentelle EXAFS-Spektren üblich, unter Verwendung von Modellstrukturen einen „Least-Squares-Fit" durchzuführen. Oft können verschiedene Modellstrukturen mit völlig unterschiedlicher chemischer Bedeutung die experimentellen EXAFS-Daten gleich gut beschreiben. Als gute Alternative zum konventionellen Kurven-Fit bietet sich das modifizierte Tikhonov-Regularisationsverfahren an. Ergänzend zur Tikhonov-Standardvariationsmethode enthält der in dieser Arbeit vorgestellte Algorithmus zwei weitere Schritte, nämlich die Anwendung des „Method of Separating Functionals" [1] und ein Iterationsverfahren mit Filtration im realen Raum [2].

Um das modifizierte Tikhonov-Regularisationsverfahren zu testen und zu bestätigen wurden sowohl simulierte als auch experimentell gemessene EXAFS-Spektren einer kristallinen U(VI)-Verbindung mit bekannter Struktur, nämlich Soddyit $(UO_2)_2SiO_4 \times 2H_2O$, untersucht [3]. Die Leistungsfähigkeit dieser neuen Methode zur Auswertung von EXAFS-Spektren wird durch ihre Anwendung auf die Analyse von Proben mit unbekannter Struktur gezeigt, wie sie bei der Sorption von U(VI) bzw. von Pu(III)/Pu(IV) an Kaolinit auftreten [4].

Ziel der Dissertation war es, die immer noch nicht voll ausgeschöpften Möglichkeiten des modifizierten Tikhonov-Regularisationsverfahrens für die Auswertung von EXAFS-Spektren aufzuzeigen. Die Ergebnisse lassen sich in zwei Kategorien einteilen. Die erste beinhaltet die Entwicklung des Tikhonov-Regularisationsverfahrens für die Analyse von EXAFS-Spektren von Mehrkomponentensystemen, insbesondere die Wahl bestimmter Regularisationsparameter und den Einfluss von Mehrfachstreuung, experimentell bedingtem Rauschen, etc. auf die Strukturparameter (*r, N,* σ^2). Der zweite Teil beinhaltet die Speziation von sorbiertem U(VI) und Pu(III)/Pu(IV) an Kaolinit, basierend auf experimentellen EXAFS-Spektren, die mit Hilfe des modifizierten Tikhonov-Regularisationsverfahren ausgewertet und mit Hilfe konventioneller EXAFS-Analyse durch „Least-Squares-Fit" bestätigt wurden.

[1] A.L. Ageev, T.V. Antonova, T.Ye. Reich, T. Reich, C. Hennig: Method of separating functionals for extracting local atomic structure. *Math. Modelling* **16**, 81 - 92 (2004) (in Russian).

[2] A.L. Ageev, M.E. Korshunov, T.Ye. Reich, T. Reich, H. Moll: Application of regularization methods to analysis of EXAFS spectra in chemical complexes. *J. Inverse Ill-Posed Problems* **15**, 767 - 784 (2007).

[3] T.Ye. Reich, M.E. Korshunov, T.V. Antonova, A.L. Ageev, H. Moll, T. Reich: New regularization method for EXAFS analysis. (Conference Proceedings of 13th International Conference (XAFS13), 2006) *Am. Inst. Phys.* **882**, 153 – 155 (2007).

[4] T.Ye. Reich, N.L. Banik, R.A. Buda, S. Amayri, J. Drebert, J.V. Kratz, N. Trautmann, A.L. Ageev, M.E. Korshunov, T. Reich: EXAFS study of plutonium sorption onto kaolinite. (Workshop Proceedings „Speciation, Techniques and Facilities for Radioactive Materials at Synchrotron Light Sources", 2006) *OECD* **6288**, 273 – 279 (2007).

1. INTRODUCTION

Extended X-ray absorption fine structure (EXAFS) spectroscopy is a powerful tool for the determination of the local atomic structure, i.e., the species of atoms present and their locations in amorphous materials, solid solutions and liquids. Usually, the near-neighbor surrounding of absorbing atoms contains different types of atoms, e.g., oxygen, silicon, uranium or other elements. Except for the preliminary treatment of the raw data, the difficulty in the EXAFS analysis consists in the determination of several partial radial distribution functions (RDFs), i.e., one RDF for each type of neighboring atom (O, Si, U, etc.) from one EXAFS spectrum. Precise extracting of RDFs in often complicated, multi-element materials is especially difficult, even with refined experimental techniques (synchrotron X-ray sources) and good standard data-analysis packages currently available.

To solve this problem, the conventional EXAFS analysis based on one or several assumed structural models for the near-neighbor environment of the central atom is commonly used. The best theoretical model and its corresponding structural parameters, i.e., coordination numbers, interatomic distances, and Debye-Waller factors for each coordination shell, are determined by least-squares fits to the experimental data. However, often several structural models with completely different chemical implications can describe the experimental EXAFS data equally well.

To increase the reliability of EXAFS structural parameters, it is extremely useful to have alternative approaches to the analysis of EXAFS data. In the early 1980's, the Tikhonov regularization method has been proposed as an attractive alternative to conventional curve fitting method and a new strategy for the EXAFS data evaluation by the physicist Yu.A. Babanov. All physical reasoning behind his suggestion has been based on the mathematical foundation developed by V.V. Vasin and A.L. Ageev. The first software for a one-component system was created in this time in close cooperation between the mathematicians (V.V. Vasin and A.L. Ageev) and physicists (Yu.A. Babanov, N.V. Ershov, V.R. Shvetsov, A.V. Serikov). The direct determination of the RDFs without the need for a structural model was the advantage of this method. A little bit later, the Tikhonov regularization method was adapted to the case of a two-component system. Only twenty years later, the method was developed further for a three-component system (Yu.A. Babanov, T.Ye. Zayarnaya, A.N. Deev, A.F. Sidorenko, A.V. Ryazhkin). All this time, in a relative narrow circle of specialists, the method has been used successfully, but the difficulty in the EXAFS analysis was always the determination of several RDFs, i.e., one RDF for each type of neighboring atom, from one EXAFS spectrum. Frequently, RDFs with different physical or chemical meaning satisfied the solution of the EXAFS equation with nearly identical accuracy.

In the framework of this dissertation, a special mathematical technique is developed to include specific *a priori* physical and chemical information into the procedure for the determination of RDFs. To include *a priori* information, it is necessary that the near-neighbor environment of the central atom has a well-defined short-range ordering. The main idea suggested by the author of this dissertation is to use separating functionals that allow determining intervals in the RDFs where "true" coordination shells are absent. The experimental EXAFS spectra can be analyzed successfully if the standard Tikhonov regularization method is applied to intervals of the RDF where potential "true" coordination shells have been identified. Then the process is iterated until the RDFs functions have converged. The essential mathematical principals underlying this modified Tikhonov regularization method as well the data analysis procedure contained in a suite of programs were written by A.L. Ageev, T.V. Antonova, and M.E. Korshunov at the Institute of Mathematic and Mechanic, Ural Division of Russian Academy of Science, Ekaterinburg.

The evaluation of the modified regularization method to provide reliable structural information from EXAFS data was performed by the author of this dissertation. To test and validate the modified Tikhonov regularization method, both theoretically simulated and experimentally measured EXAFS spectra of a compound with known crystal structure, soddyite $(UO_2)_2SiO_4 \times 2H_2O$, were analyzed. In particular, the calculations show the possibilities and the limitations of the modified regularization Tikhonov method in application to systems containing uranium, oxygen and silicon or aluminium.

The potential of this new approach is illustrated by applying it to the EXAFS analysis of the unknown structures formed by adsorption of U(VI) and Pu(III)/Pu(IV) onto kaolinite.

The structural parameters obtained by the modified regularization method for soddyite and U(VI) sorption samples onto kaolinite were compared to XRD data and results of previous EXAFS studies.

Generally, this thesis is organized as follows:

Section 2 presents the basic concepts of the XAFS method. This description is intended as an overview of the theory, experimental aspects, and data analysis. A number of strategies for the EXAFS data evaluation are also presented ranging from the least-squares fitting and log-ratio/phase difference cumulant methods up to the standard Tikhonov regularization method.

Section 3 describes the methodological development of the Tikhonov regularization method. For clarity, the underlying theoretical aspects are divided into several subsections: Subs. 3.2 gives a brief description of the variation Tikhonov method, Subs. 3.3 introduces the general ideas dedicated to the method of separating functional,

Subs. 3.4 is devoted to the iteration procedure, and Subs. 3.5 shows how the structure parameters are calculated from the final RDFs of the EXAFS data.

To test the modified Tikhonov regularization method (Sect. 4), the simulated (Subs. 4.2.1) and experimental (Subs. 4.2.2) EXAFS spectra of soddyite are analyzed. The EXAFS analysis of spectra measured for U(VI) sorption onto kaolinite is given in Subs. 4.3. The mechanism of U(VI) sorption onto kaolinite as a function of several solution parameters, such as pH, U(VI) concentration, and the presence or absence of CO_2, is also discussed in Subs. 4.3. In Subs. 4.4 the new approach was applied to the EXAFS analysis of the Pu(III)/Pu(IV) sorption samples onto kaolinite.

Section 5 gives the conclusions and discusses advantages, limitations, and perspectives of the modified Tikhonov regularization method.

2. EXAFS GENERAL CONCEPTS

Roughly 70 years have elapsed since the phenomenon of EXAFS was first observed, and it has taken nearly that long to realise that accurate, detailed, structural information could be extracted from it and to develop a quantitative theory.

J. J. Rehr (EXAFS classic - 2000)

2.1 Fundamental physics of X-ray absorption

The process in which an X-ray photon is absorbed by transferring all of its energy to a deep core electron of an atom is called "*photoelectric effect*" [1]. If the energy of the incident X-ray photon is larger than the absorption threshold energy E_0, the photon excites an atomic core-orbital electron to a free or unoccupied continuum level (ionization of the core orbital). The transition is always to a state above the Fermi energy. The resulting excited electron is often referred to as photoelectron and has a defined kinetic energy $h\nu - E_0 = \hbar^2 k^2 / 2m$ (where k is the photoelectron wave number and m the electron mass) to move through the material (Fig. 1).

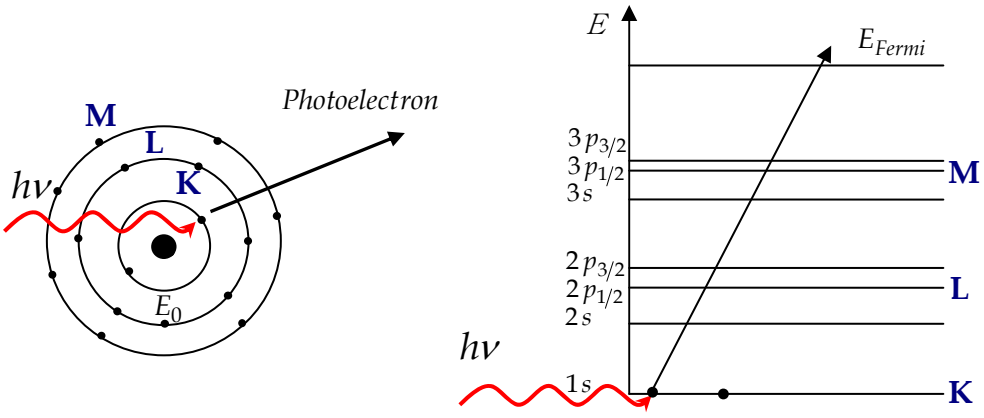

Fig. 1: Schematic view of the photoabsorption process through the "*photoelectric effect*". The nomenclature for X-ray absorption reflects the origin in the core orbital.

The absorbing atom is left in an excited state with an empty electronic level (a core hole). Immediately, the excited core level will relax back to a stable "ground state" of the atom. A core electron from a higher level drops into the core hole giving off a characteristic X-ray whose energy is the difference between the binding energies of the involved core levels. The emitted X-ray is called fluorescent X-ray and the process - "*X-ray Fluorescence*" (Fig. 2).

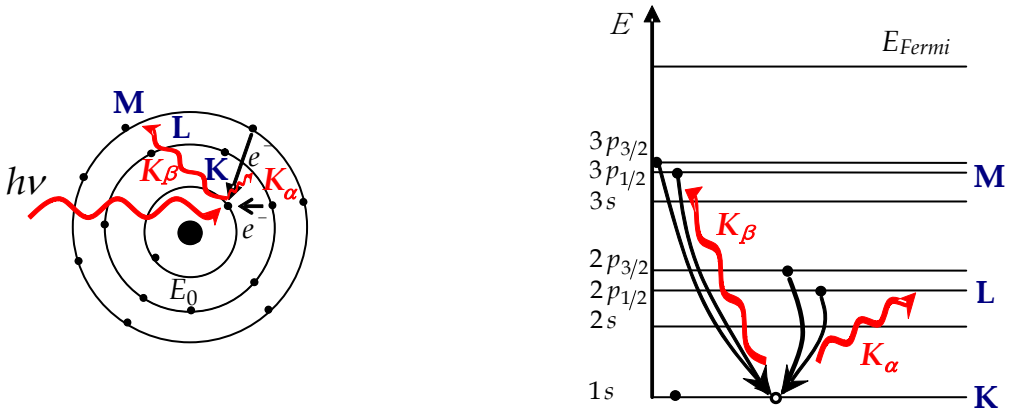

Fig. 2: The phenomenon of *X-ray Fluorescence*: Fluorescent X-ray is emitted with an energy characteristic for the absorbing atom. K_α lines are produced from transition of electrons from L to K shell. K_β lines are produced from transition of electrons from M to K shell.

Both ionization and fluorescent X-ray energies are unique to the type of atom that absorbs the incident X-ray photon, and hence themselves are signatures of the atomic species present in a material.

2.2 X-ray absorption data collection at synchrotron radiation sources

The absorption and fluorescence data are taken at synchrotron sources as a function of the incident X-ray photon energy $E = h\nu$ [2, 3]. The main elements of the beamline optics of standard design are a double-crystal monochromator (DCM) located between two bendable mirrors. The mirrors suppress the higher-order harmonics in the monochromatic beam, reduce the heat load on the monochromator, and collimate and focus the beam vertically. The DCM is equipped with a pair of Si(111) crystals and provides a fixed-exit beam [4, 5]. The scheme of a typical beamline for X-ray absorption spectroscopy is shown in Fig. 3.

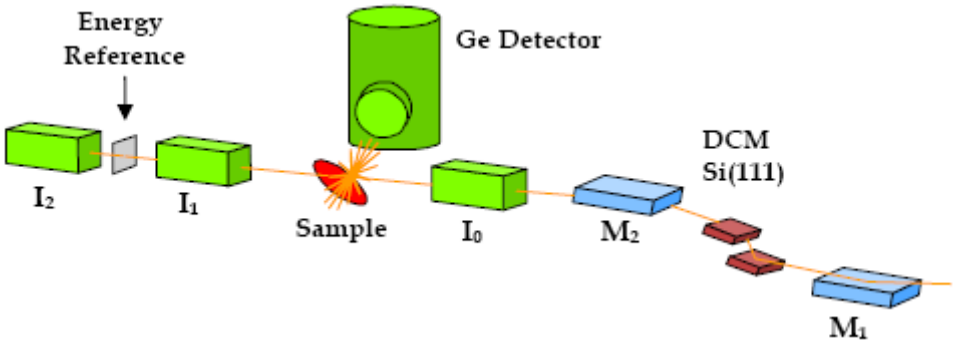

Fig. 3: Schematics of a beamline for X-ray absorption spectroscopy measurements at a synchrotron radiation source. I_0, I_1, I_2 are gas ionization chambers. DCM is a double-crystal monochromator. M_1, M_2 are two mirrors coated with Si/Pt stripes.

The X-ray absorption coefficient $\mu(E)$ can be measured in two ways. In transmission mode, $\mu(E)x=\ln(I_0/I)$ is determined directly from the decrease of the X-ray intensity I with thickness x of absorbing material. The intensity of the incoming X-ray beam I_0 is measured by the first gas ionization chamber I_0 (Fig. 3). After the X-ray beam has traversed a distance x in the sample, the intensity has been reduced to $I=I_0 e^{-\mu x}$ and is measured by the gas ionization chamber I_1. To calibrate the energy of the monochromatic beam, the absorption signal of a reference sample can be recorded by the chamber I_2 together with the sample spectrum.

In fluorescence mode, the re-filling of the core-electron hole is detected. The sample is positioned at 45° with respect to the incident X-ray beam, and the fluorescence radiation I_f is collected with a Ge solid-state detector. The absorption coefficient $\mu(E)\propto I_f/I_0$ is directly proportional to the fluorescence signal I_f. The fluorescence technique gives better data than the transmission mode when the absorption signal of the investigated element is less than a few percent of the total absorption.

The X-ray absorption coefficient $\mu(E)$ measured as function of E in transmission mode is shown in Fig. 4 for the L_I, L_{II}, and L_{III} edges of uranium.

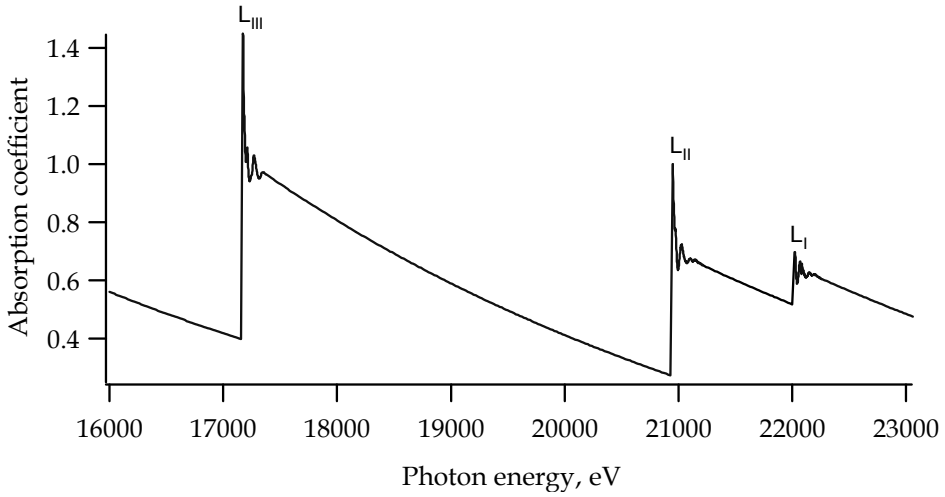

Fig. 4: Transmission mode: X-ray absorption coefficient is collected for L_I - L_{III} edges of uranium by scanning the DCM through the incident photon energies.

2.3 X-ray absorption spectra and XAFS

The X-ray absorption spectra **(**Fig. 4) reveal the following general features:

1) Overall, the absorption coefficient decreases smoothly with increasing energy;
2) When the photon energy reaches the critical value for a core-electron transition, a sharp rise of the absorption coefficient called absorption edge is observed;

3) An oscillatory structure in the X-ray absorption coefficient extending typically over ~700 eV above the absorption edge;

These features can be explained in terms of the well-understood quantum-mechanical phenomenon of X-ray absorption by atoms [6]. According to the one-electron and dipole approximations of Fermi's "golden rule", the X-ray absorption coefficient of the absorbing atom *a* is calculated as:

$$\mu_a \propto \sum_f \left| \left\langle \psi_f \left| \hat{\epsilon} \cdot r \right| \psi_i \right\rangle \right|^2 \rho(T), \quad (1)$$

where $\left\langle \psi_f \left| \psi_i \right\rangle \right.$ is the transition matrix element between the photoelectron wave function of the final state ψ_f and the initial state ψ_i of a core electron; $\hat{\epsilon} \cdot r$ is the dipole operator for the incident electromagnetic wave interacting with the material; $\rho(T)$ is the density of available final states of the photoelectron, and the sum is over all energies above the Fermi energy.

A value of μ for the defined kinetic energy $T = h\nu - E_i$ of the photoelectron is given by a transition matrix element squared. The matrix element is nonzero only in the region where the core state is nonzero – that is, near the centre of the absorbing atom. Consequently, for highly localized core electrons the transition matrix element is defined only by the value of the final state wave function ψ_f close to the absorbing atom. If the core electron is excited into the continuum, the initial state corresponds to the ground state of the atom (electron in a deep core level) and the final state includes both the ionized core level and the photoelectron wave.

The short-range-order theory [7] reflects the quantum-mechanical wavelike nature of the final, excited photoelectron state. For an isolated atom, the photoelectron can be viewed as an outgoing spherical wave as shown in Fig. 5 by solid lines. If the absorbing atom has a neighboring atom, the outgoing photoelectron wave will be backscattered, thereby producing an incoming electron wave. The final state is then the sum of the outgoing wave and all the incoming waves from each neighboring atom (dashed lines in Fig. 5).

For a wave reflected straight back by a neighboring shell of atoms (this type of scattering is often called "single scattering" or "backscattering"), the phase difference between outgoing and incoming waves is approximately $2kr$, where *r* is the distance to the shell of atoms and $k=2\pi/\lambda$, λ being the de Broglie wavelength. Thus λ decreases with increasing energy, and the modulation in μ arises from the alternating constructive or deconstructive interferences between outgoing and incoming waves as the photon energy is varied. The amount of interference also depends on the strength of the reflection from the neighboring atoms (the backscattering amplitude) and the number of scattering atoms.

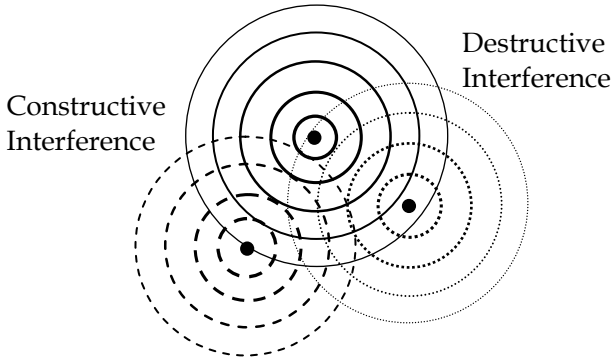

Fig. 5: Schematic view of the backscattering of an outgoing wave off neighboring atoms. The topmost atom indicated by the solid line is the original source of the wave. The dashed lines correspond to the scattering waves from the surrounding atoms. Depending on the wavelength of the photoelectron λ and the length of the scattering pathway, the scattered wave can interfere constructively or destructively with the photoelectron wave at the absorbing atom. The outgoing spherical wave gets weaker with the distance, which is reflected in the thickness of the lines symbolizing the spherical wave fronts.

The modulations of the X-ray absorption coefficient at energies near and above an X-ray absorption edge are known as X-ray Absorption Fine Structure (XAFS) [8]. They are a direct consequence of the wave nature of the photoelectron. Thus, an excited photoelectron state is not infinitely long lived, but must decay as a function of time and distance, hence XAFS can only reflect the local electronic and atomic structure of the atom in a sample over a range limited by the net lifetime (or effective mean free path) of the excited photoelectron.

2.4 Single- and multiple-scattering in XAFS theory

There are two general strategies for solving the Eq. (1). The classical approach is to accurately represent both the initial and the final photoelectron states and then explicitly evaluate the integral implied by this equation. One obvious weakness of this approach is that it takes into account only the simplest, but usually the most dominant, form of scattering, i.e., single scattering.

More generally, the photoelectron wave can scatter from more than one neighboring atom before returning to the central atom. This type of scattering is called multiple scattering (MS) and is now known to be essential for accurate calculations of the absorption coefficient in most materials [9-11]. The various kinds of scattering paths are shown schematically in Fig. 6. Each path begins and ends at the atom that absorbs the incident photon, i.e., all paths are always closed. Path 1 is an example of a single scattering path, i.e., a path with two legs. Paths 2 and 3 are examples of double scattering paths with three legs. Path 4 is an example of triple scattering path, i.e., a

path with four legs. Note that the effective path length r_{eff} for a MS path is equal to one-half of the sum of path distances involved.

Three leg paths with scattering angles between 45° and 135° (for example path 2) typically are not strong, but there can be a lot of them. Collinear paths (for example paths 3 and 4), i.e., multiple scattering by atoms along a forward direction, otherwise known as the focusing or shadowing effects, are very strong and can exceed the single, backscattering contributions in magnitude [12, 13].

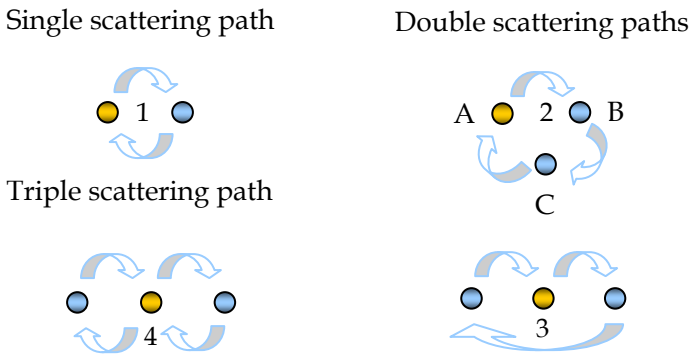

Fig. 6: A plane of atoms showing different kinds of scattering paths. Yellow coloured atoms are the absorbing atoms, often called the central atom. Blue coloured atoms are the scatterers. The photoelectron wave travels the double scattering path 2, A–B–C-A or A–C-B–A, with an effective path length $r = \left(|AB|+|BC|+|CA|\right)/2$.

The second strategy to solve Eq. (1) called real space multiple scattering theory (RSMS), is to rewrite Eq. (1) using a Green's function for the excited photoelectron in the presence of a core hole.

The method is based on a rapidly convergent separable representation of the photoelectron propagator, which permits fast, accurate calculations μ of any closed MS paths [14]. The number of significant MS paths is limited with efficient multiple-scattering path filters and a fast path-generation and sorting algorithm [15]. The Green's-function formulation is particularly advantageous for XAFS, since it can naturally incorporate inelastic losses and other quasi-particle effects and avoids the necessity of explicit calculations of wave functions. This approach also takes advantage of close connection between XAFS within the first few tens of eV of the absorption edge position and the electronic structure of the absorbing atom. Also, it provides an *ab initio* method for the general calculations of XAFS over an extended energy range [16].

2.5 Structural information in XAFS

The XAFS spectrum is typically divided into two regions: the X-ray Absorption Near-Edge Structure (XANES) and the Extended X-ray Absorption Fine Structure (EXAFS).

The division, as shown in Fig. 7, between the two regions is given as a few tens of eV above the absorption edge energy, but in practice the cut-off is somewhat arbitrary and the regions overlap.

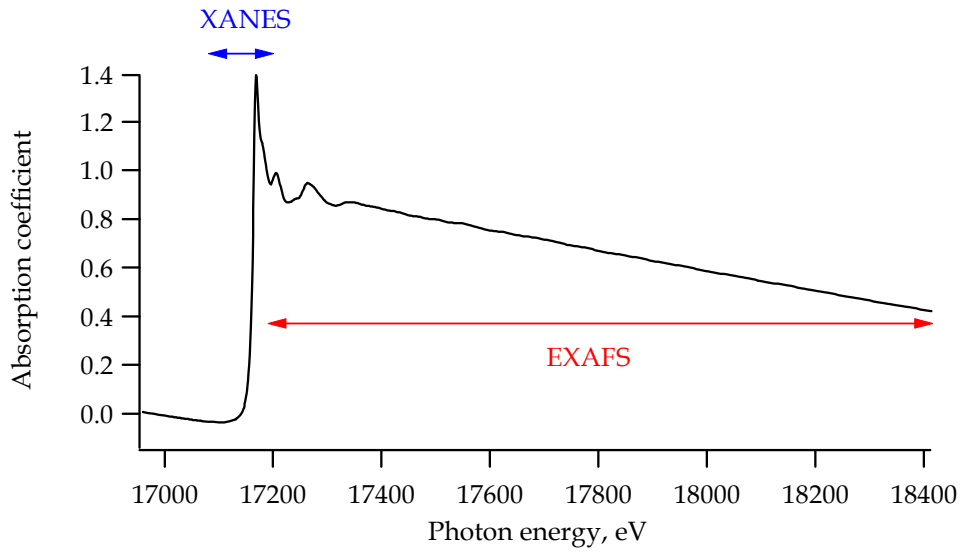

Fig. 7: XANES and EXAFS regions of a U L_{III}-edge X-ray absorption spectrum.

A better way to distinguish between the two regions is as follows: the XANES is formed due to strong scattering processes as well as local atomic resonances in the X-ray absorption, while the EXAFS is dominated by single scattering processes, i.e., scattering by neighboring atoms directly back to the absorbing atom.

XANES reflects the oxidation state and electronic structure of the absorbing atom.

EXAFS contains precise structural information such as interatomic distances, number and identity of the coordinating atoms, and the degree of thermal and structural disorder between the absorbing atom and its neighbors.

The RSMS approach gives a unified treatment of both XANES and EXAFS, although the quantitative treatment of XANES remains a challenging problem, while basic theory of EXAFS is well understood [17, 18]. Now the RSMS approach is the basis of the widely popular XAFS code FEFF [16, 19].

In RSMS theory the expression for $\mu(E)$ is factored in terms of the atomic background absorption $\mu_0(E)$ modulated by the fine structure $\chi(E)$:

$$\mu(E)=\mu_0(E)(1+\chi(E)). \qquad (2)$$

This result is consistent with the experimental definition of XAFS, i.e.,

$$\chi(E)=\frac{(\mu(E)-\mu_0(E))}{\Delta\mu_0(E_0)}, \qquad (3)$$

where $\mu(E)$ is the measured absorption and $\Delta\mu_0(E_0)$ is the jump in the atomic background absorption. The atomic background absorption $\mu_0(E)$ in XAFS is given as

energy-dependent smooth absorption from an atom embedded in the electronic environment of the condensed system, but without scattering from the neighbors, and in general is different from the "free" atom in a vacuum [20].

The XAFS measurement does not directly measure $\mu(E)$. Instead, it measures the sum of $\mu(E)$ and the absorption both of high-lying core states of the absorbing atom and the absorption due to the other atomic species in the material.

Thus, the separation of $\mu(E)$ consists of three steps:

1. Pre-edge background removal, in which most of the energy dependence of the absorption other than that from the absorption edge of interest is eliminated;
2. Normalization to the edge jump;
3. Post-edge background removal, in which a smoothly varying background function which approximates the absorption from an isolated embedded atom, $\mu_0(E)$, is subtracted from $\mu(E)$ to give $\chi(E)$.

The standard procedure of pre-edge background removal consists of fitting $\mu(E)$ data before the absorption edge with the help of "Victoreen" polynomial and extrapolation of this function throughout the energy range of the data. The "Victoreen" polynomial is given by $C\lambda^3 - D\lambda^4$, where λ is X-ray wavelength ($\lambda(\text{Å}) = hc/E = 12398.52/E(eV)$), C and D are fit coefficients.

The normalization to the edge jump is often done by a fixed value $\Delta\mu_0(E_0)$. This value is found by taking the difference in the extrapolation of smooth functional fits to the pre-edge $\mu(E)$ and post-edge background $\mu_0(E)$ at the threshold energy E_0.

Extracting the post-edge background is the most critical step of the separation of $\mu(E)$, as this function can affect the final conclusions for the structural information. The usual practice has been to approximate the background function by a piecewise polynomial, or spline [21]. By using splines, the problem of how best to approximate the background is reduced to a problem of what conditions, such as polynomial order and knot location, to put on the spline [22]. A more general approach is based on the simple idea that due to the Coulomb force, the absorbing atom is alone at the distances like a sum of neighboring atom's radii, although their near-neighboring environment is retained. A reliable post-edge background corresponds then to the absorption from this lone, but "embedded" absorbing atom. In practice, this means that whereas the standard methods of background removal chose a smooth spline to best fit the whole absorption spectrum $\mu(E)$, this approach chooses the spline to best fit only the low-frequency components of $\mu(E)$. This technique is included in AUTOBK [23], IFEFFIT [24], SIXPack [25], and ATHENA [26] programs for the XAS data processing.

Fig. 8 shows the measured absorption spectrum $\mu(E)$ at the uranium L_{III}-edge for soddyite $(UO_2)_2SiO_4$ x $2H_2O$ with both pre-edge and post-edge background curves overlaid.

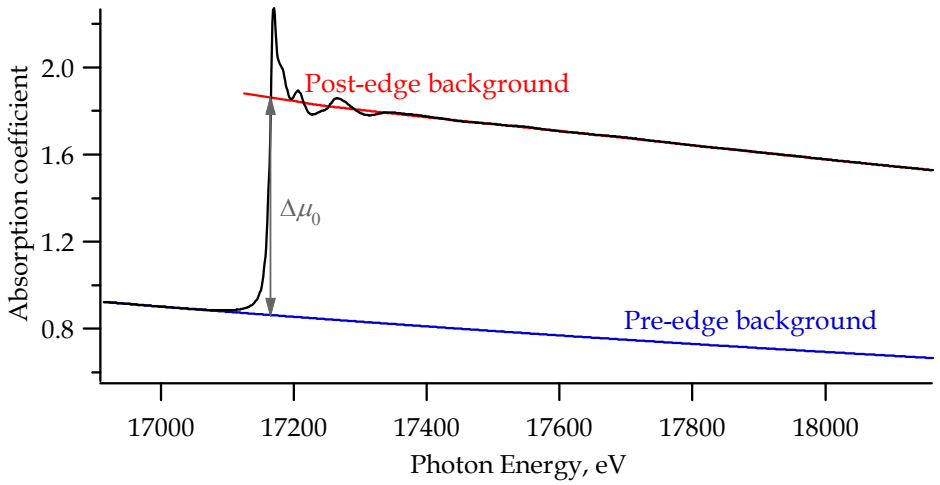

Fig. 8: X-ray absorption spectrum collected in transmission mode at the U L_{III}-edge for soddyite $(UO_2)_2SiO_4$ x $2H_2O$. The blue and red lines represent pre- and post-edge background absorption, respectively. $\Delta\mu_0(E_0)$ is the jump in the atomic background absorption.

It is convenient to convert $\chi(E)$ from the energy scale (eV) to the photoelectron wave number or k scale (Å^{-1}) by $k=\sqrt{2m(E-E_0)}/\hbar$. The resulting $\chi(k)$ (Fig. 9) has the atomic-like absorption contributions removed, but retains essentially all the local structural information about the near-neighbor environment of the absorbing atom. It is then ready for a careful analysis of the effect of the local structure on the XAFS.

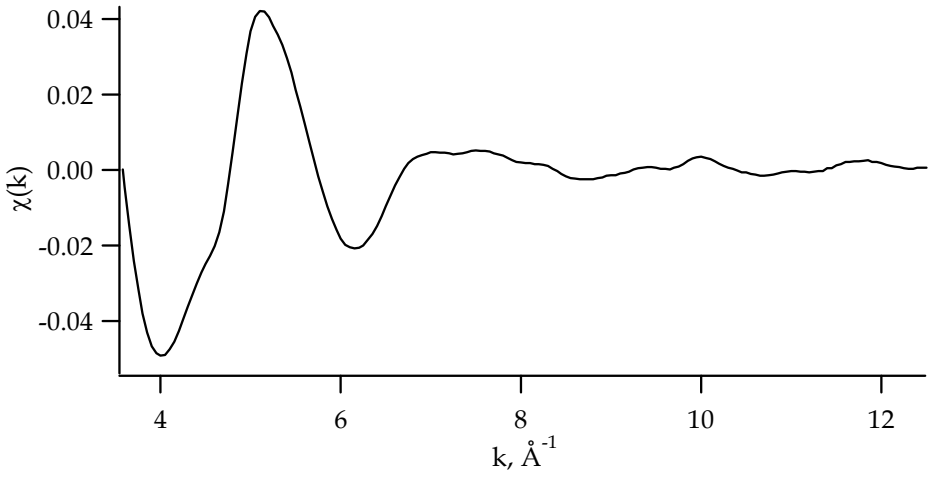

Fig. 9: U L_{III}-edge EXAFS spectrum for soddyite $(UO_2)_2SiO_4$ x $2H_2O$.

2.6 EXAFS data analysis

2.6.1 EXAFS equation

The structural information is contained in the XAFS interference function $\chi(k)$. Within the RSMS theory, this function can be written as a coherent sum over the oscillatory contributions from each individual scattering path in a form identical to the original EXAFS equation of Sayers et. al. [27]

$$\chi(k) = S_0^2 \sum_r \frac{N_r \left| f_{eff}(k) \right|}{kr^2} e^{-\frac{2r}{\lambda(k)}} e^{-2\sigma^2 k^2} \sin\left(2kr + 2\delta_c(k) + \Phi(k)\right) \quad (4)$$

except that all quantities must be redefined to include curved-wave and many-body effects implicitly. Here, the structural parameters are the interatomic distances (or effective path length) $r_{eff} = r_{path}/2$ (Å), the coordination number N, At. (or number of equivalent scatterers), and the temperature-dependent Debye-Waller factor σ^2 (Å^2), which also includes the effects due to structural disorder.

The dependence of the oscillatory structure on the interatomic distance and energy is reflected by the $\sin(2kr)$ term. The decay of the wave due to the mean-free path $\lambda(k)$ or finite lifetime (including core-hole lifetime) of the photoelectron is captured by the exponential term $e^{-2r/\lambda(k)}$. The strength of the reflected interfering waves depends on the type and number of neighboring atoms through the effective backscattering amplitude $\left| f_{eff}(k) \right|$, and hence is primarily responsible for the magnitude of the EXAFS signal. The spherical wave factor $1/kr^2$ and mean-free path term are secondary but important for a quantitative behaviour of the EXAFS amplitude. The phase factor $\Phi(k) = \arg f_{eff}(k)$ reflects the quantum-mechanical wavelike nature of the backscattering. A larger contribution to the overall phase shift $\psi(k) = 2\delta_c(k) + \Phi(k)$ is given by the phase shift $\delta_c(k)$ at the absorbing atom, since the photoelectron sees the potential created by this atom twice. The total phase shift accounts for the difference between the measured and geometrical interatomic distance, which is typically a few tenths of an Å and must be corrected. The Debye-Waller factor, which is given with a good approximation by the $e^{-2\sigma^2 k^2}$ term, is due to thermal and structural disorder effects that smear the sharp interference pattern of the rapidly varying $\sin(2kr)$ term. The Debye-Waller effect becomes more pronounced the shorter the wavelength of the photoelectron, and hence it cuts off the EXAFS at sufficiently large energy beyond about $k \sim 1/\sigma$, which is typically of order 10 Å^{-1}. Finally, the overall amplitude factor S_0^2 is a many-body effect due to the relaxation of the system in response to the creation

of the core hole. Although S_0^2 is weakly energy dependent, it is usually approximated by a constant $0.7 < S_0^2 < 1.0$, which is found for the central atom, and is completely correlated with the value of the coordination number.
Nowadays, the scattering functions $f_{eff}(k), 2\delta_c(k), \Phi(k), \lambda(k)$ are calculated using the program FEFF.

2.6.2 Fourier transform

2.6.2.1 General principles

The Eq. (4) obviously contains a great deal of structural information about the local environment. To further justify the use of the Fourier transform (FT) to receive this information, we can rewrite the EXAFS equation as a sum over the i coordination shells:

$$\chi(k) = \sum_i A_i(k) \sin(2kr_i + \psi_i(k)) \tag{5}$$

with

$$A_i(k) = S_0^2 \frac{N_i |f_i(k)|}{kr_i^2} e^{-\frac{2r_i}{\lambda(k)}} e^{-2\sigma_i^2 k^2} \tag{6}$$

and total phase shift

$$\psi_i(k) = 2\delta_c(k) + \Phi_i(k). \tag{7}$$

Isolating the local structure from EXAFS data with the Fourier technique is feasible because the primary *k* dependence in Eq. (5) is the $\sin$ term, and the Fourier transform from the product of the functions $A_i(k)$ and $\sin(a_i k)$ equals the Fourier transform from the same function $A_i(k)$ but with the argument reduced by a_i:

$$FT[A_i(k)\sin(a_i k)](r) = \frac{1}{2i}\{FT[A_i(k)](r_i - a_i) - FT[A_i(k)](r_i + a_i)\}, \tag{8}$$

where a_i depends on the total phase shift $\psi_i(k)$. Hence, after the Fourier transform every coordination shell that is written as $A_i(k)\sin(2kr_i + \psi_i(k))$ shows peaks in the so-called Pseudo Radial Distribution Function (PRDF) which is slightly shifted to lower *r* compared to the actual interatomic distance.
The EXAFS PRDF $\chi(r)$ is generally given by:

$$\chi(r) = \frac{1}{4\pi^{1/2}} \int_{k_{\min}}^{k_{\max}} \chi(k) k^m e^{-2ikr} dk \tag{9}$$

Here the values $k_{\min}$ and $k_{\max}$ are actually limited both by the approximate theory and the experimental evidence and restrict the *k* range of the transformed $\chi(k)$ data.

The type of e^{-2ikr} Fourier transform in contrast to common used e^{-ikr} is due to the presence of a factor of two in $\sin(2kr)$ term in the EXAFS equation.

The weighting of the spectrum by a factor k^m, where m is typically chosen to be from one to three, has several consequences:

1. It gives a uniform amplitude of the weighted $\chi(k)$ data over the k range, i.e., compensates the combined attenuation effects of the term $A_i(k)$;
2. The higher the k weighting of the $\chi(k)$ data, the narrower the peaks are in the PRDF;
3. The higher the k weighting of the $\chi(k)$ data, the worse the signal to noise relation is in the PRDF;
4. The higher the k weighting of the $\chi(k)$ data, the larger the contribution to the PRDF from high–Z elements in comparison with low–Z elements.

The FT makes $\chi(r)$ complex. Usually only the power spectrum $|\chi(r)|$ of the FT is examined, but all phase information is missing in it:

$$|\chi(r)| = \left\{ [\mathrm{Re}(\chi(r)]^2 + [\mathrm{Im}(\chi(r)]^2 \right\}^{1/2} \tag{10}$$

Examination of the real and imaginary components of the FT can be useful since due to the phase information its shape is more characteristic of the types of atoms that make up a given shell. A typical power spectrum and also real and imaginary components of the FT are shown in Fig. 10.

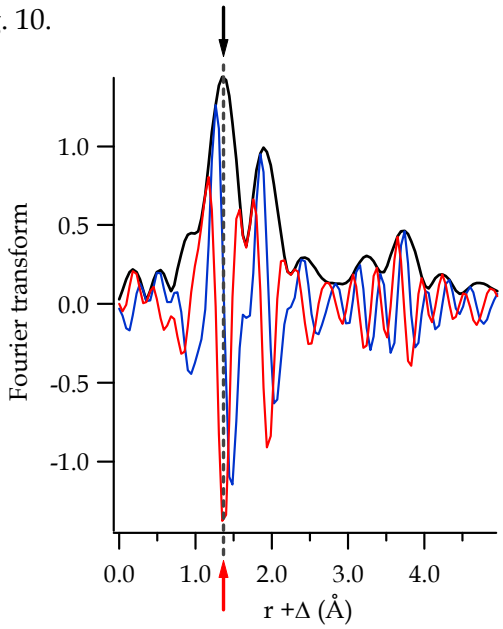

Fig. 10: FT for experimental U L_{III}-edge k^3-weighted EXAFS spectrum of $(UO_2)_2SiO_4$ x $2H_2O$. Least-squares refinement of the soddyite structure was done over k range 3.50 ÷ 16.2 Å^{-1}. The black, blue and red lines represent the magnitude, real, and imaginary parts of PRDF, respectively. The imaginary part of the FT should peak at the peak of the power spectrum when the threshold energy E_0 has been corrected (symbolized by coincided black and red arrows).

The peaks in the power spectrum correspond to the coordination shells surrounding the absorbing atom. Their radial positions are shifted to the distances r + Δ (Å), where Δ is approximately half the average phase shift slope for a given interaction. A shift of ~-0.5 Å is typical.

2.6.2.2 Fourier transform techniques

One of the practical problems associated with the Fourier transformation is due to the finite range of $\chi(k)$ data, particularly the necessity to omit the low *k* range data. This means that $\chi(k)$ cannot be recovered by simply taking the inverse Fourier transform of $\chi(r)$. Because of truncation effects, the transformation is contaminated with spurious peaks often interfering with the physical features of interest. This truncation ripple is easy to understand in terms of the convolution theorem when transforming over a finite *k* range. The "true" infinite range transformation is convoluted with the transformation of the window function. For example, making use of the simplest window function,

$$W(k) = \begin{cases} 1 & k_{\min} \le k \le k_{\max} \\ 0 & k < k_{\min}\,;\; k > k_{\max} \end{cases} \tag{11}$$

the Fourier transform (9) can be rewritten as:

$$\chi(r) = \frac{1}{4\pi^{1/2}} \int_{-\infty}^{+\infty} \chi(k) k^m W(k) e^{-2ikr}\, dk \tag{12}$$

or in the formal form:

$$\chi(r) = FT\left[\chi(k) k^m W(k)\right] \tag{13}$$

The Fourier transform from the product of the functions equals the convolution of the Fourier transforms from these functions, where the convolution is defined as:

$$\chi(k) W(k) = \int_{-\infty}^{+\infty} \chi(r) W(k-r)\, dr. \tag{14}$$

Then the expression of the Fourier transform (Eq. (13)) can be factored as:

$$\chi(r) = FT\left[\chi(k) k^m\right] FT\left[W(k)\right] \tag{15}$$

and the Fourier transform of the window function in Eq. (11) can be calculated in an explicit form:

$$FT\left[W(k)\right] = e^{-i(k_{\max}+k_{\min})r}\, \frac{\sin(k_{\max}-k_{\min})}{r}. \tag{16}$$

Fig. 11 schematically shows the window function (see Eq. (11)) and the corresponding Fourier transform. The presence of factor $FT[W(k)]$ in $\chi(r)$ significantly increases the width of peaks in the power spectrum and in the imaginary part. After applying the

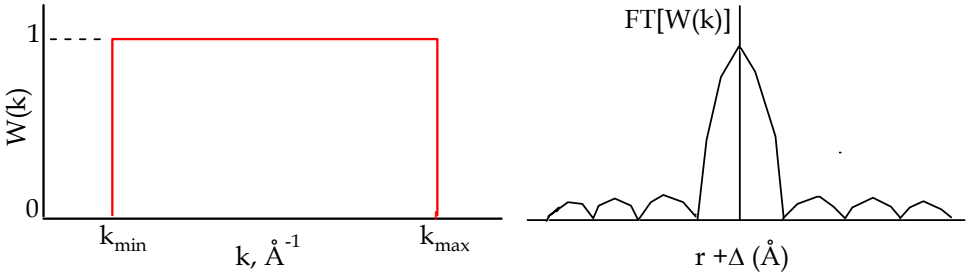

Fig. 11: Option of *k* window is given. The window function specifies the range of the *k* data to be transformed. This has the effect of reducing the "ringing" effects in the transform, but broadens transforms peak. The larger the *k* range employed, the narrower the peaks in the PRDF.

window function, the side lobes located at the distances $(0.5+2n)\pi/k_{\max}-k_{\min}$ Å from the main maximum appear. The amplitude of the highest-level side lobes is approximately 10 % of the main maximum. There are different types of window functions available, each with their own advantage and preferred application [28]. For example, Hanning or Kaiser-Bessel windows, by which the near side lobes tend to be lower than 10 %, are often used.

In summary, window functions have several purposes:

1. To weight different portions of the data. For instance, *k* data at low *k* tend to be less reliable because of errors in chemical transferability and other effects of approximations in the theory. Greater weighting of the data at high *k* deemphasizes this problem.
2. To truncate the data smoothly at the ends of the transform range in order to minimize truncation ripple, but at the expense of some peak broadening.

Broadening of the peaks and the near side lobes can lead to the loss of true local atomic structure.

Generally, the PRDF provides a qualitative picture of the local environment surrounding the absorbing atom, giving the information about various shell radii and amplitudes, disorder, and noise level, but quantitative structural information is not obtained from the PRDF itself.

2.6.2.3 Inverse Fourier transform

It is presumed that a peak (coordination shell) in $\chi(r)$ and the Fourier transform of $\chi(k)$ contain Fourier components from one particular neighbor only. This peak is

multiplied by a window function and Fourier back-transformed over the selected *r* range to create a filtered k^m-weighted $\chi(k)$ spectrum for a single shell of the isolated scatterer. As an example, Fig. 12 (right) shows the experimental U L_{III}-edge k^3-weighted $\chi(k)$ spectrum of soddyite and the contribution from the first coordination shell U-O in it. The back-transform window is indicated by the hatches surrounding the first shell U-O peak in Fig. 12 (left).

There are several pitfalls in choosing back-transforming ranges. Because the window is

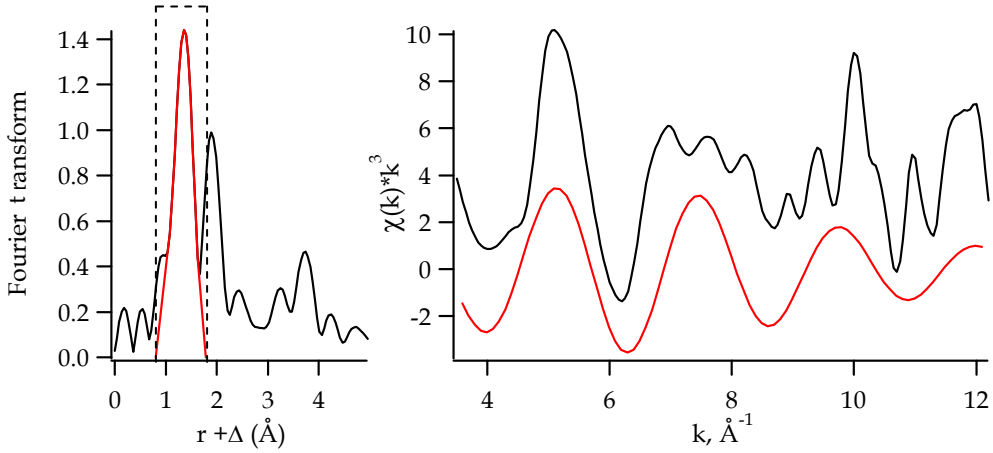

Fig. 12: On the left-hand side panel, the FT magnitude for soddyite $(UO_2)_2SiO_4$ x $2H_2O$ (black line) with the first U–O coordination shell (red line) to be transformed are shown. The boundaries of the back-transform window are indicated by the hatches surrounding the peak of the U-O shell. In the right-hand side panel, the experimental U L_{III}-edge k^3-weighted $\chi(k)$ spectrum of soddyite (black line) and Fourier filtered k^3-weighted $\chi(k)$ spectrum corresponding to the first U-O coordination shell (red line) are represented.

rounded at the position of the transform peak, a shift in window position will affect a shift in apparent peak position in *k* space with the resulting error in the distance determination. Also, if too small of a back-transforming range is used, both the coordination number and Debye-Waller factor can be incorrect. Very large errors may result if an attempt is made to separately back transform the two if they are not truly isolated, interfering of one shell with other shells: their proximity often results in a back-transformed $k^m\chi(k)$, which contains the contributions from more than one coordination shell.

2.6.2.4 EXAFS data analysis methods based on Fourier transform technique

Once the data have been Fourier filtered, the back-transformed k^m-weighted $\chi(k)$ spectrum is then analyzed to obtain structural information such as type of neighbours, their interatomic distance *r*, coordination number *N*, and Debye-Waller factor σ^2. Most empirical curve–fitting [21, 29] and log-ratio/phase difference cumulant [30-35]

methods involve the comparison of an unknown spectrum to a standard material whose structure is well known.

The least-squares fitting method works by parameterizing the isolated $\chi_{St}(k)$ of the standard and optimizing those parameters to best fit the isolated $\chi_{Calc}(k)$ of the unknown material. Typically, up to four variables for each shell (N, r, σ^2, and E_0) are allowed to "float" during the curve fitting process. The number of varied parameters is limited by:

$$N_P \approx \frac{2\Delta k \Delta r}{\pi}, \tag{17}$$

where Δk and Δr are the *k* and *r* ranges of the usable data.

The goodness of fit F is estimated by minimizing the sum of squares of the differences between standard and calculated curves relative to the parameters that are being varied:

$$F = \left[\sum k^6 (\chi_{St} - \chi_{Calc})^2 \,/\, \sum k^6 (\chi_{St})^2 \right]^{1/2}, \tag{18}$$

Here the sum is taken over the *k* data points used for the analysis.

The expected resolution ΔR in distance, which is the smallest difference in interatomic distances resolvable for two similar coordination shells, is given by:

$$\Delta R = \frac{\pi}{2\Delta k} \tag{19}$$

The log-ratio/phase difference cumulant method is model independent in the sense that no parameterization is made. Instead, the back-transformed $\chi(k)$ functions of the standard and the unknown compounds are compared by computing the log of the ratio of amplitude functions and the difference of the phase functions. Polynomials are regressed to these difference functions. The coefficients of the polynomials are then related to the changes in the cumulants of the radial distribution functions between the standard and the unknown.

Both of these empirical approaches have long histories of successful contribution to EXAFS data analysis, but both suffer from significant limitations.

2.6.2.5 Types of problems in data analysis with Fourier transform technique

In general, the least-squares curve fitting and log-ratio/phase difference cumulant methods have provided satisfactory results for amorphous materials, liquids, and aqueous solutions, where a high degree of local order has been preserved about the X-ray absorbing atoms [36–39]. But even in these systems, the data analysis requires experience and sophistication for reliably use.

The main shortcomings of the empirical methods are:

- The dependence on a suitable material to serve as an analytical standard;

- The need to isolate specific Fourier components in the $\chi(r)$ spectrum has quite a strong dependence on transformed *k* and *r* ranges, weighting, and other parameters.

The dependence on a standard includes also the problem of the handling of unusual neighbor pairs. Many samples have scatterers that simply do not form suitable standard compounds with the absorbing atom, such as compounds with mixed shells, i.e., coordination shells with two more species.

Moreover, although examples certainly exist of materials in which at least the first and even higher shells can be successfully isolated, the overlap of shells is quite common. Because of the overlapping of shells, it would be impossible to isolate a single shell $\chi(k)$ spectrum in the manner required for empirical analysis.

The data analysis in a one component system is already difficult, since two or more shells in $\chi(r)$ spectrum are poorly resolved or when any decomposition into shells is ambiguous. A nonparametric analysis of the PRDF by log-ratio/phase difference cumulant method is often useful in such cases, but suffers from potential lack of convergence within the data range at high disorder and fitting correlations between cumulants [34, 40].

But usually, the near-neighbor surrounding of the absorbing atoms contains different types of atoms. To solve this problem, the conventional EXAFS analysis is based on one or several assumed structural models for the near-neighbor environment of the absorbing atom. The best theoretical model and its corresponding structural parameters, i.e., coordination numbers, interatomic distances, and Debye-Waller factors for each coordination shell, are determined by fits to the experimental data. However, often several structural models with completely different chemical implications can describe the experimental $\chi(k)$ data equally well.

As an alternative to empirical methods based on the Fourier transform technique that are difficult in many cases of EXAFS data treatment, the nonparametric regularization methods are suggested, which have already been applied to the EXAFS analysis successfully [41-44].

2.6.3 Partial radial distribution functions (RDFs) probed by EXAFS

In the multi-component case of disordered systems, the EXAFS spectrum $\chi_l(k)$, observed at the edge of the absorbing atom l, can be generalized [45–47] to include the sum of contributions from all different types of neighboring atoms $j = 1, 2, ..., n$ integrated over the corresponding partial radial distribution functions $g_{lj}(r)$:

$$\chi_l(k) = S_0^2 4\pi\rho_0 \sum_{j=1}^{n} C_{lj} \frac{|f_{lj}(k)|}{k} \int_0^\infty g_{lj}(r) e^{-\frac{2r}{\lambda_l(k)}} \sin(2kr + \psi_{lj}(k)) dr \qquad (20)$$

where the value $4\pi\rho_0 r^2 C_{lj} g_{lj}(r)$ denotes the density of probability to find a neighbor atom of type j at the interatomic distance *r* from the absorbing atom l. If the material with the average atomic density ρ_0 consists of the *n* elements with the concentration C_{lj}, then $N = n(n+1)/2$ RDFs are required to describe the local atomic structure.

For a weak disorder, a particular distribution function is often approximated by a Gaussian, i.e., assuming a Gaussian distribution of neighbors around the average distance *r* with variance σ^2:

$$g(r) = \frac{1}{4\pi\rho_0} \sum_i \frac{N_i}{r_i^2 \sigma_i \sqrt{2\pi}} e^{-\frac{(r-r_i)^2}{2\sigma_i^2}} \tag{21}$$

In this case a possible asymmetry in the RDF is lost since this function is described by a Gaussian distribution with a certain Debye-Waller factor. The number of atoms contained in the coordination sphere i is determined by integrating the function $4\pi\rho_0 r^2 C g(r)$ in the appropriate distance $r \geq 0$. The full width at half maximum (*FWHM*) of this function is $2\sigma\sqrt{2\ln 2} = 2.355\sigma$.

Any reasonable partial RDF should satisfy the following requirements:

- $g_{lj}(r)$ and its first derivative should be smooth;
- $g_{lj}(r) = 0$ if $0 < r_{lj} \leq a_{lj}$, where a_{lj} is the sum of atomic radii of neighboring atoms ~1.5 Å;
- $g_{lj}(r) \geq 0$ for $0 \leq r_{lj} < \infty$;
- $g_{lj}(r) = 1$ if $r_{lj} \geq b_{lj}$, where $b_{lj} >> a_{lj}$;
- $g_{lj}(r) = g_{jl}(r)$. (22)

In spite of the infinite upper integration limit in the Eq. (20), the sensitivity of $\chi_l(k)$ oscillations to the surrounding structure is limited to the neighborhood of the absorbing atom within the interval $[a_{lj}, b_{lj}]$, typically within 5 – 10 Å from the central atom. Replacing the infinite limit of the integration in the Eq. (20) by $[a_{lj}, b_{lj}]$ results in:

$$U_l(k) = S_0^2 \frac{4\pi\rho_0}{k} \sum_{j=1}^{n} C_{lj} \frac{|f_{lj}(k)|}{f_{l0}(k)} \int_{a_{lj}}^{b_{lj}} g_{lj}(r) e^{-\frac{2r}{\lambda_l(k)}} \sin(2kr + \psi_{lj}(k)) dr, \tag{23}$$

where

$$U_l(k) = \chi_l(k) - T_l(k) \tag{24}$$

with

$$T_l(k) = S_0^2 \frac{4\pi\rho_0}{k} \sum_{j=1}^{n} C_{lj} \frac{|f_{lj}(k)|}{f_{l0}(k)} \int_{b_{lj}}^{\infty} g_{lj}(r) e^{-\frac{2r}{\lambda_l(k)}} \sin(2kr + \psi_{lj}(k)) dr, \quad (25)$$

and

$$f_{l0}(k) = \sum_{j=1}^{n} C_{lj} f_{lj}(k, b_{lj}) \quad (26)$$

Here, the amplitude function $f_{l0}(k)$ has the same effect on the EXAFS spectrum as the k^m weighting.

As an example, the partial RDFs for uranium as central atom in soddyite are presented in Fig. 13. The RDFs were simulated according to Eq. (21) using the X-ray diffraction data of $(UO_2)_2SiO_4 \times 2H_2O$ [48]. The parameters inserted into the calculation of the RDFs are listed in Table 1. The calculations were performed over the r ranges 3.0 ÷ 6.0, 2.40 ÷ 6.0, and 1.50 ÷ 6.0 Å for the RDFs U-U, U-Si, and U-O, respectively. As can be seen from Fig. 13, the RDFs have a specific appearance: Except for a small number of peaks at certain distances, the RDFs are equal to zero over large r intervals.

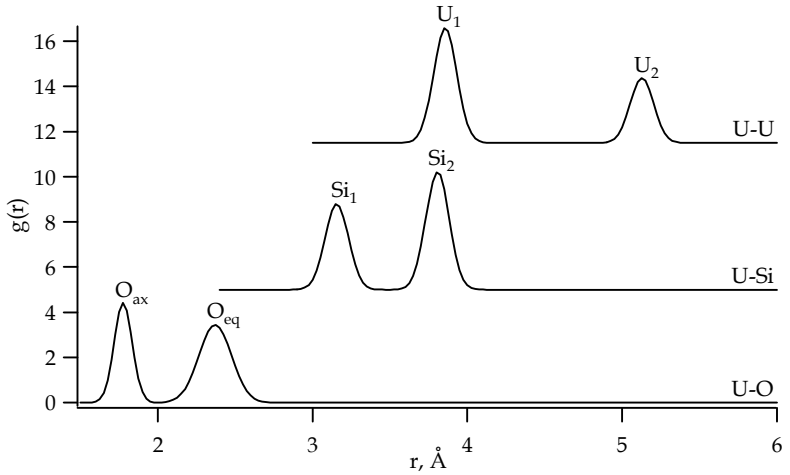

Fig. 13: Simulated RDFs U-U, U-Si, and U-O for uranium as central atom in soddyite.

Table 1: Structural parameters of the coordination shells in soddyite used in the model calculations of the RDFs U-U, U-Si, and U-O and the U L_{III}–edge EXAFS spectrum.

	N, At.	*r*, Å	σ^2, Å^2
U_1	2	3.86	0.0057
U_2	2	5.15	0.0057
Si_1	1	3.16	0.0057
Si_2	2	3.81	0.0057
O_{ax}	2	1.78	0.0034
O_{eq}	5	2.38	0.0110

The calculation of an unknown partial RDF, which corresponds to some given EXAFS spectrum $U_l(k)$, by solving the integral Eq. (23) is not a common computation because the EXAFS equation is ill-conditioned [49]. These kinds of problems are generally plagued mathematically with the lack of properties such as existence, uniqueness and stability of the solutions, and are called inverse ill-posed problems [50].
The regularization is a powerful method that allows solving a variety of ill-posed problems, and in particular the numerical solving of the EXAFS equation [51-53].

2.6.4 Application of regularization method to ill-posed EXAFS problem

In order to avoid unusual complications, the single-scattering approximation of the EXAFS equation for a given absorption edge is utilized to describe the regularization approach to the data analysis throughout the following work. The basic EXAFS Eq. (23) or more generally the Fredholm integral equation of the first kind can be written as:

$$U(k) = \sum_{j=1}^{n} \int_{a_j}^{b_j} A^j(k,r)\, g^j(r) dr, \tag{27}$$

where the integral operators A^j represent the kernel of the EXAFS equation relating $g^j(r)$ to $U(k)$ and are defined as:

$$A^j(k,r) = S_0^2 \frac{4\pi\rho_0}{k} \sum_{j=1}^{n} C^j \frac{\left|f^j(k)\right|}{f_0(k)} \int_{a_j}^{b_j} e^{-\frac{2r}{\lambda(k)}} \sin\left(2kr + \psi^j(k)\right) dr. \tag{28}$$

Here, a_j, b_j (Å) are finite real numbers, which limit the r range of desired $g^j(r)$ RDF. $f^j(k), \psi^j(k)$ are the backscattering amplitude and total phase shift of the neighboring atom of type j, respectively. n is the number of the elements in the system. $U(k)$ is restricted to the finite range $[c,d]$ (Å^{-1}) both by the experimental evidence and the EXAFS theory. All operators act from space $L_2[a,b]$ to $L_2[c,d]$.

The Fredholm integral Eq. (27) can be solved with respect to the $g^j(r)$ using the Tikhonov regularization algorithm [54]. The variation Tikhonov approach [41] incorporates all available *a priori* information such as the conditions (22) for the RDF and the nonlinear phase shift in search for the solution that minimizes the Tikhonov functional in space L_2:

$$\min M\left[g^j\right] = \min\left\{ \left\| \sum_{j=1}^{n} A^j g^j - U \right\|_{L_2[c,d]}^2 + \sum_{j=1}^{n} \alpha^j \left\| g^j \right\|_{L_2\left[a_j,b_j\right]}^2 \right\} \tag{29}$$

The introduction of small positive regularization parameters α^j in the Tikhonov functional renders the problem stable. In the case of $\alpha^j = 0$, the problem (29)

transforms to the least-squares fitting leading to the non-unique determination of the partial RDFs. Vice versa, due to the term with positive α^j, the number of possible RDFs solutions is restricted. These solutions should satisfy not only the minimum of the residual norm $\left\| \sum_{j=1}^{n} A^j g^j - U \right\|^2$, but also the desired $g^j(r)$ should be smooth.

$g^j(r)$ minimizes the Tikhonov functional when the first variation of this functional $\delta M[g^j, \Delta g^j]$ equals zero:

$$\delta M[g^j, \Delta g^j] + O(\Delta g^j) = M[g^j + \Delta g^j] - M[g^j], \tag{30}$$

where Δg^j is an increment of the g^j, and $O(\Delta g^j) \to 0$ when $\Delta g^j \to 0$.
The discretization of the Eq. (27) gives:

$$U_q = \sum_{j=1}^{n} \sum_{p=1}^{P} A_{qp}^j g_p^j \qquad (q = 1, 2, \ldots, Q), \tag{31}$$

where $U_q = U(k_q)$, $g_p^j = g^j(r_p)$ are vectors, and $A_{qp}^j = A^j(k_q, r_p)$ is a matrix. The k range $[c, d]$ of the usable U_q data consists of $q = 1, 2, \ldots, Q$ points with step $\Delta k = (d - c)/q$, and the r ranges $[a_j, b_j]$ of the RDFs data consist of $p = 1, 2, \ldots, P$ points with step $\Delta r = (b_j - a_j)/p$.

The condition $\delta M[g_p^j, \Delta g_p^j] = 0$ leads to the system of linear algebraic equations:

$$\sum_{j=1}^{n} \left(A_{qp}^{j*} A_{qp}^j + \alpha^j I_{pp} \right) g_p^j = A_{qp}^{j*} U_q \tag{32}$$

Here, A_{qp}^{j*} is the matrix transposed to A_{qp}^j and I_{pp} represents the identity matrix of size p, i.e., is the p-by-p square matrix with ones on the main diagonal and zeros elsewhere. α^j are the small positive regularization parameters.
Eq. (32) provides the approximated so-called Tikhonov solutions that are given by:

$$g_p^j = (A_{qp}^{j*} A_{qp}^j + \alpha^j I_{pp})^{-1} A_{qp}^{j*} U_q \tag{33}$$

The Tikhonov solutions depend drastically on the value of the regularization parameters [51]. The closer they are to zero the nearer the approximated solutions are to the exact ones, but simultaneously the matrix $(A_{qp}^{j*} A_{qp}^j + \alpha^j I_{pp})$ can be ill-conditioned or even degenerate and the resulting solutions can not be accurate. Fig. 14 shows the influence of the regularization parameters on the Tikhonov solutions calculated from the simulated U L_{III}–edge EXAFS spectrum of soddyite. Extracted

Tikhonov solutions (left and top right) are compared with the model RDFs U-U, U-Si, and U-O (structural parameters of the coordination shells in soddyite involved in the calculations are given in Table 1). The $[Ag](k)$ functions calculated using the model $g^j(r)$ and the Tikhonov solutions with $\alpha^j = 10^{-6}$ are shown at bottom right of Fig. 14 by solid and dotted lines, respectively.

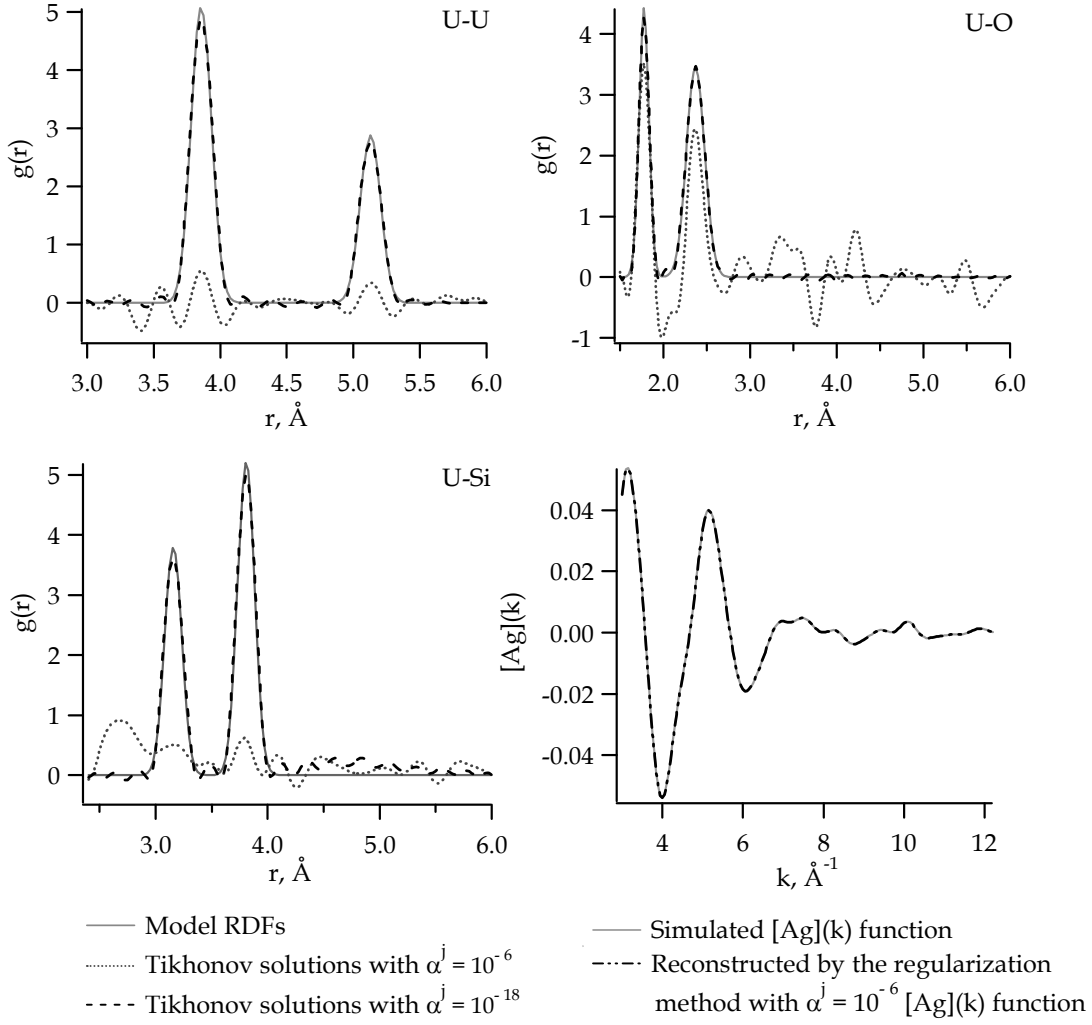

Fig. 14: Reconstruction of the RDFs U-U, U-Si, and U-O for the simulated soddyite structure by the Tikhonov method using different regularization parameters α^j.

The Tikhonov solutions calculated with the $\alpha^j = 10^{-18}$ reproduce the model RDFs with very good accuracy. However, the $[Ag](k)$ function obtained from the experimental raw data suffers both from the statistical and systematic errors entering XAFS measurements and the data processing [55]. This makes it impossible to treat the RDFs from measured XAFS data with $\alpha^j < 10^{-10}$. Usually the regularization parameters used

for the treatment of experimental data are from 10^{-5} to 10^{-7}. As illustrated in Fig. 14, the Tikhonov solutions both with $\alpha^j = 10^{-18}$ and 10^{-6} provide fast and exact estimates of the interatomic distances of the main coordination shells. Although the Tikhonov solutions obtained with the $\alpha^j = 10^{-6}$ differ significantly from the input model RDFs, there are no shortcomings of the Tikhonov method. The comparison of the simulated $[Ag](k)$ function with the reconstructed one using the regularization method (Fig. 14, right bottom) shows practically no discrepancy between them.

In most real research problems, the choice of the optimal regularization parameters is a difficult task. Although this field is the subject of current investigations [43, 56, 57], a complete understanding remains elusive.

Once the Tikhonov solutions have been obtained, they must be refined to obey *a priori* physical requirements (Eqs. (22)). Usually, each approximate RDF solution can be improved using the iteration procedure [58, 59]:

$$g_p^j(k+1) = (A_{qp}^{j*} A_{qp}^j + \alpha^j I_{pp})^{-1} (A_{qp}^{j*} U_q + \alpha^j I_{pp} g_p^j(k)), \qquad (34)$$

where k specifies the number of the iteration steps. The end of the iterations is determined by minimizing the discrepancy between the current solution $g_p^j(k+1)$ and the previous one, $g_p^j(k)$.

Often, but not always necessary, the peaks of the RDF solutions are approximated by Gaussian functions (Eq. (21)) to obtain precise structural information for each coordination shell such as interatomic distances r, coordination numbers N, and Debye-Waller factors σ^2.

One obvious problem of the RDF solutions, which are approximated by the Tikhonov regularization method, is that they can contain both "true" and "false" peaks corresponding to real coordination shells and artifacts, respectively, in the material under investigation.

3. METHODOLOGICAL DEVELOPMENT OF TIKHONOV REGULARIZATION METHOD

3.1 Introduction

Except for the treatment of the raw data, the most complicated step in the local atomic structure determination is to solve the EXAFS equation (Fredholm integral equation of the first kind). The partial radial distribution functions (RDFs or $g^j(r)$) are the solutions to this equation. The calculation of RDFs from experimental data is a typical example of an ill-posed problem. To address the problem of the non-uniqueness of the solutions $g^j(r)$, the following *a priori* information is included in the analysis: Most of the samples represent materials in which at least the first and second coordination shell of the same RDF can be successfully isolated. Hence, each RDF $g^j(r)$ of such samples consists of a small number of narrow peaks which are separated in distance by intervals Δr.

The advanced algorithm for the determination of $g^j(r)$ consists of the following steps: Tikhonov variation method [41], application of the method of separating functionals to distinguish between "true" peaks representing coordination shells and "false" peaks due to artifacts in $g^j(r)$ [60], and the iteration method with filtration in real space [61]. The mathematical principles underlying this modified Tikhonov regularization method have been developed by A.L. Ageev, T.V. Antonova, and M.E. Korshunov and published in [60, 61].

The algorithm described below has been developed to determine three RDFs from one EXAFS spectrum, i.e., $j=1,2,3$.

3.2 Tikhonov variation method [41]

The relationship between the normalized oscillating part $U(k)$ and the $g^j(r)$ RDFs is given by the equation:

$$Ag \equiv \sum_{j=1}^{3} A^j g^j =$$

$$= \frac{4\pi\rho_0}{k} S_0^2(k) \sum_{j=1}^{3} C^j \int_{a^j}^{b^j} f^j(k,r) e^{\frac{-2r}{\lambda(k)}} \times \sin\left(2kr + \psi^j(k,r)\right) g^j(r) dr \equiv U(k) \qquad (35)$$

where $k \in [c,d]$ is the wave vector, $f^j(k,r)$ represents the backscattering amplitude, $\psi^j(k,r)$ represents the overall scattering phase shift, $\lambda(k)$ represents the inelastic mean-free path, $S_0^2(k)$ represents the amplitude reduction factor, and ρ_0 represents

the density of the material consisting of j, $j=1,2,3$ types of elements with the concentration C_j.

To obtain the first solution of g^j, the Tikhonov variation method is applied:

$$\min M\left[g^j\right]=\min\left\{\left\|\sum_{j=1}^{3}A^j g^j-U\right\|^2_{L_2[c,d]}+\sum_{j=1}^{3}\alpha^j\left\|g^j\right\|^2_{L_2\left[a^j,b^j\right]}\right\}. \tag{36}$$

For the sake of simplicity the L_2 norm of the solution is used. α^j represents three regularization parameters that are small positive values in the orders of 10^{-5} – 10^{-7}. The Tikhonov solutions $g^j(r)$ are strongly dependent upon the choice of these parameters. This is because the majority of known ways to choose the optimal regularization parameters α^j require special knowledge of the errors entering the measurement and processing of EXAFS data. The methods for a quantitative estimation of these errors have still not been completely developed. Therefore, until now, the regularization parameters could only be determined through individual knowledge and experience of the experimenter. On the other hand, the determination of more than one regularization parameter represents a serious mathematical problem. A possible method for determining the three parameters, although it is incorrect (as confirmed by numerical experiments), is to make all of these parameters equal. The reason why this way is not possible is that the contributions from the different RDFs to the EXAFS spectrum are of different magnitude.

The proposed solution to the problem of α^j determination is to obtain one "initial" regularization parameter and make the other parameters proportional to it. The following procedure, in most cases, has shown acceptable results:

If the "initial" regularization parameter equals α and the contribution of the $g^j(r)$ functions to the EXAFS spectrum is associated with $R=\max\left\{\left\|A^j\right\|_{L_2},\ j=1,2,3\right\}$, then the desired regularization parameters can be expressed as:

$$\alpha^j=\frac{\alpha\left\|A^j\right\|_{L_2}}{R} \tag{37}$$

This approach of choosing the regularization parameters allows to reduce the influence of the operators A^j in which the Tikhonov solutions are interdependent on. Hereinafter, the "initial" regularization parameter α will be shown.

The calculated g^1(UU), g^2(USi), and g^3(UO) for soddyite show significant deviations from the expected RDFs, due to the non-uniqueness of the Tikhonov solution with $\alpha^j=10^{-6}$ (Fig. 14). Since it is impossible to obtain a unique solution for Eq. (35) from

the experimental EXAFS spectrum, additional *a priori* information is used to stabilize the Tikhonov solution. In particular, each peak in $g^j(r)$ of the first Tikhonov solution (Fig. 14) is analyzed whether it is a "true" or "false" peak using the method of separating functionals [60].

3.3 Method of separating functionals [60]

The method of separating functionals is used to distinguish between "true" peaks corresponding to real coordination shells and "false" peaks due to artifacts in each partial $g^j(r)$ function. Artifacts being referred to here are the peaks in the $g^j(r)$ function due to irregularities and the interdependency of the $g^j(r)$ functions.

It is assumed that the coordination shells of $g^j(r)$ are separated from one another in distance r by the constant Δr_{ik}^j, $i \neq k$ and that each i peak has a certain finite width $\tau_i^j < \Delta r_{ik}^j$. For example, Fig. 15 shows the intervals for the analysis of the first coordination shell of g^3(UO) RDF for soddyite.

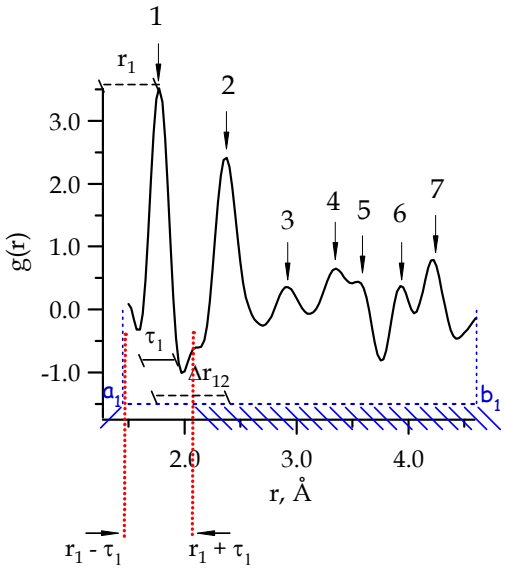

Fig. 15: Illustration of the intervals used for determining the "true" or "false" character of the first coordination shell in the function g^3(UO) using the method of separating functionals. g^3(UO) for soddyite is obtained by the Tikhonov variation method. r_i, i=1,2,....,M are the potential interatomic distances of the RDF coordination shells. The interval between a_1 and b_1 represents the interval for the defined function. The shaded area in the interval represents the area not included in the analysis of the first coordination shell in the function g^3(UO) by the method of separating functionals.

Usually, for a weak disorder, the partial distribution function is approximated by a sum of Gaussians, i.e., assuming a symmetric Gaussian distribution of neighbors around the average distance *r* with variance $(\sigma_i^j)^2$:

$$g^j(r)=\frac{1}{4\pi\rho_0}\sum_i^{M^j}\frac{N_i^j}{(r_i^j)^2\sigma_i^j\sqrt{2\pi}}e^{-\frac{(r-r_i^j)^2}{2(\sigma_i^j)^2}} \tag{38}$$

In cases of high disorder, partial distribution functions can be approximated by δ functions, i.e., assuming flexible asymmetric distribution, which is often useful, because it takes into account the inharmonic behavior in the RDFs that can correspond to the real atomic structure of the sample. The $g^j(r)$ function, then, can be rewritten as:

$$g^j(r)\approx\sum_{i=1}^{M^j}\Lambda_i^j\delta(r-r_i^j), \tag{39}$$

where $r_i^j, i=1,2,....,M^j$ are the potential interatomic distances of the RDF coordination shells (Å) , and the values Λ_i^j are proportional to the area of the corresponded peaks.

In summary, the initial assumptions of the method of separating functional are:

- RDF peaks are separated from one another by a given constant

$$0 < \Delta r_{ik}^j \le \min\left\|r_i^j - r_k^j\right\|, \quad i\neq k, \tag{40}$$

- RDF peaks are represented by δ functions as in Eq. (39),
- RDF peaks are located in the intervals

$$\left[r_i^j-\tau_i^j, r_i^j+\tau_i^j\right], i=1,2,....,M^j, \tag{41}$$

where M^j are positive integer numbers.

If the number of peaks M^j and approximations of the potential interatomic distances $r_i^j, i=1,2,....,M^j$ are obtained, then the corresponding columns of the matrix A^j are given by:

$$U_i^j(k)=A^j\cdot\delta(r-r_i^j) \tag{42}$$

Taking into account that the experimental EXAFS normalized oscillating part $U(k)$ is known only with some accuracy ς, so that:

$$\left\|U(k)-U(k)^{\varsigma}\right\|\le\varsigma. \tag{43}$$

The basic EXAFS Eq. (35) can be rewritten as a sum of contributions from every particular peak of corresponding $g^j(r)$ function:

$$\sum_{j=1}^{3}\sum_{i=1}^{M^j}\Lambda_i^j U_i^j(k)=U^{\varsigma}(k), \tag{44}$$

This equation is solved with respect to unknown Λ_i^j (all other values of the equation are known) only when $U_i^j(k)$, i=1,2,....,M^j are linearly independent. The linear independence of $U_i^j(k)$ is equivalent to the existence in the scattering set of the input matrix A^j the data that corresponds to some $\{k,l\}$ RDF peaks and only for which the separating functional $\hat{U}$ is not equal zero, i.e. $\langle \hat{U}, U_l^k \rangle \neq 0$, whereas for all other $\{i, j\}$ RDF peaks $\langle \hat{U}, U_i^j \rangle = 0$. Here, $\langle ...,... \rangle$ means scalar product in Hilbert space. Then, it is possible to calculate Λ_l^k as:

$$\Lambda_l^k = \frac{\langle \hat{U}, U^{\varsigma} \rangle}{\langle \hat{U}, U_l^k \rangle}, \tag{45}$$

where U^{ς} is the experimental EXAFS normalized oscillating part known with the accuracy ς, and U_l^k are the columns of the input matrix A^j corresponding to the $\{k,l\}$ RDFs peaks with non- zero value of the separating functional $\hat{U}$.

The columns of the matrix A^j are described as:

$$U_i^j(k) \equiv 4\pi\rho_0 C^j \sum_{i=1}^{M^j} \frac{f_i^j(k,r)}{f_0(k,b^j)} \left\{ \frac{e^{-\frac{2(r+\Delta/2)}{\lambda(k)}}}{\left(-\frac{2}{\lambda(k)}\right)^2 + (2k)^2} \times \right.$$

$$\times \left[-\frac{2}{\lambda(k)} \sin\left(2k(r+\Delta/2) + \psi_i^j(k,r) + \pi\right) - 2k\cos\left(2k(r+\Delta/2) + \psi_i^j(k,r) + \pi\right) \right] -$$

$$- \left[-\frac{2}{\lambda(k)} \sin\left(2k(r-\Delta/2) + \psi_i^j(k,r) + \pi\right) - 2k\cos\left(2k(r-\Delta/2) + \psi_i^j(k,r) + \pi\right) \right] \times$$

$$\left. \times \frac{e^{-\frac{2(r-\Delta/2)}{\lambda(k)}}}{\left(-\frac{2}{\lambda(k)}\right)^2 + (2k)^2} \right\} \tag{46}$$

Because backscattering amplitudes, phases, and the term $e^{-\frac{2r}{\lambda(k)}}$ which characterizes the decay of the electron wave, are varying in k space slower than the $\sin(2kr)$ term, the $U_i^j(k)$ are represented as distorted $\sin$ functions, and the value of the separating

functional $\hat{U}$ depends from a concrete set of scattering functions $\psi_i^j(k,r)$ and $f_i{}^j(k,r)$ of the material.

In contrast to the previous data treatments which include the operator A^j that is defined as in Eq. (28), the similar operator $\hat{A}^j$, but without integration on the intervals:

$$\left[\hat{a}_i^j, \hat{b}_i^j\right] = \left[a_i^j, b_i^j\right] - \left[r_i^j - \tau_i^j, r_i^j + \tau_i^j\right] \tag{47}$$

is introduced into analysis.

For example, the operator $\hat{A}^3$ for the determination between "true" or "false" of the first coordination shell in the g^3(UO) function of soddyite is defined only in the interval $[r_1 - \tau_1, r_1 + \tau_1]$, (see Fig. 15). The corresponding overall operator should be rewritten as $\breve{A}^j = (A_1, A_2, \hat{A}^3)$ and the column of the input matrix A^j is defined as $U_1^3(k) = A^3 \cdot \delta(r - r_1^3)$.

The functional $\hat{U}$ represents the $(\in, \mu)-$separating functional for the distance r_i^j, if the following two conditions are satisfied:

Definition:

$$1) \quad \left\| \breve{A}^* \hat{U} \right\|_C \le \in \tag{48}$$

$$2) \left| \langle \hat{U}, U_i^j \rangle \right| = \mu > 0 \tag{49}$$

The norm $\|...\|_C$ is defined in the k space ($k \in [c,d]$) of linear, continuous functions, and is determined as:

$$\left\| \breve{A}^* \hat{U} \right\|_C = \max_{[c,d]} \left| \breve{A}^* \hat{U} \right| \le \in . \tag{50}$$

Thus the parameter $\in$ is small, and the separating functional $\hat{U}$ represents approximately the null vector of the operator $\breve{A}^*$. The * symbol indicates transposition. The relation $q = \in / \mu$ describes the separating functional quality. High-quality functional has a small value of this relation and allows estimating Λ_i^j values according to Eq. (45). Since the Λ_i^j values are proportional to the squares of the RDFs peaks and hence are associated with the coordination number of the elements in the material, they are indicative for the real coordination shells in RDFs.

The practical calculation of a separating functional is as follows:

For the sake of simplicity, the first condition (Eq. (48)) is modified to use the $L_2[c,d]$ norm:

$$3)\left\|\breve{A}^{*}\hat{U}\right\|_{L_2} \le \in_1 \tag{51}$$

where $\in_1$ is a small value, $\in \neq \in_1$.

Since the operator $\breve{A}^{*}$ represents a smooth function, the smallness of parameter $\in_1$ vouches for the smallness of parameter $\in$, hence enforcing the first condition (Eq. (48)).

Thus, to obtain the separating functional $\hat{U}$, the Tikhonov variation method in form:

$$\min\left\{\left\|\breve{A}^{*}U^{\varsigma}\right\|^{2}_{L_2} + \beta\left\|U^{\varsigma} - \nu U_i^j\right\|^{2}_{L_2}\right\} \tag{52}$$

is applied. Here ν is defined as:

$$\nu = \frac{1}{\left\|U_i^j\right\|} \tag{53}$$

β is a small positive regularization parameter, different from the regularization parameters α^j, that were used to receive the Tikhonov solutions of Eq. (35).

The first and second terms of Eq. (52) provide the performance of the first and second conditions (Eqs. (48 and 49)) of the definition of separating functional, respectively. Additionally, the second term of Eq. (52) stabilizes the variation task of Eq. (52).

The regularization solution U^{β} of Eq. (52) is then normalized.

On the assumption of $U^{\varsigma} = \hat{U} - \nu U_i^j$ and denoting $F = -\nu\breve{A}^{*}U_i^j$, Eq. (52) can be rewritten in standard form of Tikhonov variation method:

$$\min\left\{\left\|\breve{A}^{*}U^{\varsigma} - F\right\|^{2}_{L_2} + \beta\left\|U^{\varsigma}\right\|^{2}_{L_2}\right\} \tag{54}$$

Suppose N presents zero space, or in other words the kernel of the operator $\breve{A}^{*}$, i.e. N is the set of points which go to zero when multiplied by the matrix operator $\breve{A}^{*}$. Then, to the existence of the $(0,\mu)$- separating functional in the distance r_i^j of r space, it is necessary and enough, that the projection of the vector νU_i^j on the subspace N -vector $\overline{U}$ is not equal zero. The last statement is equivalent to:

$$\left\langle N, \nu U_i^j \right\rangle \neq 0 \tag{55}$$

Because the space N is closed, the vector $\overline{U}$ is always uniquely determined. It is also always correct, that any $(0,\hat{\mu}), \hat{\mu} \neq 0$ separating functional, for which $\hat{U} = \overline{U} / \left\| \overline{U} \right\|$, will be also $(0,\mu)$ –the separating functional with $\mu \geq \hat{\mu}$.

According to the classical theory of ill-posed problems (see, for example, [49]) the following result can be stated:

Theorem:

Let $\hat{U}$ be a $(0,\mu)$- separating functional in the distance r_i^j of *r* space and let ς be a given error level of the EXAFS normalized oscillating part U, so that: $\left\| U - U^{\varsigma} \right\| \leq \varsigma$.

Then, U^{β}, the solution of the regularization problem of Eq. (52), allows to find a good approximation to the separating functional $\hat{U}$, so that:

$$\hat{U}^{\beta} = U^{\beta} + \nu A^j \cdot \delta(r - r_i^j) \rightarrow \hat{U} \tag{56}$$

with

$$\frac{\varsigma^2}{\beta} \rightarrow 0, \ \beta \rightarrow 0. \tag{57}$$

This means that instead of the exact defined separating functional $\hat{U}$, the approximation $\hat{U}^{\beta}$ is calculated. Except for an error in the EXAFS normalized oscillating part U, the $\hat{U}^{\beta}$ depends on the value of the regularization parameter β. The problem of choosing the parameter β is solved much easier than the determination of three α^j regularization parameters in the case of the Tikhonov solutions of Eq. (36). First of all, the regularization parameter is one, instead of three. Furthermore, it is not necessary that $\hat{U} \cong \hat{U}^{\beta}$, it is only important that $\left\langle \hat{U}^{\beta}, U_l^k \right\rangle = C^{\beta} \neq 0$, whereas for all others $\{i, j\}$ RDFs peaks the value of $\left\langle \hat{U}^{\beta}, U_i^j \right\rangle \approx 0$ or is negative.

The values Λ_i^j are then computed as:

$$\Lambda_i^j = \frac{\left\langle \hat{U}^{\beta}, U^{\varsigma} \right\rangle}{\left\langle \hat{U}^{\beta}, U_i^j \right\rangle}, \tag{58}$$

and they are used to distinguish between the "true" peaks corresponding to real coordination shells and "false" peaks due to artefacts in each partial $g^j(r)$ function. In particular, a negative or small parameter Λ_i^j is indicative of a "false" peak.

The segments of $g^j(r)$ functions where "false" peaks were identified are set to zero. Then, the Tikhonov variation method (Eq. (36)) is applied again but only to the restricted intervals of the RDFs where potential "true" peaks have been identified. Thus, new RDFs Tikhonov solutions are determined. Now, they consist of a small number of narrow peaks that are separated in distance and associated with the true coordination spheres. The final RDFs solutions are then determined by an iteration method with filtration in real space [61].

3.4 Iteration method with filtration in real space [61]

The method of separating functionals allows determining the intervals $\left(S_0^j\right)$ in the RDFs where potential "true" peaks have been identified.

Once the Tikhonov variation method has been applied to these intervals $\left(S_0^j\right)$ of the RDFs:

$$\min M\left[g^j\left(S_0^j\right)\right]=\min\left\{\left\|\sum_{j=1}^{3}A^j\left(S_0^j\right)g^j\left(S_0^j\right)-U\right\|^2_{L_2[c,d]}+\sum_{j=1}^{3}\alpha^j\left\|g^j\left(S_0^j\right)\right\|^2_{L_2\left[a^j,b^j\right]}\right\}, \qquad (59)$$

the process is iterated until the $g^j(r)$ functions have converged. $A^j\left(S_0^j\right)$ represents the integral operator A^j restricted on the intervals $\left(S_0^j\right)$.

The evolution of the Tikhonov solutions to the final $g_m^j(r)$, where m is a number of the iterations, can be described as follows:

$$g_m^j=\sum_{j=1}^{3}\begin{pmatrix}A^{*j} & A^j & +B^j\\ S_m^j & S_m^j & S_m^j\end{pmatrix}^{-1}\begin{pmatrix}A^{*j} & U+B^j & g_{m-1}^j\\ S_m^j & S_m^j & \end{pmatrix} \qquad (60)$$

The procedure of filtration in real space is nothing more than an assumption that the real coordination peaks are simultaneously the biggest ones. The maximum D_{m-1}^j of the previous solution g_{m-1}^j is estimated according to:

$$D_{m-1}^j=\sum_{j=1}^{3}\max_{\left(S_m^j\right)}\left|g_{m-1}^j\right| \qquad (61)$$

This value is associated, then, with 100 percent and used to obtain a so-called "detection" threshold p varied between zero and one. For example, for a given value of $p_{m-1}^{j}=0.3$, all peaks of the g_m^j functions with a height below 30% with respect to the corresponded D_{m-1}^{j} maximum value of the previous g_{m-1}^{j} solutions are eliminated.

Usually, during the first two to three iterations the g_m^j functions are changing, and after approximately five iterations, they are practically stabilized. Application of the procedure described above, results in a substantial improvement of the g_m^j solutions.

This is an important trend in the data analysis using the method of separating functionals and then the iteration procedure that even when, sometimes for example, in cases of very similar backscattering phases of the elements in the material, the method of separating functionals can not distinguish between "false" and "true" peaks. Even when some of the "false" peaks are left in the Tikhonov solutions on the intervals $\left(S_0^j\right)$ with significant intensities, which sometimes exceed the height of the "true" peaks, "false" peaks tend to decrease during the iteration procedure and completely disappear after a few iterations, while the intensity of "true" peaks increases and becomes stabile.

3.5 Calculation of structure parameters

The final RDFs are analyzed to obtain structural information. In particular, interatomic distances (Å) and coordination numbers of each peak in RDFs are calculated after the iteration procedure. Because the final solutions are not approximated by Gaussian function, the full width at half maximum (*FWHM*) instead of the Debye-Waller factor in least-squares fitting is determined to give an estimate of the peak widths. The interatomic distances correspond to the maximums of the RDFs peaks.

Since the coordination numbers N_i^j are associated with the square Λ_i^j of the M^j-peak in the $g_i^j(r)$ located in the intervals $[r_i^j-\Delta/2, r_i^j+\Delta/2]$, and the narrow peaks were replaced by δ functions (Eq. (39)), the N_i^j are calculated as:

$$N_i^j = 4\pi\rho_0 C^j \int_{r_i^j-\Delta/2}^{r_i^j+\Delta/2} (r_i^j)^2 \Lambda_i^j \, \delta(r-r_i^j)dr, \qquad (62)$$

where $r_i^j, i=1,2,....,M^j$ are the interatomic distances of the RDFs coordination shells (Å), and the values Λ_i^j are determined by the method of separating functionals. ρ_0 represents the atomic density of the material consisting of $j, j=1,2,3$ types of elements with the concentration C_j.

Fig. 16 illustrates the determination of structural parameters by the modified regularization method. In case of disordered systems not all, but some of the coordination shells have an asymmetric distribution of interatomic distances. As can be seen in Fig. 16, the RDFs peak corresponding to such coordination shell is asymmetrical, that logically leads to an interatomic distance that differs from those received assuming a Gaussian distribution.

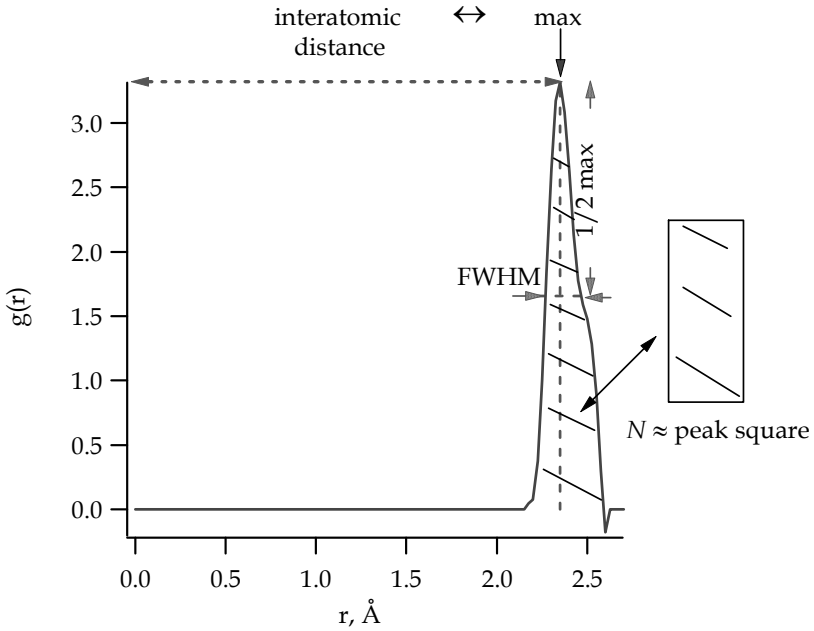

Fig. 16: The determination of structural parameters from RDFs as obtained by the modified regularization method.

Generally, the interatomic distances received by the modified regularization method can additionally characterize the degree of disorder of the local environment of the absorber. The distances obtained by least-squares fitting using a Gaussian distribution and the values determined by the proposed algorithm agree only in case of symmetric coordination shells.

4. TESTING OF THE MODIFIED TIKHONOV REGULARIZATION METHOD

4.1 Introduction

EXAFS analysis through shell-by-shell fitting provides reliable quantitative information on the number, distance, and identity on first- and second-neighbor shells around an absorbing element comparable to that obtained in X-ray diffraction analysis. Regarding the molecular-level speciation of uranium in a variety of uranyl UO_2^{2+}-containing complexes, numerous EXAFS studies [62–115] have been able to detect the first two oxygen shells around U^{6+} (axial $O(O_{ax})$ and equatorial $O(O_{eq})$) and in some cases to identify more distant neighbor shells around the uranyl ion by shell fitting. The detection and identification of the atoms in distant coordination shells is essential for detecting the formation of inner-sphere or outer-sphere complexes on mineral surfaces and precipitation of three-dimensional uranium-containing phases with an unknown structure. However, often several structural models based on different distant neighbor shells describe the experimental EXAFS data equally well. This can lead to an inadequate interpretation of the structure and makes the analysis sometimes impossible without prior knowledge of the local environment.

This study is part of a larger study of actinide speciation at the surface of the clay mineral kaolinite KGa-1b (BMWi (Bundesministerium für Wirtschaft und Technologie) under project № 02E9653). Instead of trying to find the best structural model that fits the available EXAFS data, the modified Tikhonov regularization method was applied to determine the speciation of U(VI) in the samples directly without assuming any specific structural model.

To evaluate the ability of the method to provide reliable structural information for samples with unknown structure, the method was applied first to simulated and experimental U L_{III}-edge EXAFS spectra of soddyite $(UO_2)_2SiO_4 \times 2H_2O$, which has a known crystal structure. Soddyite is an appropriate model compound for samples with U(VI) sorbed on kaolinite, because the same RDFs U-O, U-Si, and U-U should be calculated for soddyite and the sorption samples [116]. In particular, these calculations will show the possibilities and limitations of the modified Tikhonov regularization method as applied to systems containing uranium, oxygen and silicon or aluminium. Finally, the potential of the new approach will be illustrated by applying it to the EXAFS analysis of samples with unknown structure, i.e., U(VI) and Pu(III)/Pu(IV) sorbed on kaolinite.

The outline for this chapter is as follows: In Section 4.2 the modified Tikhonov regularization method is applied to the simulated and experimental U L_{III}-edge EXAFS spectra of soddyite. For this compound, three RDFs, i.e., U-O, U-Si, and U-U, are

calculated from one EXAFS spectrum. The "true" coordination shells in the RDFs U-O and U-U are not difficult to identify from theoretical $\chi(k)$ and also from experimental EXAFS spectra of soddyite. This section describes in detail how the U-Si contribution can be detected in simulated and experimental L_{III}-edge EXAFS spectra of soddyite. This section is the key to extracting structural information from the EXAFS spectra of all actinide-containing systems with oxygen, silicon, or aluminium.

The results of the EXAFS analysis of the samples with U(VI) sorbed on kaolinite is given in Section 4.3. The mechanism of U(VI) sorption on kaolinite as a function of pH, U(VI) concentration, and the presence or absence of CO_2 is discussed. The analysis of the binding sites on the kaolinite surface suggests that uranyl ion can be sorbed along the edges of kaolinite, on the $[Si(O,OH)_4]$ sites from the tetrahedral sheet and/or on the $[Al(O,OH)_6]$ sites from the octahedral sheet. Depending on the U(VI) concentration, multiple surface species, which are attributed to binding of monomeric or polymeric complexes to aluminol or silanol sites, are possible to detect.

In Section 4.4, the uptake mechanism of plutonium by kaolinite was investigated by applying X-ray absorption spectroscopy to batch sorption samples. The structural models used in the least-squares fits were confirmed by an alternative EXAFS data analysis approach based on the modified Tikhonov regularization method.

The structural parameters obtained by the modified Tikhonov regularization method for soddyite and the samples with U(VI) or Pu sorbed on kaolinite are compared to published structures obtained by previous EXAFS studies and/or single-crystal X-ray diffraction (XRD).

General information about the minerals soddyite and kaolinite, and some details of the samples preparation, EXAFS measurements, and EXAFS data treatment are given in Appendixes I and II.

4.2 Soddyite

4.2.1 Model calculations

Theoretical U L_{III}-edge EXAFS spectra of soddyite were calculated according to Eq. (35) in the k range 3.00 ÷ 12.2 $Å^{-1}$ with the RDFs U-U, U-Si, and U-O simulated on the base of $(UO_2)_2SiO_4 \times 2H_2O$ X-ray diffraction data [48]. The RDFs U-U, U-Si, and U-O were calculated in the r intervals 3.0 ÷ 6.0, 2.40 ÷ 6.0, 1.50 ÷ 6.0 Å, respectively. The structural parameters used for the model calculations are listed in Table 2. The model A has an atomic structure completely coinciding with the known XRD data of soddyite [48]. Instead of the U-Si interaction at 3.16 Å (model A), the RDF g^2(USi) of the model B contains one Si atom at 2.70 Å. To investigate the dependence of the feature at 2.70 Å in the g^2(USi) on the input data of the RDF g^3(UO), models C and D coincided completely with the XRD data of soddyite but only with the axial U-O coordination shell (model

C) or only with the equatorial U-O coordination shell (model D). The only one difference in the input model A and E data is the absence of the first peak at 3.86 Å in the U-U contribution. This was done to explain the appearance of a feature at the distance 4.23 Å in RDFs U-O and U-Si (see below).

Table 2: The structural parameters for the RDFs U-U, U-Si, U-O used for calculations of models A-E (*r* - distance (Å), *N* – coordination number, σ^2 – Debye-Waller factor (Å^2)).

Model	O_{ax} σ^2=0.0025		O_{eq} σ^2=0.0100		Si^1 σ^2=0.0057		Si^2 σ^2=0.0057		U^1 σ^2=0.0057		U^2 σ^2=0.0057		U^3 σ^2=0.0057	
	r	*N*	*r*	*N*	*r*	*N*	*r*	*N*	*r*	*N*	*r*	*N*	*r*	*N*
A	1.78	2	2.38	5	3.16	1	3.81	2	3.86	2	5.15	2	5.83	4
B	1.78	2	2.38	5	2.70	1	3.81	2	3.86	2	5.15	2	5.83	4
C	1.78	2	-	-	3.16	1	3.81	2	3.86	2	5.15	2	5.83	4
D	-	-	2.38	5	3.16	1	3.81	2	3.86	2	5.15	2	5.83	4
E	1.78	2	2.38	5	3.16	1	3.81	2	-	-	5.15	2	5.83	4

Since experimental EXAFS data contain always some noise, it was added to the theoretical EXAFS spectra according to:

$$[Ag]_{noise}(k)=[Ag](k)+noise, \tag{63}$$

where *noise* was calculated by the enoise function of the software IGOR PRO [117]:

$$noise=enoise(0.0001) \tag{64}$$

The enoise function (Fig. 17) returns a random value such that an infinite number of values would be evenly distributed between -0.0001 and 0.0001. The result has nearly 2^{32} distinct values and the sequence of random numbers has a period in excess of 10^{18}.

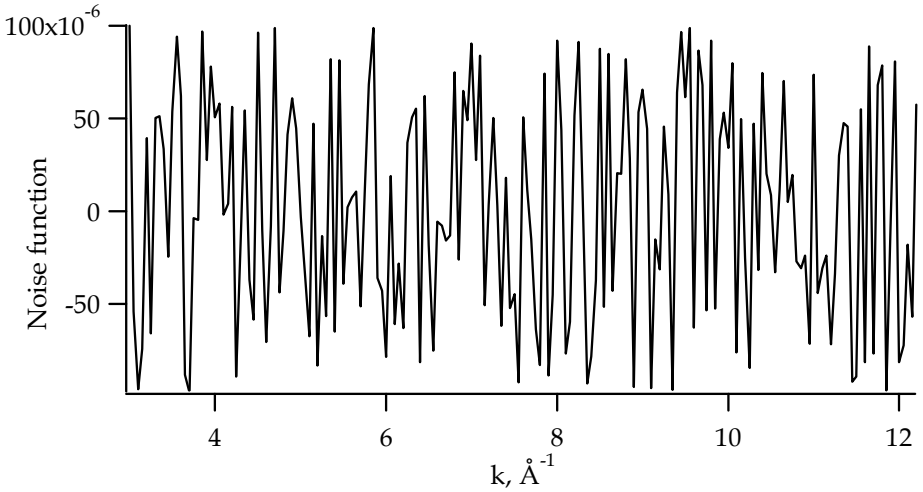

Fig. 17: Noise function in order of 10^{-4} - 10^{-6} that was added to all theoretical U L_{III}-edge EXAFS spectra of soddyite.

4.2.1.1 Tikhonov solutions

For all models, the first solution for the functions $g^j(r)$ was calculated by the Tikhonov variation method (Eq. (36)) with the "initial" regularization parameter $\alpha = 10^{-5}$. Although the Tikhonov solutions obtained with this parameter α are still far from the model RDFs, they qualitatively estimate the interatomic distances of the main coordination shells. As an illustration, Tikhonov solutions of model A are shown in Fig. 18. In model A the interatomic distances and coordination numbers are the same as in the crystal structure of soddyite [48]. As can be seen in Fig. 18, the most significant deviations from the model calculation are observed in Tikhonov solutions g^2(USi) at ~2.70 Å and also g^3(UO) at ~4.23 Å.

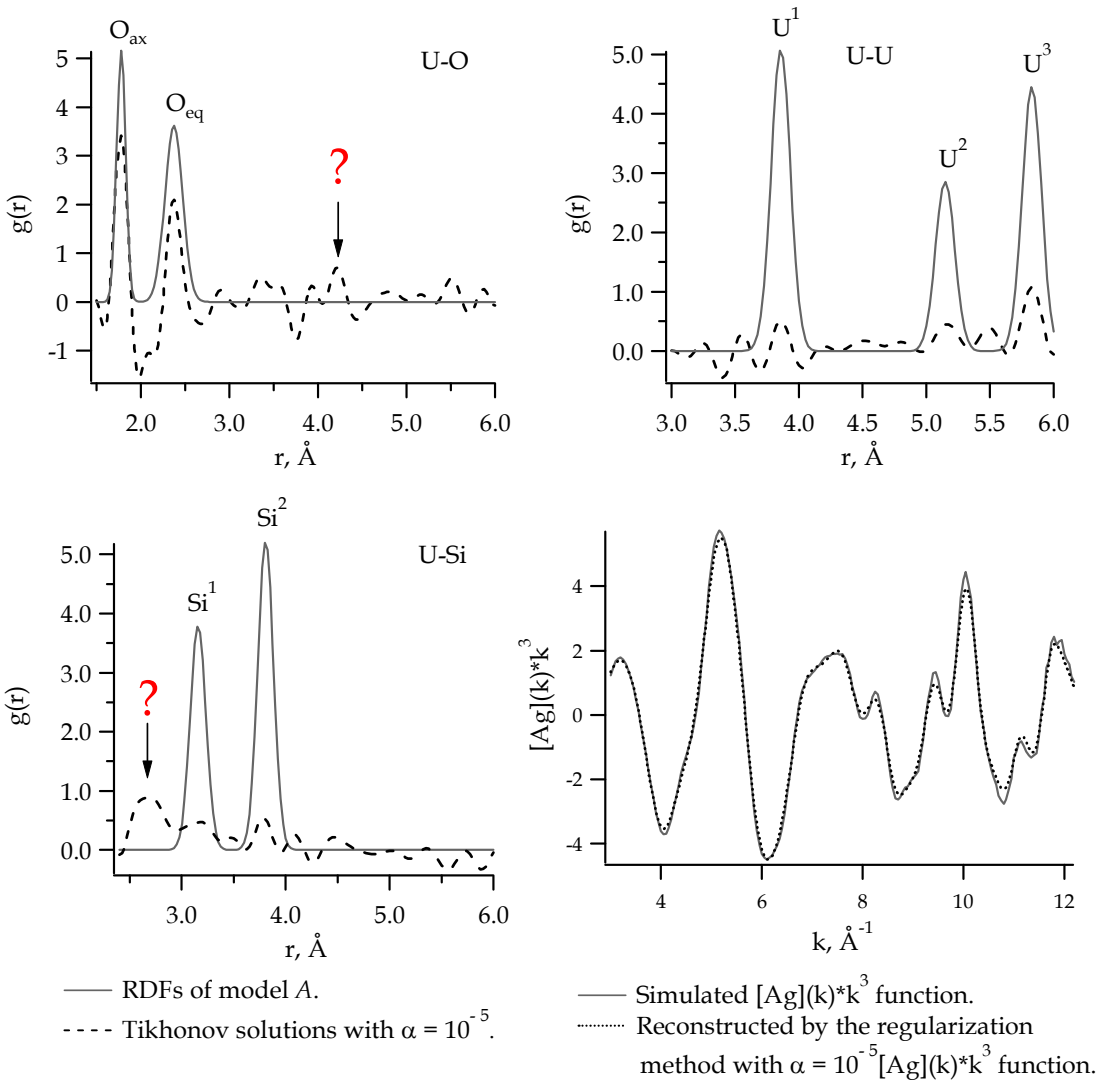

Fig. 18: Reconstruction of model A for soddyite. Tikhonov solutions show not only the peaks of the model but also some false peaks. The biggest of them (with symbol ?) are in g^2(USi) at the distance ~2.70 Å and in g^3(UO) at ~4.23 Å.

To understand the reason for the appearance of an additional broad peak in the Tikhonov solution g^2(USi), models B, C, and D were constructed. The model E was simulated to explain the discrepancy at ~4.23 Å in Tikhonov solution g^3(UO).

Comparison of the Tikhonov solutions for models A and B:
Instead of the U-Si interaction at 3.16 Å (model A), the RDF g^2(USi) of the model B contains one Si atom at 2.70 Å. As can be seen in the Fig. 19, the locations of all peaks except of the feature at 2.70 Å in the RDF g^2(USi) are fairly stabile against the change in the model, while the heights of the peaks are shown to be relatively easily influenced.

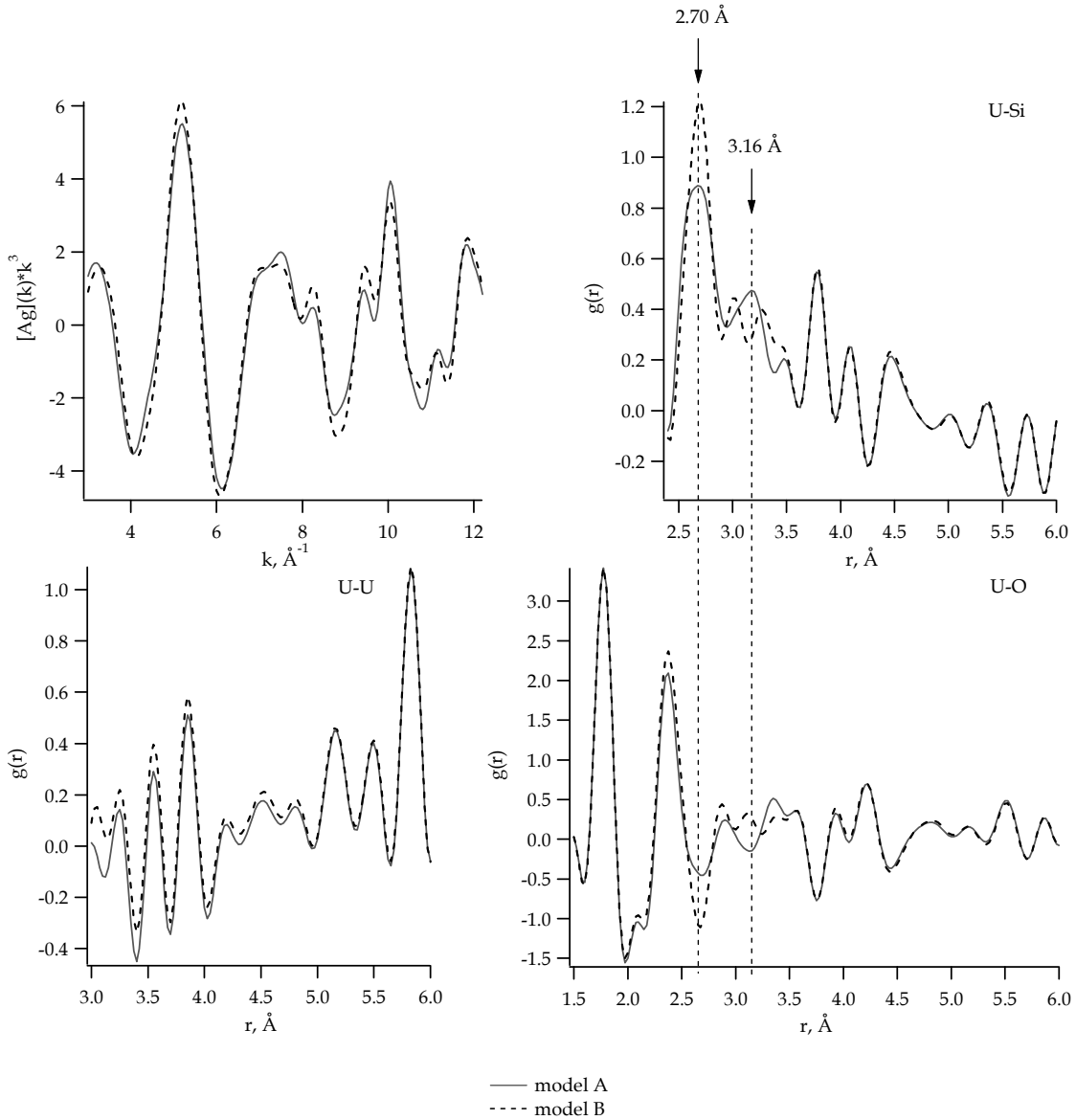

Fig. 19: Comparison of the Tikhonov solutions and calculated k^3-weighted [Ag](k) functions for models A and B. In both cases the "initial" regularization parameter was equal $\alpha = 10^{-5}$. The hatches correspond to the distances 2.70 and 3.16 Å in the g^2(USi) and g^3(UO).

Tikhonov solutions of the model B are essentially equivalent to those received by model A in the r region above 3.50 Å in all RDFs. In both models the Tikhonov solutions g^2(USi) show a big feature at 2.70 Å, also when it was not in the input data of the model A. Although the input RDF g^3(UO) of the model A is exactly the same as in model B, g^3(UO) Tikhonov solutions show the evident discrepancy both at 2.70 and 3.16 Å. The higher are the amplitudes of the signals in RDF g^2(USi), the lower are the corresponding minimums in the g^3(UO) and vice versa. The Tikhonov solutions g^1(UU), g^2(USi), and g^3(UO) of the models A and B provide slightly different $[Ag](k)$ functions.

Models A and B. Some conclusions:

The Tikhonov solutions of the simulated soddyite system are interdependent. In particular, changes in the input RDF g^3(UO) lead to changes in the Tikhonov solution g^2(USi) and vice versa.

The amplitude of the peak at 2.70 Å in the RDF g^2(USi) is too high to explain this origin only by U-Si contribution for model B, and cannot be associated with the U-Si contribution in model A.

Changes in the input RDF g^2(USi) does not influence the Tikhonov solution g^1(UU).

Comparison of the Tikhonov solutions for the models C and D:

To investigate the dependence of the feature at 2.70 Å in the g^2(USi) on the input data of the RDF g^3(UO), models C and D are employed with the atomic species completely coinciding with the XRD data of soddyite (see Table 2), but only with axial U-O coordination shell (model C) or only with equatorial U-O coordination shell (model D). The first Tikhonov solutions g^1(UU), g^2(USi), and g^3(UO) for both models are shown in Fig. 20. In spite of the same input U-Si data, the difference between the output g^2(USi) Tikhonov solutions is evident. As demonstrated in Fig. 20, the spurious peak at 2.70 Å is caused by the contribution of the equatorial oxygen coordination shell. Discrepancies between $[Ag](k)$ functions provided by the Tikhonov solutions g^1(UU), g^2(USi), and g^3(UO) are largely attributable to the difference in input U-O data of models C and D, which give dominated low- frequency oscillations to the $[Ag](k)$ functions.

Models C and D. Some conclusions:

The occurrence of the feature at 2.70 Å in Tikhonov solution g^2(USi) for model D is caused by the contribution of the equatorial U-O coordination shell.

It is also found that the Tikhonov solution g^2(USi) is strongly deformed over the r range until 5.0 Å when the equatorial U-O coordination shell is included in the input model data. Simultaneously, the RDF g^1(UU) is shown to be almost independent from the locations of the U-O coordination shells.

Comparison of the Tikhonov solutions for models A and E:

Whereas the only difference in the input of models A and E is the absence of the first

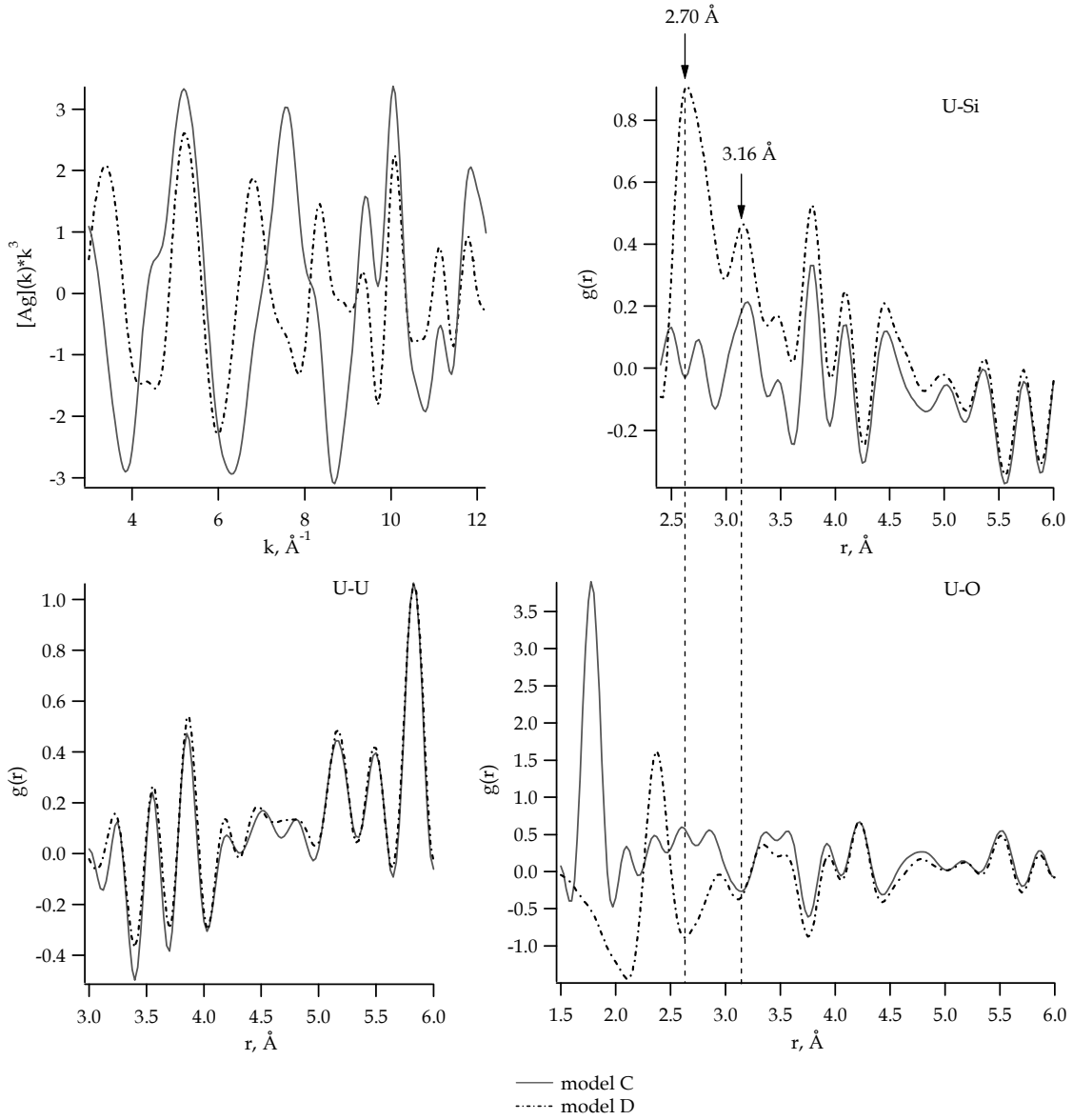

Fig. 20: Comparison of the Tikhonov solutions and calculated k^3-weighted [Ag](k) functions for models C and D. The hatches correspond to the distances 2.70 and 3.16 Å in the g^2(USi) and g^3(UO).

U-U peak at 3.86 Å, there are several distinctions in the corresponding Tikhonov solutions. In particular, the differences are not only in the Tikhonov solution g^1(UU) but also in g^2(USi) and g^3(UO). As can be seen from the Fig. 21, for the model A the U-U coordination shell at 3.86 Å in the input data contributes with the phase shift ~0.3 Å to the Tikhonov solutions g^2(USi) and g^3(UO). It is also found that the location of these additional features in *r* space is practically the same, i.e. ~4.23 Å. The absence of the U-U coordination shell in the model E (dashed line in Fig. 21) leads to disappearance of both the local minimum in g^2(USi) and the spurious peak in g^3(UO).

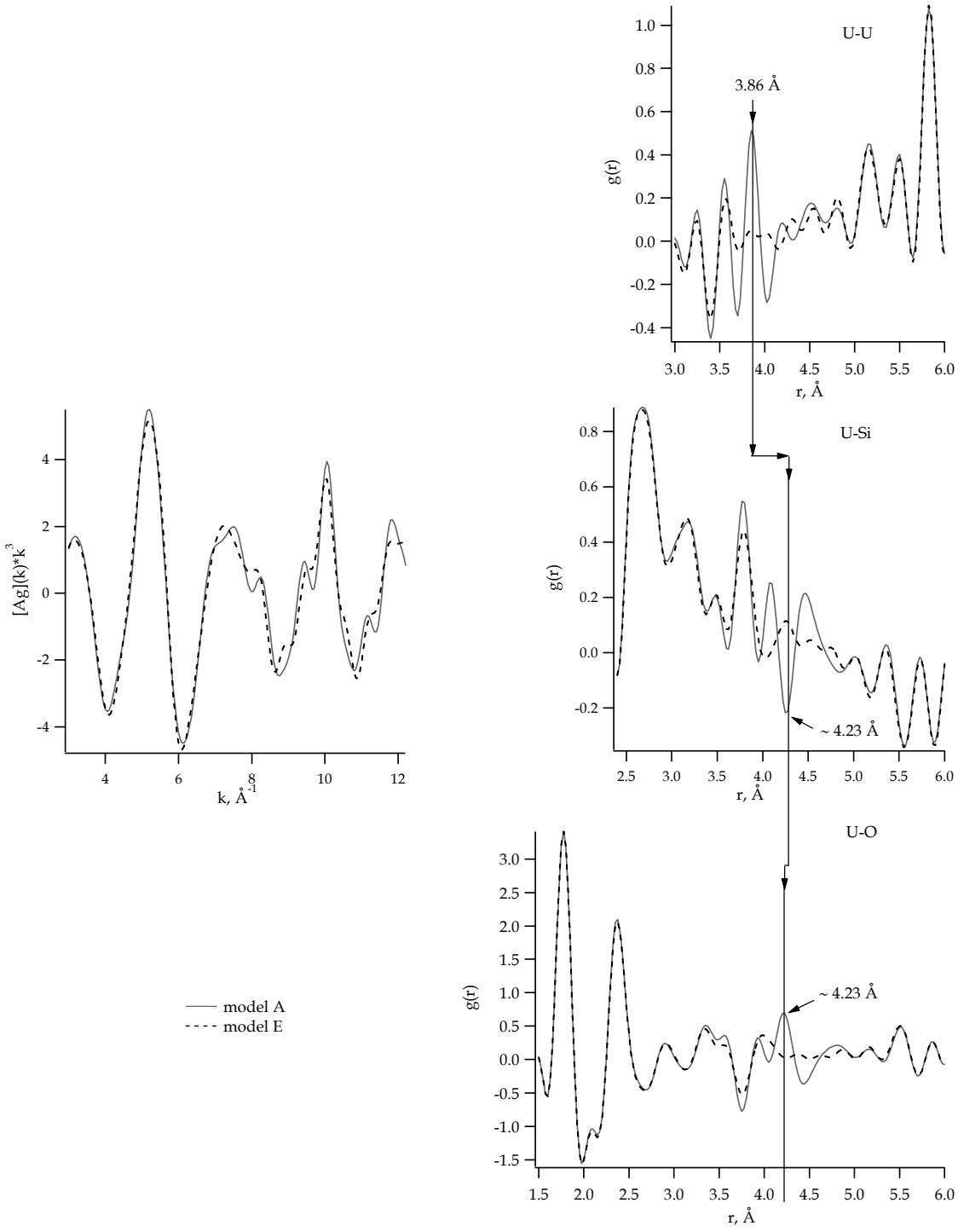

Fig. 21: Comparison of the Tikhonov solutions and calculated k^3-weighted [Ag](k) functions for models A and E. The vertical line shows the influence of the first U-U coordination shell at the distance 3.86 Å on the Tikhonov solutions g^2(USi) and g^3(UO).

The Tikhonov solutions g^1(UU), g^2(USi), and g^3(UO) of models A and E provide slightly different $[Ag](k)$ functions.

Models A and E. Some conclusions:

It should be noted here that the input U-O and U-Si data for both models does not contain any atoms at 4.23 Å; hence it is reasonable to certain that these features in the corresponding Tikhonov solutions arise from the first peak at 3.86 Å in U-U contribution.

The simultaneous presence of both features in the Tikhonov solutions, i.e., the local minimum in g^2(USi) and the peak in g^3(UO) at ~4.23 Å, can be indicative for the presence of a U-U coordination shell at 3.86 Å.

4.2.1.2 Method of separating functionals

Since it is impossible to obtain unique Tikhonov solutions for the Eq. (35) from the input model data, additional *a priori* information is used to stabilize the Tikhonov solutions. In particular, each peak in the functions $g^j(r)$ of the first Tikhonov solutions of all models is analyzed whether it is a "true" or "false" peak using the method of separating functionals [60]. A negative or small parameter Λ is indicative of a "false" peak. The maximums of RDFs peaks correspond to the interatomic distances, which will be refined during the iteration procedure.

Before a separate inquiry of the solutions for each model, it is very informative to look at the trend within each type of shell among the present Tikhonov solutions for all models. The values of separating functionals with their quality parameters for the prominent peaks of the Tikhonov solutions g^1(UU), g^2(USi), and g^3(UO) are listed in Tables 3, 4, and 5, respectively.

Table 3. The values of separating functionals Λ with their quality parameters q for the prominent peaks of the Tikhonov solution g^1(UU) for models A-E.

Model	U^1			U^2			U^3		
	r, Å	Λ	q	*r*, Å	Λ	q	*r*, Å	Λ	q
A	3.85	14.02	1.43	5.15	9.88	1.35	5.83	13.92	1.16
B		14.38			9.72			14.08	
C		13.80			9.75			13.89	
D	3.88	14.95	1.42	5.18	10.25	1.34		13.72	
E	3.85	0.60	1.43	5.15	9.22	1.35		13.87	

As can be seen in Table 3, the functional values for the accounted U-U coordination shells are consistent among all models. The corresponding quality parameters can be reported as relative good. Reasonable discrepancy of the interatomic distances for the first two U-U shells of model D in comparison with all other models is due to the changes in the U-O input data for this model. Generally, the Tikhonov solution g^1(UU)

is very stable and almost independent from the g^2(USi), and g^3(UO) solutions for all models.

Although it was proved by the comparison of the Tikhonov solutions for models C and D that the feature at 2.70 Å in the g^2(USi) is an artifact, this is not directly evident from the values of separating functionals in Table 4.

Table 4. The values of separating functionals Λ with their quality parameters q for the prominent peaks of the Tikhonov solution g^2(USi) for models A-E.

Model	Si^1			Si^2			Si^3		
	r, Å	Λ	q	*r*, Å	Λ	q	*r*, Å	Λ	q
A	2.68	18.49	3.53	3.18	7.67	3.53	3.78	28.26	3.50
B	2.70	34.94	3.51	-	-	-		29.13	
C	2.75	0.64	3.49	3.20	10.91	3.52		25.79	
D	2.65	19.13	3.54	3.15	7.57			28.57	
E	2.68	18.97	3.53	3.18	9.44	3.53	3.80	20.47	

The values of separating functionals Λ for the Si^1 feature for models A, D, and E are approximately the same. For model B, the only model where this shell is really simulated, the corresponding value is approximately twice time more, and only for the model C it is almost zero. The derived interatomic distances for all features of the g^2(USi) are in relatively poor agreement among the models.

All these findings coincide with the results obtained by comparing the Tikhonov solutions of models A-E. The fact that the interatomic distances of the Si^1 feature are sufficiently differed among the models confirms the suggestion about its spurious origin. Why are the values for the separating functionals of the Si^1 feature for all models except C so large? While all of them contain the contribution of the equatorial U-O coordination shell in the Tikhonov solution g^2(USi). Firstly, when this contribution is absent (model C), the separating functionals value for the Si^1 feature becomes almost zero, and a U-Si coordination shell at 3.16 Å can be accurately analyzed. Hence, only in the absence of the equatorial oxygen coordination shell (model C) the method of separating functional could distinguish between "true" or "false" coordination shells in the Tikhonov solution g^2(USi). To understand why this is the case, it is useful to review the basic aspect of the method of separating functional. The method works quite well, when the atoms of the investigated system have different scattering parameters in operator A^j (Eq. (35)), generally different backscattering phases.

The backscattering phases for the U, Si, and O of soddyite are shown in Fig. 22. From the Fig. 22 becomes evident that Si and O backscattering phases are too similar to allow the method of separating functional to distinguish between "true" or "false" coordination shells for these elements. Notice that the last statement is a question of

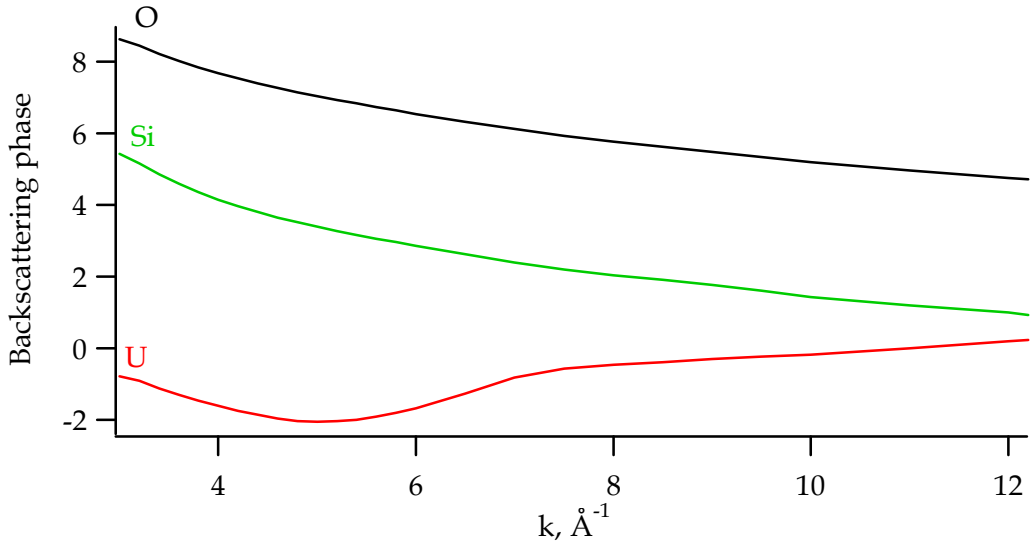

Fig. 22: Atomic backscattering phases of O, Si, and U calculated with the program FEFF 8.20 at the distances 2.40 Å, 2.50 Å, 3.0 Å from the central U atom, correspondingly. The method of the separating functionals is not able to distinguish between "true" or "false" U-Si coordination shells at the distance approximately 2.40 Å due to the similarity of the U-O and U-Si backscattering phases.

central importance for silicon atoms more distant than oxygen. Depending on the geometry of a particular structure, the scattering power of Si atoms is not large enough to make a discernible contribution to the EXAFS spectra. Moreover, Si shells tend to contribute to a region of the EXAFS spectra that is cluttered with the strongest spectral contribution from oxygen atoms. That is the reason why the method of separating functional can with a good quality distinguishes U-O coordination shells but not U-Si shells. The lack of good quality parameter for the separating functional for the Tikhonov solution g^2(USi) in Table 4 also confirms this conclusion.
As can be seen from Table 5, the situation for the analysis of the Tikhonov solution g^3(UO) by the method of separating functional is better.

Table 5. The values of separating functionals Λ with their quality parameters q for the potential "true" peaks of the Tikhonov solution g^3(UO) for models A-E.

Model	O_{ax}			O_{eq}			O_4.23		
	r, Å	Λ	q	*r*, Å	Λ	q	*r*, Å	Λ	q
A	1.78	18.58	0.18	2.38	12.20	0.54	4.23	8.38	0.53
B		18.43			13.51	0.60	4.20	8.28	
C		20.87		2.35	-1.08	0.54	4.23	7.59	
D	-	-	-	2.38	13.58		4.23	8.50	
E	1.78	18.58	0.18	2.38	12.07		-	-	-

All results including separating functional values, their quality parameters, as well as interatomic distances of the coordination shells are in good agreement with the U-O input data of the presented models. The problem with the Tikhonov solution g^3(UO) is reduced to a problem of what to do with O_4.23 feature, which has a relatively large value of the separating functional. Generally, in case of a peak with a relatively large Λ value, it should be kept as a potential "true" coordination shell. As will be demonstrated later, even when some of the "false" peaks are left in the Tikhonov solutions, during the iteration procedure the "false" peaks tend to decrease and after a few iterations they completely disappear, while the "true" peaks shoot up and stabilize.

Some conclusions:

1. It is already a very satisfactory basis for the evaluation of the results of the method of separating functional that the functional values are consistent among the models.
2. Although the method of separating functional is quite reliable for the analysis of the Tikhonov solutions g^1(UU) and g^3(UO), it fails in case of the Tikhonov solution g^2(USi) because of the similarity in the Si and O backscattering phases. This makes it impossible to distinguish the U-Si contributions from the U-O contributions.
3. The quality parameter of separation functionals can predict the ability of the method to reliably analyze a particular Tikhonov solution.
4. The quality of the scattering characteristics calculated by program FEFF 8.20 can affect the results of the separating functional analysis dramatically.

In Tables 3, 4, 5 only the prominent peaks of the Tikhonov solutions g^1(UU), g^2(USi), and g^3(UO) are shown for each model. In reality, much more features (all maximums of the Tikhonov solutions) are analyzed by the method of separating functionals.

The decision on whether to include a shell or not is based on the following criteria:

1. The residual ε between the EXAFS experimental data and [Ag] function in the form of a normalized χ^2 value.
2. The visual quality of calculated [Ag] function in comparison with the EXAFS experimental data.
3. The Λ value of separating functional.

It has been found that the Λ value is the most important criterion.

For example, the determination of "true" or "false" RDFs peaks is demonstrated for model A. Note that the input data of this model completely coincides with the known XRD data of soddyite.

The Λ values for all RDFs peaks with the corresponding interatomic distances for model A are shown in Table 6.

Table 6. Determination of "true" and "false" RDF peaks of the Tikhonov solutions g^1(UU), g^2(USi), and g^3(UO) for model A using the method of separating functionals.

№	g^1(UU)		g^2(USi)		g^3(UO)	
	r, Å	Λ	*r*, Å	Λ	*r*, Å	Λ
1	3.25*	4.88	2.68	18.49	1.78	18.58
2	3.55	7.98	3.18	7.67	2.10*	-8.23
3	3.85	14.02	3.48*	-2.34	2.38	12.20
4	4.20*	2.65	3.78	28.26	2.90*	1.15
5	4.53*	0.48	4.08	10.79	3.35*	3.98
6	4.80*	-1.20	4.48	12.88	3.55*	2.02
7	5.15	9.88	5.00*	2.43	3.93*	3.22
8	5.50*	-2.41	5.35	16.49	4.23	8.38
9	5.83	13.92	5.73	11.04	4.80*	0.85
10	-	-	-	-	5.18*	1.64
11	-	-	-	-	5.53*	4.59
12	-	-	-	-	5.88*	-2.41

* - Negative or small positive Λ values are indicative for "false" peaks.

As can be seen, it is not difficult to identify the true coordination shells in the RDF g^1(UU) by the method of separating functionals. With the exception of the feature at 4.23 Å, all other analyzed peaks in the Tikhonov solution g^3(UO) are also clearly separated into two groups, i.e., "true" or "false". The most complicated case is with the Tikhonov solution g^2(USi). The analyzed peaks of g^2(USi) are not separated into "true" or "false". After the analysis with the method of separating functionals, only the peaks at 3.48 and 5.00 Å can be identified as "false" in the Tikhonov solution g^2(USi).
Based on the Λ values shown in Table 6, the following segments of Tikhonov solutions where "false" peaks were identified are set to zero:

U-U: [3.00, 3.40], [4.20, 4.95], [5.35, 5.65];
U-Si: [3.40, 3.60], [4.80, 5.20];
U-O: [2.025, 2.125], [2.70, 4.05], [4.45, 6.00].

It should be noted that all features with relative large Λ values are left in the corresponding Tikhonov solutions for further analysis.

4.2.1.3 Iteration method with filtration in real space

Once the variation Tikhonov method has been applied to the restricted intervals, the "initial" regularization parameter is reduced to 10^{-7}. This parameter is used to iterate the new solutions for functions g^j of all models until they have converged (Fig. 23). The values of the finite width τ (Eq. (41)) for the RDFs peaks are equal to 0.15, 0.15, and 0.25 Å for g^1(UU), g^2(USi), and g^3(UO) functions, respectively to correspond to the

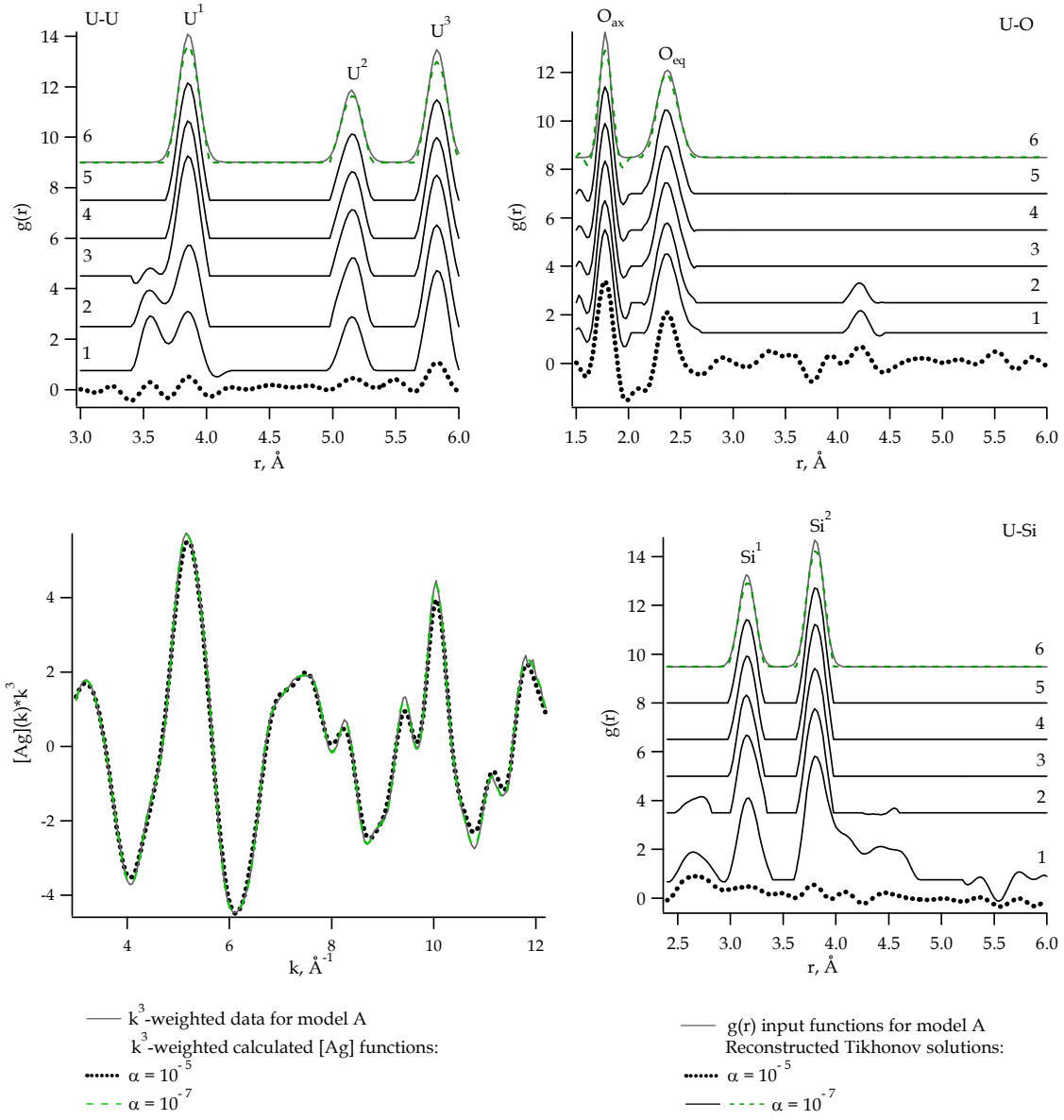

Fig. 23: Evolution of the Tikhonov solutions for model A. Solid grey lines represent the data of model A: k^3-weighted EXAFS (left) and functions g^j (right). Dots correspond to the solutions with $\alpha = 10^{-5}$: calculated k^3-weighted [Ag](k) function (left) and the first Tikhonov solutions (right). Solid black lines represent the first five iterations of Tikhonov solutions on restricted intervals ($\alpha = 10^{-7}$). Dashed green lines are the final solutions g^j and the corresponding k^3-weighted [Ag](k) function.

expected Debye-Waller factors. As can be seen from the Fig. 23, during the first three iterations all RDFs functions are essentially changed, i.e., peaks not associated with the structural model decrease and then completely disappear, while the "true" peaks shoot up and stabilize. The final solutions (dashed green lines in the Fig. 23) reconstruct the data of model A quite well. The evolution of the Tikhonov solutions to the final ones is

described also in Table 7, including the "initial" regularization parameter α, the "detection" threshold p , and the residual ε between the experimental data and corresponding function [Ag] in the form of a normalized χ^2 value varied during the iteration procedure.

Table 7. The characteristics describing the iteration procedure for the model A.

Iteration №	"Initial" α	p , %	Residual, ε
1	1.0E-7	20	0.000072
2	1.0E-7	20	0.000094
3	1.0E-7	20	0.000106
4	1.0E-7	20	0.000116
5	1.0E-7	20	0.000115
6	1.0E-7	20	0.000115

After the application of the method of separating functionals to the first Tikhonov solutions for models B-E, the corresponding final solutions were determined by the iteration method in a similar manner as for model A (tables with complete Λ values and the final solutions are not shown). It should be noticed that all models are contaminated with the same statistical noise comparable to the error level of the experimental data of soddyite, but without any multi-scattering contribution. For all models, the iteration method with filtration in real space is found to converge within five-seven iterations which is much faster than an iteration procedure with trial functions. Moreover, the obtained coordination numbers and interatomic distances for all models are very close to the input data. The derived structural parameters for all models are compared to the input data in Table 8.

The knowledge of suitable regularization parameter α is an essential element of information for all future applications of the modified regularization method to systems containing U, Si, and O. The value of $\alpha=10^{-7}$ provides not only a very low residual value ε (see Table 7) between simulated EXAFS data and functions [Ag] for all investigated models, but, more important, guarantees the agreement between input and derived interatomic distances within ± 0.02 Å, as well as a good agreement between the coordination numbers (Table 8). The exceptions are discussed below. Models A, B, D, E consist of a uranyl moiety with five O_{eq} atoms at 2.38 Å. When both axial and equatorial oxygen shells at 1.78 and 2.38 Å (models A, B, E), respectively, are included in the structural model, small discrepancies in bond distances and coordination numbers between the model (input) and the final solution (output) appear. As can be seen from Table 8, the U-O_{eq} bond distance is shorter by 0.02 Å and the O_{eq} coordination number is smaller by 8 - 10% than in the model. However, these discrepancies are within the error bars of the analysis. For the O_{ax} shell the EXAFS structural parameters agree completely with the input data. This is also the case when

Table 8. Interatomic distances *r* in Å and *N* – coordination numbers of coordination shells for RDFs in input data and in final solutions (output) for models A-E.

Model		O_{ax}		O_{eq}		Si^1		Si^2		U^1		U^2		U^3	
		r	*N*	*r*	*N*	*r*	*N*	*r*	*N*	*r*	*N*	*r*	*N*	*r*	*N*
A	input	1.78	2	2.38	5	3.16	1	3.81	2	3.86	2	5.15	2	5.83	4
	output	1.78	2.0	2.36	4.6	3.16	0.9	3.81	1.9	3.86	1.8	5.16	1.9	5.83	3.6
B	input	1.78	2	2.38	5	2.70	1	3.81	2	3.86	2	5.15	2	5.83	4
	output	1.78	2.0	2.36	4.6	2.70	0.9	3.81	1.9	3.86	1.8	5.16	1.9	5.83	3.6
C	input	1.78	2	-	-	3.16	1	3.81	2	3.86	2	5.15	2	5.83	4
	output	1.78	2.0	-	-	3.16	1.0	3.81	1.9	3.86	1.8	5.16	1.9	5.83	3.6
D	input	-	-	2.38	5	3.16	1	3.81	2	3.86	2	5.15	2	5.83	4
	output	-	-	2.37	4.9	3.16	1.0	3.81	1.9	3.86	1.8	5.16	1.9	5.83	3.6
E	input	1.78	2	2.38	5	3.16	1	3.81	2	-	-	5.15	2	5.83	4
	output	1.78	2.0	2.36	4.5	3.16	0.9	3.81	1.9	-	-	5.15	1.9	5.83	3.6

only one oxygen coordination shell was considered in the input model, i.e., without O_{eq} (model C) or without O_{ax} (model D). Both interatomic distances and coordination numbers derived from the final solutions g^3(UO) coincide with model values.

Another situation is with the coordination shell U^3. Although the input and the derived interatomic distances are absolutely the same, the final coordination numbers are always ~0.4 atoms smaller. It is believed that this discrepancy can be readily explained. Both the *r* range (3.0 ÷ 6.0 Å for g^1(UU)) and the *k* range (3.00 ÷ 12.2 $Å^{-1}$ of the simulated EXAFS spectra) are too short to reproduce well the coordination number of the coordination shell U^3 at a large distance.

It can be concluded, that in the model calculations the Tikhonov solutions converged quickly and contained only the coordination shells of the input data. This is achieved by combining of the method of separating functionals with the iteration method with filtration in real space.

4.2.1.4 Main conclusions based on model calculations for soddyite

The aim of the model calculations was to present the main trends of the treatment of EXAFS data by the modified regularization method in a manner that is applicable for the analysis of experimental data.

1. Some conclusions after the first step of treatment, i.e., after the application of the standard variation Tikhonov method, are:

- Although the direct determination of the first Tikhonov solutions g^1(UU), g^2(USi), and g^3(UO) is the advantage of the method, they show significant deviations from the input model data.
- The Tikhonov solutions of the investigated soddyite system are interdependent.
- In particular, changes in the input RDF g^3(UO) leads to changes in the Tikhonov solution g^2(USi) and vice versa.
- The spurious peak in Tikhonov solution g^2(USi) at 2.70 Å is caused by the contribution of the equatorial U-O coordination shell.
- It is also found that the Tikhonov solution g^2(USi) is strongly deformed over the r range until 5.0 Å when the equatorial U-O coordination shell is included in the input model data.
- The RDF g^1(UU) is shown to be almost independent from the locations of U-O and U-Si radial distribution peaks.
- The simultaneous presence of the local minimum in the Tikhonov solution g^2(USi) and the peak in the g^3(UO) at the same distance ~4.23 Å can be indicative for the existence of a U-U coordination shell at 3.86 Å.
- The suggested value of the "initial" regularization parameter is $\alpha = 10^{-5}$.

⇛ The first Tikhonov solutions can predict the locations of radial distribution peaks, but for a more satisfactory reconstruction of RDFs, the next two steps of treatment are necessary.

2. Some conclusions after the second step of treatment, i.e., after the application of the method of separating functionals, are:

- The method of separating functionals has a good efficiency to analyze whether a peak in the g^j functions is "true" or "false", when each atom j of the investigated system has discriminating scattering parameters in operator A^j (Eq. (35)), generally different backscattering phase.
- Although the method of separating functionals is quite reliable for the analysis of the Tikhonov solutions g^1(UU) and g^3(UO), it fails in case of the Tikhonov solution g^2(USi) because of the identical Si and O backscattering phases that make the distinction between U-Si and U-O contributions uncertain.
- The results of the method of separating functionals are consistent among the models.
- The quality parameter of the separation functionals can predict the ability of the method to reliably analyze a particular Tikhonov solution.

- The quality of the scattering characteristics calculated by the program FEFF can affect the results of the analysis by the method of separating functionals dramatically.

⇛ The method of separating functionals allows to determine intervals in the RDFs where "true" peaks are unlikely.

3. The variation Tikhonov method is applied again to intervals restricted by the method of separating functionals. Then the process is iterated until the RDFs functions have converged. The general observations about the iteration procedure are the following:

- The value of the "initial" regularization parameter should be reduced to the order of $\alpha = 10^{-7}$.
- During the first three iterations, all RDFs functions are essentially changed, i.e., features not associated with the model data decrease and then completely disappear, while the "true" peaks shoot up and stabilize.
- For models containing only statistical noise (Eq. (64)), the iteration method with filtration in real space converges within five-seven iterations. This is much faster than an iteration procedure with trial functions.
- The derived coordination numbers and interatomic distances for the final g^j functions of all models are very close to their input data.

⇛ It can be concluded, that in the model calculations the Tikhonov solutions converged quickly and contained only the coordination shells of the input data. This is achieved by combining of the method of separating functionals with the iteration method with filtration in real space.

Generally:

- The modified regularization method has a very good efficiency as a combination of all three steps for the determination of the functions g^j, i.e., the variation Tikhonov method, application of separating functionals, and the iteration method with filtration in real space.
- Seeing the trends in the model experiments should lend significant insight into the interpretation of the experimental EXAFS data of soddyite as also for other U, Al/Si, and O containing compounds.

4.2.2 Experimental data of soddyite

The synthesis of the soddyite $(UO_2)_2SiO_4 \times 2H_2O$ sample is described in [118]. Uranium L_{III}-edge EXAFS spectra of synthetic soddyite were collected in transmission mode at

room temperature at the Hamburger Synchrotronstrahlungslabor HASYLAB [119] and at 15 K at the Rossendorf Beamline (ROBL) at ESRF, Grenoble [5]. General information about soddyite, as also some details of the samples preparation, EXAFS measurements, and EXAFS preliminary treatment are given in Appendix I.

4.2.2.1 Multiple-scattering correction

Although the multiple scattering (MS) of the photoelectron wave from the absorbing atom to the neighboring atoms and back also play a role in the EXAFS normalized oscillating part $\chi(k)$, the application of the Tikhonov regularization method to solve the EXAFS equation actually means that only single-scattering (SS) paths are taken into account and MS paths are neglected. Hence, it is necessary to subtract the multiple-scattering contribution from experimental EXAFS data before using of this method. Of course this can be done only for certain MS paths, which are exactly known to be in the spectra.

In soddyite $(UO_2)_2SiO_4$ x $2H_2O$, as in many other U^{6+} containing compounds, uranium is found as the uranyl ion $(UO_2)^{2+}$. This specie consists of a U^{6+} atom tightly bound to two axial oxygen atoms O_{ax} in a symmetric linear structure (Fig. 24).

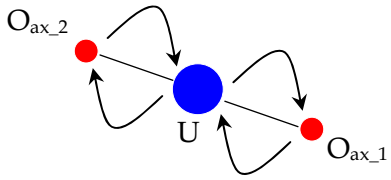

Fig. 24: Schematic representation of uranyl moiety $(UO_2)^{2+}$ including four-legged focusing MS associated with the axial oxygen atoms.

Four-legged MS UO_{ax_1} – UO_{ax_2} is a special case of focusing MS paths that is well known to give a significant contribution to EXAFS spectra for majority of uranyl compounds [13]. Since the measured U L_{III}-edge EXAFS for soddyite is also influenced by this MS, the multiple-scattering contribution of the linear UO_2^{2+} moiety was subtracted from the raw EXAFS data measured both at room temperature and at 15 K prior to the analysis by the modified regularization method.

The procedure of the MS correction is the following:

1) The UO_{ax} distance is determined from the first Tikhonov solution g^3(UO);
2) A theoretical EXAFS spectrum containing only the MS path associated with the axial oxygen atoms $\chi_{MS}(k)$ is calculated by the program FEFF 8.20 [120].
3) The isolated $\chi_{MS}(k)$ contribution is subtracted from the experimental EXAFS data $\chi(k)$.

Fig. 25 shows the experimental U L_{III}-edge $\chi(k)*k^3$ soddyite spectra collected at 15 K and room temperature after subtraction of the MS contribution of the linear UO_2^{2+} moiety. The simulated spectrum based on the XRD data of soddyite [48], i.e., containing only single-scattering paths (model A) is also plotted for comparison. All features of the model A (see Table 2) are present in the experimental spectra, although

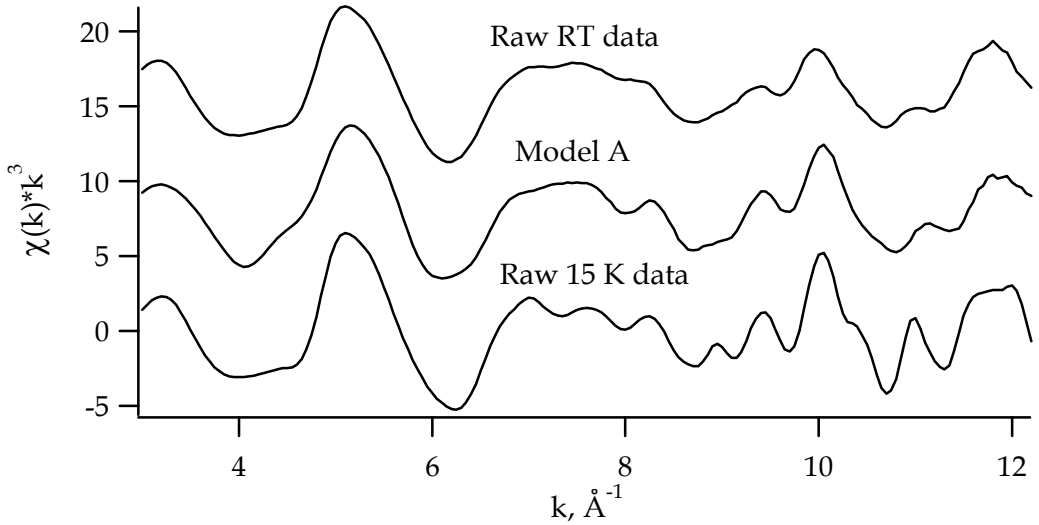

Fig. 25: Experimental and simulated U L_{III}-edge $\chi(k)*k^3$ spectra for soddyite.

with a different intensity at higher *k* values. The differences between spectra collected at ambient temperature and at 15 K in comparison with the simulated spectrum arise generally from the smaller thermal disorder at low temperature, which results in stronger contributions from distant atoms (e.g., U in case of the 15 K spectrum). Also longer MS paths that involve atoms more distant than O_{eq} contribute weakly to both experimental spectra. From the comparison it is also evident that the investigated experimental spectra are not affected by any impurities in the synthesized soddyite specimen. These results indicate that although a successful calculation of soddyite experimental data by the regularization method would require the subtraction of all significant MS contributions from the raw EXAFS data, in reality the subtraction of the MS contribution of the linear UO_2^{2+} moiety is already sufficient to make the data already similar to the EXAFS spectrum calculated from SS paths only. This enables the application of the advanced Tikhonov algorithm as described in the following paragraphs.

4.2.2.2 Treatment by the modified regularization method

The experimental U L_{III}-edge MS corrected soddyite data are utilized over the same k range $3.00 \div 12.2$ Å^{-1} to receive the first Tikhonov solutions g^1(UU), g^2(USi), and

g^3(UO) over r ranges 3.0 ÷ 6.0, 2.40 ÷ 6.0, 1.50 ÷ 6.0 Å, respectively. In accordance to the model calculations of soddyite, the "initial" regularization parameter for the variation Tikhonov method (Eq. (37)) is equal to 10^{-5}. The first Tikhonov solutions from soddyite spectra collected both at 15 K (Fig. 26) and at ambient temperature (Fig. 27) have almost the same locations for the RDFs peaks as for model A. This similarity suggests that the observed RDFs features arise primarily from single scattering within the soddyite species, perhaps with a weak contribution from the double-scattering U-Si-O_{eq} path and more distant oxygen atoms in the equatorial plane. As expected, the amplitudes of all RDFs peaks for the first solutions are far from the final values. It should also be noted here that the Tikhonov solutions g^2(USi) for both experimental spectra show a big feature at 2.70 Å, but in contrast to those received from the model spectra the artifacts at 2.70 Å are asymmetrical. This is due to the anisotropy of the parental U-O_{eq} shell in the real crystal structure of soddyite [48]. In the Tikhonov solutions g^3(UO) a feature at ~4.20 Å is observed in addition to the two peaks corresponding to the axial and equatorial oxygen shells of the uranium atom.

The prediction of the location of the coordination shells from the first Tikhonov solutions is something that must be examined carefully. To illustrate this point, the values of the separating functionals Λ for all features in the functions g^j from experimental soddyite data are shown in Tables 9 and 10 for 15 K and room temperature, respectively.

Table 9. Determination of "true" and "false" RDF peaks for the functions g^1(UU), g^2(USi), and g^3(UO) for the soddyite spectrum at 15 K using the method of separating functionals.

№	g^1(UU)		g^2(USi)		g^3(UO)	
	r, Å	Λ	r, Å	Λ	r, Å	Λ
1	3.03*	-0.31	2.60	14.67	1.78	17.85
2	3.28	11.61	2.73	18.19	2.10*	-8.57
3	3.58	9.12	3.13	7.44	2.38	15.18
4	3.88	26.08	3.50	6.47	2.63*	-4.96
5	4.15	8.20	3.83	30.74	2.90*	5.27
6	4.50*	-3.12	4.08	32.21	3.38*	4.44
7	4.78*	-0.55	4.63	29.93	3.60*	4.66
8	5.10	15.63	5.00*	-8.09	3.93*	-1.47
9	5.38	14.02	5.33	19.99	4.23	18.57
10	5.55*	-10.25	5.75*	-44.07	4.88*	2.19
11	5.85	28.27	-	-	5.10*	3.06
12	-	-	-	-	5.48*	3.14
13	-	-	-	-	5.90	5.27

* - Negative or small positive Λ values are indicative for "false" peaks.

Table 10. Determination of "true" and "false" RDF peaks for the Tikhonov solutions g^1(UU), g^2(USi), and g^3(UO) for the soddyite spectrum at RT using the method of separating functionals.

№	g^1(UU)		g^2(USi)		g^3(UO)	
	r, Å	Λ	*r*, Å	Λ	*r*, Å	Λ
1	3.05*	-1.79	2.58	1.47	1.80	17.96
2	3.28	7.56	2.75	17.98	2.10*	-7.63
3	3.58	0.60	3.08*	-2.49	2.38	11.51
4	3.88	9.67	3.53	4.06	2.90*	4.19
5	4.13*	-3.65	3.83	13.15	3.40*	2.40
6	4.60*	-1.42	4.08	9.98	3.60*	3.41
7	4.80*	-0.13	4.65	20.00	3.95*	-3.14
8	5.18	6.05	5.03*	-9.59	4.25	12.00
9	5.58*	-6.45	5.38	9.35	4.95*	3.66
10	5.88	11.76	5.78*	-7.78	5.58*	-0.82
11	-	-	-	-	5.93*	1.52

* - Negative or small positive Λ values are indicative for "false" peaks.

Note that the received Δ values for the radial distribution peaks of the experimental soddyite spectra are similar to that found for the model A, with only one exception of the feature at ~4.20 Å in the Tikhonov solution g^3(UO). The enormous value of separating functional for the peak $O_{4.2}$ (especially for the 15 K spectrum) is caused perhaps by contribution of distant oxygen atoms in the *r* range of 4.10 ÷ 4.45 Å which, by the way, are predicted by FEFF 8.20 to have significant amplitudes.
Based on the parameters of the separating functionals, the segments of RDFs where "false" peaks were identified are set to zero (Table 11).

Table 11. The segments of RDFs where "false" peaks are identified.

	Soddyite 15 K	Soddyite RT
g^1(UU)	[3.00, 3.125], [4.30, 4.95], [5.45, 5.70]	[3.00, 3.15], [4.075, 4.975], [5.425, 5.70]
g^2(USi)	[4.90, 5.15], [5.50, 6.00]	[4.95, 5.15], [5.60, 6.00]
g^3(UO)	[2.00, 2.15], [2.60, 4.00], [4.60, 6.00]	[2.00, 2.15], [2.70, 4.05], [4.60, 6.00]

As can be seen from Fig. 26 and 27, all features of the first RDFs solutions with relative large Λ values were left in the intermediate Tikhonov solutions on the restricted intervals. The RDFs intervals, which were truncated in accordance with the data of Table 11, were used by the variation method (Eq. (36)) to recompute the Tikhonov solutions. The values for the finite width τ (Eq. (41)) of the g^1(UU), g^2(USi), and g^3(UO) peaks were fixed to 0.12 (0.15), 0.15 (0.20), and 0.15 (0.25) Å for the soddyite spectra at

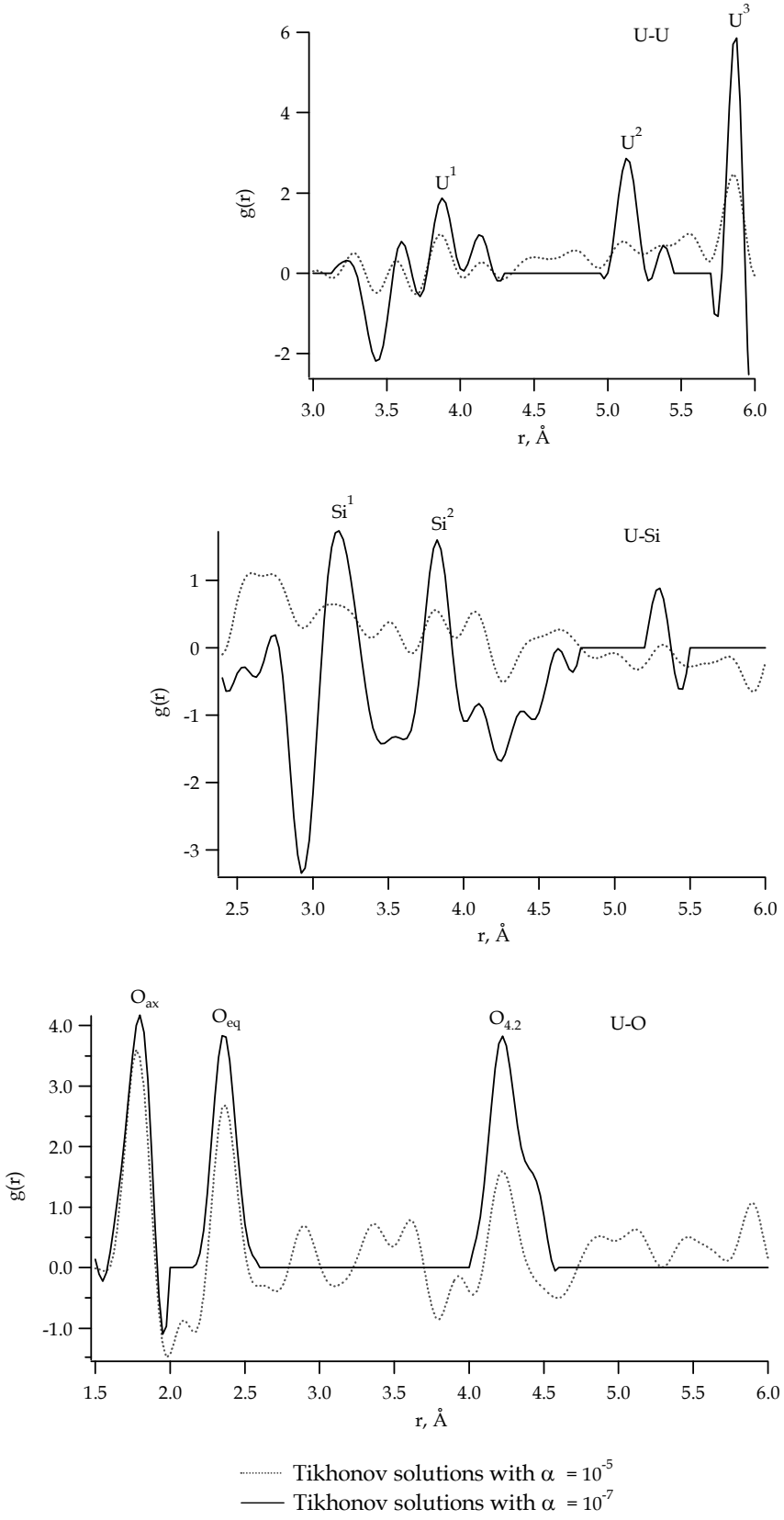

Fig. 26: Evolution of RDFs solutions for soddyite spectrum collected at 15 K.

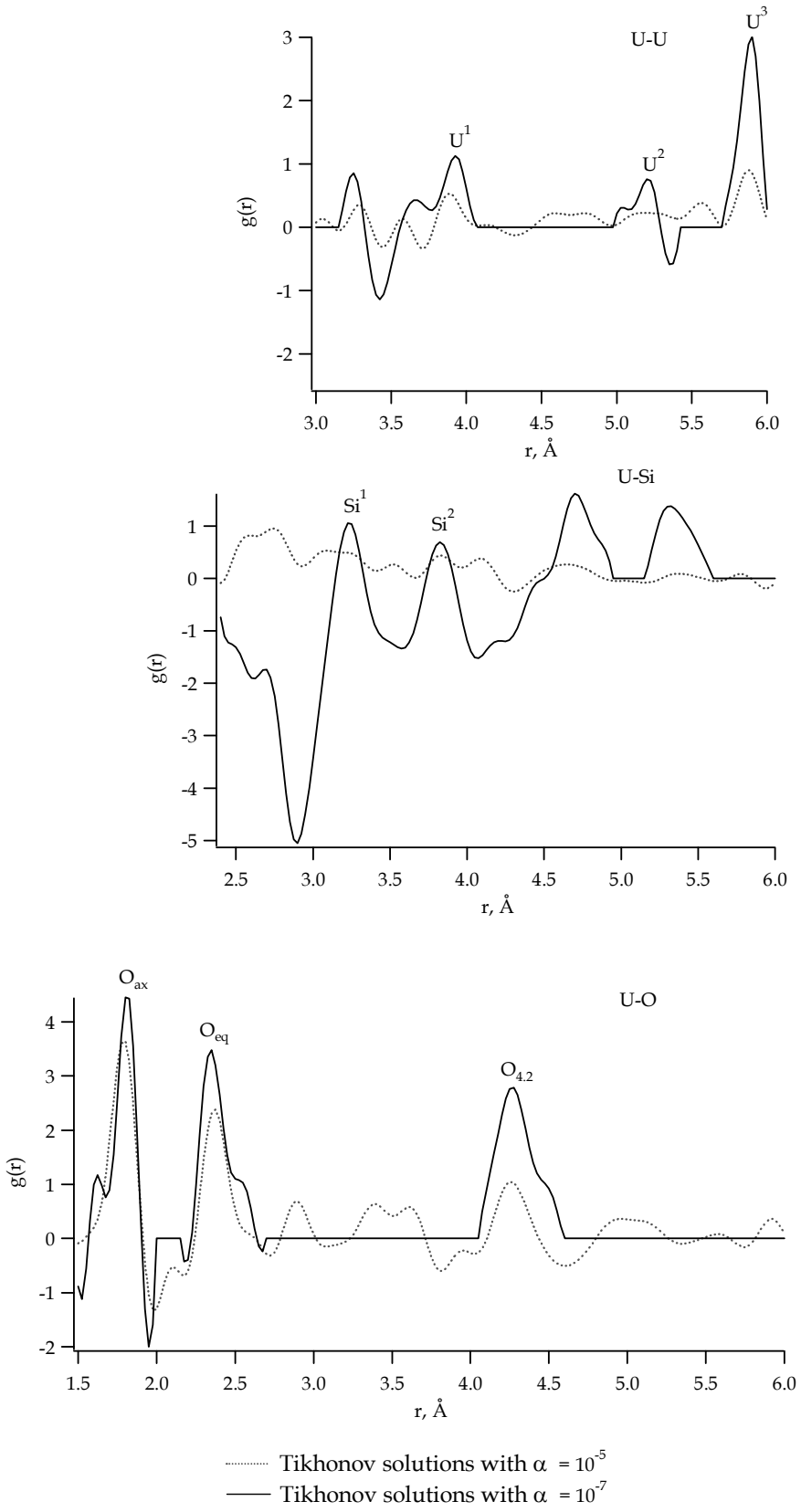

Fig. 27: Evolution of RDFs solutions for soddyite spectrum collected at ambient temperature.

15 K (ambient temperature), respectively. Simultaneously, the "initial" regularization parameter was reduced to 10^{-7}. Figs. 26 and 27 show that generally, in comparison with the first Tikhonov solutions, the amplitude of RDFs peaks of the intermediate Tikhonov solutions on the intervals increase. Although, the peak at 2.70 Å of g^2(USi) was not detected as "false" by the method of separating functionals (Tables 9, 10), it completely disappears already in the intermediate Tikhonov solution g^2(USi) for both soddyite spectra. This *in corpore* agrees with the XRD data confirming that this feature of g^2(USi) is an artifact and not existing in the real crystal structure of soddyite. Contrary to expectations, the peak at ~4.20 Å in the g^3(UO) essentially enhances, supporting the previous assignment of this feature to arise from contribution of approximately ten distant oxygen atoms over the *r* range of 4.10 ÷ 4.45 Å. Negative parts of RDFs are provoked by the interdependency of Tikhonov solutions. As expected, they are significantly diminished as the solutions become stable.

The final solutions are determined by the iteration method with filtration in real space. Figs. 28 and 29 (for spectra at 15 K and ambient temperature, correspondingly) show a close but not exact agreement between the final RDFs and g^1(UU), g^2(USi), and g^3(UO) RDFs calculated based on crystallographic data.

The major part of this discrepancy can be readily explained:

1. The RDFs calculations using the EXAFS spectra of soddyite were performed in the *k* range of 3.00 ÷ 12.2 Å^{-1}. Although it is evident that this *k* range is not long enough to reproduce correctly the RDFs g^1(UU) and g^2(USi), especially in case of the measurement at ambient temperature, the *k* range can not be changed. It was chosen as 3.00 ÷ 12.2 Å^{-1} because the calculations for soddyite should provide an appropriate model for the calculations of RDFs for U(VI) sorbed on kaolinite. Unfortunately, the EXAFS spectra of U(VI) sorption on kaolinite have a relative low signal-to-noise ratio, i.e., they never start below *k* equal to 3 Å^{-1} and never end above *k* equal to 12.2 Å^{-1}. This may be relevant for the differences in the RDF peak amplitudes observed between the final solutions derived by the modified regularization method and calculated ones based on XRD data.
2. The better detection of U coordination shells from the soddyite spectrum measured at 15 K is attributed to the lower thermal disorder at low temperature. This leads to a stronger contribution from atoms at a larger distance, most of all from the high-Z atoms like U, but also from Si atoms. As can be seen in Fig. 29, g^1(UU) received from the room temperature spectrum does not have the correct amplitude for the first and third U shells and does not show any evidence for the second U coordination shell.
3. In contrast to a previous study of soddyite [107], the modified regularization method did not show that the O_{eq} shell is split into two subshells, although this shell has a significant asymmetry in comparison to the model data. This is not unreasonable, considering that one of the equatorial ligands is a H_2O molecule, the other are SiO_4

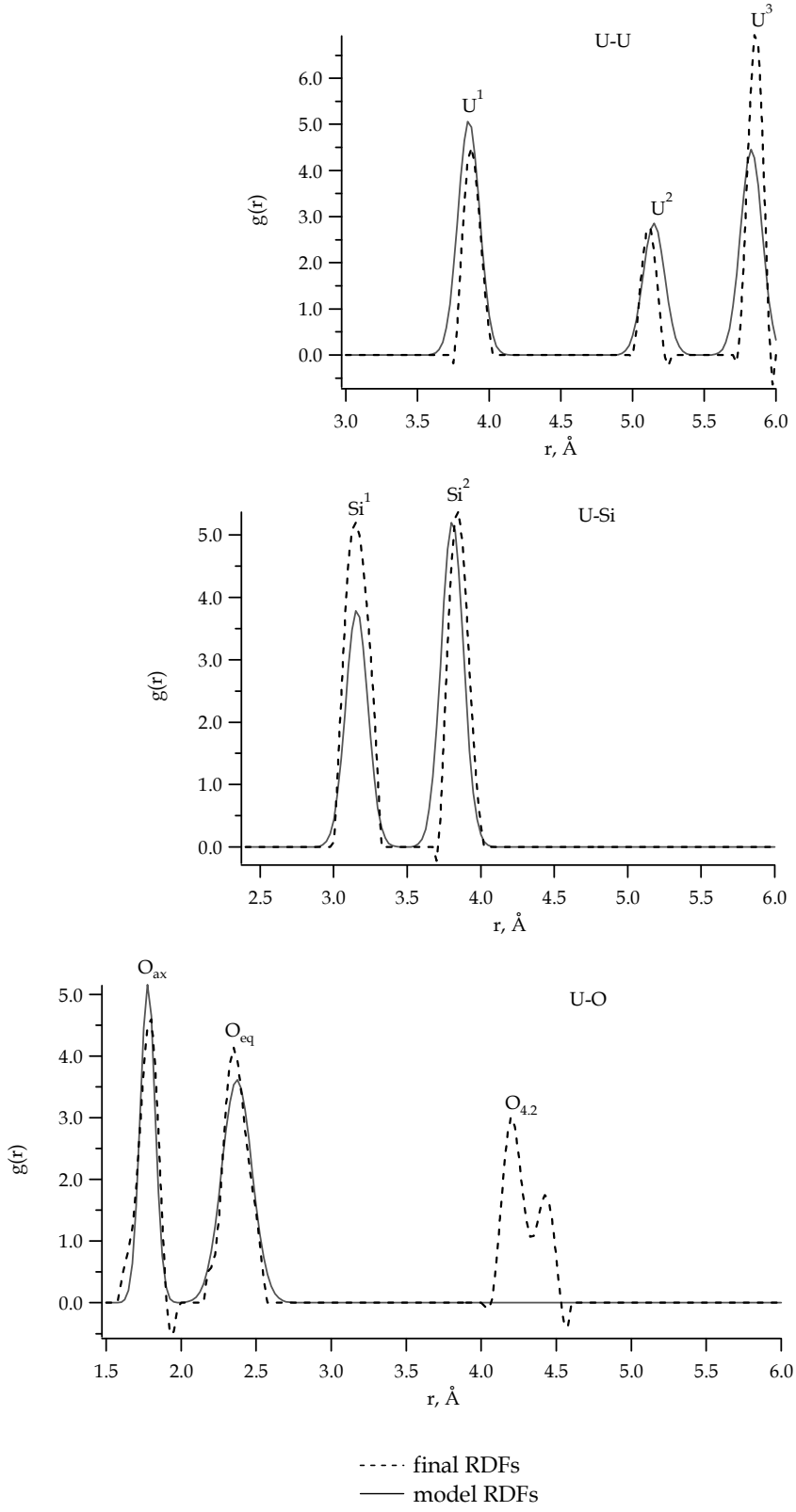

Fig. 28: Soddyite 15 K: final RDFs in comparison with the model based on the crystal structure of soddyite [48].

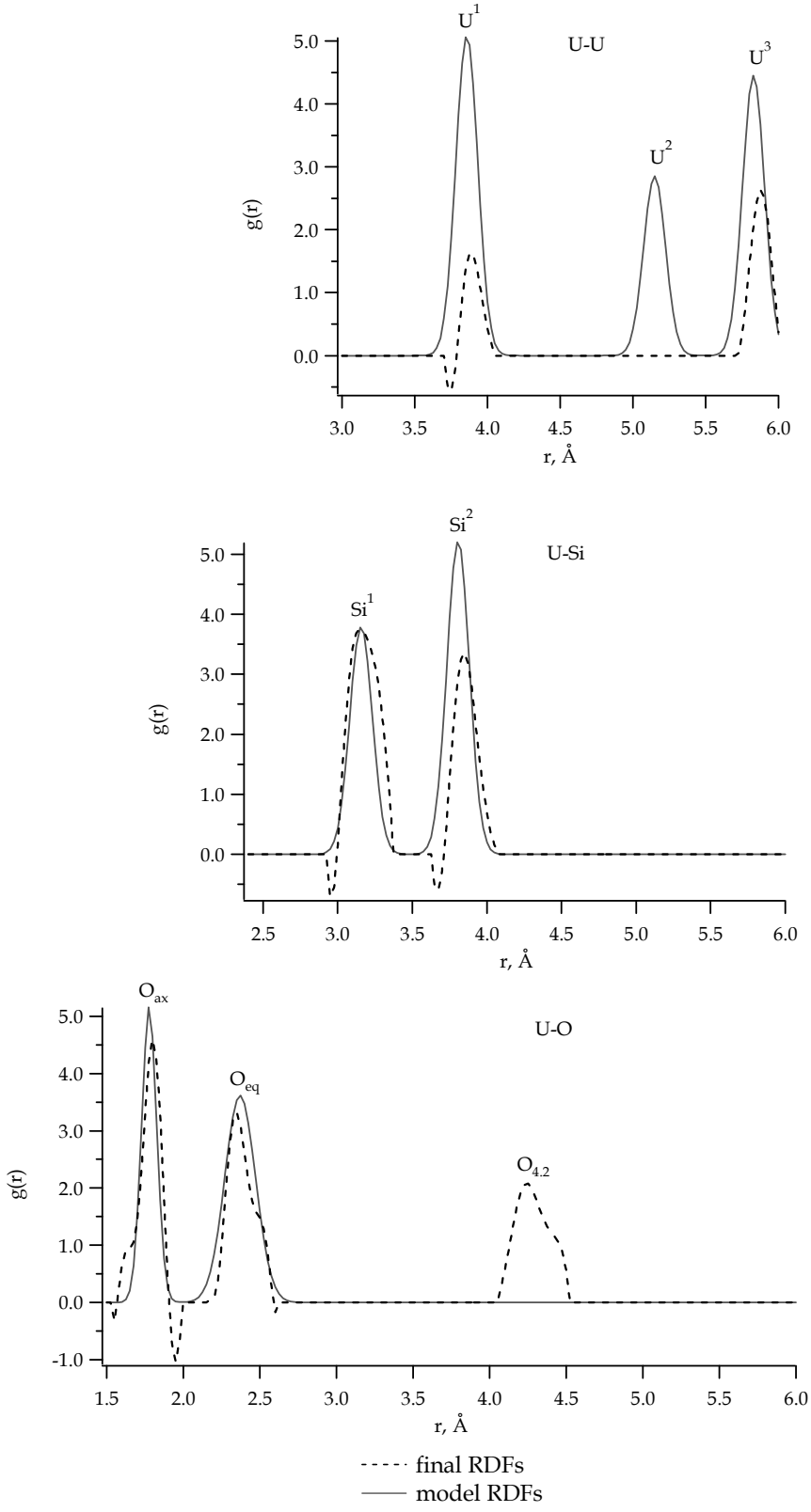

Fig. 29: Soddyite RT: final RDFs in comparison with the model based on the crystal structure of soddyite [48].

tetrahedra connected with pentagonal bipyramids centred on U through either one or two oxygen atoms (Fig. 30).

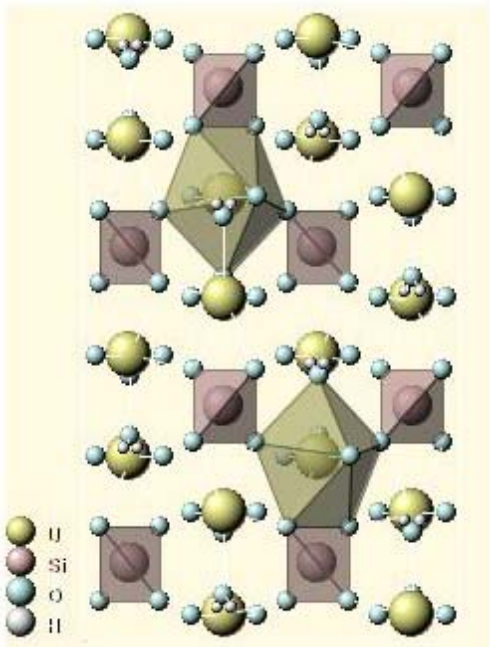

Fig. 30: The orthorhombic crystal structure of soddyite [48]. Two oxygen atoms, O_{ax}, are the apices of the bipyramid centred on the uranium atom. Five equatorial oxygen atoms are in one plane with the uranium atom and form the basis of a pyramid.

4. The amplitudes and hence the coordination numbers of coordination shells for all RDFs strongly depend on the value of the "initial" regularization parameter. A nonoptimal choice of α always leads to an uncertainty in the determination of the coordination numbers.
5. Except for the four-legged MS $UO_{ax\_1} - UO_{ax\_2}$ contribution of the linear UO_2^{2+} moiety, no other MS paths were subtracted from the raw EXAFS data. Not taking into account possible longer MS paths that involve atoms more distant than O_{ax} can slightly affect the values of structural parameters for RDFs peaks.

As an alternative to the Tikhonov regularization method, both soddyite spectra were analyzed by the standard least-squares fitting procedure, using the AUTOBK and EXAFSPAK software packages. Details of the EXAFS data analysis by shell-by-shell fitting and related information are given in Appendix I.
The coordination numbers *N*, interatomic distances *r*(Å), and the full width at half maximum (*FWHM*) (Å) obtained by the modified regularization method are compared with those from conventional EXAFS analysis and data from single-crystal XRD (Tables 12, 13).

Table 12. The structural parameters of oxygen and silicon coordination shells obtained by least-squares fitting (**1**) and with the modified regularization method (**2**) for soddyite in this work (NOW) and compared to literature EXAFS [107] and XRD [48] data.

By	Method / Spectrum			O_{ax}			O_{eq}			Si^1			Si^2		
				r	*N*	*FWHM*	*r*	*N*	*FWHM*	*r*	*N*	*FWHM*	*r*	*N*	*FWHM*
NOW	EXAFS	**1**	15 K	1.78	2*	0.1000	2.37	5*	0.2012	3.16	1*	0.1030	3.84	2*	0.1508
		2		1.79	2.0	0.1465	2.35	4.6	0.1935	3.15	1.5	0.2088	3.84	1.8	0.1635
		1	RT	1.78	2*	0.1154	2.36	5*	0.2319	3.15	1*	0.1615	3.90	2*	0.1854
		2		1.80	2.0	0.1415	2.35	3.8	0.1961	3.15	1.3	0.2716	3.85	1.2	0.1845
[107]		**1**		1.77	2.0	0.1178	2.33 2.48	2* 3*	0.1224 0.1984	3.15	1*	0.2355	3.90	2*	0.1854
[48]	XRD		RT	1.78	2	-	2.31 2.42	2 3	-	3.16	1	-	3.81	2	-

* Parameter fixed during least-squares fitting.

Table 13. The structural parameters of uranium coordination shells obtained by least-squares fitting (**1**) and with the modified regularization method (**2**) for soddyite in this work (NOW) and compared to literature EXAFS [107] and XRD [48] data.

By	Method / Spectrum			U^1			U^2			U^3		
				r	*N*	*FWHM*	*r*	*N*	*FWHM*	*r*	*N*	*FWHM*
NOW	EXAFS	**1**	15 K	3.86	2*	0.0942	5.10	2*	0.1373	5.84	4*	0.1268
		2		3.87	1.3	0.1423	5.11	1.2	0.1269	5.86	4.1	0.1267
		1	RT	3.88	2*	0.1508	5.18	2*	0.2259	5.85	4	0.2234
		2		3.89	0.5	0.1485	-	-	-	5.88	2.1	0.1654
[107]		**1**		3.82	2*	0.1665	5.14	2*	0.2355	-	-	-
[48]	XRD		RT	3.86	2	-	5.15	2	-	5.83	4	-

* Parameter fixed during least-squares fitting.

Note that $\chi(k)$ of soddyite were taken in different *k* ranges: $3.00 \div 17.0$ Å $^{-1}$ in [107], $3.50 \div 16.2$ Å^{-1} at 15 K, and $3.0 \div 12.2$ Å^{-1} at ambient temperature. The structural parameters characterizing the speciation of U(VI) in soddyite are nearly identical in all studies listed in Tables 12, 13. In addition to the common set of soddyite coordination shells, thirteen and eleven oxygen atoms at a distance ~4.20 Å were detected by the

modified regularization method for the spectra recorded at 15 K and ambient temperature, respectively (not shown in Table 12).
Despite some differences between the simulated RDFs and the final RDFs solutions, the U L_{III}-edge k^3-weighted EXAFS spectra and Fourier transformations calculated from the RDFs derived by the modified method agree quite well with the experimental data (Fig. 31).

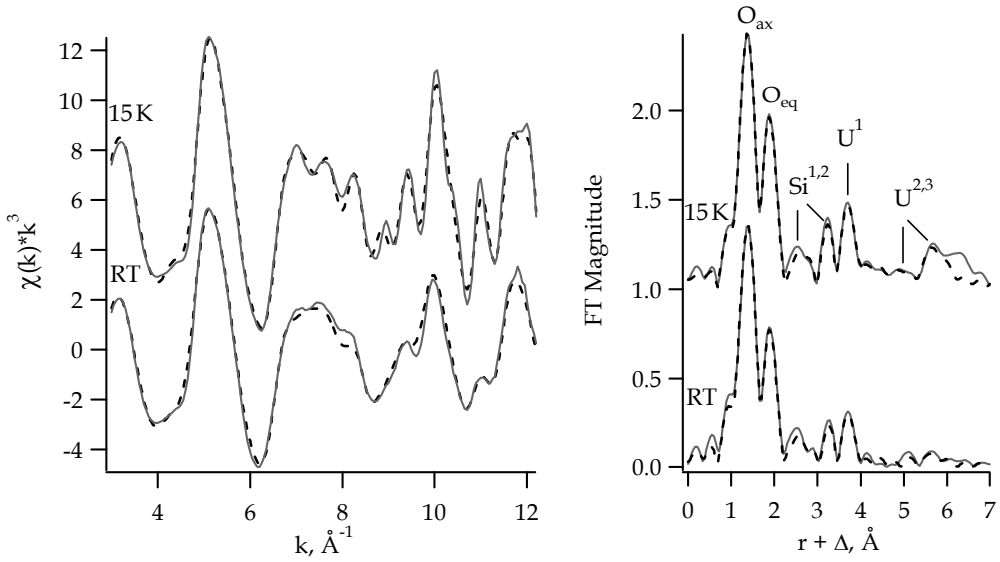

Fig. 31: U L_{III}-edge k^3-weighted soddyite EXAFS spectra (left) and corresponding Fourier transforms (right). Solid line – experimental data, dashed line – calculated from final RDFs.

The EXAFS spectra and FTs shown in Fig. 31, were calculated using the structural data collected in Tables 12 and 13 and included one O_{ax} shell, one O_{eq} shell, two Si shells, and three (15 K) or two U shells (room temperature).

4.2.3 Main conclusions based on calculations for soddyite

On the basis of the analysis of simulated and experimental EXAFS spectra of soddyite using the modified regularization method, the following conclusions can be drawn:

- The known multiple-scattering contributions to EXAFS spectra, as for example MS caused by the linear UO_2^{2+} moiety in uranyl containing materials, should be subtracted from raw data prior to the analysis by the modified regularization method.
- The first Tikhonov solutions simulated with $\alpha^j = 10^{-18}$ reproduce the model RDFs with very good accuracy. In this case the standard variation Tikhonov method is necessary and sufficient to receive the final RDFs solutions.
- The error level of experimental data significantly affects the values of regularization parameters. Recommended "initial" regularization parameters

for experimental data treatment were found to be from 10^{-5} to 10^{-7}. With such parameters the first Tikhonov solutions can predict the locations of radial distribution peaks, but are not able quantitatively reconstruct RDFs.

- The method of separating functionals has a good efficiency to analyze whether a peak in the functions g^j is "true" or "false", when each atom j of the investigated system has distinct scattering parameters in operator A^j (Eq. (35)), generally different backscattering phases.
- The results of the analysis using separating method have to be consistent among a series of data (if a series exist).
- The quality of the scattering characteristics calculated by the program FEFF 8.20 can affect the results of the analysis by separating functional dramatically.
- The proposed solution to the problem of the determination of regularization parameters is to obtain one "initial" regularization parameter and make the other parameters proportional to it. While the "initial" regularization parameter is generally attributed to the matrix operator A^j and the noise level in raw EXAFS data, it is recommended to determine "initial" regularization parameters during model calculations, where random noise has been added to the theoretical $\chi(k)$. Then this value for α can be applied to the analysis of the experimental data.
- The method of separating functionals allows to determine intervals in the RDFs where "true" peaks are absent.
- The experimental EXAFS spectrum can be analyzed successfully if the Tikhonov variation method is applied to intervals of the RDF where "true" peaks have been identified.
- The modified regularization method has a very good efficiency for the determination of the functions g^j by combining all three steps, i.e., variation Tikhonov method, application of separating functionals, and the iteration method with filtration in real space.

⇛ In summary, the calculations for soddyite show the ability of the modified regularization method to receive reasonable structure parameters (i.e., *r, N, FWHM*) in multi-component systems without imposing any structural model.

4.3 Sorption of U(VI) onto kaolinite

The triclinic structure of kaolinite has been determined by single-crystal XRD [121, 122]. As can be seen in Fig. 32, $Si(O,OH)_4$ sheets are bonded on one side to an octahedral $[Al(O,OH)_6]$ gibbsite-type layer. The gibbsite-type layer consists of aluminum atoms coordinated by hydroxyl groups, with some hydroxyls replaced by the oxygen atoms of the Si-O sheet.

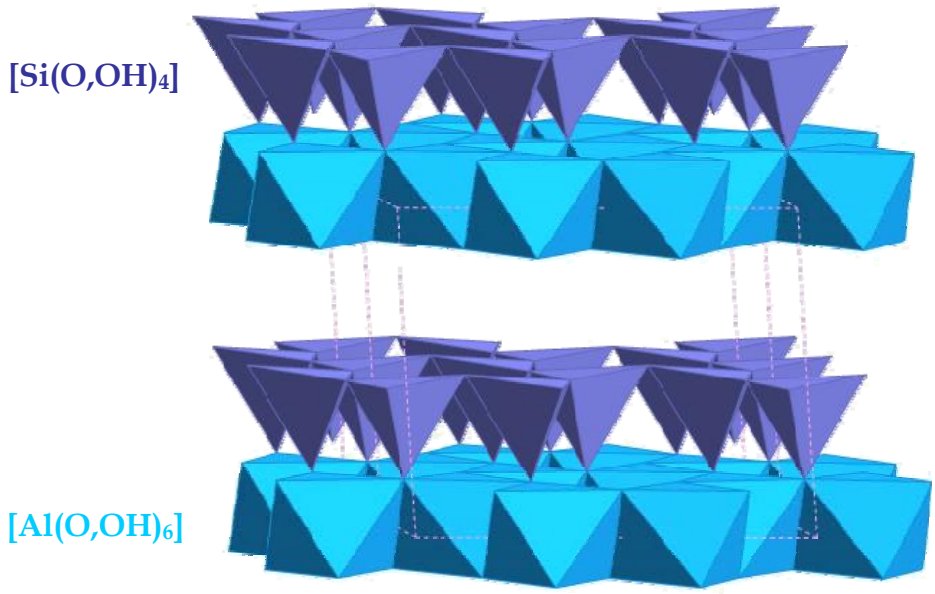

Fig. 32: Drawing illustrating the crystal structure of kaolinite. The $[Si(O,OH)_4]$ tetrahedral and the $[Al(O,OH)_6]$ octahedral sheets are violet and blue colored. The kaolinite unit cell is outlined.

The relative large surface area (10 m^2/g) predicts a high uptake of uranium by kaolinite. The analysis of the binding sites on the kaolinite surface suggests that U(VI) can be adsorbed along the edges of kaolinite, on the $[Si(O,OH)_4]$ sites from the tetrahedral sheet and/or on the $[Al(O,OH)_6]$ sites from the octahedral sheet.

Particular to the EXAFS study of uranium sorption at the kaolinite surface, possible backscattering atoms are O, Al, Si, and U. Since aluminium is indistinguishable from silicon by the EXAFS technique, three RDFs g^1(UU), g^2(UAl/Si), and g^3(UO) can be calculated from the U L_{III}-edge EXAFS spectra using the same modified regularization algorithm as for soddyite in Sect. 4.2.

Eleven samples were prepared for the EXAFS measurements at different chemical conditions (Table 14) such to determine the speciation of U(VI) at the kaolinite surface as a function of pH, total uranium concentration, and presence or absence CO_2. General information about the kaolinite mineral and some details of the sample preparation are given in Appendix II. To study the influence of the uranium concentration, samples 1-4 were prepared at pH 7.0 with 5, 10, and 20 µM total U(VI) and CO_2 present. Samples

6-9 were made from 10 μM U(VI) under ambient conditions at pH 5.0, 6.0, 7.0, and 8.5, respectively. Sample 10 was prepared at pH 8.5 and 10 μM U(VI) under Ar atmosphere for comparison with sample 9 prepared under identical conditions in the presence of CO_2. In an effort not to disturb the solid-water interface, all samples but 5 and 11 were measured as wet paste. The sample holders were sealed with Kapton tape and two layers of polyethylene foil for EXAFS measurements. Samples 7 and 11 were prepared under identical conditions in the presence of CO_2 but collected at ambient temperature and 28 K to see if it is possible to receive more structural information from the low temperature measurement. For the measurement at 28 K, the sample 11 was air-dried and loaded in a Teflon sample holder. To study the effect of drying on the EXAFS results, samples 3 and 5 were prepared identically, except that sample 3 was a wet paste and sample 5 a dry powder. Both samples were measured at room temperature.

Table 14. Analytical information about the EXAFS samples with U(VI) sorbed on kaolinite.

Sample	$[U(VI)]_{total}$, μM	pH_{final}	ppm sorbed	% sorbed	CO_2 presence	Sample condition
1	5	7.0	291	97.6	yes	wet paste
2	10	7.0	581	97.6	yes	wet paste
3	20	7.0	1161	97.6	yes	wet paste
4	50	7.0	2972	99.9	yes	wet paste
5	20	7.0	1189	99.9	yes	dry powder
6	10	5.0	99	16.6	yes	wet paste
7	10	6.0	468	78.6	yes	wet paste
8	10	7.0	540	90.7	yes	wet paste
9	10	8.5	73	12.2	yes	wet paste
10	10	8.5	591	99.3	no	wet paste
11	10	6.0	422	70.9	yes	air dried

The uranium L_{III}-edge EXAFS spectra were recorded in fluorescence mode at room temperature and 28 K at the Rossendorf Beamline ROBL [5] at the European Synchrotron Radiation Facility (ESRF). Depending on the amount of uranium in the sample, three to sixteen scans were averaged, calibrated using the K-edge (17038 eV) energy of a Y foil as reference, and corrected for detector dead time. The multiple-scattering contribution from the linear UO_2^{2+} moiety was subtracted from all raw EXAFS data in the same way as described in Sect. 4.2.2.1. Fig. 33 shows the measured EXAFS spectra of all samples after subtraction of MS contribution from the UO_2^{2+} moiety. The experimental spectrum of soddyite collected at room temperature is also plotted for comparison. It is evident from Fig. 33 that the noise level in the spectra of

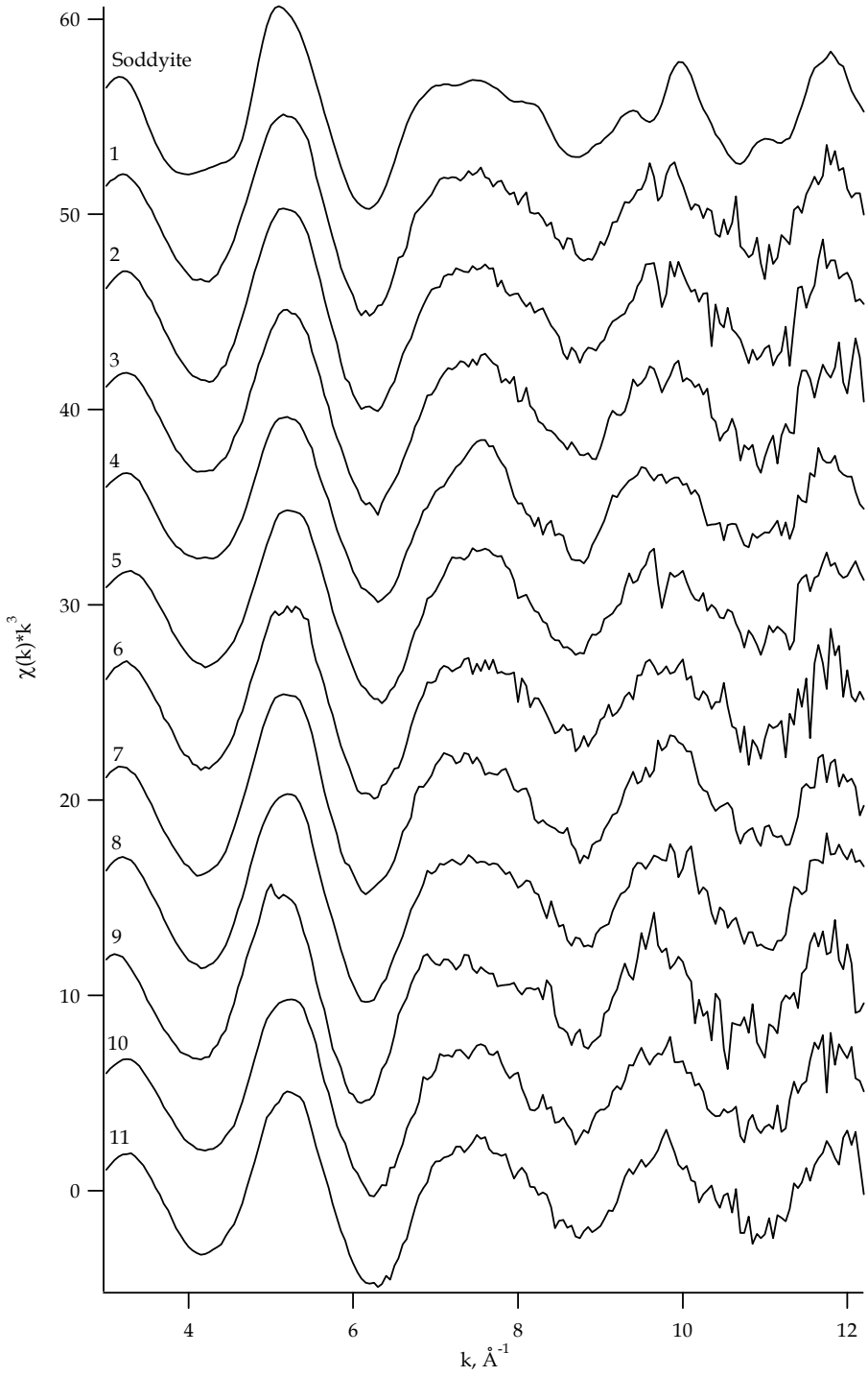

Fig. 33: U L_{III}-edge k^3-weighted spectra of U(VI) sorption on kaolinite and soddyite. All spectra but spectrum 11 were collected at ambient temperature. Spectrum 11 was measured at 28 K.

the sorption samples is higher than in the EXAFS spectrum of soddyite. This is first of all due to the uranium loadings, which are approximately two orders of magnitude lower than for the EXAFS measurements of soddyite. This means that the detection limit for the uranyl environment in the sorption samples is higher than in the soddyite

sample. Moreover, there are several reasons for difficulties in detecting certain atoms out to ~4 - 5 Å range in U(VI) structures [72, 77]. Atoms with a low atomic number such as Al, Si are weak photoelectron scatterers, resulting in weak spectral contributions over extended distances, i.e., the scattering from Al/Si at distances greater than 3.6 Å in uranyl structures is difficult, through not impossible to detect (for example, in a good quality samples of soddyite it was possible to detect the Si shell at 3.8 Å). It was found also in the calculations for soddyite described above that the single- and likely some of multiple-scattering paths of equatorial oxygen atoms interfere with U-Si single scattering paths. Each of these factors affects the ability of the EXAFS technique, both by least-squares fitting or Tikhonov regularization, to detect neighboring atoms at large distances in the sorption samples.

All parameters used in the analysis by means of the modified Tikhonov regularization method were the same as for the soddyite data. The RDFs of the sorption samples were calculated in the same r intervals as for soddyite, i.e., 3.0 ÷ 6.0, 2.40 ÷ 6.0, 1.50 ÷ 6.0 Å for U-U, U-Al/Si, and U-O contributions, respectively. To receive the first solution of g^j functions, for the Tikhonov variation method (Eq. (36)) the "initial" regularization parameter α was 10^{-5}. The values of the finite width τ (Eq. (41)) of the RDFs peaks during the iteration process with filtration in real space were fixed at 0.15, 0.15, and 0.25 Å for g^1(UU), g^2(UAl/Si), and g^3(UO) functions, respectively. Note that for clarity and due to the experimental noise in the data, the RDFs g^1(UU), g^2(UAl/Si), and g^3(UO) are not displayed in the following figures over the entire r intervals used in the calculations but have been limited to r_{max} of 5.0, 4.0, and 4.5 Å, respectively.

Considering the quality of EXAFS data, the accuracy was estimated as ± 0.01 ÷ 0.03 Å in the absorber-neighbor distances and ± 0.15 ÷ 0.25 % in the coordination numbers.

4.3.1 Speciation of U(VI) as a function of uranium concentration

The first Tikhonov solutions g^1(UU), g^2(UAl/Si), and g^3(UO) for the U L_{III}-edge EXAFS data of samples 1-4 are shown in Fig. 34. The Tikhonov solutions g^1(UU) from all spectra demonstrate almost the same oscillations corresponding to level of the experimental noise in EXAFS data except probably the feature at ~3.90 Å (number 4 in Fig. 34, left) , which has an increasing amplitude with increasing U(VI) concentration in solution. The RDF g^1(UU) of sample 3 shows the feature that becomes split at two discrete distances ~3.80 Å and ~4.00 Å. All Tikhonov solutions g^2(UAl/Si) present a big feature at 2.70 Å (numbers 1 and 2 in Fig. 34, middle), which asymmetry increases systematically from the sample 1 with the lowest U(VI) concentration to the sample 4 with the largest U(VI) loading. There is an evidence of a possible splitting of the corresponding O_{eq} shells (peak number 2 in Fig. 34, right) in the g^3(UO) Tikhonov solutions. The amplitude of the Al/Si feature at ~ 2.70 Å is approximately the same in

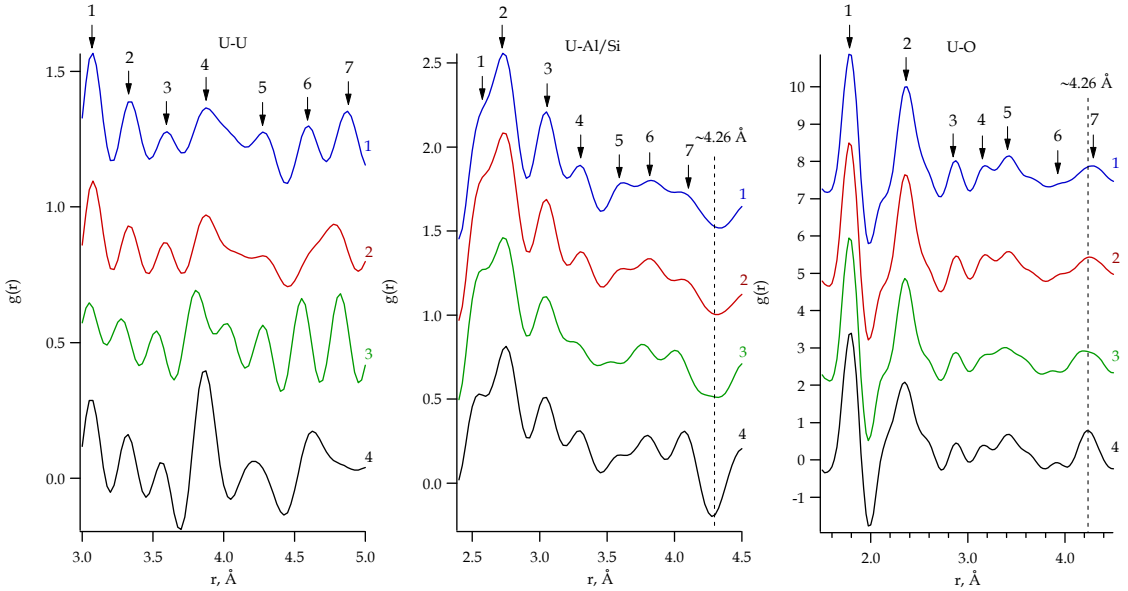

Fig. 34: The first Tikhonov solutions g^1(UU), g^2(UAl/Si), and g^3(UO) for the samples 1–4 prepared in air at room temperature at pH 7 with the total U(VI) concentration ranging from 5 to 50 μM. All RDF peaks are numerated to be analyzed by the method of separating functionals.

all functions g^2(UAl/Si), with a week trend to lower amplitudes with increasing U(VI) concentration. Hence, it seems likely that the coordination numbers of the parental O_{eq} shells also slightly decrease with the growth in U(VI) concentration. The feature Al/Si at ~3.10 Å (number 3 in Fig. 34, middle) is quite well seen in the g^2(UAl/Si) RDFs for all four samples. This possible Al/Si coordination shell for sample 1 shows a significant larger amplitude than are found for the other three RDFs g^2(UAl/Si). Features at ~3.30 Å (number 4 in Fig. 34, middle) in the RDF g^2(UAl/Si) can be ascribed to a second shell of silicon or aluminium around the central uranium atom. In accordance with the model calculations for soddyite, the local minimum at ~4.26 Å in all g^2(UAl/Si) as also the features at the same distance in the Tikhonov solutions g^3(UO) are attributive to existence of the coordination shell at ~3.90 Å in the U-U contribution. The Tikhonov solutions g^3(UO) are similar for samples 1-4, except that with increasing of U(VI) concentration, the equatorial oxygen shell (number 2 in Fig. 34, right) asymmetrically broadens, diminishes in amplitude, and moves to slightly shorter distances.

In order to avoid an inconsistent determination of the coordination shells, all features of RDFs are examined by the method of separating functionals. The values of separating functionals Λ for the prominent peaks of the Tikhonov solutions g^1(UU), g^2(UAl/Si), and g^3(UO) are given in Tables 15, 16, and 17, respectively. The trends noted in Tikhonov solutions are more apparent in the Λ values for the features of g^1(UU) (Table 15). The functionals values change quite similar for the EXAFS data of samples 1-4. All Λ values of sample 1 are negative or only small positive. The growth

Table 15. The values of separating functionals Λ for some peaks of the Tikhonov solution g^1(UU) received for the EXAFS data of samples 1-4.

Sample	U^1		U^2		U^3		U^4		U^5		U^6		U^7	
	r, Å	Λ	*r*, Å	Λ	*r*, Å	Λ	*r*, Å	Λ	*r*, Å	Λ	*r*, Å	Λ	*r*, Å	Λ
1	3.08*	1.45	3.35*	1.26	3.60*	-1.20	**3.88***	**2.70**	4.28*	-0.42	4.60*	-0.01	4.88*	2.59
2	3.08*	1.38	3.33*	-0.59	3.58*	-1.91	**3.88**	**5.44**	4.28*	-3.21	-	-	4.78*	-0.42
3	3.05*	0.87	3.28*	1.24	3.53*	0.67	**3.80**	**6.05**	4.28	2.56	4.55	6.96	4.83	7.55
4	3.08*	4.12	3.33*	3.46	3.55*	-0.70	**3.88**	**12.70**	4.23*	-1.59	4.63	7.46	5.03*	-1.25

* - Negative or small positive Λ values are indicative for "false" peaks.

of the U(VI) concentration in the samples is clearly indicated by the increasing of Λ values for the feature at ~3.90 Å (bold type in Table 15). Starting with sample 2, the Λ values predict the existence of the coordination shell of uranium atoms at ~3.90 Å. The splitting of this shell in the uranyl moiety environment structure for sample 3 is also reflected in the corresponded Λ values, i.e., all but U^5 of it RDF features are shifted in distances. Following the Λ values for the Tikhonov solutions g^1(UU), the coordination numbers of the shell at ~3.90 Å are going up from sample 1 to 4.

Table 16. The values of separating functionals Λ for some peaks of the Tikhonov solution g^2(UAl/Si) received for the EXAFS data of samples 1-4.

Sample	Al/Si^1		Al/Si^2		Al/Si^3		Al/Si^4		Al/Si^5		Al/Si^6		Al/Si^7	
	r, Å	Λ	*r*, Å	Λ	*r*, Å	Λ	*r*, Å	Λ	*r*, Å	Λ	*r*, Å	Λ	*r*, Å	Λ
1	-	-	2.73	20.68	3.05	8.65	3.30	-0.73	3.63	5.02	3.83	2.66	4.03*	-0.70
2	-	-	2.73	19.38	3.05	5.70	3.30	-2.78	3.63	6.01	3.80	3.97	4.05*	-1.22
3	-	-	2.73	12.59	3.05	8.92	-	-	3.53*	-3.22	3.75	5.64	4.00	6.11
4	2.55*	-3.16	2.75	12.02	3.05	5.88	3.30	2.83	3.60	2.06	3.80	7.52	4.08	16.45

* - Negative or small positive Λ values are indicative for "false" peaks.

As can be seen in Table 16, without prior knowledge of the nature of the feature at ~2.70 Å, it would be identified by the method of separating functionals as originating from backscattering U-Al/Si. At the same time, the feature at ~2.70 Å is remarkable in that it has nearly similar amplitude and *r* position (see numbers 1 and 2 in Fig. 34, middle) as was previously found for the experimental data of soddyite. This is very reasonable, because, as it was shown in Sect. 4.2, it originates from the contribution of O_{eq} shell, which is practically the same in the structure of soddyite and the sorption samples. Any way, all peaks with relative large Λ values are left in the Tikhonov solutions g^2(UAl/Si). The exceptions were made only for Al/Si_4 features, while they were not really separated from the Al/Si_3 potential coordination shell. Note again, a separation of the peaks in distance is one of the necessary conditions for the method of

separating functionals to work (Eq. (40)), i.e., in case the peaks positions are too close to each other, it is better not to truncate the Tikhonov solutions abundantly.

Table 17. The values of separating functionals Λ for some peaks of the Tikhonov solution g^3(UO) received for the EXAFS data of samples 1-4.

Sample	O_1		O_2		O_3		O_4		O_5		O_6		O_7	
	r, Å	Λ	*r*, Å	Λ	*r*, Å	Λ	*r*, Å	Λ	*r*, Å	Λ	*r*, Å	Λ	*r*, Å	Λ
1	1.78	14.89	2.38	11.10	2.88*	1.65	3.18*	0.61	3.43*	3.68	-	-	4.28*	4.10
2	1.78	16.19	2.35	11.83	2.88*	0.62	3.18*	1.35	3.43*	3.39	-	-	4.25*	4.93
3	1.78	14.86	2.35	10.94	2.88*	1.65	-	-	3.38*	2.46	3.88*	-1.36	4.20*	3.92
4	1.80	16.93	2.35	7.23	2.88*	0.78	3.18*	0.89	3.43*	4.29	3.93*	-0.95	4.23*	8.24

* - Negative or small positive Λ values are indicative for "false" peaks.

The tendencies shown by Λ values for the features of the Tikhonov solution g^3(UO) (Table 17) are very similar among samples 1-4 as also to those found for the experimental soddyite spectra (see Tables 9 and 10). Probably only one exception is the feature at ~4.26 Å (number 7 in Table 17). The larger value of separating functionals for the feature O_7 in sample 4 is caused by stronger contribution of the coordination shell of uranium atoms at ~3.90 Å, indirectly confirming their existence. Generally, the Λ values clearly suggest two coordination shells for the Tikhonov solution g^3(UO), the first one at ~1.78 – 1.80 Å and the second one at ~2.35 – 2.38 Å.
When the segments of all RDFs, where "false" peaks were identified, were set to zero, the final solutions have been determined by the iteration method with filtration in real space. The experimental EXAFS data with the corresponding k^3-weighted spectra calculated from the final RDFs are shown in Fig. 35.

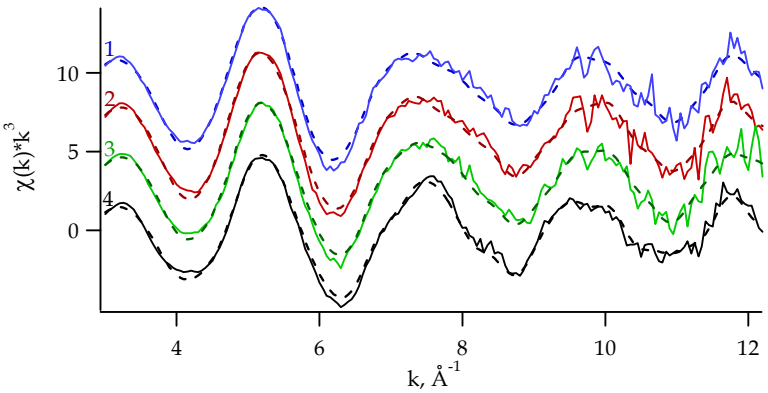

Fig. 35: U L_{III}-edge k^3-weighted EXAFS data of the samples 1-4: Spectra calculated from the final RDFs (dashed lines), experimental data (solid lines).

Backscattering of the oxygen coordination shells gives strong low frequency oscillations that dominate in the low *k* region of the EXAFS data for samples 1-4 (Fig. 35). The presence of more distant atoms (Al, Si, and U) is expected in the high

k region of the EXAFS data. Closer inspection of the *k* region below ~7.00 Å^{-1} reveals a significant change of the EXAFS pattern for the fourth sample with the largest total U(VI) concentration in comparison to the samples with lower uranium loading. Trends noted in EXAFS spectra are more apparent and can be understood quantitatively in the corresponding RDFs, which are shown in Fig. 36.

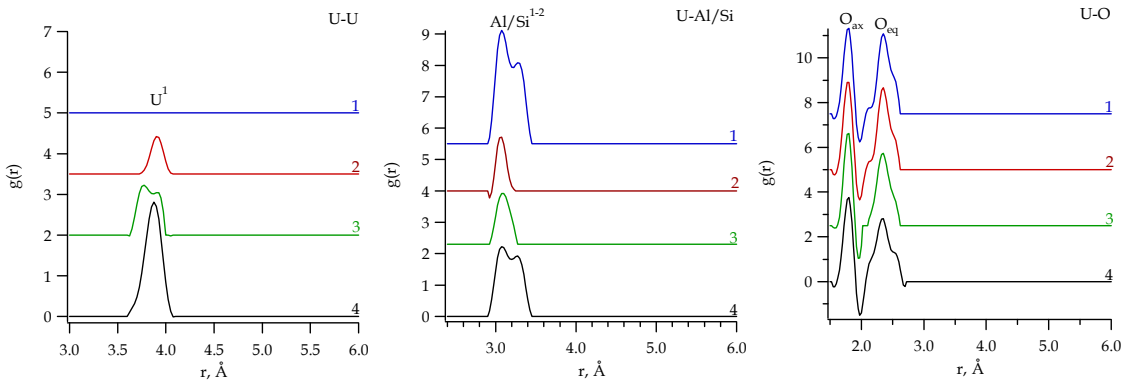

Fig. 36: Final solutions for the RDFs g^1(UU), g^2(UAl/Si), and g^3(UO) of sorption samples 1-4.

The following tendencies are observed in the final solutions:

g^1(UU): No U-U interaction was detected for the sample 1 with 5 µM of U(VI) loading; the total U(VI) concentration of 10 µM is enough to see a week U-U contribution; the further increasing of the U(VI) concentration up to 50 µM is reflected in a simultaneous growth of the U-U contribution. The observed U-U interaction at ~3.90 Å indicates the formation of polynuclear U(VI) species at the kaolinite surface at pH 7. As one could expect, the amount of these polynuclear species increases with increasing uranium concentration.

g^2(UAl/Si): All final solutions show a Al/Si coordination shell at the distance ~3.10 Å. At the lowest and highest U(VI) concentration (samples 1 and 4), the RDFs display a large and broad peak with a maximum at ~3.10 Å and a shoulder at ~3.30 Å. To comment these results, Fig. 37 illustrates the different possibilities of UO_2^{2+} interaction with the kaolinite structure units, i.e., [Si(O,OH)$_4$] tetrahedron and [Al(O,OH)$_6$] octahedron.

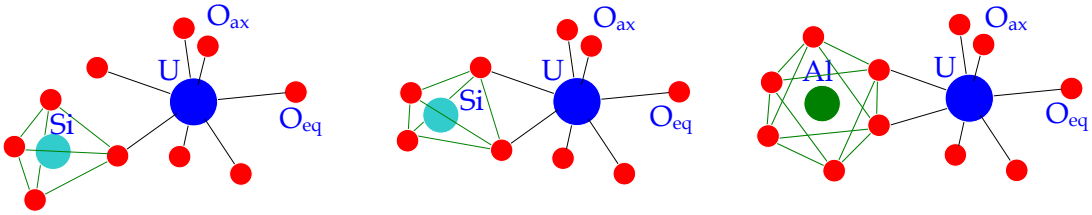

Fig. 37: Model structures for the monodentate (left) and bidentate (middle) surface complexes of uranyl moiety on kaolinite, showing the corner-sharing and edge-sharing bonds with a silicon tetrahedron. The drawing on the right illustrates the other possible bidentate surface complex of the uranyl moiety onto kaolinite, i.e., edge-sharing bond with an aluminium octahedron.

Complexation at silanol sites usually results in U-Si distances ~2.70 - 3.20 Å in bidentate (edge-sharing) or ~3.50 - 3.80 Å in monodentate (corner-sharing) fashions. The edge-sharing of uranyl units connected to $Si(O,OH)_4$ tetrahedron with U-Si distances equal to 3.08 and 3.16 Å were found in samples of uranyl sorbed onto silica [83] and soddyite [48], respectively. Monodentate coordination between $[UO_2O_5]$ pentagonal bipyramids and $Si(O,OH)_4$ tetrahedron with the distances 3.61 and 3.80 Å was observed in the crystal structure of $Ba(UO_2)(Si_2O_6)$ [123] and soddyite [48], respectively. Complexation of the U(VI) polyhedron at aluminol sites in edge-sharing connection gives U-Al distances of ~3.30 – 3.50 Å, which were obtained assuming typical Al-O distances of ~1.85 – 1.97 Å [124] and U-O_{eq} distance of 2.35 Å for uranyl sorbed on montmorillonite [93]. Similar U-Al interatomic distances have been reported for uranyl sorbed on the imogolite surface [113].

In view of the discussion above, atomic distances of ~3.10 Å and coordination numbers of one or less detected in samples 1-4 are indicative of bidentate coordination of U(VI) with $Si(O,OH)_4$. Also, bidentate coordination of U(VI) to $[Al(O,OH)_6]$ octahedra of kaolinite is in agreement with the experimental distance of ~3.30 Å in the RDF g^2(UAl/Si) for samples 1 and 4.

g^3(UO): As can be seen from Fig. 36, the final solutions for g^3(UO) of samples 1-4 consist of two peaks at 1.79 Å and ~2.35 – 2.34 Å corresponding to axial and equatorial oxygen shells about the uranium atom. The splitting of the O_{eq} shell is likely to be present and may be the reason of the asymmetric broadening of the O_{eq} shell. But an accurate determination of the coordination numbers of subshells and their interatomic distances was not possible in the *k* range of the EXAFS spectra due to the quality of the raw data.

The EXAFS analysis using the modified Tikhonov regularization method was done to confirm and supplement the results of the conventional structural analysis by means of least-squares fitting (see Appendix II). The bond lengths, coordination numbers, and *FWHM* received by both methods are summarized in Tables 18, 19.

As can be seen from Table 18, the results of EXAFS analysis by both methods are in relative good agreement for the U-U contribution: only at the total U(VI) concentration of 50 μM both of them detect a shell of uranium atoms at distance ~3.90 Å. The modified Tikhonov regularization method was able to detect a week U-U contribution to EXAFS data also at 10 μM total U(VI) concentration. Additionally, a splitting of the U-U coordination shell in the sample 3 (20 μM total U(VI)) was observed. Generally, the final solutions g^1(UU) obtained by the Tikhonov regularization method confirm the tendency that polynuclear U-U species are formed at the kaolinite surface as the U(VI) concentration in solution increases. The conventional structural analysis by means of least-squares fitting indicates the formation of polymeric surface complexes only at the total U(VI) concentration of 50 μM.

Table 18. Sorption of U(VI) onto kaolinite as a function of total U(VI) concentration. Uranium and silicon coordination shells: interatomic distances *r* and *FWHM* in Å, and coordination numbers *N* obtained by least-squares fitting (**1**) are in comparison with those determined by the modified regularization method (**2**).

Spectrum /Method			U[1]			Si[1]			Al/Si[2]		
			r	*N*	*FWHM*	*r*	*N*	*FWHM*	*r*	*N*	*FWHM*
EXAFS	**1**	**1**	-	-	-	3.09	1.3[#]	0.1290[#]	3.30	1.2[#]	0.1290[#]
		2	-	-	-	3.08	1.0	0.1743	3.28	0.8	0.1824
	2	**1**	-	-	-	3.10	1.1[#]	0.1290[#]	3.31	1.0[#]	0.1290[#]
		2	3.91	0.3	0.1529	3.07	0.3	0.1451	-	-	-
	3	**1**	-	-	-	3.11	0.7[#]	0.1290[#]	3.32	0.5[#]	0.1290[#]
		2	3.77/3.91	0.7	0.2837	3.09	0.4	0.2106	-	-	-
	4	**1**	3.90	2.0[¤]	0.2040	3.11	0.9[#]	0.1290[#]	3.31	1.0[#]	0.1290[#]
		2	3.88	1.3	0.2040	3.08	0.6	0.1778	3.27	0.5	0.1854

* Parameter fixed during least-squares fitting.

[#] Al/Si coordination numbers were calculated with fixed at 0.0030 Å^2 DW factor.

[¤] U coordination numbers were calculated with fixed at 0.0075 Å^2 DW factor.

In addition to the formation of polynuclear U(VI) species as a function of U(VI) concentration at pH 7, another trend is observed in case of the U-Al/Si interaction. In particular, both analysis methods, but the regularization more obviously, show that the coordination numbers for U-Si interaction at 3.09 ± 0.02 Å decrease in samples 1-4. The second g^2(UAl/Si) coordination shell, which is suspected to be attributive for bidentate coordination of U(VI) to [Al(O,OH)$_6$] octahedron, was derived from the EXAFS spectra of the samples 1-4 by the conventional fitting analysis but was observed in the g^2(UAl/Si) functions only for samples 1 and 4, i.e., at the lowest and highest U(VI) concentration. In a qualitative way, these results can be viewed as a competition for the excess of UO_2^{2+} cations to kaolinite surface sites with increasing U(VI) concentration. Namely, at pH 7.0 and at the lowest U(VI) concentration (sample 1) all surface sites are in excess. This leads to a large and stable U-Al/Si interaction. As the U(VI) concentration increases, easily available surface sites are filled, and the quantity of U-Al/Si bonds decreases. This is reflected in the coordination numbers of Al/Si shells (samples 2 and 3). At pH 7.0, this tendency along with the appearance of polynuclear U-U species with increasing U(VI) concentration suggests that U(VI) precipitates at the kaolinite surface. Moreover, the detection of Al/Si atoms in the near-neighbor environment of uranium indicates the formation of inner-sphere complexes of U(VI) with kaolinite.

All structural parameters determined using the modified regularization method for O_{ax} and O_{eq} coordination shells are essentially equivalent to those received by conventional

EXAFS analysis by means of least-squares fitting (see Table 19).

Table 19. Sorption of U(VI) onto kaolinite as a function of total U(VI) concentration. Oxygen coordination shells: interatomic distances *r* and *FWHM* in Å, and coordination numbers *N* obtained by least-squares fitting (**1**) are in comparison with those determined by the modified regularization method (**2**).

Spectrum /Method			O_{ax}			O_{eq}		
			r	*N*	*FWHM*	*r*	*N*	*FWHM*
EXAFS	**1**	**1**	1.79	2*	0.1201	2.38	5*	0.2633
		2	1.79	2.0	0.1637	2.35	5.1	0.2433
	2	**1**	1.79	2*	0.1129	2.37	5*	0.2622
		2	1.79	2.0	0.1618	2.35	5.0	0.2269
	3	**1**	1.79	2*	0.1053	2.36	5*	0.2826
		2	1.79	2.0	0.1534	2.34	4.8	0.2498
	4	**1**	1.79	2*	0.1178	2.36	5*	0.3405
		2	1.79	1.9	0.1637	2.34	4.8	0.2703

* Parameter fixed during least-squares fitting.

As can be seen, the modified regularization method is quite accurate in calculating both axial and equatorial coordination numbers. The results are comparable to the coordination numbers, which were fixed during least-squares fitting. One evident discrepancy is that the equatorial bond lengths are systematically shifted to shorter distances. This is not unexpected and can be clearly explained. The maximums of the peaks in the final RDFs differ always from the maximums of the Gaussian distributions used by least-squares fitting, if the coordination shells have an asymmetric distribution of interatomic distances (see Sect. 3.5).

It is found by both methods that in samples 1-4: (1) the distances and the coordination numbers determined for O_{ax} are nearly the same and fairly stabile against changes in the U(VI) concentration; (2) both interatomic distances and coordination numbers of the O_{eq} shell decrease only slightly, within the error limit of their determination, with increasing U(VI) concentration. The possibility of a split O_{eq} shell (as indicated by a bigger *FWHM* than that associated with a single O_{eq} shell and by visual inspection of the final g^3(UO) and the first Tikhonov solution g^2(UAl/Si) is an indication of disorder in the U(VI) surface species. Moreover, relative short O_{eq} distances along with no ionic strength dependence in batch experiments at pH 7.0 [125, 126] indicate inner-sphere sorption of U(VI) onto kaolinite.

Finally, the results of the two alternative EXAFS analysis methods show that at pH 7.0 and a total U(VI) concentration of 10 – 50 μM, U(VI) forms inner-sphere surface complexes at the kaolinite surface. The increase of the U(VI) concentration up to 50 μM leads to the precipitation of U(VI) at the kaolinite surface. The U-Al/Si interaction

determined at the distance of ~3.10 Å with a coordination number of one or less detected in samples 1-4 are attributive for bidentate coordination of U(VI) to $Si(O,OH)_4$. The U-Al/Si distance of ~3.30 Å can be rationalized as bidentate coordination (edge-sharing) of U(VI) to $[Al(O,OH)_6]$ octahedra of kaolinite. However, these possibilities need to be investigated further, for example, by measuring the EXAFS spectra of suitable reference samples.

4.3.2 Speciation of U(VI) as a function of pH

Fig. 38 shows the sorption behavior of U(VI) (total concentration 10 µM) on kaolinite as a function of pH. At low pH (until ~4) uptake of U(VI) is very low, but as pH increases from 4 to 6 the percentage of uranium sorbed onto kaolinite increases drastically from 3 % to over 80 %. In the air-equilibrated system, the uptake of U(VI) from solution by

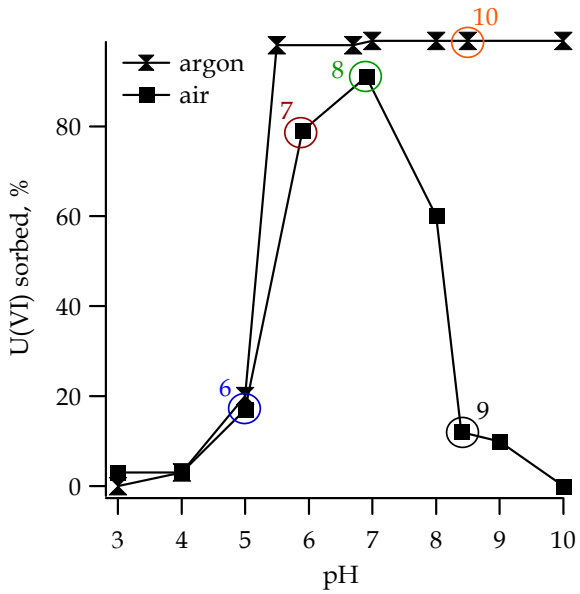

Fig. 38: Sorption of U(VI) (total concentration 10 µM) onto kaolinite in the presence or absence of ambient CO_2 as a function of pH. Refer to Table 14 for the description of samples 6-10.

kaolinite decreases above pH 7 due to the formation of strong carbonato complexes in aqueous solution. Logically, no decrease in uptake is observed in the absence of CO_2. These observations have been published in [127, 128] and agree with previous batch experiments [129, 130]. Thus, the uptake experiments suggest that several sorption mechanisms are operating under different solution conditions, possible resulting in the formation of different sorption species. Hence, the aim of two comparative EXAFS studies (conventional analysis by means of least-squares fitting and modified regularization method) was to determine what has happened with the local coordination environment of U(VI) at the kaolinite-water interface at different pH values.

The first Tikhonov solutions g^1(UU), g^2(UAl/Si), and g^3(UO) for the U L_{III}-edge EXAFS data of samples 6-9 are shown in Fig. 39.

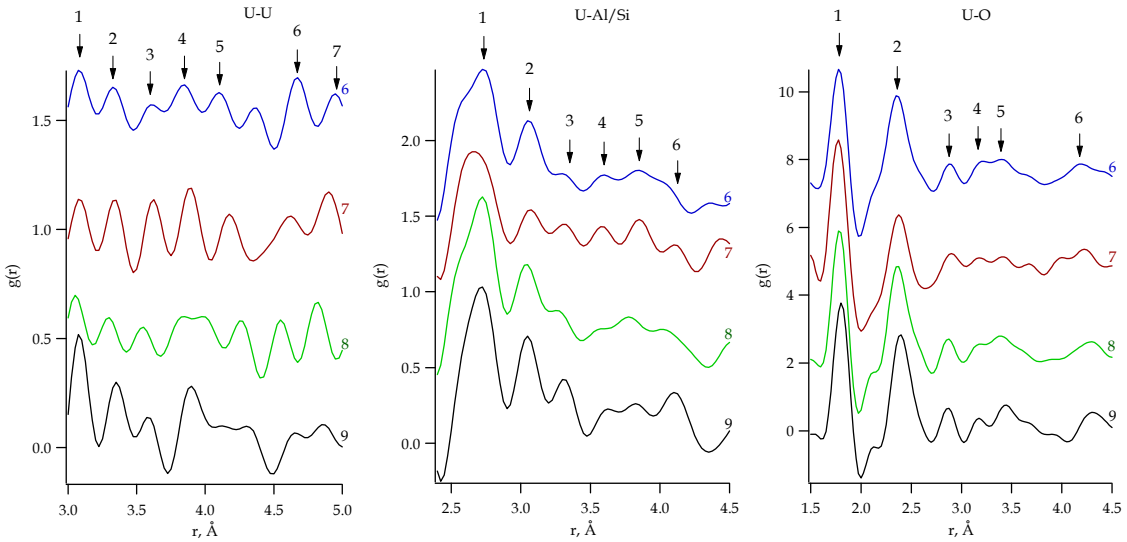

Fig. 39: First Tikhonov solutions g^1(UU), g^2(UAl/Si), and g^3(UO) for samples 6-9. All RDF peaks are numerated to be analyzed by the method of separating functionals.

Upon initial inspection, the Tikhonov solutions g^1(UU) demonstrate only a weak, if at all existing, contribution of U-U interactions to EXAFS spectra, i.e., practically, it not exceeds the noise level of the data. Confirming the oxygen origin of the Al/Si feature (number 1 in Fig. 39, middle), all Tikhonov solutions g^2(UAl/Si) show a big and to a variable degree asymmetrical signal at ~2.70 Å. All Tikhonov solutions g^2(UAl/Si) show Al/Si feature at ~3.10 Å (number 2 in Fig. 39, middle). Although, the corresponding peak of sample 7 (pH 6) shows a significant smaller amplitude than for the other three g^2(UAl/Si). Features at ~3.30 Å (number 3 in Fig. 39, middle) in the g^2(UAl/Si) that could be ascribed to the aluminium shell around the central uranium atom are not clear, except perhaps for sample 9 (pH 8.5). g^3(UO) solutions are remarkable in that the equatorial oxygen shells (number 2 in Fig. 39, right) significantly change with increasing pH. Namely, the following trends are observed with increasing pH: the equatorial oxygen peak becomes more symmetrical, suddenly diminishes in amplitude at pH 6 and then increases again, and moves to longer distances.

Based on the sorption behaviour of U(VI) on kaolinite (Fig. 38) and its aqueous speciation (Fig. 40) calculated at the same experimental conditions with the chemical equilibrium software MEDUSA [131] (the U(VI) hydrolysis and carbonato constants were evaluated in [132]), the formation of uranyl (hydroxide/carbonate) species at pH 8.5 (sample 9) is most likely.

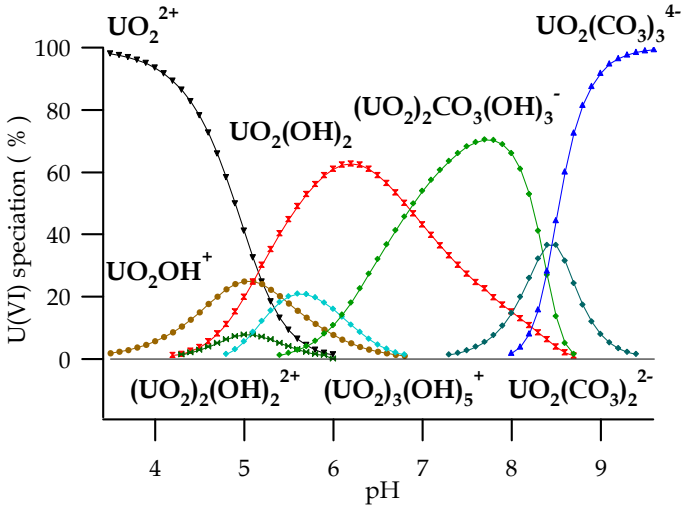

Fig. 40: Calculated speciation of 10 μM U(VI) solution (0.1 M $NaClO_4$ background electrolyte) in equilibrium with atmospheric CO_2 ($p\ CO_2 = 10^{-3.5}$ atm.).

In this case, the coordination shell of the distal oxygen atoms (O_{dist}) of the carbonate groups $[UO_2(CO_3)_n]^{(2n-2)-}$, n=2 or 3 at ~4.25 Å should be detected reflecting the appearance of U-C interaction. But at first sight, the O^6 feature in g^3(UO) of sample 9 seems to be ordinary phantom of the U coordination shell at ~3.90 Å (see model calculations of soddyite in Sect. 4.2.1).

For a more satisfactory reconstruction of the RDFs, all their features were analyzed by the method of separating functionals. The results for the Tikhonov solutions g^1(UU), g^2(UAl/Si), and g^3(UO) are summarized in Tables 20, 21, and 22, respectively.

Table 20. The values of separating functionals Λ for some peaks of the Tikhonov solution g^1(UU) received for the EXAFS data of samples 6-9.

Sample	U^1		U^2		U^3		U^4		U^5		U^6		U^7	
	r, Å	Λ	r, Å	Λ	r, Å	Λ	r, Å	Λ	r, Å	Λ	r, Å	Λ	r, Å	Λ
6	3.08*	-3.02	3.33*	-2.87	3.60*	-0.41	**3.85***	**1.51**	4.10*	1.11	4.68	11.68	4.95	6.72
7	3.08*	7.17	3.35	8.41	3.63	8.27	**3.90**	**8.40**	4.18*	3.10	4.63*	6.08	4.90*	7.62
8	3.05*	-3.78	3.30*	-3.56	3.55*	-3.56	**3.85***	**-0.06**	4.25*	2.23	4.55*	-0.46	4.83*	1.78
9	3.08*	4.78	3.35*	5.95	3.58*	0.09	**3.90**	**9.89**	4.13*	5.11	4.65*	4.96	4.85*	3.43

* - Negative or small positive Λ values are indicative for "false" peaks.

As can be seen from Table 20, the Λ values for sample 8 indicate no U-U interaction. Since there is no *priori* knowledge about the presence or absence of U-U interaction in samples 6, 7, and 9, their possible "true" RDFs features (without * in Table 20) were kept for the iteration procedure with filtration in real space.

Table 21. The values of separating functionals Λ for some peaks of the Tikhonov solution g^2(UAl/Si) received for the EXAFS data of samples 6-9.

Sample	Al/Si^1		Al/Si^2		Al/Si^3		Al/Si^4		Al/Si^5		Al/Si^6	
	r, Å	Λ	r, Å	Λ	r, Å	Λ	r, Å	Λ	r, Å	Λ	r, Å	Λ
6	2.73	16.18	3.05	1.89	3.30	-10.3	3.60	4.94	3.85	9.51	-	-
7	2.65	17.79	3.08	6.95	3.30	4.02	3.58	10.8	3.85	16.9	4.10*	4.30
8	2.73	23.59	3.05	4.18	3.25	-3.24	-	-	3.78*	1.49	4.03*	-0.84
9	2.73	20.08	3.05	10.47	3.30	1.29	3.63	7.05	3.83	2.61	4.10	15.57

* - Negative or small positive Λ values are indicative for "false" peaks.

All comments presented for the first solution g^2(UAl/Si) of samples 1-4 (see after Table 16) can be adopted here for the samples 6-9. In view of the fact that the U-Al/Si contribution is difficult to detect in a signal that is dominated by U-O and also U-U contributions (see [133] as also Sect. 4.2 in this work), the general strategy is to leave all suspicious features of g^2(UAl/Si) to the following iteration procedure. Of course, this should be done according to the detection limit of the EXAFS data for the samples investigated, i.e., only the Al/Si features in the r range of 2.40 ÷ 4.0 Å were taken into consideration.

Table 22. The values of separating functionals Λ for some peaks of the Tikhonov solution g^3(UO) received for the EXAFS data of samples 6-9.

Sample	O^1		O^2		O^3		O^4		O^5		O^6	
	r, Å	Λ	r, Å	Λ	r, Å	Λ	r, Å	Λ	r, Å	Λ	r, Å	Λ
6	**1.78**	**15.59**	**2.35**	**10.08**	2.88*	-0.92	3.23*	3.31	3.40*	1.87	4.20*	3.91
7	**1.78**	**21.73**	**2.38**	**9.99**	2.90*	3.87	3.18*	3.01	3.43*	2.10	4.23*	5.59
8	**1.78**	**16.99**	**2.38**	**11.60**	2.88*	0.76	3.20*	0.35	3.40*	2.69	4.30*	4.43
9	**1.80**	**18.88**	**2.40**	**12.94**	2.88*	0.98	3.18*	0.77	3.45	6.48	4.30	5.30

* - Negative or small positive Λ values are indicative for "false" peaks.

As usually, the simplest situation is with the features of g^3(UO): two clear defined peaks (numbers 1 and 2 at right in Fig. 39, bold in Table 22), representing axial and equatorial coordination shells, are the result of the analysis by separating functionals for samples 6-9. It is interesting to note that the O_{ax} interatomic distance of sample 9 (pH = 8.5) is longer than for all other the samples with lower pH values. The growth of the O_{eq} interatomic distances with increasing pH is also evident from Table 22. To be sure that uranyl carbonate complexes are not formed at the kaolinite surface, the O^5 and O^6 features of sample 9 were also kept as a potential "true" coordination shells. The final RDFs solutions for samples 6-9 after iteration refinement are shown in Fig. 41. Corresponding $[Ag](k)$ functions are shown in Fig. 42. The bond lengths, coordination

numbers, and *FHWM* are summarized in Tables 23 and 24. In particular to the

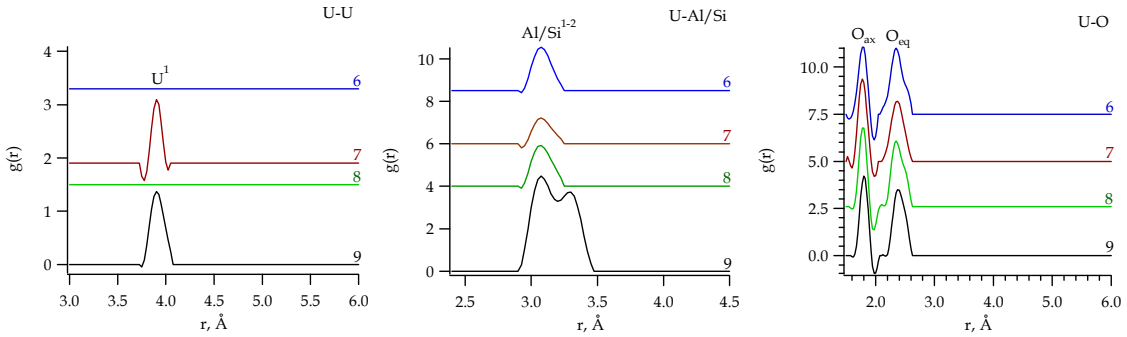

Fig. 41: Final solutions for the RDFs g^1(UU), g^2(UAl/Si), and g^3(UO) of sorption samples 6-9.

study of the pH dependence of the U(VI) interaction with the kaolinite-water interface, there are several implications from the results displayed in Fig. 41.

At the lowest pH conditions ($5.0 \leq pH \leq 7.0$) and in the presence of air, the lack of U-U interaction (samples 6 and 8) is indicative of the predominance of mononuclear U(VI) species, even if minor multiple species (sample 7) coexist. At slightly higher pH values ($7.1 \leq pH \leq 8.5$), the contribution of U-U interaction seems to become a little bit stronger. This could indicate the formation of polynuclear U(VI) species at the kaolinite surface. However, the precipitation of homogeneous U phase can not be seriously considered, because the solutions from which uranium was sorbed were undersaturated with respect to uranyl trioxide dehydrate {$UO_3 \times 2H_2O$} and uranyl hydroxide {β - $UO_2(OH)_2$}. Equilibrium solution speciation was calculated for the experimental conditions using the program Visual MINTEQ 2.50.

For the discussion of the pH dependence of uranyl complexation with aluminol and silanol sites, the values for pH_{pzc} that are defined as the pH at which net surface charge due to proton exchange is zero (pzc corresponds to "point of zero charge") should be considered. The structure of kaolinite makes pH_{pzc} estimation more difficult because of distinct sets of functional groups that are present: a basal siloxane layer, a basal gibbsite-like layer, and edges composed of aluminol and silanol sites (Fig. 32). Since solute adsorption is site specific, U(VI) sorption on kaolinite should include all of the different surface sites. There are two kinds of charges on kaolinite surface. The permanent charge arises from substitution of Si^{IV} or Al^{III} by cations of lower valence. Another type of charge for kaolinite, i.e., variable charge can be related to the reactions between ionisable aluminol and silanol surface groups located at the edges or at the gibbsite basal plane and the ions present in aqueous solution [134]. In terms of the Triple Layer Model [135, 136], the pH_{pzc} of the gibbsite layer and of the edge sites are treated separately and were estimated to be 6.0 and 8.0, respectively, for kaolinite

KGa-1 provided by the Clay Mineral Society (Columbia, MO) [130]. An apparently averaged value was 4.66, which would presumably reflect the contribution from the silanol functionality. In the pH range of this work ($5.0 \le pH \le 8.5$), the silanol groups ($\equiv SiOH$) at the edges contribute exclusively to the negative charge, through formation of $\equiv SiO^-$ surface complexes [137]. The aluminol groups at the edges are amphoteric. They undergo protonation at low pH and deprotonation at high pH, resulting in the formation of the surface complexes $\equiv AlOH_2^+$ and $\equiv AlO^-$ [138-140]. The other factor, which can be taken into account, is the dissolution rate of kaolinite at the experimental conditions. Kaolinite dissolution during the experiments is reflected by the release of Si and Al into solution. According to [134], in a broad interval of the ionic strength values (from 0.025 M to 0.5 M), the observed minimum of Al concentration is between pH 6 to 7. Whereas, an Al release into solution of less than 1 % was found [134], Si release was not detected at all, i.e., Si concentration in solution was always below the detection limit.

Thus, it appeared reasonable to exclude kaolinite dissolution as a factor influencing the U(VI) sorption. The main conclusion from the above discussion is that with increasing pH most of the sorption activity occurs along the kaolinite edges because of their growing negative charge. In other words at higher pH values the uranyl complexation with the aluminol and silanol groups becomes more likely due to increasing deprotonation of the edge sites. This result is consistent with the increasing of U-Al/Si contribution to the EXAFS data of sample 9 (pH 8.5).

Silicon, a second uranyl ion neighbor at a distance ~3.10 Å, is present in spectra under all of studied pH conditions (Fig. 41, middle), undoubtedly indicating inner-sphere complexation of U(VI) by kaolinite. Concerning Al/Si feature at ~3.30 Å, it was detected only at pH 8.5 and with approximately the same coordination number as the shell at ~3.10 Å. However, within the limits established by the quantity (only one sample by pH 8.5 in the presence of air) and quality (relative high noise level of the experimental spectrum), it is impossible to come to far-reaching conclusions how exactly uranium is associated with kaolinite at the condition of higher pH values.

The final g^3(UO) function of all samples (Fig. 41, right) consists of only two peaks corresponding to the axial and equatorial oxygen shells about the uranium atom. The O_{eq} distance increases with increasing pH from 5.0 to 8.5 in the presence of CO_2. All these distances are shorter than 2.41 Å, the average O_{eq} distance of the U(VI) aquo ion [75] that corroborates inner-sphere sorption of U(VI) onto the kaolinite surface. The coordination shell of the distal oxygen atoms (O_{dist}) of the carbonate groups $[UO_2(CO_3)_n]^{(2n-2)-}$, n=2 or 3 at ~4.25 Å was not detected in the RDF g^3(UO) of sample 9.

It should be noted that one more question arises after closer inspection of the RDFs as a function of pH. Specifically, the Al/Si and O_{eq} coordination peaks at pH 6 strongly

diminish in amplitude in comparison to other pH values. Probably, these is due to specific sorption onto amphoteric sites at kaolinite edges [134], but to explain this observation additional investigations, combining spectroscopic measurements with detailed surface complexation modelling, are necessary. Moreover, it will be useful to provide such investigations not only for kaolinite, but in parallel for gibbsite (which contains only aluminol sites) and silica or quartz (with only silanol sites).
As can be seen in Fig. 42, the structural trends observed in final RDFs solutions are confirmed by good agreement of calculated $[Ag](k)$ functions with the experimental EXAFS data.

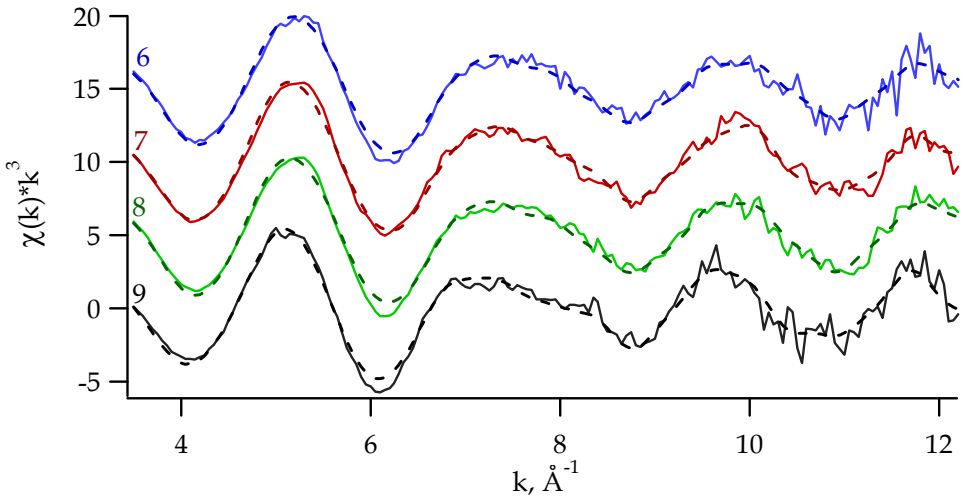

Fig. 42: U L_{III}-edge k^3-weighted EXAFS data of samples 6-9: Spectra calculated from the final RDFs (dashed lines), experimental data (solid lines).

The results of the conventional structural analysis by means of least-squares fitting (see Appendix II) and the modified regularization method obtained for spectra 6-9 are compared in Tables 23 and 24. The agreement between the interatomic distances derived by two alternative EXAFS analysis methods is generally within the experimental error of ± 0.02 Å; exceptions are related to the different way of their estimation, i.e., with and without assuming a Gaussian distribution by least-squares fitting and the modified regularization method, respectively. That the shell Al/Si^2 was no detected by the regularization method at the lowest pH conditions ($5.0 \leq pH \leq 7.0$) can be associated with the small scattering power of these atoms which is too low to contribute to the EXAFS spectra and/or with the overlap of O_{eq} coordination shell that strongly deforms the solution g^2(UAl/Si) until 5.0 Å (see soddyite model calculation in Sect. 4.2.1). In contrast, this discrepancy in the determination of the coordination shell Al/Si^2 can be caused by the limitation imposed by the structural model used for the least-squares refinement.

Table 23. Sorption of U(VI) onto kaolinite as a function of pH. Uranium and silicon coordination shells: interatomic distances *r* and *FWHM* in Å, and coordination numbers *N* obtained by least-squares fitting (**1**) are in comparison by those determined by the modified Tikhonov regularization method (**2**).

Spectrum /Method			U[1]			Si[1]			Al/Si[2]		
			r	*N*	*FWHM*	*r*	*N*	*FWHM*	*r*	*N*	*FWHM*
EXAFS	**6**	**1**	-	-	-	3.10	1.1#	0.1290#	3.30	0.9#	0.1290#
		2	-	-	-	3.07	0.5	0.1705	-	-	-
	7	**1**	-	-	-	3.10	0.8#	0.1290#	3.29	0.8#	0.1290#
		2	3.90	0.3	0.1148	3.07	0.3	0.1669	-	-	-
	8	**1**	-	-	-	3.09	1.1#	0.1290#	3.29	0.9#	0.1290#
		2	-	-	-	3.07	0.5	0.1845	-	-	-
	9	**1**	3.92	1.0¤	0.2040	3.08	1.6#	0.1290#	3.29	1.5#	0.1290#
		2	3.90	0.5	0.1724	3.08	1.3	0.1789	3.29	1.0	0.1928

Al/Si coordination numbers were calculated with fixed at 0.0030 Å^2 DW factor.

¤ U coordination numbers were calculated with fixed at 0.0075 Å^2 DW factor.

It is evident from Table 23, both U and Al/Si coordination numbers derived by the modified regularization method are always smaller than those obtained by least-squares fitting. This can be ascribed to the choice of the "initial" regularization parameter, i.e., a no optimal choice leads to an uncertainty in the determination of the coordination numbers. But in the absence of a complete structure refinement it is difficult to say either U, as also Al/Si coordination numbers are overestimated by least-squares fitting or underestimated by the Tikhonov procedure. Any way, their relative change is the same for both methods.

Table 24. Sorption of U(VI) onto kaolinite as a function of pH. Oxygen coordination shells: interatomic distances *r* and *FWHM* in Å, and coordination numbers *N* obtained by least-squares fitting (**1**) are in comparison by those determined by the modified Tikhonov regularization method (**2**).

Spectrum /Method			O_{ax}			O_{eq}		
			r	*N*	*FWHM*	*r*	*N*	*FWHM*
EXAFS	**6**	**1**	1.79	2*	0.1268	2.37	5*	0.2766
		2	1.79	1.9	0.1674	2.35	5.1	0.2403
	7	**1**	1.78	2*	0.1129	2.37	5*	0.2569
		2	1.78	2.3	0.1716	2.37	4.6	0.2562
	8	**1**	1.79	2*	0.1053	2.38	5*	0.2536
		2	1.79	2.0	0.1522	2.35	5.0	0.2678
	9	**1**	1.80	2*	0.1105	2.40	5*	0.2307
		2	1.81	2.2	0.1565	2.39	5.2	0.2549

* Parameter fixed during least-squares fitting.

Contrary to U and Al/Si, the O coordination numbers are not so sensitive to the "initial" regularization parameter. This is not surprising taking into account the strong scattering power of axial and equatorial oxygen atoms. As a result, the coordination numbers for axial and equatorial shells of oxygen derived by both EXAFS analysis methods agree very well (Table 24).The average distance between uranium and its two axial oxygen atoms, O_{ax}, is nearly constant for samples 6-9 and equals 1.78 ± 0.02 Å. The average coordination number for the equatorial oxygen atoms, O_{eq}, is five. As can be seen from Table 24, the average O_{eq} distance varies between 2.37 – 2.40 and 2.35 - 2.39 Å by least-squares fitting and the modified regularization method, respectively. The splitting of O_{eq} equatorial shell is unlikely for samples 6-9 that can be indicative for absence of precipitation of homogeneous U phase by investigating experimental conditions.

Finally, the results of the two alternative EXAFS analysis methods show that for the EXAFS experiments, where CO_2 was present and the total U(VI) concentration was 10 μM, U(VI) forms monomeric, inner-sphere surface complexes with kaolinite in the pH range of 5.0 – 7.0, and polymeric, inner-sphere surface complexes with kaolinite at slightly the higher pH values (until 8.5).

The average O_{eq} bond distances of the aqueous $[UO_2(CO_3)_3]^{4-}$ complex is 2.44 ± 0.02 Å [89]. Although at higher pH values no U-C interaction was detected by both analysis methods, the observed lengthening of the O_{ax} and O_{eq} bond distances correlates with increasing amounts of CO_3^{2-}/HCO_3^- in solution. This could indicate an increasing importance of U(VI) surface complexes with carbonate on the kaolinite surface.

4.3.3 Speciation of U(VI) as a function of CO_2

Sample 10 was prepared at pH 8.5 with the total concentration 10 μM of U(VI) under argon atmosphere for comparison with sample 9 prepared under identical conditions in the presence of CO_2 (Table 14). Although polynuclear U(VI) species in presence or absence of CO_2 are known to be stable in aqueous solutions (Figs. 40, 43), the likelihood of the same species at the kaolinite surface has not been tested in sorption studies. To identify nascent kaolinite surface species, in addition to batch experiments (see Fig. 38) EXAFS data were collected in fluorescence mode at room temperature and analyzed both by the conventional least-squares fitting (see Appendix II) and the modified regularization method. Examination of the raw U L_{III}-edge k^3-weighted EXAFS spectra of samples 9 and 10 reveals a distinct change in the shape of the data between ~6.0 and ~8.5 $Å^{-1}$ (see Fig. 33). This difference in the EXAFS data can be understood qualitatively by inspecting the corresponding RDFs in Fig. 44. For both samples, the Tikhonov solutions g^1(UU) do not show a U-U interaction exceeding the noise level of the EXAFS data. As usual for all Tikhonov solutions g^2(UAl/Si), a big feature at ~2.70 Å (peak number 1 in Fig. 44, middle) is observed in each RDF. The appearance of a small

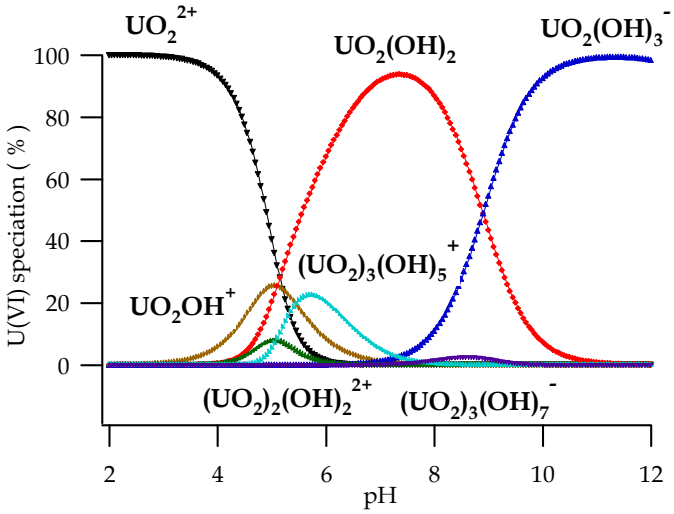

Fig. 43: Calculated speciation of U(VI) solution (total concentration of U(VI) 10 µM and 0.1 M $NaClO_4$ background electrolyte) in the absence of CO_2. Distribution of major U(VI) species was determined by the chemical equilibrium software MEDUSA [131] applying the U(VI) hydrolysis constants evaluated in [132].

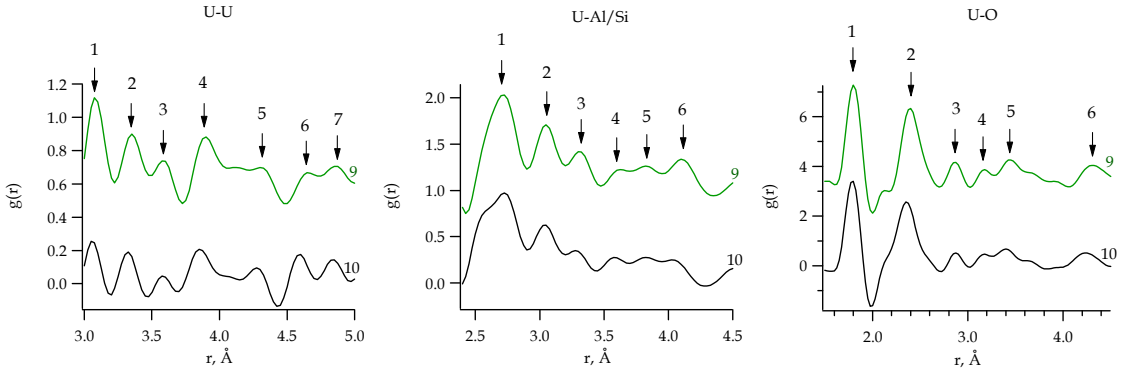

Fig. 44: First Tikhonov solutions g^1(UU), g^2(UAl/Si), and g^3(UO) for samples 9 and 10. All RDF peaks are numerated to be analyzed by the method of separating functionals.

shoulder at ~2.50 Å in the RDF of sample 10 reflects the broadening of the oxygen equatorial shell in comparison to that of sample 9. There is evidence of an Al/Si coordination shell at ~3.10 Å (peak number 2 in Fig. 44, middle) in both g^2(UAl/Si). But the corresponding peak of sample 10 (in the absence of CO_2) shows significantly smaller amplitude than sample 9. The feature at ~3.30 Å in g^2(UAl/Si) (peak number 3 in Fig. 44, middle) that can be ascribed to the aluminium shell around the central uranium atom are seen in both Tikhonov solutions g^2(UAl/Si), but less clear for sample 10. Both Tikhonov solutions g^3(UO) are very similar, with only one but significant exception that the equatorial oxygen shell (peak number 2 in Fig. 44, right) of sample 10 (in the absence of CO_2) becomes less symmetrical and shifts to a shorter distance. A

similarity of the O^6 feature in g^3(UO) and the presence of a local minimum in g^2(UAl/Si) at practically the same distance of ~4.25 Å for both samples indicates similar uranyl complexation at the kaolinite surface, independent of the presence or absence of CO_2 during sample preparation. The O^6 feature in g^3(UO) for both samples is presumably a phantom of a U coordination shell at ~3.90 Å and can not be ascribed as an O_{dist} shell of the carbonate groups.
To analyze the Tikhonov solutions, the method of separating functionals is applied. The results for the prominent features of the Tikhonov solutions g^1(UU), g^2(UAl/Si), and g^3(UO) are given in Tables 25, 26, and 27, respectively.

Table 25. The values of separating functionals Λ for some peaks of the Tikhonov solution g^1(UU) received for the EXAFS data of samples 9-10.

Sample	U^1		U^2		U^3		U^4		U^5		U^6		U^7	
	r, Å	Λ	r, Å	Λ	r, Å	Λ	r, Å	Λ	r, Å	Λ	r, Å	Λ	r, Å	Λ
9	3.08*	4.78	3.35*	5.95	3.58*	0.09	3.90	9.89	4.30*	-2.42	4.65*	4.96	4.85*	3.43
10	3.05*	-1.29	3.33*	3.46	3.58*	-0.10	3.85	7.29	4.28*	-3.16	4.60*	6.48	4.85*	5.50

* - Negative or small positive Λ values are indicative for "false" peaks.

Those of U features that were estimated by the method of separating functionals as potentially "true" and which were close to the detection limit of EXAFS were kept for further iteration calculations.

Table 26. The values of separating functionals Λ for some peaks of the Tikhonov solution g^2(UAl/Si) received for the EXAFS data of samples 9-10.

Sample	Al/Si^1		Al/Si^2		Al/Si^3		Al/Si^4		Al/Si^5		Al/Si^6	
	r, Å	Λ	r, Å	Λ	r, Å	Λ	r, Å	Λ	r, Å	Λ	r, Å	Λ
9	2.73	20.08	3.05	10.47	3.30	1.29	3.63	7.05	3.83	2.61	4.10	15.57
10	2.73	14.61	3.05	5.28	3.28	-5.90	3.58	3.86	3.83	7.18	4.03*	2.18

* - Negative or small positive Λ values are indicative for "false" peaks.

While the contribution U-Al/Si is difficult to determine from the EXAFS data due to the dominating contributions of U-O and U-U (see [133] as also Sect. 4.2 in this work), the general strategy was to leave all suspicious features of g^2(UAl/Si) to the following iteration procedure. An exception was made for the feature Al/Si^3 of sample 10, because it was not really separated from the potential coordination shell Al/Si^2.

Two features (bold in Table 27) are clearly identified as "true" peaks by the method of separating functionals and represent axial and equatorial coordination shells of oxygen. The obtained interatomic distances are very interesting. At pH 8.5, independent of presence/absence CO_2 in the initial solution, the method of separating

Table 27. The values of separating functionals Λ for some peaks of the Tikhonov solution g^3(UO) received for the EXAFS data of samples 9-10.

Sample	O^1		O^2		O^3		O^4		O^5		O^6	
	r, Å	Λ	r, Å	Λ	r, Å	Λ	r, Å	Λ	r, Å	Λ	r, Å	Λ
9	**1.80**	**18.88**	**2.40**	**12.94**	2.88*	0.98	3.18*	0.77	3.45	6.48	4.30	5.30
10	**1.80**	**17.78**	**2.35**	**9.69**	2.88*	-0.37	3.18*	0.97	3.40*	3.62	4.23*	5.42

* - Negative or small positive Λ values are indicative for "false" peaks.

functionals predicts the interatomic distance O_{ax} to be ~1.80 Å, whereas the average distance of the equatorial oxygen atoms O_{eq} increases from 2.35 to 2.40 Å in the presence of CO_2. To be sure that a possible formation of uranyl carbonate complexes at kaolinite surface is not overlooked, the features O^5 and O^6 of sample 9 were kept as a potential "true" coordination shells during the following iteration procedure.

The final RDFs solutions after iteration refinement and the corresponding $[Ag](k)$ functions are represented in Fig. 45. The bond lengths, coordination numbers, and *FHWM* are summarized in Tables 28 and 29.

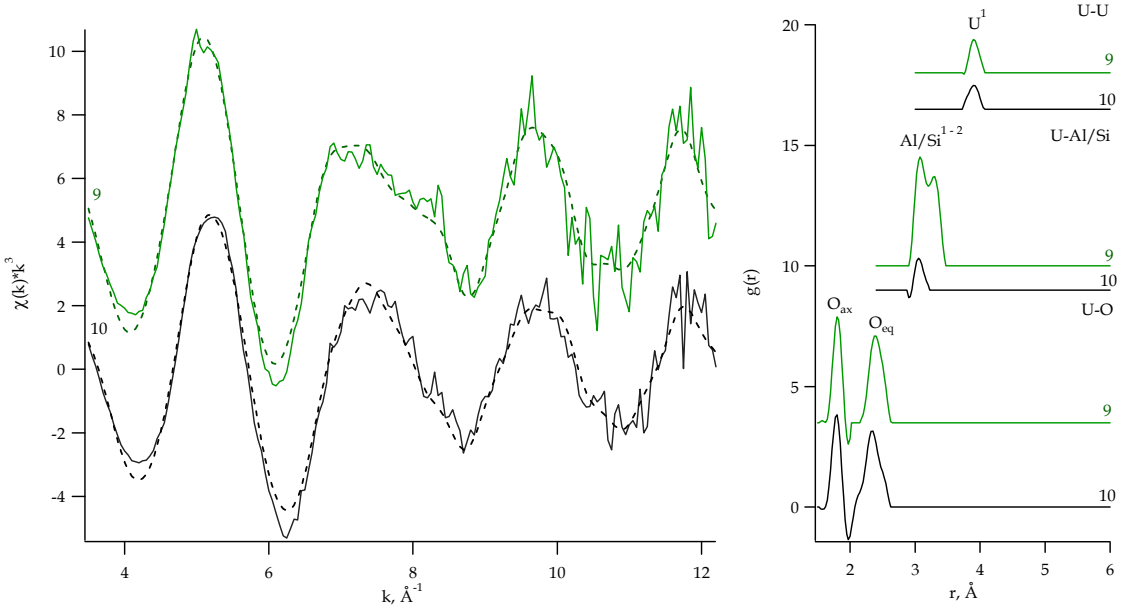

Fig. 45: U L_{III}-edge k^3-weighted EXAFS spectra (left) and calculated according to Eq. (36) final solutions (right) for samples 9 and 10. Solid line – experimental data, dashed line – received from final solutions.

Although the agreement between the functions $[Ag](k)$ and the experimental data is not exact (Fig. 45, left), the spectra calculated using Eq. (35) reproduce all features observed in the experimental data of the samples prepared in the presence/absence of CO_2. The final solution g^1(UU) for both samples represents a single peak at ~3.90 Å

(Fig. 45, right, top). The number of uranium atoms constituting each sorption complex (in presence/absence of CO_2) is essentially the same within the experimental error. This result is promising, because the formation of polynuclear U(VI) sorption species, even in the presence of CO_2, increases the capacity of kaolinite for uranium over what might be possible if only mononuclear species would form. At higher pH values uranyl complexation with the aluminol and silanol groups becomes more likely due to increasing deprotonation of the edge sites. This is consistent with the increase of the U-Al/Si contribution to the EXAFS data of sample 9 (pH 8.5, CO_2 presence).

The decrease of the U-Al/Si contribution to the EXAFS data at the condition of the same pH but CO_2 absence (g^2(UAl/Si) of sample 10 in Fig. 45, right, middle) is not unexpected, because a change of pH from 5 to 8.5 does not have any influence on the sorption process in CO_2-free samples. Namely, the uranyl complexation at the kaolinite surface of sample 10 is similar to those of samples 6 and 7, which were prepared at air at pH 5.0 and 6.0 (see Fig. 41 and 42). The consistency among the U-Al/Si contributions, significantly shorter average distance of the equatorial oxygen atoms, O_{eq}, only weak U-U interaction, as well as similar EXAFS data pattern are as satisfactory basis for the evaluation of the similarity of the uranyl complexation.

Any way, the contribution U-Al/Si to the EXAFS data confirms that all of the uranium species formed in the presence/absence of CO_2 are inner-sphere sorption complexes.

The final solution g^3(UO) of samples 9 and 10 (Fig. 45, right, bottom) consists of two peaks corresponding to the axial and equatorial oxygen shells of uranium.

Table 28. Sorption of U(VI) onto kaolinite as a function of CO_2. Uranium and silicon coordination shells: interatomic distances *r* and *FWHM* in Å, and coordination numbers *N* obtained by least-squares fitting (**1**) are compared to those determined by the modified Tikhonov regularization method (**2**).

Spectrum /Method			U[1]			Si[1]			Al/Si[2]		
			r	*N*	*FWHM*	*r*	*N*	*FWHM*	*r*	*N*	*FWHM*
EXAFS	**9**	**1**	3.92	1.0[¤]	0.2040	3.08	1.6[#]	0.1290[#]	3.29	1.5[#]	0.1290[#]
		2	3.90	0.5	0.1724	3.08	1.3	0.1789	3.29	1.0	0.1928
	10	**1**	3.91	0.8[¤]	0.2040	3.09	0.9[#]	0.1290[#]	3.29	0.9[#]	0.1290[#]
		2	3.91	0.4	0.1990	3.06	0.3	0.1543	-	-	-

[#] Al/Si coordination numbers were calculated with fixed at 0.0030 Å^2 DW factor.

[¤] U coordination numbers were calculated with fixed at 0.0075 Å^2 DW factor.

As can be seen from Tables 28 and 29, the agreement between the interatomic distances derived by the two alternative EXAFS analysis methods is generally within the experimental error of ± 0.02 Å; exceptions are related to the assumption of a Gaussian distribution in the least-squares fitting procedure. The coordination numbers of shells

U-U and U-Al/Si derived by the modified regularization method are smaller than those obtained by least-squares fitting (Table 28). The reason of the decrease remains the same as was discussed above, i.e., probably a no optimal choice of the "initial" regularization parameter.

Table 29. Sorption of U(VI) onto kaolinite as a function of CO_2. Oxygen coordination shells: interatomic distances *r* and *FWHM* in Å, and coordination numbers *N* obtained by least-squares fitting (**1**) are compared to those determined by the modified Tikhonov regularization method (**2**).

Spectrum /Method			O_{ax}			O_{eq}		
			r	*N*	*FWHM*	*r*	*N*	*FWHM*
EXAFS	9	1	1.80	2*	0.1105	2.40	5*	0.2307
		2	1.81	2.2	0.1565	2.39	5.2	0.2549
	10	1	1.80	2*	0.1178	2.37	5*	0.2903
		2	1.79	1.9	0.1554	2.34	4.7	0.2554

* Parameter fixed during least-squares fitting.

O_{ax} and O_{eq} coordination numbers derived by both EXAFS analysis methods agree very well (Table 29).A lengthening of the O_{eq} bond distance in the presence of CO_2 (Sample 9) is evident from Table 29. Thus, although an O_{dist} coordination shell of carbonate ligands was not observed, the lengthening of the O_{eq} bond distance confirms the increased importance of U(VI) complexes with carbonate on the kaolinite surface at pH 8.5.

Finally, the results of the two alternative EXAFS analysis methods show that for the EXAFS experiments, where pH was kept at 8.5 and total U(VI) concentration of the samples was 10 μM, U(VI) forms polymeric, inner-sphere surface complexes with kaolinite both in absence and in presence of CO_2, that increases the capacity of kaolinite for uranium.

No U-C interaction was detected for sample 9. Hence, the applied analysis methods suggest that formed U(VI) species are for the most part the product of the coordination environment at the kaolinite surface, which is independent of the predominant U(VI) species in solution. Although from other side, the observed lengthening of the O_{eq} bond distance indicates an increased importance of U(VI) surface complexes with carbonate on the kaolinite surface.

4.3.4 Changes of U(VI) speciation at kaolinite surface upon drying

4.3.4.1 Ambient and low-temperature measurements

Two samples (7 and 11) were prepared under identical conditions at pH 6.0 and a total U(VI) concentration of 10 μM in the presence of CO_2. Sample 7 was prepared as a wet

paste and placed for EXAFS measurement at ambient temperature in a sample holder which was sealed with Kapton tape and two layers of polyethylene foil. To measure sample 11 at low temperature, the wet paste was air-dried and loaded in a Teflon sample holder. The fluorescence spectrum for sample 11 was collected at 28 K. The raw U L_{III}-edge k^3-weighted EXAFS spectra for the samples 7 and 11 are shown in Fig. 33 and reveal some differences in the shape of the data between ~6.0 and ~8.5 $Å^{-1}$. This difference in the EXAFS data could be caused by the different temperatures during the EXAFS experiment but also by the sample drying. To understand the changes in EXAFS data, they were analyzed over the k range 3.00 ÷ 12.2 $Å^{-1}$ both by least-squares fitting (see Appendix II) and the modified regularization method.
Comparison of the first Tikhonov solutions derived from the EXAFS data of wet and air-dried samples is shown in Fig. 46.

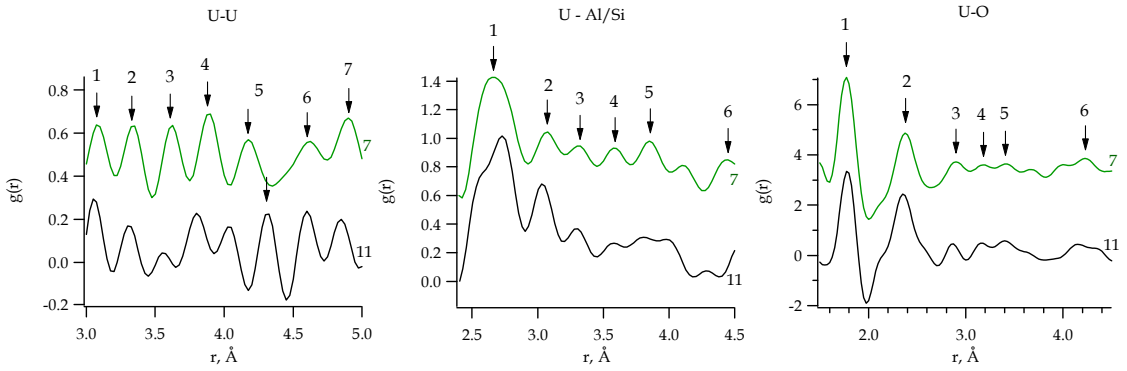

Fig. 46: First Tikhonov solutions g^1(UU), g^2(UAl/Si), and g^3(UO) for samples 7 and 11. All RDF peaks are numerated to be analyzed by the method of separating functionals.

The weak amplitude of the solutions g^1(UU) reflects only a small or no contribution of U-U interaction to the EXAFS spectra. The Tikhonov solutions g^2(UAl/Si) demonstrate a feature at ~ 2.70 Å (peak number 1 in Fig. 46, middle), the shoulder at 2.55 Å by sample 11 reflects the broadening of the oxygen equatorial shell in comparison to that of sample 7. Dampened vibrational disorder at low temperature would cause a larger amplitude of the Al/Si coordination shell at ~3.10 Å (peak number 2 in Fig. 46, middle) for the sample 11 than that found for sample 7. The Tikhonov solutions g^3(UO) are similar for both samples, except that the interatomic equatorial distance (peak number 2 in Fig. 46, right) is notable shorter at low temperature than the similar value derived at ambient temperature. Moreover, at low temperature the equatorial oxygen shell is asymmetric and has larger amplitude.
The next step of the EXAFS data treatment by the modified regularization method is the application of separation functionals to every feature of the RDFs. The results for the prominent features of Tikhonov solutions g^1(UU), g^2(UAl/Si), g^3(UO) are shown in Tables 30, 31, and 32, respectively.

Table 30. The values of separating functionals Λ for some peaks of the Tikhonov solution g^1(UU) received for the EXAFS data of samples 7 and 11.

Sample	U^1		U^2		U^3		U^4		U^5		U^6		U^7	
	r, Å	Λ	r, Å	Λ	r, Å	Λ	r, Å	Λ	r, Å	Λ	r, Å	Λ	r, Å	Λ
7	3.08*	7.17	3.35	8.41	3.63	8.27	3.90	8.40	4.18*	3.10	4.63*	6.08	4.90*	7.62
11	3.05*	3.56	3.30*	3.60	3.55*	1.38	3.80	8.34	4.33	9.17	4.60	9.59	4.85	8.16

* - Negative or small positive Λ values are indicative for "false" peaks.

Table 31. The values of separating functionals Λ for some peaks of the Tikhonov solution g^2(UAl/Si) received for the EXAFS data of samples 7 and 11.

Sample	Al/Si^1		Al/Si^2		Al/Si^3		Al/Si^4		Al/Si^5		Al/Si^6	
	r, Å	Λ	r, Å	Λ	r, Å	Λ	r, Å	Λ	r, Å	Λ	r, Å	Λ
7	2.65	17.79	3.08	6.95	3.30	4.02	3.58	10.80	3.85	16.90	4.10*	4.30
11	2.73	12.91	3.03	8.02	3.30	2.97	3.58	4.55	3.80	7.99	4.28*	-3.93

* - Negative or small positive Λ values are indicative for "false" peaks.

Table 32. The values of separating functionals Λ for some peaks of the Tikhonov solution g^3(UO) received for the EXAFS data of samples 7 and 11.

Sample	O^1		O^2		O^3		O^4		O^5		O^6	
	r, Å	Λ	r, Å	Λ	r, Å	Λ	r, Å	Λ	r, Å	Λ	r, Å	Λ
7	1.78	21.73	2.38	9.99	2.90*	3.87	3.18*	3.01	3.43*	2.10	4.23*	5.59
11	1.78	14.60	2.35	10.33	2.88*	1.62	3.15*	2.28	3.40*	3.76	4.15*	4.51

* - Negative or small positive Λ values are indicative for "false" peaks.

With the segments of all RDFs, where "false" peaks were identified, set to zero, the final solutions are determined by the iteration method with filtration in real space. The final RDFs solutions and the k^3-weighted experimental EXAFS spectra in comparison with the corresponding spectra calculated from the final RDFs are shown in Fig. 47. The backscattering of the oxygen coordination shells gives strong low frequency oscillations that dominate in the low k region of the EXAFS data for both samples (Fig. 47). The final g^3(UO) of the samples (Fig. 47, right, bottom) consists of two peaks corresponding to the axial and equatorial oxygen shells about the uranium atom. As can be seen, the equatorial oxygen shell for sample 11 is significantly more asymmetric than the corresponding peak of the wet sample 7. Moreover, the equatorial shell of g^3(UO) for sample 11 measured at low temperature is notably shorter than the O_{eq} distance for sample 7 measured at ambient temperature. These observations are very interesting, because they can not be attributable to the effect of low temperature itself. It is reasonable to suggest that drying may have effected the aqueous character of the

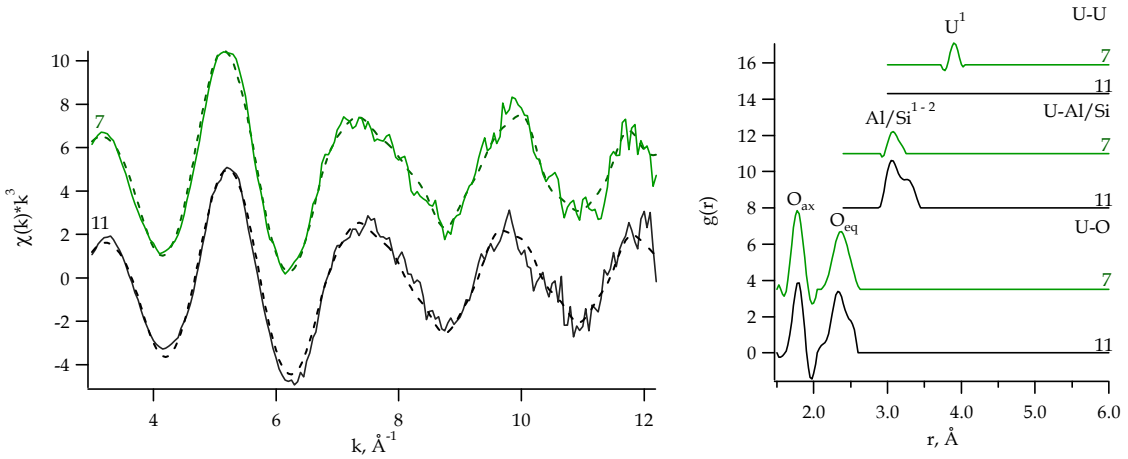

Fig. 47: U L_{III}-edge k^3-weighted EXAFS spectra (left) and calculated according to Eq. (36) final solutions (right) for samples 7 and 11. Solid line – experimental data, dashed line – received from final solutions.

sorbed species. It should be noted that the lower vibrational disorder at low temperature EXAFS measurements results in a stronger contributions from distant atoms (e.g., U). Hence, although minor multiple U-U species were found in the spectrum at ambient temperature (sample 7), the lack of U-U interaction in the spectrum at 28 K (sample 11) is indicative of the predominance of mononuclear U(VI) species at the pH 6 in the presence of air. The same reason can explain the increasing contribution of U-Al/Si interaction at 28 K (sample 11), i.e., Al/Si shells become relatively more significant at low temperature. The detection of Al/Si atoms in the near-neighbor environment of U indicates the formation of inner-sphere complexes of U(VI) with kaolinite at pH 6 and a total concentration of 10 μM U(VI) at both ambient and low temperature. Bond lengths, coordination numbers, *FWHM* for the coordination shells received by least-squares fitting (**1**) and the modified regularization (**2**) methods are compared in Tables 33 and 34.

Table 33. Sorption of U(VI) onto kaolinite as a function of temperature. Uranium and silicon coordination shells: interatomic distances *r* and *FWHM* in Å, and coordination numbers *N* obtained by least-squares fitting (**1**) are compared to those determined by the modified Tikhonov regularization method (**2**).

Spectrum /Method			U^1			Si^1			Al/Si^2		
			r	*N*	*FWHM*	*r*	*N*	*FWHM*	*r*	*N*	*FWHM*
EXAFS	7	**1**	-	-	-	3.10	0.8#	0.1290#	3.29	0.8#	0.1290#
		2	3.90	0.3	0.1148	3.07	0.3	0.1669	-	-	-
	11	**1**	-	-	-	3.08	0.9#	0.1290#	3.29	0.7#	0.1290#
		2	-	-	-	3.06	0.7	0.1741	3.26	0.4	0.1998

Si coordination numbers were calculated with fixed at 0.0030 $Å^2$ DW factor.

A minor U-U contribution to the EXAFS data measured at ambient temperature (sample 7) was found only by the regularization method. The Al/Si coordination numbers for both samples 7 and 11 derived by the modified regularization method are smaller than those obtained by least-squares fitting. The absence of more distant Al/Si atom at ~3.30 Å in the final g^2(UAl/Si) at ambient temperature is possible because of the strong deformation of the Tikhonov solution g^2(UAl/Si) due to the O_{eq} shell, which contributes to the g^2(UAl/Si) and therefore masks the silicon contribution.

Table 34. Sorption of U(VI) onto kaolinite as a function of temperature. Oxygen coordination shells: interatomic distances *r* and *FWHM* in Å, and coordination numbers *N* obtained by least-squares fitting (**1**) are compared to those determined by the modified Tikhonov regularization method (**2**).

Spectrum /Method			O_{ax}			O_{eq}		
			r	*N*	*FWHM*	*r*	*N*	*FWHM*
EXAFS	**7**	**1**	1.78	2*	0.1129	2.37	5*	0.2569
		2	1.78	2.3	0.1716	2.37	4.6	0.2562
	11	**1**	1.79	2*	0.1129	2.37	5*	0.2855
		2	1.79	1.9	0.1558	2.33	5.1	0.2779

* Parameter fixed during least-squares fitting.

All structural parameters determined using the modified regularization method for O_{ax} and O_{eq} coordination shells are essentially equivalent to those received by the conventional least-squares fitting. As can be seen, the modified regularization method is quite accurate in calculating both axial and equatorial coordination numbers in comparison with the values fixed during least-squares fitting. One obvious discrepancy is the shift in the equatorial bond length of the air-dried sample 11 to a shorter distance. From one side, it is due to the asymmetry of the O_{eq} coordination shell as shown by the modified Tikhonov regularization method. From the other side, the shortening of the O_{eq} bond length is very large and could be caused by the drying of sample 11.

The main conclusions of the least-squares fitting and modified regularization method are following:

Although the preparation conditions were the same (pH 6.0 and 10 μM of U(VI) total concentration in the presence of CO_2), the sorption complexes with the kaolinite surface of wet sample 7 measured at ambient temperature and air-dried sample 11 collected at 28 K are slightly different. The change of the sorption structure is observed both by a shorter equatorial oxygen bond length and by an asymmetry of the equatorial shell in the air-dried sample and can be caused by sample drying. Besides

this, both methods indicate the formation of monomeric, inner-sphere surface complexes of U(VI) with kaolinite at both ambient and low temperature.

4.3.4.2 Ambient temperature measurements

To ascertain that the drying does affect the uranium sorption at the kaolinite-water interface, samples 5 and 3 were prepared at the same chemical conditions at pH 7.0 and 20 μM total U(VI) concentration in the presence of CO_2 as dry powder or wet paste, respectively, and were measured at ambient temperature.
The first Tikhonov solutions of the samples are shown in Fig. 48.

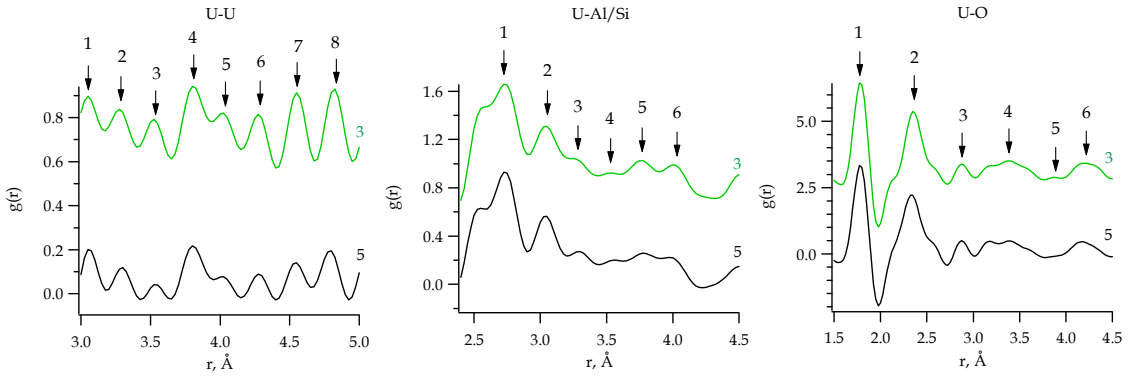

Fig. 48: First Tikhonov solutions g^1(UU), g^2(UAl/Si), and g^3(UO) for samples 3 and 5. All RDF peaks are numerated to be analyzed by the method of separating functionals.

As can be seen from Fig. 48, the first Tikhonov solutions are nearly identical for both samples. As usually, the features at ~2.70 and ~3.1 Å (peaks numbers 1 and 2 in Fig. 48, middle) are pronounced in the first Tikhonov solutions g^2(UAl/Si).
In accordance with the model calculations for soddyite, the simultaneous presence of a local minimum in g^2(UAl/Si) and a peak in g^3(UO) at ~4.23 Å is considered to be indicative for a U-U coordination shell at ~3.86 Å. Both first Tikhonov solutions g^1(UU) show a relative weak U-U contribution which is split into two discrete distances at~3.80 Å and ~4.00 Å (peak numbers 4 and 5 in Fig. 48, left).
The solutions g^3(UO) of wet (3) and dry powder (5) samples are quite similar, but the equatorial oxygen shell (peak number 2 in Fig. 48, right) of sample 5 becomes less symmetrical and shifts to a shorter distance.
In compliance with the values Λ of the separating functionals listed for the samples 3 and 5 in Tables 35 and 36, respectively, the segments of the functions g^j where "false" peaks were identified are set to zero (Table 37).
As can be seen in Fig. 49, the main contribution to EXAFS spectra of both samples is given by g^3(UO) (in Fig. right, bottom) consisting of two peaks at distances 1.79 Å and

Table 35. Sample 3. Determination of "true" and "false" RDF peaks for the Tikhonov solutions g^1(UU), g^2(UAl/Si), and g^3(UO) using the method of separating functionals.

	U		Al/Si		O	
№	r, Å	Λ	r, Å	Λ	r, Å	Λ
1	3.05*	0.87	2.73	12.59	1.78	14.86
2	3.28*	1.24	3.05	8.92	2.35	10.94
3	3.53*	0.67	3.53*	-3.22	2.88*	1.65
4	3.80	6.05	3.75	5.64	3.38*	2.46
5	4.03*	1.38	4.00	6.11	3.88*	-1.36
6	4.28	2.56			4.20*	3.92
7	4.55	6.96				
8	4.83	7.55				

* - Negative or small positive Λ values are indicative for "false" peaks.

Table 36. Sample 5. Determination of "true" and "false" RDF peaks for the Tikhonov solutions g^1(UU), g^2(UAl/Si), and g^3(UO) using the method of separating functionals.

	U		Al/Si		O	
№	r, Å	Λ	r, Å	Λ	r, Å	Λ
1	3.05*	-2.12	2.55*	-3.76	1.80	14.41
2	3.30*	-1.31	2.73	18.32	2.33	9.92
3	3.53*	-2.88	3.05	5.73	2.88*	1.52
4	3.80	1.51	3.30	-3.17	3.18*	1.33
5	4.03*	-1.96	3.55*	-4.03	3.40*	1.50
6	4.28*	-1.11	3.78*	2.02	4.18*	3.69
7	4.55*	-0.21	3.98	4.45		
8	4.80	1.22				

* - Negative or small positive Λ values are indicative for "false" peaks.

Table 37. The segments of RDFs for wet and dry powder samples where "false" peaks were identified by the method of separating functionals.

	Sample 3	Sample 5
g^1(UU)	[3.00, 3.55], [4.00, 4.025], [4.90, 6.00]	[3.00, 3.60], [4.00, 4.60], [4.90, 6.00]
g^2(UAl/Si)	[3.45, 3.60], [4.00, 6.00]	[2.40, 2.575], [3.40, 3.85], [4.00, 6.00]
g^3(UO)	[2.05, 2.10], [2.725, 6.00]	[2.725, 6.00]

2.34 – 2.32 Å with *N* equal 1.9 (O_{ax}) and 4.6 – 5.0 (O_{eq}), for 3 and 5 samples, respectively. For both samples a splitting in the O_{eq} shell was not detected, although O_{eq} of the dry powder (sample 5) displays a broad and asymmetric peak that could be caused by drying. The final g^2(UAl/Si) (Fig. 49, right, middle) shows one peak with ~0.4 Si atoms

at 3.08 – 3.07 Å in both wet and dry-powder samples. The most distant peak, which was discernible from the EXAFS data, was ~1.0 uranium atom coordinated to the central U atom at ~3.77 and ~3.90 Å. Despite some uncertainty in the U-U contribution, the U L_{III}-edge k^3-weighted EXAFS spectra calculated from RDFs agree quite well with the experimental data (Fig. 49, left).

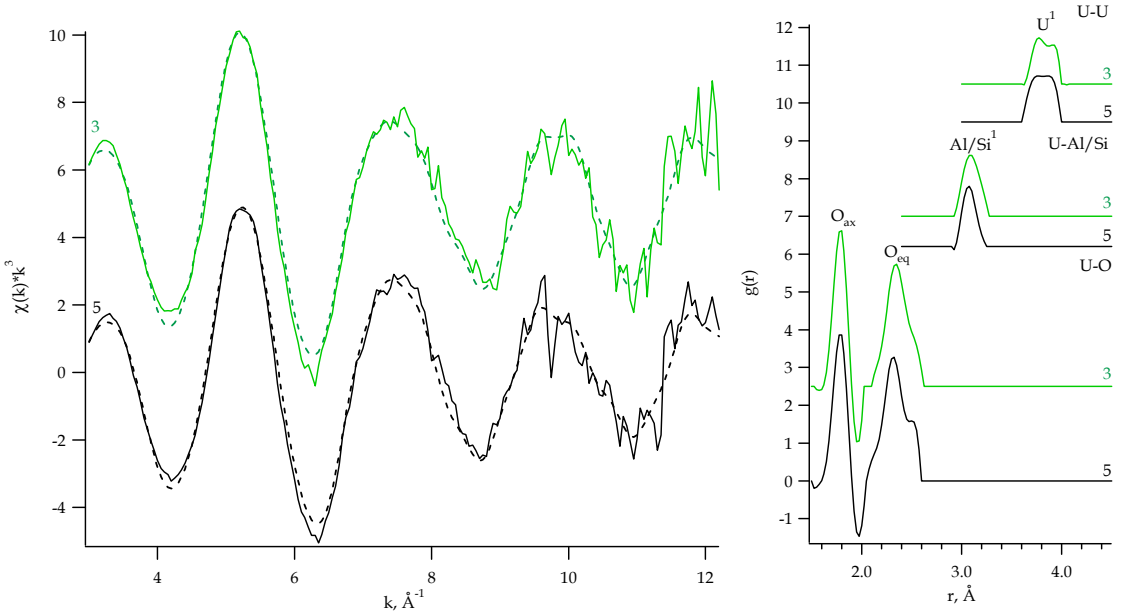

Fig. 49: U L_{III}-edge k^3-weighted EXAFS spectra (left) and calculated according to Eq. (36) final RDFs (right) for samples 3 and 5. Solid line – experimental data, dashed line – received from final RDFs.

The EXAFS structural parameters determined by the modified regularization method in comparison with those from conventional EXAFS analysis using least-squares fitting (see Appendix II) are shown in Tables 38 and 39.

Table 38. Changes of U(VI) speciation at kaolinite surface upon drying. Uranium and silicon coordination shells of the wet-paste sample 3 and the dry-powder sample 5: interatomic distances *r* and *FWHM* in Å, and coordination numbers *N* obtained by least-squares fitting (**1**) are compared to those determined by the modified Tikhonov regularization method (**2**).

Spectrum /Method			U^1			Si^1			Al/Si^2		
			r	*N*	*FWHM*	*r*	*N*	*FWHM*	*r*	*N*	*FWHM*
EXAFS	**3**	**1**	-	-	-	3.11	0.7#	0.1290#	3.32	0.5#	0.1290#
		2	3.77/3.91	0.7	0.2837	3.09	0.4	0.2106	-	-	-
	5	**1**	-	-	-	3.11	0.7#	0.1290#	3.32	0.5#	0.1290#
		2	3.77/3.89	0.8	0.3145	3.08	0.5	0.2106	-	-	-

U – Si coordination numbers were calculated with fixed at 0.0030 $Å^2$ DW factor.

The U and Al/Si coordination numbers for samples 3 and 5 derived by the modified regularization method are nearly the same (within the experimental error) as those obtained by least-squares fitting. The U-Al/Si species are fairly stabile against the drying and are indicative of inner-sphere complexation with kaolinite surface. The splitting of U^1 coordination shell for both spectra becomes evident by the analysis with the modified regularization method (see Fig. 49, right, top). The observation of a U-U interaction in the EXAFS spectra both prepared as wet paste and dry powder samples implies that the kaolinite surface species are polynuclear.

Table 39. Changes of U(VI) speciation at kaolinite surface upon drying. Uranium and silicon coordination shells of the wet-paste sample 3 and the dry-powder sample 5: interatomic distances *r* and *FWHM* in Å, and coordination numbers *N* obtained by least-squares fitting (**1**) are compared to those determined by the modified Tikhonov regularization method (**2**).

Spectrum /Method			O_{ax}			O_{eq}		
			r	*N*	*FWHM*	*r*	*N*	*FWHM*
EXAFS	**3**	**1**	1.79	2*	0.1053	2.36	5*	0.2826
		2	1.79	2.0	0.1534	2.34	4.8	0.2498
	5	**1**	1.78	2*	0.1154	2.33	5*	0.2997
		2	1.79	1.9	0.1578	2.32	5.0	0.2424

* Parameter fixed during least-squares fitting.

O_{ax} and O_{eq} coordination numbers and interatomic distances derived by both EXAFS analysis methods agree very well. As in the case of sample 11 measured at 28 K, the shortening of the O_{eq} bond distance was found for sample 5 prepared as dry powder and measured at ambient temperature.
Thus although no change in U-U or U-Al/Si coordination upon drying was observed, the shortening of the O_{eq} bond distance confirms that U(VI) cations partly lose their water coordination sphere, forming polymeric, inner-sphere complexes with the kaolinite surface at pH 7.0 and 20 μM total U(VI) concentration in the presence of CO_2.
In order to support this interpretation of the results, additional wet and dry samples prepared at different pH values should be investigated.

4.3.5 Conclusions based on calculations of U(VI) speciation at kaolinite surface

The sorption behaviour of UO_2^{2+} on the kaolinite surface has been studied in the pH range 5 – 8.5 with a total U(VI) concentration of 10 – 50 μM, and in presence and absence of CO_2. The analysis based on the modified regularization method, confirms the results of the conventional structural analysis using least-squares fitting.
The following conclusions can be drawn:

- In all cases the results indicate the presence of the linear uranyl structure UO_2^{2+}, with axial oxygen bond lengths of 1.78 – 1.80 Å. The average coordination number for the equatorial oxygen atoms, O_{eq}, is five. The average O_{eq} distance varies between 2.32 – 2.39 Å.
- At the pH 7.0 and total U(VI) concentrations of 10 – 50 μM, U(VI), forms inner-sphere surface complexes. The determined U-Al/Si interaction with one or less atom at the distance of ~3.10 Å is indicative for bidentate coordination of U(VI) with $Si(O,OH)_4$. The Al/Si distance at ~3.30 Å can be rationalized as bidentate coordination (edge-sharing) of U(VI) to $[Al(O,OH)_6]$ octahedra of kaolinite. However, these possibilities need to be investigated further, for example, by measuring the EXAFS spectra of suitable reference samples.
- For EXAFS experiments, where CO_2 was present and the total U(VI) concentration of the samples was 10 μM, U(VI) forms monomeric, inner-sphere surface complexes with kaolinite in the pH range of 5.0 – 7.0, and polymeric, inner-sphere surface complexes with kaolinite at slightly higher pH values (until 8.5).
- For EXAFS experiments, where the pH was kept at 8.5 and the total U(VI) concentration of the samples was 10 μM, U(VI) forms polymeric, inner-sphere surface complexes with kaolinite both in the absence and the presence of CO_2, that increases the capacity of kaolinite for uranium. No U-C interaction was detected by these experimental conditions in the presence of CO_2. Hence, the applied analysis methods suggest that U(VI) species formed are mostly the product of the coordination environment at the kaolinite surface, which is independent of the predominant U(VI) species in solution. The average O_{eq} bond distances of the aqueous $[UO_2(CO_3)_3]^{4-}$ complex is 2.44 ± 0.02 Å [89]. Although no U-C interaction was detected at higher pH values by both analysis methods, the observed lengthening of the O_{ax} and O_{eq} bond distances correlates with the increasing concentration of CO_3^{2-}/HCO_3^- in solution, confirming the increased importance of U(VI) surface complexes with carbonate on the kaolinite surface.
- Although the preparation conditions were identical (pH 6.0 and 10 μM total U(VI) concentration in the presence of CO_2), the sorption complexes with the kaolinite surface of wet-paste sample measured at ambient temperature and air-dried sample collected at 28 K are slightly different. The change of sorption structure is observed both in a shorter equatorial oxygen bond length and in an asymmetric equatorial shell of the air-dried sample and can be caused by drying. Besides this, both methods indicate the formation of monomeric, inner-sphere surface complexes of U(VI) with kaolinite at both ambient and low temperature.
- For ambient temperature measurements of wet-paste and dry-powder samples, no change in the U-U or U-Al/Si coordination upon drying was observed, but the shortening of the O_{eq} bond distance confirms that U(VI) cations partly lose their water

coordination sphere, forming polymeric, inner-sphere complexes with the kaolinite surface at pH 7.0 and 20 μM total U(VI) concentration in the presence of CO_2. In order to support this interpretation, more wet and dry samples at different pH values should be investigated.

The majority of these results agree very well with the conclusions of a related study of uranyl sorption by kaolinite performed by Thompson et. al. [77].

Generally, the reliability of EXAFS structural analysis for unknown structures of U(VI) sorbed onto the kaolinite surface was essentially increased as two alternative approaches for the data analysis were applied.

- ✓ In contrast to common shell-fitting routines, the proposed algorithm does not require any structural model as input.
- ✓ The moot point about the complexation of uranium atoms at silanol sites that can result in U-Si distances of ~2.70 – 3.20 Å in bidentate (edge-sharing) fashion was unambiguously decided by the modified regularization method in favour of ~3.10 Å.
- ✓ The method of separating functionals is more sensitive to U-U contribution as standard conventional structural analysis, realizing the opportunity of uranium detection also at relatively small concentrations.
- ✓ The peaks of the final RDFs are not approximated by Gaussian functions; hence, their maximums have to differ always from the average position obtained by a Gaussian distribution in least-squares fitting procedure, when the coordination shells are anisotropic, i.e., asymmetric, owing to, for example, disorder in the structure of the sorbed species.
- ✓ The possibility of visual observation of a splitting of the O_{eq} shell (that is determined in least-squares fitting procedure only by a bigger Debye-Waller factor than that associated with a single O_{eq} shell) in the final RDF g^3(UO) by the modified regularization method brings additional information about the investigated complexes, in particular for uranyl sorption to kaolinite it can be an indication of disorder in the U(VI) species.
- ✓ Also, a shortcoming of the regularization method, i.e., the interdependence of the first Tikhonov solutions, can be of beneficial use. For example, for the EXAFS data of uranyl sorption by kaolinite, the simultaneous presence of a local minimum in g^2(UAl/Si) and a peak in g^3(UO) at ~4.23 Å is considered to be indicative for a coordination U-U shell at ~3.86 Å. As also, the symmetry or asymmetry of a spurious peak in the Tikhonov solution g^2(UAl/Si) at ~2.70 Å reflects the peculiarities of the equatorial O_{eq} coordination shell.

4.4 Sorption of Pu onto kaolinite [141]

For the safety assessment and design of nuclear waste repositories, detailed studies of the migration behavior of plutonium are necessary. Its migration behavior in a potential rock formation of a repository and in the aquifer after a possible radionuclide release from the repository must be known. Besides salt and granite, clay might be a relevant host rock for which the kinetics, thermodynamics, redox behavior, and speciation of plutonium must be investigated. Since clays are an important component of many soils, the sorption of plutonium onto clay surfaces is an important factor influencing the migration of this element. Plutonium has a strong tendency to co-exist in different oxidation states, where each of them can interact differently with the clay. In this part of the study, batch experiments of Pu(III) and Pu(IV) sorption on the reference clay mineral kaolinite have been combined with Pu L_{III}-edge EXAFS spectroscopy to obtain molecular-level information that is fundamental for understanding the interaction of plutonium with the water-kaolinite interface.

4.4.1 Experimental

4.4.1.1 Batch experiments

Before preparing samples for the EXAFS measurements, the sorption of tri- and tetravalent plutonium onto kaolinite was investigated over the pH range 0-11 by batch-type experiments at Pu concentrations relevant for XAFS [142, 143]. The sorption experiments were carried out at room temperature and in the presence of light using 15 mL polypropylene screw cap centrifuge tubes. Kaolinite KGa-1b (Source Clays Repository) was suspended in de-ionized water (4 g/L). The suspension was preconditioned in 0.1 M $NaClO_4$ and shaken for 48 - 64 h. The pH was adjusted using 0.1 M $HClO_4$ or 0.1 M NaOH solutions. Then, ^{239}Pu was added to give a total concentration of 1 - 10 μM with immediate readjustment of the pH. After a contact time of 48 - 120 h, the solid and liquid phases were separated by centrifugation (2500 rpm for 1 h). The plutonium uptake by kaolinite was determined by measuring the content of free Pu ions in the liquid phase using liquid scintillation counting. The sorption studies have been performed both under aerobic and anaerobic conditions.

Fig. 50 shows the sorption of Pu(III) and Pu(IV) as a function of pH under ambient air conditions. Pu(IV) is strongly sorbed over the entire pH range with the sorption edge (50 % sorption) occurring at very acidic conditions of pH ~1. The sorption edge for Pu(III) is observed at a higher pH of ~5.5, and maximum sorption was at pH ~10. In summary, the interaction of tetravalent plutonium with kaolinite is stronger, i.e., sorption extends over a larger pH range than for Pu(III).

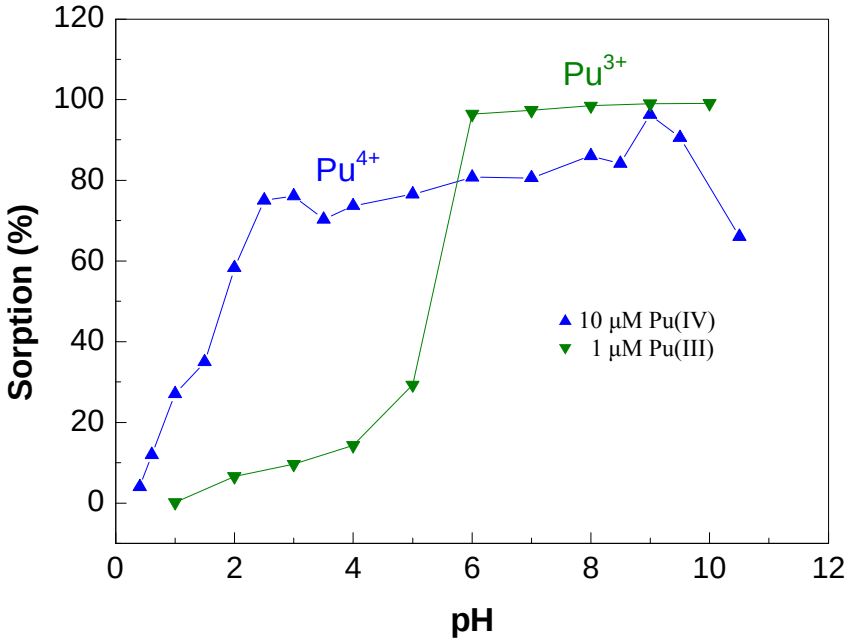

Fig. 50: Comparison of the sorption of tri- and tetravalent plutonium onto kaolinite as a function of pH; $p(CO_2) = 10^{-3.5}$ atm, 4 g/L, contact time 120 h.

4.4.1.2 EXAFS experiments and data treatment

Four samples A-D (see Table 40) were prepared with a total concentration of 10 µM ^{244}Pu following the same procedure as for the batch experiments. The Pu(IV) samples A, C, and D were air equilibrated. Sample B was prepared with Pu(III) in a glove box under argon atmosphere.

Table 40. Summary of plutonium loaded kaolinite samples examined by XAFS.

Sample	Pu	pH	Atmosphere	Pu loading (ppm)
A	IV	1	air	94
B	III	6	argon	243
C	IV	4	air	370
D	IV	9	air	412

All samples were measured as wet pastes at the Angströmquelle Karlsruhe (ANKA) at the INE beamline [144]. Plutonium L_{III}-edge XAFS data were collected in fluorescence mode at room temperature. Theoretical scattering phases and amplitudes were obtained with FEFF 8.20 [120]. An atomic cluster of 252 atoms based on the crystal structure of soddyite [48] was used to define the Hedin-Lundqvist self-energy potentials for the FEFF calculations. The automatic overlap of the self-consistent muffin-tin potentials was 1.3. Least-squares refinement of the near-neighbor surrounding of plutonium sorbed onto kaolinite was done with the EXAFSPAK

program [22] over the k ranges 2.1 ÷ 7.5 Å^{-1} for the sample A and 2.3 ÷ 9.7 Å^{-1} for samples B, C, and D, respectively.
Since it was difficult to find a unique structural model for modeling the experimental data using EXAFSPAK, the raw spectra were analyzed in addition by a modified Tikhonov regularization method [60, 61] that does not require a structural model as input.

4.4.2 Results and discussion

The plutonium oxidation state in samples A-D was identified by the corresponding Pu L_{III}-edge XANES spectra (Fig. 51, left). In all XANES spectra neither a shift in the absorption-edge energy nor a significant structural difference at the high energy side of XANES was observed, indicating that the plutonium in all samples is sorbed at the surface of kaolinite as Pu(IV). It can be concluded that the initial Pu(III) in sample B was oxidized to Pu(IV).

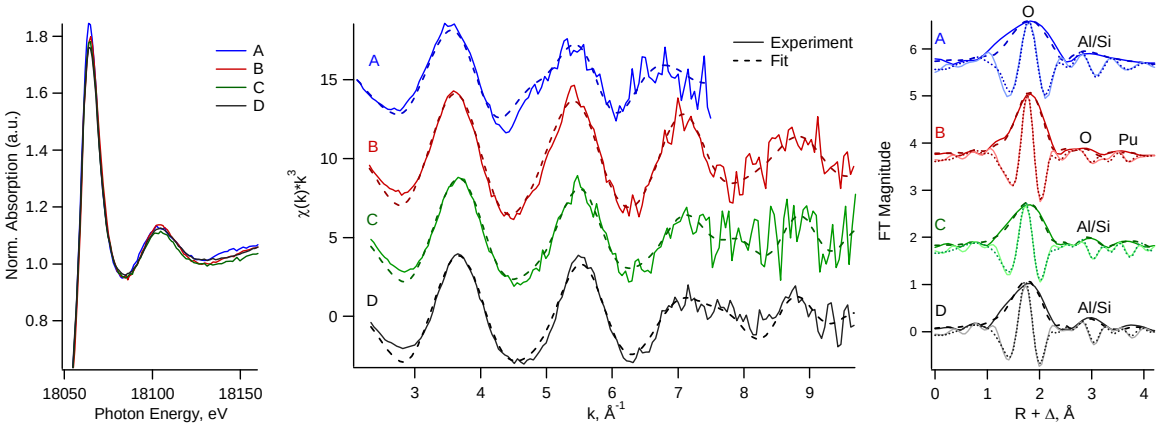

Fig. 51: Pu L_{III}-edge XANES (left) and k^3-weighted EXAFS spectra (middle) with corresponding Fourier transform magnitudes (right). Calculations were performed by non-linear least-squares fits using EXAFSPAK.

The k^3-weighted experimental EXAFS data and least-squares fits for samples A-D are shown in Fig. 51 (middle). All but one (sample A) of them show a good signal-to-noise ratio out to a k value of ~10 Å^{-1}. All spectra are dominated by a low-frequency oscillation due to the backscattering from the nearest oxygen atoms. The EXAFS spectra of samples A, C, and D are very similar. Sample B shows a different EXAFS pattern, in particular in the k range 6 - 8 Å^{-1}. The Fourier transform (FT) of the EXAFS spectra (Fig. 51, right) represents a pseudo radial distribution function of the plutonium near-neighbor surrounding. The most prominent peak in all spectra is at ~1.8 Å (uncorrected for phase shift) and arises from the backscattering caused by eight oxygen atoms coordinated to Pu(IV). A Pu-Pu interaction at ~3.7 Å with two plutonium atoms is observed in all spectra, indicating the formation of polynuclear

plutonium species at the kaolinite surface. In addition to the Pu-O and Pu-Pu coordination shells, a third shell at an intermediate distance had to be included in all fits. The best fit to the data of samples A, C, and D, which were prepared with $1x10^{-5}$ M Pu(IV), was obtained with a Pu-Al/Si coordination shell at 3.6 – 3.7 Å. In case of sample B, a second Pu-O shell at 3.25 ± 0.02 Å had to be included in the shell fit. The metrical parameters for samples A-D are given in Table 41.

Table 41. Results of least-squares refinement. The coordination numbers were fixed. Distances *r* to Pu neighbors are in Å (± 0.02 Å). Debye-Waller factors σ^2 are in Å^2 (± 0.004 Å^2).

	8 x O_1		2 x O_2		2 x Al/Si		2 x Pu	
	r	σ^2	*r*	σ^2	*r*	σ^2	*r*	σ^2
A	2.34	0.0212	-	-	3.66	0.0054	3.70	0.0080
B	2.31	0.0110	3.25	0.0070	-	-	3.70	0.0150
C	2.28	0.0169	-	-	3.62	0.0091	3.69	0.0076
D	2.27	0.0154	-	-	3.62	0.0050	3.68	0.0145

To increase the reliability of the structural analysis by least-squares fitting, the EXAFS analysis of samples B and C was repeated using the modified regularization method described before. Interatomic distances and corresponding coordination numbers were derived from the position of the maximum and the area, respectively, of the RDF peaks displayed in Figs. 52 and 53. The following results were obtained: The RDF *g*(Pu-O) for sample B has one peak corresponding to ~8 oxygen atoms centered at 2.32 Å followed by a broad peak ranging from 2.6 - 3.5 Å with ~9 oxygen atoms (Fig. 52, left). The RDF *g*(Pu–Pu) exhibits a single peak originating from one plutonium atom at 3.69 Å (Fig. 52, right). No Pu-Al/Si interaction was detected for sample B. Sample C is similar to sample B in that the RDFs in Fig. 53 show a peak of ~8 oxygen atoms at 2.28 Å and a peak of ~2 plutonium atoms at 3.65 Å, respectively. However, instead of a second oxygen peak as observed for sample B, *g*(Pu-Al/Si) of sample C has one peak of ~2 Al/Si atoms centered at 3.60 Å.

The results of the two alternative EXAFS analysis methods for samples B and C are given in Table 42. This comparison shows that the corresponding $g_j(r)$, which were calculated by the modified Tikhonov regularization method without assuming any structural model, agree within the experimental errors with the results from the least-squares refinement. The only significant difference is the coordination number for the second oxygen shell of sample B. The least-squares refinement assuming a Gaussian distribution resulted in two oxygen atoms at 3.25 Å (Table 42). In contrast, the modified Tikhonov regularization gave a broad distribution in the range of 2.6 - 3.5 Å (Fig. 52, left) with a peak area corresponding to nine atoms. Such a distribution cannot

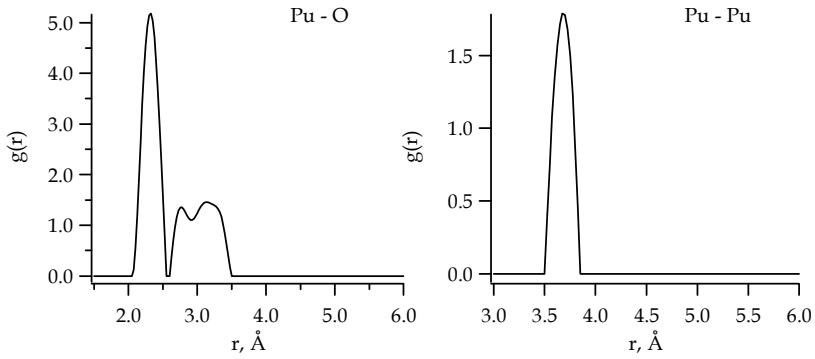

Fig. 52: Partial radial distribution functions *g(r)* for sample B. *g*(Pu-Si) is not shown since no Pu-Al/Si interaction was detected by the method of separating functionals.

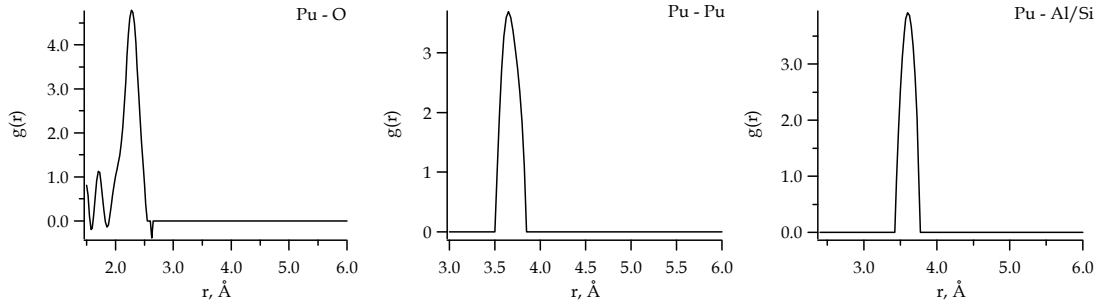

Fig. 53: Partial radial distribution functions *g(r)* for sample C.

Table 42. EXAFS structural parameters of Pu sorbed onto kaolinite. Method 1: least-squares refinement; method 2: modified Tikhonov regularization.
(*r* - distance in Å, *N* - coordination number, * - fixed values).

Sample	Method	O_1		O_2		Si		Pu	
		r	*N*	*r*	*N*	*r*	*N*	*r*	*N*
B	1	2.31	8*	3.25	2*	-	-	3.70	2*
	2	2.32	7.8	2.6 ÷ 3.5	9.2	-	-	3.69	0.8
C	1	2.28	8*	-	-	3.62	2*	3.69	2*
	2	2.28	7.5	-	-	3.60	1.7	3.65	1.6

be modeled by a single Gaussian peak. Therefore, the difference in the Pu-O coordination number could be caused by the limitation imposed by the structural model used for the least-squares refinement.

In summary, the sorption mechanism for samples A, C, and D can be rationalized by an inner-sphere sorption of polynuclear Pu(IV) species at the kaolinite surface. The EXAFS spectrum of sample B prepared from Pu(III) under argon atmosphere resulted in Pu(IV) at the kaolinite surface, but did not show indication of inner-sphere sorption

since no Pu-Al/Si interaction was observed. The Pu(IV) in sample B has a Pu-O interaction at 3.25 Å instead. Similar Pu-O distances were observed for Pu(IV) colloids [145]. The cause of the detected structural differences of sample B compared to samples A, C, and D, and the reason for the oxidation of Pu(III) to Pu(IV) are the subject of additional EXAFS measurements on new samples.

5. CONCLUSIONS AND OUTLOOK

To determine metrical parameters for the near-neighbor surrounding of an absorbing atom, it is common to perform least-squares fits to experimental EXAFS spectra using structural models. The model that approximates the unknown structure consists of one or several coordination shells of different backscattering atoms. It is sometimes difficult to find a unique model for shell fitting if little is known about the local atomic surroundings in the sample.

The relative positions of different pairs of atoms in a sample can be described by partial radial distribution functions (RDFs). Instead of trying to find the best structural model that fits the data, the RDFs are determined from the EXAFS spectrum directly by solving a system of Fredholm integral equations of the first kind.

A significant problem in determining the correct element speciation in complex environmental systems is the non unique solution of the EXAFS equation, which leads to an interdependence of the obtained RDFs. Although this is a formidable task and far from complete, the procedure for the determination of RDFs developed and investigated in this Ph. D. project so far has been surprisingly successful.

The results can be divided into two categories. The first contains the development of the Tikhonov regularization method for the analysis of EXAFS spectra of multi-component systems, including some important recommendations such as the choice of regularization parameters or the influence of multi-scattering contributions, experimental data noise, etc. on the derived structural parameters (i.e., *r, N,* σ^2). The second category includes the speciation of U(VI) and Pu(III)/Pu(IV) sorbed onto kaolinite, based on experimental EXAFS spectra, which were analyzed by the modified regularization method, and confirmed by the results of the conventional EXAFS analysis by means of least-squares fitting.

Generally, for the first category:

- The proposed algorithm for the determination of RDFs consists of the following steps: variation Tikhonov method, application of separating functionals, and iteration method with filtration in real space.
- In contrast to common shell-fitting routines, the developed algorithm does not require any structural model as input.
- The experimental EXAFS spectrum can be analyzed successfully if the standard Tikhonov regularization method is applied to intervals of the RDF were "true" peaks have been identified.
- The method of separating functionals allows the determination of intervals in the RDFs where "true" peaks are absent.

On the basis of the analysis of model and experimental soddyite EXAFS spectra using the modified regularization method, the following conclusions can be drawn:

- The known multiple-scattering contributions to EXAFS spectra, as for example MS caused by the linear UO_2^{2+} moiety in uranyl containing materials, should be subtracted from the raw data prior to the analysis by the modified regularization method.
- The first Tikhonov solutions simulated with the $\alpha^j = 10^{-18}$ reproduce the model RDFs with very good accuracy. In this case the standard variation Tikhonov method is necessary and sufficient to receive the final RDFs solutions.
- The error level of the experimental data significantly affects the values of regularization parameters. Recommended "initial" regularization parameters for the treatment of experimental data were found to be from 10^{-5} to 10^{-7}. With such parameters the first Tikhonov solutions can predict the locations of radial distribution peaks, but are not able to reconstruct the RDFs quantitatively.
- The method of separating functionals has a good efficiency to analyze whether a peak in the function g^j is true" or "false", if each atom j of the investigated system has district scattering parameters in operator A^j (Eq. (35)), generally different backscattering phases.
- The quality of the scattering characteristics calculated by the program FEFF 8.20 can affect the results of the separating functional analysis dramatically.
- The proposed solution to the problem of determining the regularization parameters is to obtain one "initial" regularization parameter and make the other parameters proportional to it. While the "initial" regularization parameter is attributed to the matrix operator A^j and the noise level in raw EXAFS data, it is recommended to determine the "initial" regularization parameter in model calculations before applying it to experimental data.
- As a combination of all three steps the modified regularization method has a very good efficiency for the determination of g^j functions, i.e., variation Tikhonov method, application of separating functionals, and the iteration method with filtration in real space.

⇛ Basically, the calculations for soddyite show the ability of the modified regularization method to receive reasonable structure parameters (i.e., *r, N,* σ^2) in multi-component systems without any starting model.

As appears from the modified regularization analysis of experimental EXAFS spectra of U(VI) sorbed on kaolinite :

- The results of the analysis using the method of separating functionals have to be consistent among a series of data (if a series exist).

- The peaks of the final RDFs are not approximated by Gaussian functions; hence, their maximums have to differ always from the average position obtained by a Gaussian distribution in least-squares fitting procedure, when the coordination shells are anisotropic, i.e., asymmetric, owing to, for example, disorder in the structure of the sorbed species.

Between categories one and two are the several results that are possible to receive only by modified regularization method but which are related to the U(VI) speciation on kaolinite:

- The method of separating functionals is more sensitive to U-U contribution as standard conventional structural analysis, realizing the opportunity of uranium detection also at relatively small concentrations.
- The moot point about the complexation of uranium atoms at silanol sites that can result in U-Si distances of ~2.70 – 3.20 Å in bidentate (edge-sharing) fashion was unambiguously decided by the modified regularization method in favour of ~3.10 Å.
- The possibility of visual observation of a splitting of the O_{eq} shell (that is determined in least-squares fitting procedure only by a bigger Debye-Waller factor than that associated with a single O_{eq} shell) in the final RDF g^3(UO) by the modified regularization method brings additional information about the investigated complexes, in particular for uranyl sorption to kaolinite it can be an indication of disorder in the U(VI) species.
- Also, a shortcoming of the regularization method, i.e., the interdependence of the first Tikhonov solutions, can be of beneficial use. For example, for the EXAFS data of uranyl sorption by kaolinite, the simultaneous presence of a local minimum in g^2(UAl/Si) and a peak in g^3(UO) at ~4.23 Å is considered to be indicative for a coordination U-U shell at ~3.86 Å. As also, the symmetry or asymmetry of a spurious peak in the Tikhonov solution g^2(UAl/Si) at ~2.70 Å reflects the peculiarities of the equatorial O_{eq} coordination shell.

Concerning the second category of results, adsorption behaviours of UO_2^{2+} on kaolinite surface have been studied within the pH range 5 - 8.5 with total U(VI) concentration of 10 - 50 μM, and in presence or absence of CO_2.

On the basis of the regularization analysis of experimental EXAFS spectra, confirmed by the results of the conventional structural analysis means least-squares fitting, the following findings are noted:

- In all cases the results indicate the presence of the linear uranyl structure UO_2^{2+}, with axial oxygen bond lengths of 1.78 – 1.80 Å. The average

- At the pH 7.0 and total U(VI) concentrations of 10 – 50 μM, U(VI), forms inner-sphere surface complexes. The determined U-Al/Si interaction with one or less atom at the distance of ~3.10 Å is indicative for bidentate coordination of U(VI) with $Si(O,OH)_4$. The Al/Si distance at ~3.30 Å can be rationalized as bidentate coordination (edge-sharing) of U(VI) to $[Al(O,OH)_6]$ octahedra of kaolinite. However, these possibilities need to be investigated further, for example, by measuring the EXAFS spectra of suitable reference samples.
- For EXAFS experiments, where CO_2 was present and the total U(VI) concentration of the samples was 10 μM, U(VI) forms monomeric, inner-sphere surface complexes with kaolinite in the pH range of 5.0 – 7.0, and polymeric, inner-sphere surface complexes with kaolinite at slightly higher pH values (until 8.5).
- For EXAFS experiments, where the pH was kept at 8.5 and the total U(VI) concentration of the samples was 10 μM, U(VI) forms polymeric, inner-sphere surface complexes with kaolinite both in the absence and the presence of CO_2, that increases the capacity of kaolinite for uranium. No U-C interaction was detected by these experimental conditions in the presence of CO_2. Hence, the applied analysis methods suggest that U(VI) species formed are mostly the product of the coordination environment at the kaolinite surface, which is independent of the predominant U(VI) species in solution. The average O_{eq} bond distances of the aqueous $[UO_2(CO_3)_3]^{4-}$ complex is 2.44 ± 0.02 Å [89]. Although no U-C interaction was detected at higher pH values by both analysis methods, the observed lengthening of the O_{ax} and O_{eq} bond distances correlates with the increasing concentration of CO_3^{2-}/HCO_3^- in solution, confirming the increased importance of U(VI) surface complexes with carbonate on the kaolinite surface.
- Although the preparation conditions were identical (pH 6.0 and 10 μM total U(VI) concentration in the presence of CO_2), the sorption complexes with the kaolinite surface of wet-paste sample measured at ambient temperature and air-dried sample collected at 28 K are slightly different. The change of sorption structure is observed both in a shorter equatorial oxygen bond length and in an asymmetric equatorial shell of the air-dried sample and can be caused by drying. Besides this, both methods indicate the formation of monomeric, inner-sphere surface complexes of U(VI) with kaolinite at both ambient and low temperature.
- For ambient temperature measurements of wet-paste and dry-powder samples, no change in the U-U or U-Al/Si coordination upon drying was observed, but

the shortening of the O_{eq} bond distance confirms that U(VI) cations partly lose their water coordination sphere, forming polymeric, inner-sphere complexes with the kaolinite surface at pH 7.0 and 20 µM total U(VI) concentration in the presence of CO_2. In order to support this interpretation, more wet and dry samples at different pH values should be investigated.

The majority of these results agree very well with the conclusions of a related study of uranyl sorption by kaolinite performed by Thompson et. al. [77].

The uptake mechanism of plutonium by kaolinite was investigated by applying X-ray absorption spectroscopy to batch sorption samples (total Pu concentrations 1 and 10 µM; 4 g kaolinite/L in 0.1 M $NaClO_4$; $1 \leq pH \leq 9$; presence and absence of ambient CO_2). For XAFS measurements, one sample was prepared from a Pu(III) solution at pH 6 under argon atmosphere. Three samples were obtained by sorption of Pu(IV) at pH 1, 4, and 9 in an air-equilibrated system.

The results of the two alternative EXAFS analysis methods are following:

- The Pu L_{III}-edge XANES spectra indicated that in all samples, including the Pu(III) sample, plutonium is sorbed at the kaolinite surface as Pu(IV).
- The Pu L_{III}-edge k^3-weighted EXAFS spectra showed eight oxygen atoms at an average Pu-O distance of 2.3 Å.
- Two Pu atoms were detected at ~3.7 Å in all spectra, indicating the formation of polynuclear Pu(IV) species at the kaolinite surface.
- For the sample prepared from Pu(III) solution, an additional Pu-O shell at 3.2 Å was observed. Similar Pu-O distances were observed for Pu(IV) colloids [145].
- The spectra of samples prepared from Pu(IV) included a Pu-Al/Si coordination shell at approximately 3.6 Å, indicating formation of inner-sphere sorption complexes.

⇛ Generally, the reliability of EXAFS structural analysis for both unknown structures of U(VI) and Pu sorbed onto the kaolinite surface was essentially increased as two alternative approaches for the data analysis were applied.

This dissertation has been devoted to demonstrate the still not fully exploited potential of the modified regularization method for the evaluation of EXAFS data. In the presence, the most troubling and difficult aspect of the application of the regularization method is the suitable choice of the regularization parameter. It depends not just on the peculiarities of the matrix operator A^j, but also significantly on the noise level in raw experimental EXAFS data. Indeed, much work along this line is currently in progress. In the future more information on the coordination of a heavy metal could perhaps be received by a more sophisticated analysis of the asymmetry of peaks observed in several RDFs, for example, in the equatorial coordination shell of RDF g^3(UO). Such

asymmetric peaks could indicate an asymmetric distribution of bond lengths in a coordination shell, which are too close in distance to be resolved as separate peaks in the RDF.

The cause of the detected structural differences of the sample prepared from Pu(III) compared to the samples prepared from Pu(IV), and the reason for the oxidation of Pu(III) to Pu(IV) are the subject of additional EXAFS measurements on new samples.

The implementation of a more sophisticated "initial" regularization parameter, the interpretation of a possible asymmetric distribution of bond distances of a given coordination shell, and the further development of the software suggest that the modified regularization method will continue to improve. The modified method is yet far from perfect, but it has successfully captured fundamental aspects of EXAFS and does not need an input model. It is therefore a very useful tool for direct speciation of elements in a wide range of environmentally relevant systems.

APPENDIX I: SODDYITE-DATA ACQUISITON AND LEAST-SQUARES FITTING

General Information about Soddyite

Soddyite

Chemical Formula:	$(UO_2)_2SiO_4 \times 2H_2O$		
Composition:	Molecular Weight = 668.17 g/mol		
	Uranium	71.25 % U	80.83 % UO_2
	Silicon	4.20 % Si	8.99 % SiO_2
	Hydrogen	0.60 % H	5.39 % H_2O
	Oxygen	23.95 % O	
		100.00 %	95.21 %
			TOTAL OXIDE
Environment:	Mixed with curite in oxidized uranium ores.		
Locality:	Shinkolobwe; Democratic Republic of the Congo (Zaire); South Australia; Canada; Czech Republic; France; Germany; USA.		
Name Origin:	Named for Frederick Soddy (1877-1956), British radiochemist and physicist.		
Year of Discovery:	1922		
Synonyms:	ICSD 66313, PDF 35-491, Soddyit, Soddyita		

Crystallography of Soddyite

Cell Dimensions:	a = 8.32 Å, b = 11.21 Å, c = 18.71 Å, Z = 8;
	V = 1,745.03 $Å^3$ (Calculated from Unit Cell)
Crystal System:	Orthorhombic – Dipyramidal
	Space Group: Fddd

Physical Properties of Soddyite

Colour:	Yellow, Canary yellow, Yellowish green, Yellow.
Density:	Experimental value 4.627 g/cm^3 / 0.0709At/$Å^3$
	Calculated from the crystal structure 5.09 g/cm^3 / 0.0780At/$Å^3$
Habits:	Prismatic - Crystals Shaped like Slender Prisms (e.g. tourmaline).
	Striated - Parallel lines on crystal surface or cleavage face.
	Pyramidal - Crystals are shaped like pyramids.
Luminescence:	Fluorescent and radioactive.
Luster:	Vitreous (Glassy)

Data bank of soddyite U L_{III}-edge EXAFS data (Table 1+)

Table 1+. EXAFS data examined in this work

Data set	Raw File name	Sweeps	Conditions/ Comments
HASYLAB Okt.1994 Soddyite Synthesized product	FZR239.RM FZR240.RM FZR241.RM	- - -	Reich/Moll [118] Room Temp. Pressed in Carbowax 31.9 mg U/ 400 mg Carbowax
U0-9 ESRF March 2000 Soddyite Synthesized product	FZR_0300_60	.00 .01	Reich/Moll [118] T = 15K Pressed in Teflon 25.5 mg U/ 400 mg Teflon Reference: Y K-edge
U0-24 ESRF March 2000 Apparatus function	FZR_0300_115	.00	Funke Room Temp. 350mg Teflon Reference: Y K-edge

Data processing

Data processing includes the steps needed to reduce the raw experimental data to the normalized EXAFS data for analysis:

1. Energy scale (re-calibration of the energy scale by reading standard data from a raw XAS file)
2. The averaging of the raw XAS data
3. Smoothing and removal of the apparatus function
4. Pre-edge and post-edge background removal
5. Data normalization
6. EXAFS in *k* space

Energy scale

Uranium L_{III}-edge EXAFS spectra of synthetic soddyite were collected in transmission mode at room temperature at the Hamburger Synchrotronstrahlungslabor HASYLAB [119] and at 15 K at the Rossendorf Beamline (ROBL) at ESRF, Grenoble [5]. The photon energy of the sample measured at 15 K at the ESRF was calibrated using the K-edge (17038 eV) energy of a Y foil standard with the help of program EXAFSPAK [22].

The averaging of the raw XAS data

The program MAVE (EXAFSPAK) has generated an averaged soddyite data file.

Removal of the apparatus function

For EXAFS measurements, synthetic crystalline $(UO_2)_2SiO_4$ x $2H_2O$ powder was mixed with an inert material (carbowax and Teflon for room temperature and 15 K measurements, respectively) and pressed into a pellet. The apparatus function was determined only for the measurement at 15 K by collecting the X-ray absorption spectrum of a Teflon pellet in the energy range of the U L_{III}-edge spectrum. The noise in the apparatus function data taken "quickly" at synchrotron source ESRF was removed before further processing. The data was fitted with a polynomial of fifth order and then interpolated through the distinctive region.

The transmission spectrum of the 15 K sample is obtained as $\ln\left(\frac{I_0}{I_1}\right)$,

the spectrum of the Teflon matrix is given as $\ln\left(\frac{I_0}{I_2}\right)$.

The actual absorption signal without apparatus function according to the Beer-Lambert Law is $I_1=(I-I_0)e^{-\mu x}$,

i.e., the absorption coefficient is presented as: $\mu(E)x=\ln\left(\frac{I_0}{I_1}\right)-\ln\left(\frac{I_0}{I_2}\right)$.

Pre-edge and post-edge background removal

Spline fitting was performed using the AUTOBK [23] program. AUTOBK parameters for samples at 15 K and room temperature are in Tables 2+, 3+, respectively. Fig. 1+ shows the measured soddyite absorption spectra $\mu(E)$ at the uranium L_{III}–edge together with the post-edge background. The EXAFS data were then extracted to be analyzed either by the modified regularization method shown in Sec. 4.2 of this work or by non-linear least-squares fitting described below.

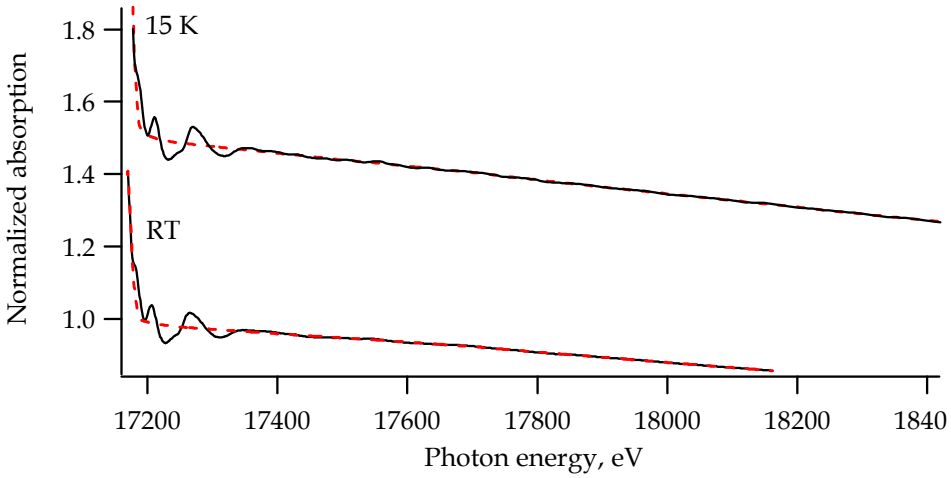

Fig. 1+: Absorption spectra collected at 15 K and ambient temperature in transmission mode at the U L_{III}-edge of soddyite $(UO_2)_2SiO_4$ x $2H_2O$. Solid black line represents the experimental data and dashed red line post-edge background absorption in energy region of white line and above.

Table 2+. AUTOBK parameters for 15 K soddyite spectrum.

%----------% autobk.inp %----------%
title = soddyite 15 K, with standard χ(k)
data = sd15.frm
standart = chi_standsod.dat
fixamp = true % fix amp of standard
output = sod_158.frm
E0 = 17173.4 fixE0 = true % don't fit E0
%----------% end of autobk.inp %----------%
---------- automatic background removal----------
soddyite 15 K, with standard χ(k)
---
input xmu data file name and skey: sd15.frm ASCII
---
input theory chi file name and skey: chi_standsod.dat ASCII
first document line: $(UO_2)_2(SiO_4)$ x $2H_2O$ U_{III}-edge Acta Cryst. C48 1992
--------fitting parameters---------
e0 fixed at = 17173.400000
pre-edge range = -200.000000 -50.000000
pre-edge line = 0.620058E-05 * Energy + -0.105749E+00
edge step = 0.999324
post-edge curve for edge_step = 0.712522E+01 + -0.524638E-03 * Energy
+ -0.524638E-03 * Energy^2
energy range = 17172.955100 18420.136700
k range = 0.000000 18.050000
k weight = 1.000000
fourier transform window:
sills: dk1, dk2 = 0.000000 0.000000
# of knots in spline = 11
background r range = 0.000000 0.981748
the theory was scaled by = 1.000000
1st shell r range = 0.981748 2.975923

Table 3+. AUTOBK parameters for room temperature soddyite spectrum.

```
%------------------%    autobk.inp    %-------------------%
 title    = soddyite RT, with standard  χ(k)
 data     = sdhspr.dat
 standart = chi_standsod.dat
 fixamp   = true                        % fix amp of standard
 rbkg     = 0.88
 Emin     = 6
  %------------------% end of autobk.inp %-------------------%
---------------------- automatic background removal-----------------------
 soddyite RT, with standard  χ(k)
  ----------------------------------
  input xmu data file name and skey: sdhspr.dat  ASCII
  ----------------------------------
  input theory chi file name and skey: chi_standsod.dat  ASCII
  first document line: (UO2)2(SiO4) x 2H2O UIII-edge Acta Cryst. C48 1992
  ----------------------------------
  --------fitting parameters---------
  E0 fixed at              =    17166.000000
  pre-edge range           =     -200.000000     -50.000000
  pre-edge line            =   0.531125E-04 * Energy + -0.903897E+00
  edge step                =    0.981144
  post-edge curve for edge_step =  0.164973E+02 + -0.166673E-02 * Energy
                + -0.166673E-02  * Energy^2
  energy range             =    17172.000000    18162.000000
  k range                  =       1.250000      16.150000
  k weight                 =       1.000000
  fourier transform window:
  sills: dk1, dk2          =       0.000000       0.000000
  # of knots in spline     =    9
  background r range       =       0.000000       0.859029
  the theory was scaled by  =      1.000000
  1st shell r range        =       0.859029       2.975923
  ---------------------------------------------------------------------
```

EXAFS Data Analysis

Theoretical scattering phases and amplitudes were obtained with FEFF8.2 [120]. The atomic cluster of 252 atoms based on the crystal structure of soddyite [48] was used to define the Hedin-Lundqvist self-energy potentials for the FEFF calculations. Self-consistent muffin-tin potentials were automatically overlapped to the value of 1.3.

Least-squares refinement of the soddyite structure was done with OPT (EXAFSPAK) program over the k ranges of $3.50 \div 16.2$ Å^{-1} and $3.0 \div 12.2$ Å^{-1} for 15 K and room temperature soddyite, respectively. All of the interactions were modeled using single scattering (SS) and multiple scattering (MS) paths derived from the model crystal compound $(UO_2)_2SiO_4$ x $2H_2O$. A total of nine paths were employed: SS UO_{ax} (axial), SS UO_{eq} (equatorial), two SS USi shells, three SS UU shells, four-legged MS UO_{ax_1}-UO_{ax_2}, and three-legged MS U-Si-O_{eq}. To avoid that the number of degrees of freedom (Eq. (17)) was greater than the number of parameters allowed to vary in the fitting process, coordination numbers (N) were fixed to crystallographic values, ΔE_0 (the difference between the threshold Fermi level of theoretical phase shift and backscattering amplitude functions and the experimental data) was allowed to vary only as a global parameter for each of the fits (i.e., the same ΔE_0 was used for each shell), and the amplitude reduction factor S_0^2 was fixed to 1.0 to be in accordance with the FEFF calculations. Since the interatomic distances (r) and Debye-Waller factors (σ^2) for SS paths were allowed to float during the non-linear least-squares routine, the parameters of the MS paths were directly linked to the corresponding values of the SS contributions.

Fig. 2+ demonstrates one of the main difficulties in the analysis of the EXAFS data of soddyite by non-linear least-squares fitting. In particular, the figure presents the fit error that was examined as a function of the interatomic distance versus the Debye-Waller factors for the first Si coordination shell. As can be seen, the first Si coordination shell can be placed with equal probability either at a distance of ~2.70 Å or at ~3.15 Å. Both structural models describe the experimental EXAFS data equally well.

Why these two minimums co-exist, is discussed in all details in Sec. 4.2 of this work. This is just one example showing that without knowing some *a priori* information about the structure of soddyite or experience in EXAFS data least-squares fitting, it is quite easy to make mistakes in the structure determination. To be consistent with the structural results obtained previously by XRD [48] for soddyite, in this work as also in [107] the minimum corresponding to the Si shell at 3.15 Å was used. Fig. 3+ shows the raw U L_{III}-edge k^3-weighted EXAFS spectra and curve fits with corresponding Fourier transformations (FT). The FT represents a pseudo radial distribution function, and the

peaks are shifted to lower *r* values as a result of the phase shift associated with U absorber–U, Si, O scatterer interactions (~0.5 Å).

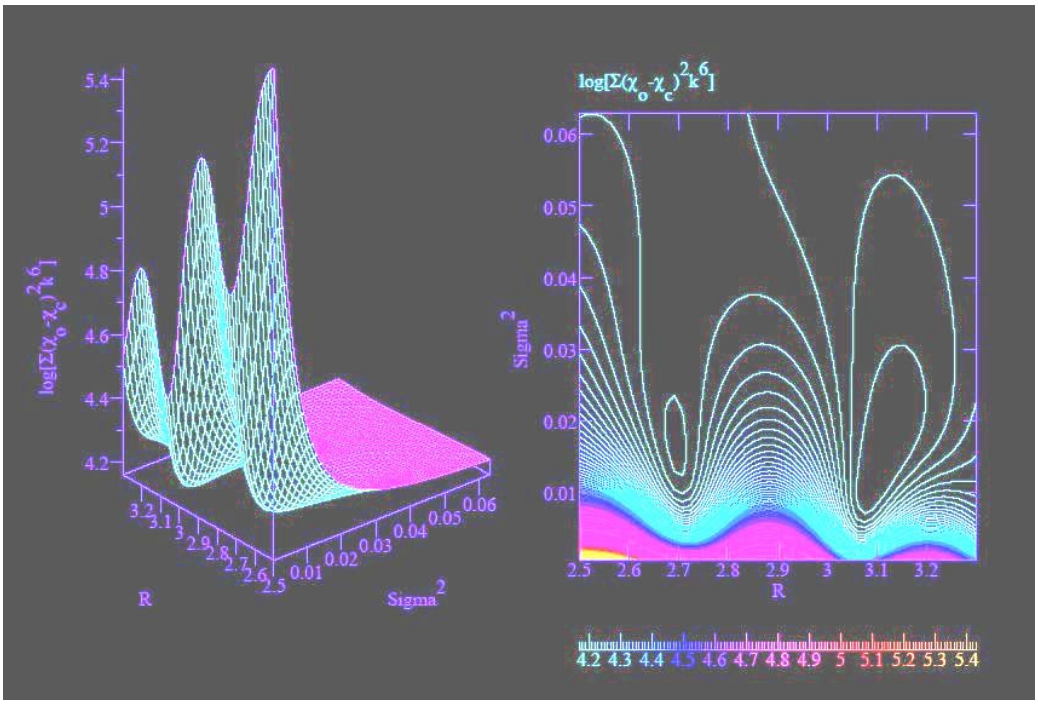

Fig. 2+: Search profile showing the inability of the least-square fitting to distinguish between two minimums found by curve fitting for the U-Si interaction in the EXAFS spectrum of soddyite.

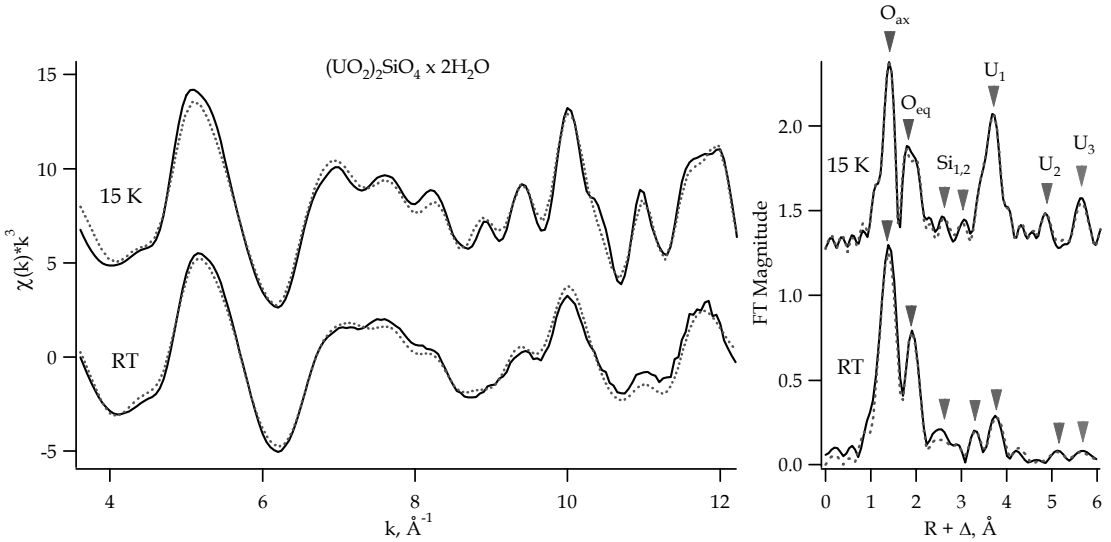

Fig. 3+: U L_{III}-edge k^3-weighted EXAFS spectra (left) and corresponding Fourier transform magnitudes of soddyite samples. Solid lines – experimental data, dashed lines – fits.

The structural results ($N, r, FWHM$) of least-squares fitting determined from the SS shells contributions in both experimental soddyite spectra are summarized in Tables 12 and 13 in Sec. 4.2 of this work.

APPENDIX II: SORPTION OF U(VI) ONTO KAOLINITE-DATA ACQUISITON

General Information about Kaolinite

Kaolinite

Chemical Formula: $Al_2Si_2O_5(OH)_4$

Composition: Molecular Weight = 258.16 g/mol

Aluminium	20.90 %	Al	39.50 %	Al_2O_3
Silicon	21.76 %	Si	46.55 %	SiO_2
Hydrogen	1.56 %	H	13.96 %	H_2O
Oxygen	55.78 %	O		
	100.00 %		100.00 %	TOTAL OXIDE

Environment: Secondary mineral derived from the weathering of alumino-silicate minerals.

Locality: Kao-Ling (China); Morro do Felipe, de Mazagao, Amapá (Brazil); Germany; Russia; Keokuk, Iowa, Georgia (USA).

Name Origin: Named after the locality in China.

Year of Discovery: 1867

Synonyms: Ancudit, China Clay, Caolinite, Kaolin, Fireclay, Pholerit, Porcelain Clay, Myelin, Collyrinum, Creniadit.

Crystallography of Kaolinite

Cell Dimensions: a = 5.14 Å, b = 8.93 Å, c = 7.37 Å, Z = 2;
$\alpha = 91.8°$, $\beta = 104.5°$, $\gamma = 90.016°$,
V = 327.35 $Å^3$ (Calculated from Unit Cell)

Crystal System: Triclinic – Pedial
Space Group: P1

Physical Properties of Kaolinite

Colour: White to cream and pale-yellow, also often stained various hues, tans and browns being common.

Density: Calculated from the crystal structure 2.60 g/cm^3 / 0.1034 $At/Å^3$

Habits: Earthy – Dull, clay-like texture with no visible crystalline affinities.

Luminescence: None and not radioactive.

Luster: Earthy (Dull)

Samples Preparation

Samples with 1 or 10 μM of ^{238}U(VI) sorbed on kaolinite were prepared in suspensions of 200 mg kaolinite KGa-1b (Source Clays Repository) in 50 mL deionised water. The ionic strength was 0.1 M $NaClO_4$. The pH was adjusted to the values given in Table 14 (Sect. 4.3) using NaOH and $HClO_4$. The uranyl uptake experiments were carried out in a glove box under Ar atmosphere or at $p(CO_2) = 10^{-3.5}$ atm. After shaking the kaolinite suspensions for 72 h, aliquots of U(VI) stock solutions were added with immediate pH readjustment. The total U(VI) concentrations are given in Table 14 (Sect. 4.3). After a contact time of 72 h, the solid and liquid phases were separated by centrifugation. The U(VI) uptake (Table 14 in Sect. 4.3) was determined by measuring the U(VI) concentration in solution using liquid scintillation counting. All but samples 5 and 11 solid residues were loaded without drying into EXAFS sample holders.

EXAFS Data Analysis

The reduction of raw fluorescence spectra of sorption samples to the normalized EXAFS data was done as described in Appendix I and not shown here. FEFF8.20 [120] calculations were performed with the same cluster and control cards as for soddyite.
EXAFSPAK [22] standard procedures were used for the EXAFS spectra analysis by conventional shell fitting. Fits were performed in *k* range of 3.0 ÷ 12.2 Å^{-1}. The scaling factor, S_0^2 , was set to 1.0. Maximum of six paths (depending on the total U(VI) concentration, pH values or CO_2 presence) were employed in EXAFS analysis: SS UO_{ax} (axial), SS UO_{eq} (equatorial), two SS USi shells, one SS UU shell, and four-legged MS U O_{ax_1} – UO_{ax_2}. To avoid that the number of degrees of freedom (Eq. (17)) was greater than the number of parameters allowed to vary in fitting process, O_{ax} and O_{eq} coordination numbers were fixed to 2.0 and 5.0, correspondingly (because the first one was known from numerous uranyl compounds EXAFS treatment and the second was only slightly varied around 5.0 in the preliminary fits without constrained parameters). ΔE_0 was allowed to vary only as a global parameter for each of the fits. The balance between coordination numbers (N) and Debye-Waller factors (σ^2) necessary for every shell varied depending on the fitting strategy, i.e., either σ^2 or N were kept constant. Among the samples, parameters can only be compared within a single strategy, of course. Since the subject of interest was to determine U(VI) speciation and the preferred type of the sorption sites on the kaolinite surface, the U and Si coordination numbers were allowed to float and corresponding σ^2 were set equal to 0.0075 and 0.0030 Å^2 [93] during the non-linear least-squares routines.

U(VI) speciation as a function of uranium concentration

Experimental U L_{III}-edge k^3-weighted EXAFS spectra that are shown in Fig. 4+ refer to the description of samples 1-4 (Table 14 in Sect. 4.3). All samples show a relative good

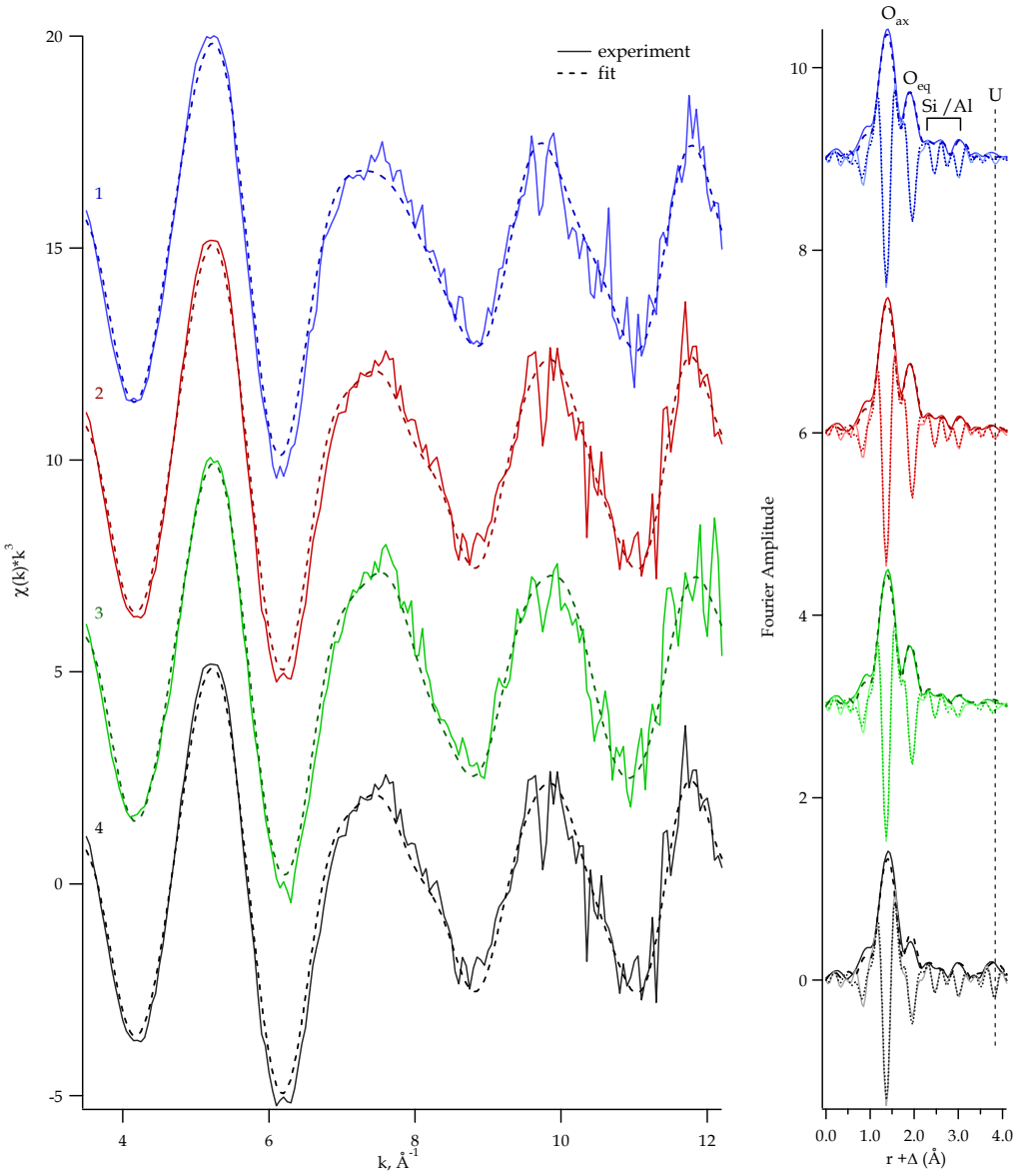

Fig. 4+: Samples 1-4. U L_{III}-edge k^3-weighted EXAFS spectra (left) and corresponding Fourier transforms (right) for U(VI) sorbed on kaolinite. Refer to Tables 18, 19 (Sect. 4.3.1).

signal-to-noise ratio out to a k value of ca. 12 Å^{-1}. All spectra are dominated by a low-frequency oscillation due to the backscattering from the nearest oxygen atoms. The Fourier transform (FT) of the EXAFS spectra represents a pseudo radial distribution function of the U near-neighbor surrounding. The prominent peaks in all FT spectra centred at ~1.3 and 1.9 Å (uncorrected for phase shift) arise from the backscattering caused by two axial and five equatorial oxygen atoms, respectively. In addition to the O_{ax}, O_{eq} coordination shells, two shells at an intermediate distance had to be included in all fits. The structural models with Al/Si backscattering atom at an average distance

of ~2.0 Å or ~2.3 Å match the experimental EXAFS data equally well. The situation is near the same as was described above for soddyite (see Fig.2+ and also Sec. 4.2). Because the least-squares fitting method could not unambiguously determine the speciation of U(VI) at the kaolinite surface, the advanced Tikhonov regularization method has been employed. All structural results of the least-squares fitting ($N, r, FWHM$) and their interpretations in comparison with the modified regularization method are presented in Sec. 4.3.1 of this work.

U(VI) speciation as a function of pH

The raw data of the U L_{III}-edge k^3-weighted EXAFS spectra of samples 6-9 together

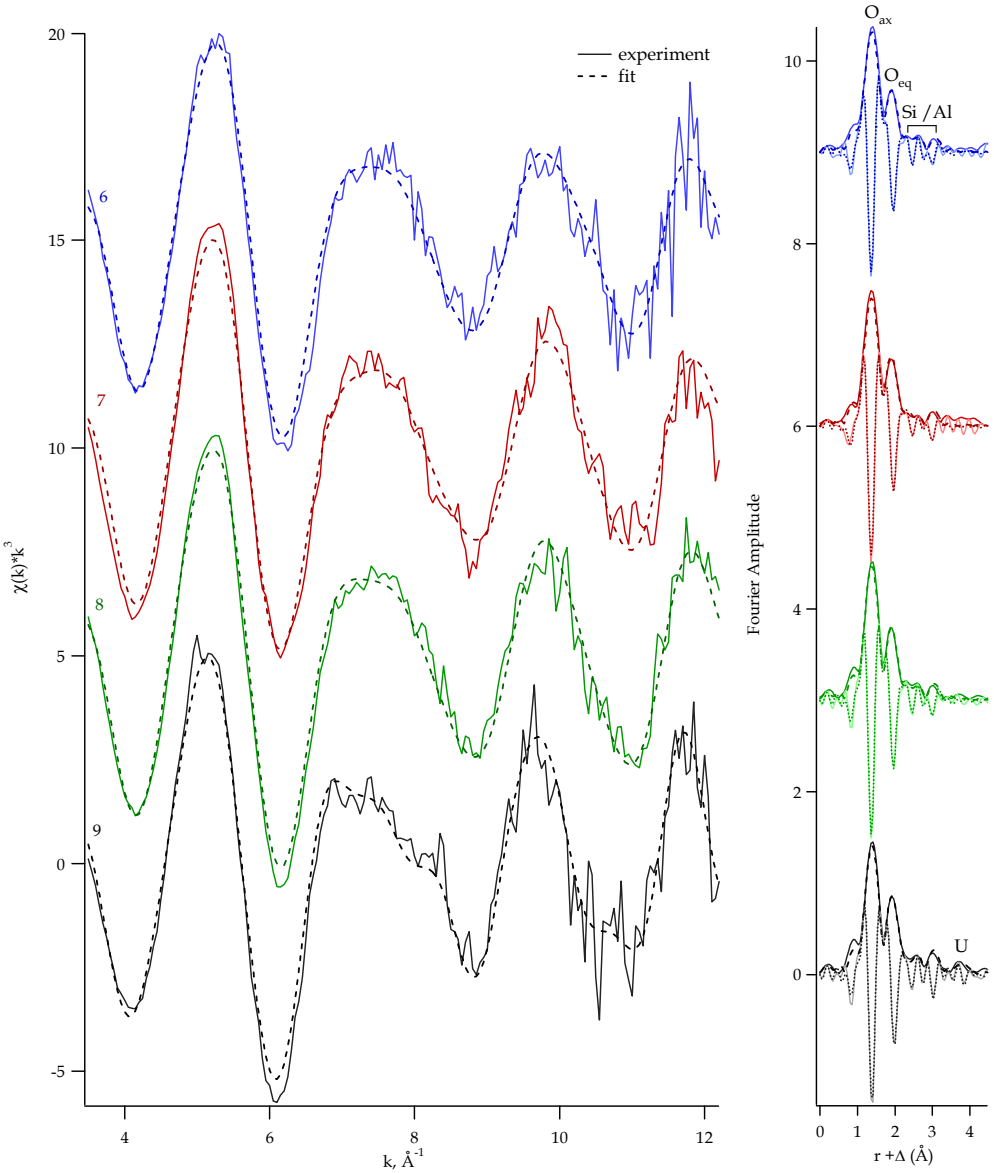

Fig. 5+: Samples 6–9. U L_{III}-edge k^3-weighted EXAFS spectra (left) and corresponding Fourier transforms (right) for U(VI) sorbed on kaolinite. Refer to Tables 23 and 24 (Sect. 4.3.2).

with the best theoretical fit to the data and the corresponding Fourier transforms (FTs) are shown in Fig. 5+. The metrical parameters derived from the least-squares fits are summarized in Tables 23 and 24. In addition to single O_{ax}, O_{eq} shells, scattering from Al/Si at ~2.3 Å or ~2.7 Å (uncorrected for phase shift) were included in all fits. It was attempt to fit a carbonate contribution (C shell at ~2.0 Å and O_{dist} at ~3.6 Å (uncorrected for phase shift)) to EXAFS data of sample 9 (pH 8.5), but this did not improve the fit. As expected for U(VI), the average distance between uranium and its two axial oxygen atoms, O_{ax}, is nearly constant for all samples and equals 1.79 ± 0.01 Å. The average coordination number for the equatorial oxygen atoms, O_{eq}, is five. The average distance of the equatorial oxygen atoms, O_{eq}, increased from 2.37 ± 0.02 Å to 2.40 ± 0.02 Å with increasing pH. Only the EXAFS fit of sample 9 (pH 8.5) included a weak U-U interaction at 3.91 ± 0.02 Å. All structural results of the least-squares fitting ($N, r, FWHM$) and their interpretations in comparison with the modified regularization method are presented in Sec. 4.3.2 of this work.

U(VI) speciation as a function of CO_2

While most of the investigated samples were prepared under atmospheric conditions at $pCO_2 = 10^{-3.5}$ atm., one (sample 10) was prepared in a glove box in argon atmosphere for comparison with sample 9 prepared under identical conditions (pH 8.5 and 10 µM U(VI)) in the presence of CO_2. The influence of HCO_3^-/CO_3^{2-} was investigated.
The U L_{III}-edge k^3-weighted EXAFS spectra of samples 9 and 10 with corresponding Fourier transforms are shown in Fig. 6+.

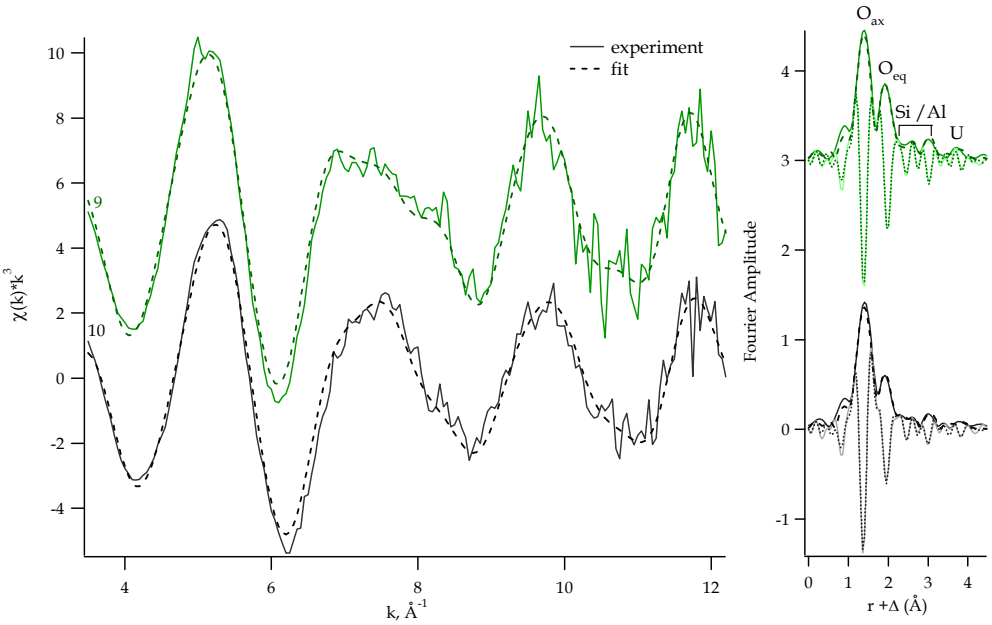

Fig. 6+: Samples 9 and 10. U L_{III}-edge k^3-weighted EXAFS spectra (left) and corresponding Fourier transforms (right) for U(VI) sorbed on kaolinite. Refer to Tables 28 and 29 (Sect. 4.3.3).

The metrical parameters are summarized in Tables 28 and 29 in Sec.4.3.3 of this work. Both spectra show U-Al/Si interaction at 3.1 ± 0.02 and 3.3 ± 0.02 Å, indicative of inner-sphere sorption of U(VI) on kaolinite, in agreement with previous EXAFS results of Thompson et al. [77]. The main difference between the fits for samples 9 and 10, which were prepared at pH 8.5 at air and in argon atmosphere, respectively, is the average distance of the equatorial oxygen atoms, O_{eq}, which decreased from 2.40 ± 0.02 Å to 2.37 ± 0.02 Å. Both EXAFS fits of samples 9 and 10 included a weak U-U interaction at 3.91 ± 0.02 Å, indicative for the formation of polynuclear U(VI) species at the kaolinite surface. In the absence of CO_2, sample 10 (pH 8.5) shows a similar spectrum as samples 6 and 7 (pH 5.0 and 6.0), i.e., the average O_{eq} distance of 2.37 ± 0.02 Å, analogous U-Al/Si interaction and weak U-U interaction.

Changes of U(VI) speciation at kaolinite surface upon drying: *Ambient and low temperature EXAFS measurements (pH 6.0 and 10 µM of U(VI) in presence of CO_2)*

The same six shells (SS UO_{ax} (axial), SS UO_{eq} (equatorial), two SS USi shells, and four-legged MS UO_{ax_1}-UO_{ax_2}) of atoms were fitted to the spectra of the wet paste sample 7 and air-dried sample 11 (both prepared at pH 6.0 and 10 µM of U(VI) total concentration in the presence of CO_2). The spectra of samples 7 and 11 were collected at ambient temperature and 28 K, respectively. The fits with six shells account for most spectral features of both spectra (Fig. 7+).

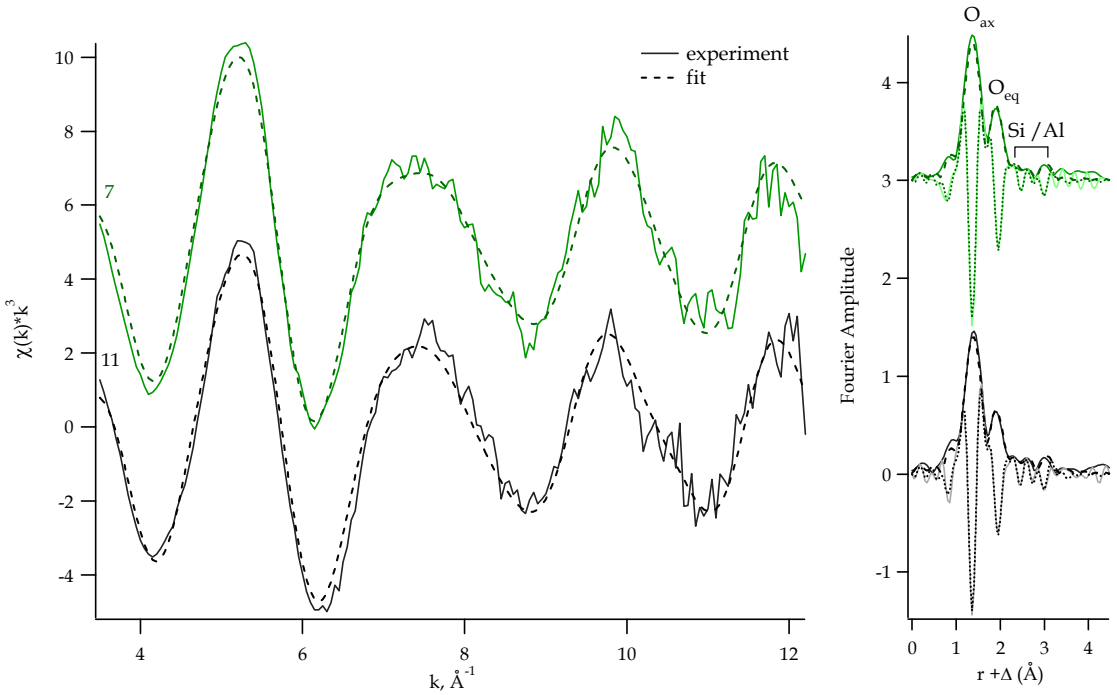

Fig. 7+. Samples 7 and 11. U L_{III}-edge k^3-weighted EXAFS spectra (left) and corresponding Fourier transforms (right) for U(VI) sorbed on kaolinite. Refer to Tables 33 and 34 (Sect. 4.3.4.1).

While both EXAFS fits of sample 7 and 11 do not include a U-U interaction, they show U-Al/Si interaction at 3.1 ± 0.02 and 3.3 ± 0.02 Å, indicative of mononuclear inner-sphere sorption of U(VI) on the kaolinite surface (see Table 33 in Sec.4.3.4.1 of this work). As expected for U(VI), the average distance between uranium and its two axial oxygen atoms, O_{ax}, is nearly constant for both samples and equals 1.79 ± 0.01 Å. The average coordination number for the equatorial oxygen atoms, O_{eq}, is five. The samples 7 and 11 did not show any change in the average distance of the equatorial oxygen atoms, O_{eq} (see Table 34 in Sec.4.3.4.1 of this work), but significantly larger DW factor, as well as *FWHM* of air-dried sample equatorial oxygen shell in absence of thermal damping at low temperature measurement can be an indication of disorder upon drying. All least-squares fitting structural results ($N, r, FWHM$) and their interpretations in comparison with the modified regularization method are presented in Sec. 4.3.4.1of this work.

Changes of U(VI) speciation at kaolinite surface upon drying: *Ambient temperature EXAFS measurements (pH 7.0 and 20 µM of U(VI) in presence of CO_2)*

Ambient temperature EXAFS measurements of samples 3 and 5, which were identically prepared at pH 7.0 and 20 µM of U(VI) in presence of CO_2, were carried out to see in details the effect of drying on the uranium sorption at the kaolinite-water interface. The raw data of the U L_{III}-edge k^3-weighted EXAFS spectra of samples prepared as wet paste and dry powder (3 and 5, respectively) together with the best theoretical fit to the data and the corresponding FTs are shown in Fig. 8+.

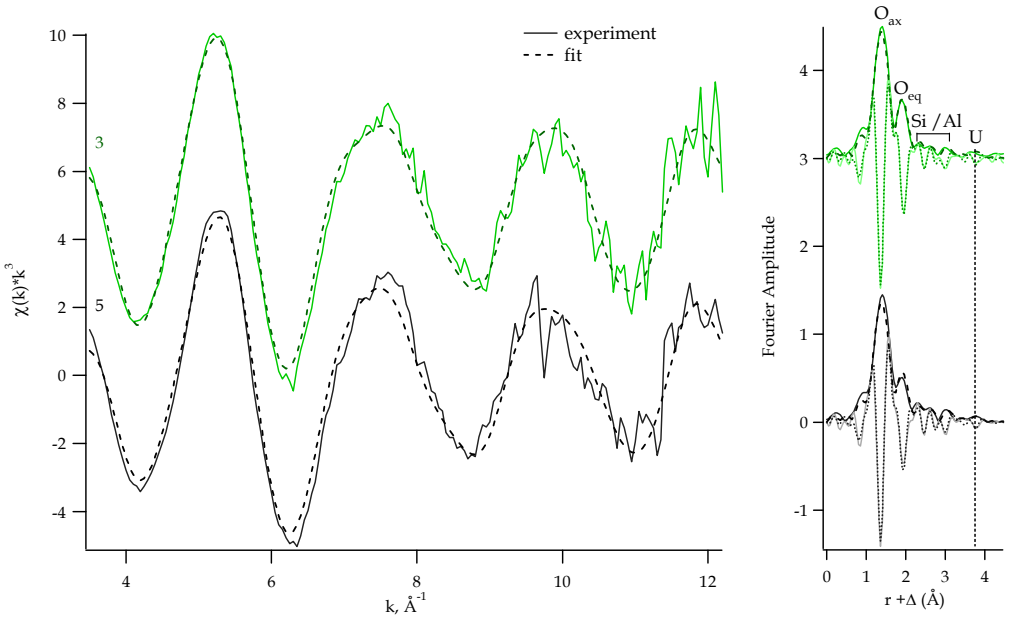

Fig. 8+. Samples 3 and 5. U L_{III}-edge k^3-weighted EXAFS spectra (left) and corresponding Fourier transforms (right) for U(VI) sorbed on kaolinite. Refer to Tables 38 and 39 (Sect. 4.3.4.2).

The average distances between uranium and its two axial oxygen atoms, O_{ax}, are 1.79 and 1.78 Å in wet paste and dry powder samples, and the average O_{eq} bond lengths of five equatorial oxygen atoms are 2.36 and 2.33 Å, correspondingly. The splitting of O_{eq} coordination shell not observed in wet paste sample is similar to that in dry powder sample, but the larger DW factor (and correspondingly *FWHM*) suggests some differences between the aqueous sorbed species in the wet paste and the dry powder samples. The absence of U-U interaction in the EXAFS spectra of samples prepared as wet paste and dry powder implies that the kaolinite surface species are mononuclear. The U-Al/Si species are fairly stabile against the drying and are indicative of inner-sphere complexation with kaolinite surface. All structural results of the least-squares fitting ($N, r, FWHM$) and their interpretations in comparison with the modified regularization method are presented in Sec. 4.3.4.2 of this work.

FIGURES INDEX

References

[1] B.K. Teo: EXAFS: Basic Principles and Data Analysis. *Springer*, Berlin (1986).

[2] D.C. Koningsberger, R. Prins: X-ray Absorption - Principles, Applications, Techniques of EXAFS, SEXAFS, and XANES. (Eds. D.C. Koningsberger, R. Prins) *John Wiley & Sons*, New York (1988).

[3] V.L. Aksenov, A.Yu. Kuzmin, J. Purans, S.I. Tyutyunnikov: EXAFS spectroscopy at synchrotron-radiation beams. *Phys. Part. Nucl.* 32(6), 675 - 707, Publisher: *MAIK Nayka* / Interperiodica Publishing, Moscow (2001).

[4] W. Matz, N. Schell, G. Bernhard, F. Prokert, T. Reich, J. Claussner, W. Oehme, R. Schlenk, S. Dienel, H. Funke, F. Eichhorn, M. Betzl, D. Pröhl, U. Strauch, G. Hüttig, H. Krug, W. Neumann, V. Brendler, P. Reichel, M. A. Denecke, H. Nitsche: ROBL - a CRG beamline for radiochemistry and materials research at the ESRF. *J. Synchrotron Rad.* **6**, 1076 - 1085 (1999).

[5] T. Reich, G. Bernhard, G. Geipel, H. Funke, C. Hennig, A. Rossberg, W. Matz, N. Schell, H. Nitsche: The Rossendorf Beam Line ROBL - a dedicated experimental station for XAFS measurements of actinides and other radionuclides. *Radiochim. Acta* **88**, 633 - 637 (2000).

[6] A.M.L. Messiah: *Quantum Mechanics. John Wiley & Sons*, New York (1966).

[7] R. de L. Kronig: *Z. Physik* **75**, 468 (1932).

[8] J.J. Rehr, R.C. Albers, C.R. Natoli, E.A. Stern: New high-energy approximation for X-ray-absorption near-edge structure. *Phys. Rev. B* **34**, 4350 - 4353 (1986).

[9] L. Fonda: Multiple-scattering theory of X-ray absorption. *J. Phys. Condens. Matter* **4**, 8269 - 8302 (1992).

[10] A. Filipponi, A. Di Cicco, C.R. Natoli: X-ray-absorption spectroscopy and *n*-body distribution functions in condensed matter. I. Theory. *Phys. Rev. B* **52**, 15122 - 15134 (1995).

[11] A. Di Cicco, M. Minicucci: Solid and liquid short-range structure determined by EXAFS multiple-scattering data analysis. *J. Synchrotron Rad.* **6**, 255 - 257 (1999).

[12] P.A. Lee, J.B. Pendry: Theory of the extended X-ray absorption fine structure. *Phys. Rev. B* **11**, 2795 - 2811 (1975).

[13] E.A. Hudson, P.G. Allen, L.J. Terminello, M.A. Denecke, T. Reich: Polarized X-ray-absorption spectroscopy of the uranyl ion: Comparison of experiment and theory. *Phys. Rev. B* **54**, 156 - 165 (1996).

[14] J.J. Rehr, R.C. Albers, S.I. Zabinsky: High-order multiple-scattering calculations of X-ray absorption fine structure. *Phys. Rev. Lett.* **69**, 3397 - 3400 (1992).

[15] S.I. Zabinsky, J.J. Rehr, A.L. Ankudinov, R.C. Albers, M.J. Eller: Multiple-scattering calculations of X-ray-absorption spectra. *Phys. Rev. B* **52**, 2995 - 3009 (1995).

[16] J.J. Rehr, R.C. Albers: Theoretical approaches to X-ray absorption fine structure. *Rev. Mod. Phys.* **73**, 621 – 654 (2000).

[17] M. Benfatto, S. Della Longa, P. D'Angelo: Advances in the theoretical analysis of the XANES (X-ray Absorption Near Edge Structure) energy region for quantitative structural use. (Conference Proceedings (12th X-Ray Absorption Fine Structure International Conference (XAFS12), 2003)) *Phys. Scr. T* **115** 28 - 30 (2005).

[18] J.J Rehr, A.L. Ankudinov: Progress in the theory and interpretation of XANES. *Coord. Chem. Rev.* **249**, 131 - 140 (2005).

[19] B. Ravel: A practical introduction to multiple scattering theory. *J. Alloys Compounds* **401**, 118 – 126 (2005).

[20] J.J Rehr, C.H. Booth, F. Bridges, S.I. Zabinsky: X-ray-absorption fine structure in embedded atoms. *Phys. Rev. B* **49**, 12347 - 12350 (1994).

[21] D.E. Sayers, B.A. Bunker: Data Analysis (Chap. 6) in: X-ray Absorption - Principles, Applications, Techniques of EXAFS, SEXAFS, and XANES. (Eds. D.C. Koningsberger, R. Prins) *John Wiley & Sons*, New York (1988).

[22] G.N. George, I.J. Pickering: EXAFSPAK – A Suite of computer programs for analysis of X-ray absorption spectra. SSRL WEB: http://www-ssrl.slac.stanford.edu/~george/ (2000).

[23] M. Newville, P. Livins, Y. Yacoby, J.J. Rehr, E.A. Stern: Near-edge X-ray absorption fine structure of Pb: A comparison of theory and experiment. *Phys. Rev. B* **47**, 14126 - 14131 (1993).

[24] M. Newville: IFEFFIT: interactive XAFS analysis and FEFF fitting. *J. Synchrotron Rad.* **8**, 322 - 324 (2001).

[25] S. Webb: SIXPack – Sam's interface for XAS package. SSRL WEB: http:// www.stanford.edu/~swebb (2002).

[26] B. Ravel, M. Newville: ATHENA, ARTEMIS, HEPHAESTUS: data analysis for X-ray absorption spectroscopy using IFEFFIT. *J. Synchrotron Rad.* **12**, 537 - 541 (2005).

[27] D.E. Sayers, E.A. Stern, F.W. Lytle: New technique for investigating noncrystalline structures. Fourier analysis of the extended X-ray-absorption fine structure. *Phys. Rev. Lett.* **27**, 1204 - 1207 (1971).

[28] R.W. Ramirez: The FFT, Fundamentals and Concepts. *Prentice–Hall*, New Jersey (1985).

[29] E.A. Stern, D.E. Sayers, F.W. Lytle: Extended X-ray absorption fine-structure technique. III. Determination of physical parameters. *Phys. Rev. B* **11**, 4836 - 4846 (1975).

[30] E. Sevillano, H. Meuth, J.J. Rehr: Extended X-ray absorption fine structure Debye-Waller factors. I. Monatomic crystals. *Phys. Rev. B* **20**, 4908 - 4911 (1979).

[31] G. Bunker: Application of the ratio method of EXAFS analysis to disordered systems. *Nucl. Instrum. Methods* **207**, 437 - 444 (1983).

[32] J.M. Tranquada, R. Ingalls: Extended X-ray-absorption fine-structure study of anharmonicity in copper(I) bromide. *Phys. Rev. B* **28**, 3520 - 3528 (1983).

[33] K. Zhang, E.A. Stern, F. Ellis, J. Sanders-Loehr, A.K. Shiemke: The active site of hemerythrin as determined by X-ray absorption fine structure. *Biochem.* **27**, 7470 - 7479 (1988).

[34] E.D. Crozier, J.J. Rehr, R. Ingalls: Amorphous and liquid systems. (Chap. 9) in: X-ray Absorption - Principles, Applications, Techniques of EXAFS, SEXAFS, and XANES. (Eds. D.C. Koningsberger, R. Prins) *John Wiley & Sons*, New York (1988).

[35] D.S. Yang, D.R. Fazzini, T.I. Morrison, L. Tröger, G. Bunker: Modelling of pair distribution functions for XAFS in disordered systems. *J. Non-Cryst. Sol.* **210**, 275 -286 (1997).

[36] P. Rabe, R. Haensel: The extended X-ray absorption fine structure and its applicability for structural analysis. *Festkörperprobl.* **20**, 43 – 86 (1980).

[37] A. Sadoc, D. Raoux, P. Lagarde, A. Fontaine: EXAFS studies of the nickel-yttrium ($Ni_{66}Y_{33}$) and copper-zirconium ($Cu_{60}Zr_{40}$) amorphous alloys: a modelling of the pair distribution function with two subshells. *J. Non-Cryst. Sol.* **50**, 331 - 349 (1982).

[38] P. Lagarde, J. Rivory, G. Vlaic: Structural studies of amorphous cobalt-phosphorus and nickel-phosphorus by EXAFS. *J. Non-Cryst. Sol.* **57**, 275 - 287 (1983).

[39] G. Calas, J. Petiau: Structure of oxide glasses: spectroscopic studies of local order and crystallochemistry. Geochemical implications. *Bull. Mineralogie* **106**, 33 -55 (1983).

[40] A. Filipponi: EXAFS for liquids. *J. Phys. Condens. Matter* **13**, R23 - R60 (2001).

[41] Yu.A. Babanov, V.V. Vasin, A.L. Ageev, N.V. Ershov: A new interpretation of EXAFS spectra in real space. I. General formalism. *Phys. Stat. Sol.B* **105**, 747 - 754 (1981).

[42] N.V. Ershov, A.L. Ageev, V.V. Vasin, Yu.A. Babanov: A new interpretation of EXAFS spectra in real space. II. A comparison of the regularization technique with the Fourier transformation method. *Phys. Stat. Sol. B* **108**, 103 - 111 (1981).

[43] G. Khelashvili, G. Bunker: Practical regularization methods for analysis of EXAFS spectra. *J. Synchrotron Rad.* **6**, 271 - 273 (1999).

[44] K. Yamaguchi,Y. Ito, T. Mukoyama, M. Takahashi, S. Emura: The regularization of the basic X-ray absorption spectrum fine structure equation via the wavelet-Galerkin method. *J. Phys. B* **32**, 1393 - 1408 (1999).

[45] P.A. Lee, G. Beni: New method for the calculation of atomic phase shifts: Application to extended X-ray absorption fine structure (EXAFS) in molecules and crystals. *Phys. Rev. B* **15**, 2862 - 2883 (1977).

[46] E.D. Crozier, A.J. Seary: Asymmetric effects in the extended X-ray absorption fine structure analysis of solid and liquid zinc. *Can. J. Phys.* **58**, 1388 - 1399 (1980).

[47] B.K. Teo, H.S. Chen, R. Wang, M.R. Antonio: EXAFS of glassy metallic alloys: amorphous and crystalline molybdenum-nickel (MoNi). *J. Non-Cryst. Sol.* **58**, 249 - 274 (1983).

[48] F. Demartin, C.M. Gramaccioli, T. Pilati: The importance of accurate structure determination of uranium minerals. II. Soddyite $(UO_2)_2SiO_4 \times 2H_2O$. *Acta Cryst. C* **48**, 1 - 4 (1992).

[49] A.N. Tikhonov, V.Ya. Arsenin: Solution of ill-posed problems. *John Wiley & Sons*, New York (1977).

[50] A. Kirsch: An Introduction to the mathematical theory of inverse problems. *Springer*, New York (1996).

[51] V.V. Vasin, A.L. Ageev: Ill-posed problems with *a priori* information. *VSP, Utrecht*, Netherlands (1995).

[52] Yu.A. Babanov, V.R. Shvetsov: EXAFS: Bond length determination for multi-component systems. *Phys. Stat. Sol. B* **131**, 1 - 4 (1985).

[53] A. Corrias, G. Navarra, S. Seatzu, F. Utreras: Two-phase regularization method in Hilbert Spaces: Description and application to EXAFS problem. *Inv. Probl.* **4**, 449 – 470 (1988).

[54] Yu.A. Babanov, N.V. Ershov, V.R. Shvetsov, A.V. Serikov, A.L. Ageev, V.V. Vasin: A new method of determining partial radial distribution functions for amorphous alloys. I. The quasibinary problem. *J. Non-Cryst. Sol.* **79**, 1 – 17 (1986).

[55] H.J. Krappe, H.H. Rossner: Error analysis of XAFS measurements. *Phys. Rev. B* **61**, 6596 – 6610 (2000).

[56] D.S. Yang, G. Bunker: Improved *R*-space resolution of EXAFS spectra using combined regularization methods and nonlinear least-squares fitting. *Phys.Rev. B* **54**(5), 3169 – 3172 (1996).

[57] M. Kunicke, I.Yu. Kamensky, Yu.A. Babanov, H. Funke: Efficient determination of optimal regularization parameter for inverse problem in EXAFS spectroscopy. (12th X-Ray Absorption Fine Structure International Conference (XAFS12), 2003) *Phys. Scr. T* **115**, 237 - 239 (2005).

[58] Yu.A. Babanov, T.Ye. Zayarnaya, T. Reich, H. Funke: EXAFS study of U(VI) compounds: A new approach to data analysis. (Workshop Proceedings „Speciation, Techniques and Facilities for Radioactive Materials at Synchrotron Light Sources", 2000) *OECD*, 105 – 116 (2002).

[59] A.N. Deev, Yu.A. Babanov: Application of trial functions in the iteration process of solving inverse ill-posed problems of EXAFS spectroscopy. *Phys. Met. Metallogr.* **95**, 433 - 440 (2003).

[60] A.L. Ageev, T.V. Antonova, T.Ye. Reich, T. Reich, C. Hennig: Method of separating functionals for extracting local atomic structure. *Math. Modelling* **16**, 81 - 92 (2004) (in Russian).

[61] A.L. Ageev, M.E. Korshunov, T.Ye. Reich, T. Reich, H. Moll: Application of regularization methods to analysis of EXAFS spectra in chemical complexes. *J. Inverse Ill-Posed Problems* **15**, 767 - 784 (2007).

[62] A.J. Dent, J.D.F. Ramsay, S.W. Swanton: An EXAFS study of uranyl ions in solution and sorbed onto silica and montmorillonite clay colloids. *J. Colloid Interface Sci.* **150**, 45 – 60 (1992).

[63] A. Manceau, L. Charlet, M.C. Boisset, B. Didier, L. Spadini: Sorption and speciation of heavy metals on hydrous Fe and Mn oxides: From microscopic to macroscopic. *Appl. Clay Sci.* **7**, 201 – 223 (1992).

[64] F. Farge, C.W. Ponader, G. Calas, and G.E. Brown Jr.: Structural environments of incompatible elements in silicate glass melt systems: II. U^{IV}, U^{V}, and U^{VI}. *Geochim. Cosmochim. Acta* **56**, 4205 – 4220 (1992).

[65] F. Farge, R.C. Ewing, and G.E. Brown Jr.: The structure of aperiodic, metamict, $(CaTh)ZrTi_2O_7$: an EXAFS study of the Zr, Th, and U sites. *J. Mat. Res.* **8**, 1983 – 1995 (1993).

[66] C.J. Chisholm-Brause, S.D. Conradson, C.T. Buscher, P.G. Eller, and D.E. Morris: Speciation of uranyl sorbed at multiple binding-sites on montmorillonite. *Geochim. Cosmochim. Acta* **58**, 3625 – 3631 (1994).

[67] T.D. Waite, J.A. Davis, T.E. Payne, G.A. Waychunas, and N. Xu: Uranium(VI) adsorption to ferrihydrite: Application of a surface complexation model. *Geochim. Cosmochim. Acta* **58**, 5465 – 5478 (1994).

[68] P.G. Allen, J.J. Bucher, D.L. Clark, N.M. Edelstein, S.A. Ekberg, J.W. Gohdes, E.A. Hudson, N. Kaltsoyannis, W.W. Lukens, M.P. Neu, P.D. Palmer, T. Reich, C.D. Tait, and B.D. Zwick: Multinuclear NMR, Raman, EXAFS, and X-ray diffraction studies of uranyl carbonate complexes in near-neutral aqueous solution. X-ray structure of $[C(NH_2)_3]_6[(UO_2)_3(CO_3)_6]$ x $6.5H_2O$. *Inorg. Chem.* **34**, 4797 – 4807 (1995).

[69] T. Reich, H. Moll, M.A. Denecke, G. Geipel, G. Bernhard, H. Nitsche, P.G. Allen, J.J. Bucher, N. Kaltsoyannis, N.M. Edelstein, and D.K. Shuh: Characterization of hydrous uranyl silicate by EXAFS. *Radiochim. Acta* **74**, 219 - 223 (1996).

[70] D.E. Morris, P.G. Allen, J.M. Berg, C.J. Chisholm-Brause, S.D. Conradson, R.J. Donohoe, N.J. Hess, J.A. Musgrave, and C.D. Tait: Speciation of uranium in Fernald soils by molecular spectroscopic methods: Characterization of untreated soils. *Environ. Sci. Technol.* **30**, 2322 – 2331 (1996).

[71] P.G. Allen, D.K. Shuh, J.J. Bucher, N.M. Edelstein, C.E.A. Palmer, R.J. Silva, S.N. Nguyen, L.N. Marquez, and E.A. Hudson: Determinations of uranium structures by EXAFS: Schoepite and other U(VI) oxide precipitates. *Radiochim. Acta* **75**, 47 - 53 (1996).

[72] H.A. Thompson, G.E. Brown Jr., and G.A. Parks: XAFS spectroscopic study of uranyl coordination in solids and aqueous solution. *Am. Mineral.* **82**, 483 – 496 (1997).

[73] M.A. Denecke, T. Reich, S. Pompe, M. Bubner, K.H. Heise, H. Nitsche, P.G. Allen, J.J. Bucher, N.M. Edelstein, and D.K. Shuh: Differentiating between monodentate and bidentate carboxylate ligands coordinated to uranyls ions using EXAFS. *J. Phys. IV France 7*, *Colloque* **C2**, 637 – 638 (1997).

[74] F. Farges, G.E. Brown Jr., and Z. Wu: Coordination of actinides in silicate melts. . *J. Phys. IV France 7*, *Colloque* **C2**, 1009 – 1010 (1997).

[75] P.G. Allen, J.J. Bucher, D.K. Shuh, N.M. Edelstein, and T. Reich: Investigation of aquo and chloro complexes of UO_2^{2+}, NpO_2^{+}, Np^{4+}, and Pu^{3+} by X-ray absorption fine structure spectroscopy. *Inorg. Chem.* **36**, 4676 – 4683 (1997).

[76] T. Reich, H. Moll, T. Arnold, M.A. Denecke, C. Hennig, G. Geipel, G. Bernhard, H. Nitsche, P.G. Allen, J.J. Bucher, N.M. Edelstein, and D.K. Shuh: An EXAFS study of uranium(VI) sorption onto silica gel and ferrihydrite. *J. Electron Spectrosc. Related Phenom.* **96**, 237 – 243 (1998).

[77] H.A. Thompson, G.A. Parks, and G.E. Brown Jr.: Structure and composition of uranium^{VI} sorption complexes at the kaolinite-water interface. (Chap. 16) in:

Adsorption of metals by geomedia. (Ed. E.J. Jenne) *Academic Press*, San Diego, California (1998).

[78] E.A. Hudson, L.J. Terminello, B.E. Viani, M.A. Denecke, T. Reich, P.G. Allen, J.J. Bucher, D.K. Shuh, and N.M. Edelstein: The structure of U^{6+} sorption complexes on vermiculite and hydrobiotite. *Clay Clays Minerals* **47**, 439 – 457 (1999).

[79] J.R. Bargar, R. Reitmeyer, and J.A. Davis: Spectroscopic confirmation of uranium(VI)-carbonato adsorption complexes on hematite. *Environ. Sci. Technol.* **33**, 2481 – 2484 (1999).

[80] T. Allards, P. Ildefonse, C. Beaucaire, and G. Calas: Structural chemistry of uranium associated with Si, Al, Fe gels in a granitic uranium mine. *Chem. Geology* **158**, 81 – 103 (1999).

[81] D.L. Clark, S.D. Conradson, R.J. Donohoe, D.W. Keogh, D.E. Morris, P.D. Palmer, R.D. Rogers, and C.D. Tait: Chemical speciation of the uranyl ion under highly alkaline conditions: Synthesis, structures, and oxo ligand exchange dynamics. *Inorg. Chem.* **38**, 1456 – 1466 (1999).

[82] U. Wahlgren, H. Moll, I. Grenthe, B. Schimmelpfennig, L. Maron, V. Vallet, and O. Gropen: Structure of uranium(VI) in strong alkaline solutions. A combined theoretical and experimental investigations. *J. Phys. Chem. A* **103**, 8257 – 8264 (1999).

[83] E.R. Sylwester, E.A. Hudson, and P.G. Allen: The structure of uranium (VI) complexes on silica, alumina, and montmorillonite. *Geochim. Cosmochim. Acta* **64**, 2431 – 2438 (2000).

[84] J.R. Bargar, R. Reitmeyer, J.J. Lenhart, and J.A. Davis: Characterization of U(VI)-carbonato ternary complexes on hematite: EXAFS and electrophoretic mobility measurements. *Geochim. Cosmochim. Acta* **64**, 2737 – 2749 (2000).

[85] L.N. Moyes, R.H. Parkman, J.M. Charnock, D.J. Vaughan, F.R. Livens, C.R. Hughes, and A. Braithwaite: Uranium uptake from aqueous solution by interaction with goethite, lepidocrocite, muscovite, and mackinawite: An X-ray absorption spectroscopy study. *Environ. Sci. Technol.* **34**, 1062 – 1068 (2000).

[86] R.J. Reeder, M. Nugent, G.M. Lamble, C.D. Tait, and D.E. Morris: Uranyl incorporation into calcite and aragonite: XAFS and luminescence studies. *Environ. Sci. Technol.* **34**, 638 – 644 (2000).

[87] H. Moll, T. Reich, and Z. Szabo: The hydrolysis of dioxouranium(VI) investigated using EXAFS and ^{17}O-NMR. *Radiochim. Acta* **88**, 411 - 415 (2000).

[88] A.J. Francis, C.J. Dodge, J.B. Gillow, and H.W. Papenguth: Biotransformation of uranium compounds in high ionic strength brine by a halophilic bacterium under denitrifying conditions. *Environ. Sci. Technol.* **34**, 2311 – 2317 (2000).

[89] G. Bernhard, G. Geipel, T. Reich, V. Brendler, S. Amayri, and H. Nitsche: Uranyl(VI) carbonate complex formation: Validation of the $Ca_2UO_2(CO_3)_3$(aq.) species. *Radiochim. Acta* **89**, 511 - 518 (2001).

[90] C. Hennig, P.J. Panak, T. Reich, A. Rossberg, J. Raff, S. Selenska-Pobell, W. Matz, J.J. Bucher, G. Bernhard, H. Nitsche: EXAFS investigation of uranium(VI) complexes formed at Bacillus cereus and Bacillus sphaericus surfaces. *Radiochim. Acta* **89**, 625 - 631 (2001).

[91] G. Redden, J.R. Bargar, and R. Bencheikh-Latmani: Citrate enhanced uranyl adsorption on goethite: An EXAFS analysis. *J. Colloid Interface Sci.* **244**, 211 – 219 (2001).

[92] R.J. Reeder, M. Nugent, C.D. Tait, D.E. Morris, S.M. Heald, K.M. Beck, W.P. Hess, and A. Lanzirotti: Co-precipitation of uranium(VI) with calcite: XAFS, micro-XAS, and luminescence characterization. *Geochim. Cosmochim. Acta* **65**, 3491 – 3503 (2001).

[93] C. Hennig, T. Reich, R. Dähn, and A.M. Scheidegger: Structure of uranium sorption complexes at montmorillonite edge sites. *Radiochim. Acta* **90**, 9 - 11 (2002).

[94] B.C. Bostick, S. Fendorf, M.O. Barnett, P.M. Jardine, and S.C. Brooks: Uranyl surface complexes formed on subsurface media from DOE facilities. *Soil Sci. Society Amer. J.* **66**, 99 – 108 (2002).

[95] C.C. Fuller, J.R. Bargar, J.A. Davis, and M.J. Piana: Mechanisms of uranium interactions with hydroxyapatite: Implications for groundwater remediation. *Environ. Sci. Technol.* **36**, 158 – 165 (2002).

[96] C.J. Dodge, A.J. Francis, J.B. Gillow, G.P. Halada, C. Eng, and C.R. Clayton: Association of uranium with iron oxides typically formed on corroding steel surfaces. *Environ. Sci. Technol.* **36**, 3504 – 3511 (2002).

[97] S.D. Kelly, K.M. Kemner, J.B. Fein, D.A. Fowle, M.I. Boyanov, B.A. Bunker, and N. Yee: X-ray absorption fine structure determination of pH-dependent U-bacterial cell wall interactions. *Geochim. Cosmochim. Acta* **66**, 3855 – 3871 (2002).

[98] C. Hennig, G. Reck, T. Reich, A. Rossberg, W. Kraus, and J. Sieler: EXAFS and XRD investigations of zeunerite and meta-zeunerite. *Z. Kristallogr.* **218**, 37 – 45 (2003).

[99] S.D. Kelly, M.G. Newville, L. Cheng, K.M. Kemner, S.R. Sutton, P. Fenter, N.C. Sturchio, and C. Spotl: Uranyl incorporation in natural calcite. *Environ. Sci. Technol.* **37**, 1284 – 1287 (2003).

[100] M. Walter, T. Arnold, T. Reich, and G. Bernhard: Sorption of uranium(VI) onto ferric oxides in sulfate-rich acid waters. *Environ. Sci. Technol.* **37**, 2898 – 2904 (2003).

[101] C. Den Auwer, R. Drot, E. Simoni, S.D. Conradson, M. Gailhanou, and J. Mustre de Leon: Grazing incidence XAFS spectroscopy of uranyl sorbed onto TiO_2 rutile surfaces. *New J. Chem.* **27**, 648 – 655 (2003).

[102] M.A. Denecke, J. Rothe, K. Dardenne, and P. Lindqvist-Reis: Grazing incidence (GI) XAFS measurements of Hf(IV) and U(VI) sorption onto mineral surfaces. *Phys. Chem. Chem. Phys.* **5**, 939 – 946 (2003).

[103] H. Moll, G. Geipel, T. Reich, G. Bernhard, T. Fanghänel, and I. Grenthe: Uranyl(VI) complexes with alpha-substituted carboxylic acids in aqueous solution. *Radiochim. Acta* **91**, 11 - 20 (2003).

[104] A. Koban, G. Geipel, A. Rossberg, G. Bernhard: Uranium(VI) complexes with sugar phosphates in aqueous solution. *Radiochim. Acta* **92**, 903 - 908 (2004).

[105] S.D. Conradson, D. Manara, F. Wastin, D.L. Clark, G.H. Lander, L.A. Morales, J. Rebizant, V.V. Rondinella: Local structure and charge distribution in the UO_2-U_4O_9 system. *Inorg. Chem.* **43**(22), 6922 - 6935 (2004).

[106] E.J. Elzinga, C.D. Tait, R.J. Reeder, K.D. Rector, R.J. Donohoe, D.E. Morris: Spectroscopic investigation of U(VI) sorption at the calcite-water interface. . *Geochim. Cosmochim. Acta* **68**, 2437 – 2448 (2004).

[107] J.G. Catalano, and G.E. Brown Jr.: Analysis of uranyl-bearing phases by EXAFS spectroscopy: Interferences, multiple scattering, accuracy of structural parameters, and spectral differences. *Amer. Mineralogist* **89**, 1004 – 1021 (2004).

[108] J.G. Catalano, and G.E. Brown Jr.: Uranyl adsorption onto montmorillonite: Evaluation of binding sites and carbonate complexation. . *Geochim. Cosmochim. Acta* **69**, 2995 - 3005 (2005).

[109] M. Del Nero, A. Froideval, C. Gaillard, G. Mignot, R. Barillon, I. Munier, A. Ozgumus: Mechanisms of uranyl sorption. *Geol. Soc. Spec. Publ.* **236**, 545 – 560 (2004).

[110] T.V. Khijniak, A.I. Slobodkin, V. Coker, J.C. Renshaw, F.R. Livens, E.A. Bonch-Osmolovskaya, N.K. Birkeland, N.N. Medvedeva-Lyalikova, J.R. Lloyd: Reduction of uranium(VI) phosphate during growth of the thermophilic bacterium Thermoterrabacterium ferrireducens. *Appl. Environ. Microbiol.* **71**, 6423 - 6426 (2005).

[111] J.A. Greathouse, H.R. Stellalevinsohn, M.A. Denecke, A. Bauer, R.T. Pabalan: Uranyl surface complexes in a mixed-charge montmorillonite: Monte Carlo computer simulation and polarized XAFS results. *Clays Clay Minerals* **53**, 278 – 286 (2005).

[112] J.G. Catalano, T.P. Trainor, P.J. Eng, G.A. Waychunas, G.E. Brown Jr.: CTR diffraction and grazing-incidence EXAFS study of U(VI) adsorption onto α-Al_2O_3 and α-Fe_2O_3 $(1\bar{1}02)$ surfaces. *Geochim. Cosmochim. Acta* **69**, 3555 - 3572 (2005).

[113] Y. Arai, M. McBeath, J.R. Bargar, J. Joye, J.A. Davis: Uranyl adsorption and surface speciation at the imogolite-water interface: Self-consistent spectroscopic and surface complexation models. *Geochim. Cosmochim. Acta* **70**, 2492 - 2509 (2006).

[114] S.M. Webb, C.C. Fuller, B.M. Tebo, J.R. Bargar: Determination of uranyl incorporation into biogenic manganese oxides using X-ray absorption spectroscopy and scattering. *Environ. Sci. Technol.* **40**, 771 – 777 (2006).

[115] M.A. Denecke: Actinide speciation using X-ray absorption fine structure spectroscopy. *Coord. Chem. Rev.* **250**, 730 – 754 (2006).

[116] T.Ye. Reich, M.E. Korshunov, T.V. Antonova, A.L. Ageev, H. Moll, T. Reich: New regularization method for EXAFS analysis. (Conference Proceedings (X-Ray Absorption Fine Structure, 13th International Conference (XAFS13), 2006)) *Am. Inst. Phys.* **882**, 153 – 155 (2007).

[117] IGOR Pro – integrated program for visualizing, analyzing, transforming and presenting data. P.O. Box 2088 / Lake Oswego, Oregon 97035 / USA, http: /www.wavemetrics.com.

[118] H. Moll, W. Matz, G. Schuster, V. Brendler, G. Bernhard, H. Nitsche: Synthesis and characterization of uranyl orthosilicate $(UO_2)_2SiO_4$ x $2H_2O$. *J. Nucl. Mat.* **227**, 40 - 49 (1995).

[119] P. Gürtler, G. Materlik, J.R. Schneider: Experimental stations at Hasylab**.** *Hamburger Synchrotronstrahlungslabor Hasylab at Deutsches Elektronen-Synchrotron DESY*, Hamburg 22 p. (1994).

[120] A.L. Ankudinov, C.E. Bouldin, J.J. Rehr, J. Sims, H. Hung: Parallel calculation of electron multiple scattering using Lanczos algorithms. *Phys. Rev. B* **65**(10), 104107/1 - 104107/11 (2002).

[121] R.B. Neder, M. Burghammer, Th. Grasl, H. Schulz, A. Bram, S. Fiedler, C. Riekel: Single-crystal diffraction by submicrometer sized kaolinite; observation of Bragg reflection and diffuse scattering. *Z. Kristallogr.* **211**, 763 – 765 (1996).

[122] R.B. Neder, M. Burghammer, Th. Grasl, H. Schulz, A. Bram, and S. Fiedler: Refinement of the kaolinite structure from single-crystal synchrotron data. *Clays Clay Minerals* **47**, 487 - 494 (1999).

[123] J.R. Plaisier, D.J.W. Ijdo, C. de Mello Donega, G. Blasse: Structure and luminescence of barium uranium disilicate ($BaUO_2Si_2O_6$). *Chem. Mater.* **7**, 738 – 743 (1995).

[124] H. Sawada: Residual electron density study of α-aluminium oxide through refinement of experimental atomic scattering factors. *Mat. Res. Bull.* **29**, 127-133 (1994).

[125] S.P. Hyun, Y.H. Cho, P.S. Hahn, S.J. Kim: Sorption mechanism of U(VI) on a reference montmorillonite: binding to the internal and external surfaces. *J. Radioanalyt. Nucl. Chem.* **250**, 55 - 62 (2001).

[126] A. Kŕepelová, S. Sachs, G. Bernhard: Uranium(VI) sorption onto kaolinite in the presence and absence of humic acid. *Radiochim. Acta* **94**, 825-833 (2006).

[127] T. Reich, S. Amayri, J. Drebert, S. Boulyga: EXAFS Study of uranium(VI) sorption on kaolinite. (Workshop Proceedings „Speciation, Techniques and Facilities for Radioactive Materials at Synchrotron Light Sources", 2004) *OECD* **6046**, 61 – 67 (2006).

[128] T. Reich, T.Ye. Reich, S. Amayri, J. Drebert, N.L. Banik, R.A. Buda, J.V. Kratz, and N. Trautmann: Application of XAFS spectroscopy to actinide environmental science. (Conference Proceedings (X-Ray Absorption Fine Structure, 13th International Conference (XAFS13), 2006)) *Am. Inst. Phys.* **882**, 179 – 183 (2007).

[129] K. Sekine, T.E. Payne, T.D. Waite, J.A. Davis: International Alligator Rivers analogue project (18): Experimental study of the uranium adsorption on kaolinite – pH dependence in air-equilibrated system. *JAERI-memo* **03-036**, 1 – 14 (1991).

[130] G.D. Redden, J. Li, J. Leckie: Adsorption of U^{VI} and citric acid on goethite, gibbsite, and kaolinite: Comparing results for binary and ternary systems. in: Adsorption of Metals to Geomedia. (Ed. E.A. Jenne) *Academic Press*, San Diego, 291 – 317 (1998).

[131] I. Puigdomenech: Chemical equilibrium software (**M**ake **E**quilibrium **D**iagrams **U**sing **S**ophisticated **A**lgorithms); Inorganic Chemistry, Royal Institute of Technology (KTH), SE-100 44 Stockholm, Sweden.

[132] I. Grenthe, J. Fuger, R.J.M. Konings, R.J. Lemire, A.B. Muller, C. Nguyen-Trung, H. Wanner: Chemical thermodynamics of uranium. *Elsevier Sci. Publ.*, Amsterdam 715 p. (1992).

[133] T.Ye. Reich, T. Reich, A.L. Ageev: Application of the Tikhonov regularization method to the detection of U-Si neighbours in soddyite using EXAFS spectroscopy. *Ann. Rep. Inst. Nucl. Chem. 2004*, University of Mainz, C4 (2005).

[134] F. Coppin, G. Berger, A. Bauer, S. Castet, M. Loubet: Sorption of lanthanides on smectite and kaolinite. *Chem. Geology* **182**, 57 - 68 (2002).

[135] J.A. Davis, J.O. Leckie: Surface ionization and complexation at the oxide/water interface. II. Surface properties of amorphous iron oxyhydroxide and adsorption of metal ions. *J. Colloid Interface Sci.* **67**, 90 – 107 (1978).

[136] J.A. Davis, D.B. Kent: Surface complexation modelling in aqueous geochemistry in: Mineral–Water Interface Geochemistry, Reviews in Mineralogy. (Eds. M.F. Hochella, A.F. White) *Min. Soc. Am.*, Washington (1990).

[137] R.K Iler**:** The chemistry of silica: solubility, polymerization, colloid and surface properties and biochemistry. *John Wiley & Sons*, New York 892 p. (1979).

[138] C.P. Huang, W. Stumm: Specific adsorption of cations on hydrous γ-Al_2O_3. *J. Colloid Interface Sci.* **43**, 409 – 420 (1973).

[139] C.P. Huang: The surface acidity of hydrous solids in: Adsorption of Inorganics. (Eds. M.A.A.J. Rubin) *Ann Arbor Sci. Publ.*, Ann Arbor, 183 - 217 (1981).

[140] S. Carroll-Webb, J.V. Walther: A surface complex reaction model for the pH-dependence of corundum and kaolinite dissolution. *Geochim. Cosmochim. Acta* **52**, 2609 - 2623 (1988).

[141] T.Ye. Reich, N.L. Banik, R.A. Buda, S. Amayri, J. Drebert, J.V. Kratz, N. Trautmann, A.L. Ageev, M.E. Korshunov, T. Reich: EXAFS study of plutonium sorption onto kaolinite. (Workshop Proceedings „Speciation, Techniques and Facilities for Radioactive Materials at Synchrotron Light Sources", 2006) *OECD* **6288**, 273 – 279 (2007).

[142] N.L. Banik, R.A. Buda, S. Bürger, J.V. Kratz, N. Trautmann: Sorption of tetravalent plutonium and humic substances onto kaolinite. *Radiochim. Acta* **95**, 569 - 575 (2007).

[143] R.A. Buda, N.L. Banik, J.V. Kratz, N. Trautmann *Radiochim. Acta* (submitted).

[144] M.A. Denecke, J. Rothe, K. Dardenne, H. Blank, J. Hormes: The INE-beamline for actinide research at ANKA. *Phys. Scr. T* **115**, 1001 – 1003 (2005).

[145] S.D. Conradson**:** Application of X-ray absorption fine structure spectroscopy to materials and environmental science. *Appl. Spectrosc.* **52**, 252A – 279A (1998).

Acknowledgements

This dissertation was conducted in the Institute of Nuclear Chemistry of Gutenberg University in Mainz. My thinking benefited a lot from the inspiring and creative atmosphere as well as the professional excellence of scientists and visiting scientists here.

This dissertation would not have been possible without unconditional and 'relentless' support of my advisor.

I am very grateful to mathematicians from Institute for Mathematic and Mechanic in Yekaterinburg for the professional software that they made for this study and for the helpful answers to my questions. I thank them for investing time and energy ideas.

I want to express my deep appreciation for my colleagues from Institute of Nuclear Chemistry of Gutenberg University for the preparation of high quality samples, which are the material background for success of this study, as also for pleasure to learn from them things that range from chemistry to social behaviour.

I gratefully acknowledge ESRF and ANKA for provision of synchrotron radiation facilities for EXAFS measurements of this study.

I would be remiss if I did not express my deepest gratitude to my family for their understanding, love, and many ways support encouraged me to carry my Ph. D. project to its conclusion. I give my sincere thanks for all of them.

Erklärung

Hiermit erkläre ich, dass ich die vorliegende Arbeit selbstständig und ohne fremde Hilfe verfasst, andere als die angegebenen Quellen und Hilfsmittel nicht benutzt und die aus fremden Quellen entnommenen Stellen als solche gekennzeichnet habe.

Mainz, den 23.05.2008

Tatiana Reich